Onderzoek naar de verbranding van alcohol-benzine-mengsels in verbrandingsmotoren

A Study of the Combustion of Alcohol-Gasoline Blends in Internal Combustion Engines

Louis Sileghem

Promotor: prof. dr. ir. S. Verhelst
Proefschrift ingediend tot het behalen van de graad van
Doctor in de Ingenieurswetenschappen: Werktuigkunde-Elektrotechniek

Vakgroep Mechanica van Stroming, Warmte en Verbranding
Voorzitter: prof. dr. ir. J. Vierendeels
Faculteit Ingenieurswetenschappen en Architectuur
Academiejaar 2014 - 2015

UNIVERSITEIT GENT

ISBN 978-90-8578-818-8
NUR 977, 978
Wettelijk depot: D/2015/10.500/62

Universiteit Gent
Faculteit Ingenieurswetenschappen en Architectuur
Vakgroep Mechanica van Stroming, Warmte en Verbranding

Promotor: prof. dr. ir. Sebastian Verhelst

Universiteit Gent
Faculteit Ingenieurswetenschappen en Architectuur

Vakgroep Mechanica van Stroming, Warmte en Verbranding
Sint-Pietersnieuwstraat 41, B-9000 Gent, België

Tel.: +32-9-264.33.59
Fax.: +32-9-264.35.90

Dit werk kwam tot stand in het kader van een aspirantenmandaat van het FWO-Vlaanderen (Fonds Wetenschappelijk Onderzoek - Vlaanderen) (FWO11/ASP/056) .

Department of Flow, Heat and Combustion Mechanics

Proefschrift tot het behalen van de graad van
Doctor in de Ingenieurswetenschappen:
Werktuigkunde - Elektrotechniek
Academiejaar 2014-2015

“To alcohol! The cause of... and solution to... all of life’s problems.”

MATT GROENING

Dankwoord

´Vier jaar lang op je eigen houtje werken aan je doctoraat in alle eenzaamheid' is waarschijnlijk één van de clichés die heerst bij veel mensen over doctoraatstudenten. Gelukkig is niets minder waar. Hierbij wil ik dan ook mijn oprechte dank betuigen aan enkele personen die op een bepaalde manier hebben bijgedragen tot mijn doctoraat.

De persoon die het meeste heeft geholpen om mijn doctoraat vorm te geven is mijn promotor, Prof. dr. ir Sebastian Verhelst. Graag zou ik hem bedanken om mij te verleiden toch te doctoreren en voor al het vertrouwen dat hij mij gaf zodat ik mij als onderzoeker kon ontwikkelen. Zijn kritische feedback heeft dit onderzoek zeker naar een hoger niveau getild.

Ik dank ook de Combustion Physics Group aan de Unversiteit van Lund en het Transportation Technology R&D Center aan het Argonne National Laboratory, in het bijzonder Prof. Alexander Konnov en dr. ir. Thomas Wallner voor de mogelijkheid tot een onderzoeksverblijf en de academische steun. Verder zou ik hen willen danken om lid te zijn van de doctoraatscommissie. Ook alle andere leden van mijn doctoraatscommissie wil ik graag bedanken, in het bijzonder het derde externe lid Prof. dr. ir. Jamie Turner.

Een speciale vermelding gaat uit naar de technische bijstand van Patrick De Pue, Yves Maenhout en Koen Chielens. In het bijzonder zou ik Koen willen bedanken voor het aangename gezelschap tijdens de vier weken Cuba. Ook Annie Harri en Griet Blondé wil ik van harte danken voor alle administratie. Verder wens ik ook de Master studenten te bedanken die via hun thesissen bijdroegen tot het experimenteel werk.

Mijn (ex-)collega's Joachim Demuynck, Jeroen Vancoillie, Jonas Galle, Stijn Broekaert, Thomas De Cuyper en Roel Verschaeren dank ik voor de discussies die bijdroegen tot het verbeteren van mijn onderzoeksresultaten, de leuke werksfeer en de aangename momenten tijdens de lunch wanneer er eens niet over ons onderzoek moest gepraat worden.

Ten slotte dank ik mijn ouders, familie en vrienden voor de steun, interesse en leuke momenten in het weekend om mijn gedachten even te verzetten.

Gent, maart 2015
Louis Sileghem

Table of Contents

Nomenclature

Symbols

A	area	m^2
B_c	collision frequency	Hz
c_p	specific heat at constant pressure	J/kgK
Da	Damköhler number	-
D_M	mass diffusivity	m^2/s
D_T	thermal diffusivity	m^2/s
f	residual gas fraction	-
h	convective heat transfer coefficient	W/m^2K
Ka	Karlovitz stretch factor	-
L	Markstein length	-
Le	Lewis number	-
m	mass	kg
Ma	Markstein number	-
p	pressure	Pa/bar
r	radius	m
Re	Reynolds number	-
S	flame speed	m/s
S_n	stretched laminar flame speed	m/s
t	time	s
T	temperature	K
u	burning velocity	m/s
u_n	stretched laminar burning velocity	m/s
u_l	unstretched laminar burning velocity	m/s
u'	root mean square turbulent velocity	m/s
v	velocity	m/s
v_g	gas velocity	m/s
V	volume	m^3
W	work	J

Greek symbols

α	stretch rate / temperature exponent	$1/s$ / -
β	pressure exponent /	-
	equivalence ratio exponent	-
δ	flame thickness	m
η	efficiency	-
θ	crank angle	°ca
κ	thermal conductivity	W/m K
λ	air-to-fuel equivalence ratio	-
λ_T	Taylor microscale	m
Λ	integral length scale	m
ν	kinematic viscosity	m^2/s
ρ	density	kg/m^3
τ	autoignition delay time	s
τ_b	burn-up time constant	s
ϕ	fuel to air equivalence ratio	-

Subscripts

0	reference conditions
b	burned
e	entrained gas
E	ethanol
G	gasoline
i	fuel component
l	laminar
M	methanol
n	non-steady or non-planar
st	stoichiometric
t	turbulent
u	unburned gas

Acronyms

ABDC	after bottom dead center
AFR	air-to-fuel ratio
ATDC	after top dead center
BBDC	before bottom dead center
BLD	borderline detonation
BMEP	brake mean effective pressure
BRICS	Brazil, Russia, India, China and South Africa
BSFC	brake specific fuel consumption
BTDC	before top dead center
BTE	brake thermal efficiency
CA50	crank angle at MFB50
CEM	controlled evaporator-mixer
CF	cool-flame
CFD	computational fluid dynamics
CFR	cooperative fuel research
CoV	Coefficient of Variance
CR	compression ratio
DI	direct injecion
E85	a mixture 85 vol% ethanol and 15 vol% gasoline
ECU	engine control unit
EGR	exhaust gas recirculation
EVC	exhaust valve closing
EVO	exhaust valve opening
FFV	flex-fuel vehicle
FID	flame ionization detector
FTIR	fourier transform infrared spectroscopy
GDI	gasoline direct injection
GEM	gasoline, ethanol and methanol
GUCCI	Ghent University Combustion Chamber I
GUEST	Ghent University Engine Simulation Tool
HCCI	homogeneous charge compression engine
ID	ignition delay
IMEP	indicated mean effective pressure
IT	ignition timing
IVC	intake valve closing
IVO	intake valve opening
KLSA	knock limited spark advance
KI	knock intensity
KIR	knock intensity ratio
KO	knock onset
LFL	lower or lean flammable limit

LHV	lower heating value
LNG	liquefied natural gas
MAPO	maximum amplitude of pressure oscillations)
MBT	minimum spark advance for best torque
MFB	mass fraction burned
MFC	mass flow controller
MON	motor octane number
MTO	methanol-to-olefins
NDIR	nondispersive infrared
NTP	normal temperature (298 K) and pressure (101325 Pa)
PFI	port-fuel injection
PM	particulate matter
PRF	primary reference fuel
QD	quasi-dimensional
RBOB	reformulated blendstock for oxygenate blending
RMSE	root mean square error
RON	research octane number
RVP	reid vapor pressure
S	sensitivity
SEPO	signal energy of pressure oscillations
SI	spark ignition
TDC	top dead center
TP	throttle position
TPA	three-pressure analysis
TRF	toluene reference fuel
TWC	three-way catalyst
UHC	unburned hydrocarbons
VVT	variable valve timing

List of publications

Publications in peer reviewed international journals

Publications directly related to the Ph.D. topic

1. Sileghem, L., Vancoillie, J., Demuynck, J. and Verhelst, S. (2012). Alternative fuels for SI engines: mixing rules for the laminar burning velocity of gasoline-alcohol blends. Energy & Fuels, 26 4721-4727.

2. Sileghem, L., Alekseev, V.A., Vancoillie, J., Van Geem, K.M., Nilsson, E.J.K., Verhelst, S. and Konnov, A.A. (2013). Laminar burning velocity of gasoline and the gasoline surrogate components iso-octane, n-heptane and toluene. Fuel, 112 355-365.

3. Sileghem, L., Alekseev, V.A., Vancoillie, J., Nilsson, E.J.K., Verhelst, S. and Konnov, A.A. (2014). Laminar burning velocities of primary reference fuels and simple alcohols. Fuel, 115 32-40.

4. Sileghem, L., Coppens, A., Casier, B., Vancoillie, J. and Verhelst, S. (2014). Performance and emissions of iso-stoichiometric ternary GEM blends on a production SI engine. Fuel, 117 286-293.

5. Sileghem, L., Wallner, T. and Verhelst, S. (2015). A quasi-dimensional model for SI engines fueled with gasoline-alcohol blends: Knock modeling. Fuel, 140 217-226.

Other journal publications

6. Vancoillie, J., Demuynck, J., Sileghem, L., Van De Ginste, M. and Verhelst, S. (2012) Comparison of the renewable transportation fuels, hydrogen and methanol formed from hydrogen, with gasoline - Engine efficiency study. International Journal of Hydrogen Energy, 37(12) 9914-9924.

7. Demuynck, J., De Paepe, M., Sileghem, L., Vancoillie, J., Verhelst, S. and Chana, K. (2012). Applying design of experiments to determine the effect of gas properties on in-cylinder heat flux in a motored SI engine. SAE Int. J. Engines 5(3).

8. Vancoillie, J., Demuynck, J., Sileghem, L., Van De Ginste, M., Verhelst, S., Brabant, L. and Van Hoorebeke, L. (2013) The potential of methanol as a fuel for flex-fuel and dedicated spark-ignition engines. Applied Energy, 102 140-149.

9. Sileghem, L., Bosteels, D., May, J., Favre, C. and Verhelst, S. (2014). Analysis of vehicle emission measurements on the new WLTC, the NEDC and the CADC. Transportation Research Part D: Transport and Environment, 32 70-85.

10. Vancoillie, J., Sileghem, L. and Verhelst, S. (2014). Development and validation of a quasi-dimensional model for methanol and ethanol fueled SI engines. Applied Energy, 132 412-425.

11. Naucler, J.D., Sileghem, L., Nilsson, E.J.K., Verhelst, S. and Konnov, A.A. (2015). Performance of methanol kinetic mechanisms at oxy-fuel conditions. Combustion and Flame, In Press. DOI: 10.1016/j.combustflame.2014.11.033.

Related publications in proceedings of international conferences

12. Sierens, R., Demuynck, J., Vancoillie, J., Sileghem, L. and Verhelst, S. (2011). Efficiency comparison of hydrogen fuelled IC engines with gasoline- and methanol fuelled engines. In: HYPOTHESIS IX, San José, Costa Rica.

13. Vancoillie, J., Verhelst, S., Demuynck, J., Galle, J., Sileghem, L. and Van De Ginste, M. (2012). Experimental Evaluation Of Lean-Burn And EGR As Load Control Strategies For Methanol Engines. In: 2012 SAE World Congress, Detroit, MI, USA. SAE paper no. 2012-01-1283.

14. Vancoillie, J., Sileghem, L., Demuynck, J. and Verhelst, S. (2012). Development And Validation Of A Quasi-Dimensional Model For (M)Ethanol-Fuelled SI Engines. In: FISITA 2012 World Automotive Conference, Beijing, China. FISITA paper no. F2012-A06-019.

15. Demuynck, J., Chana, K., De Paepe, M., Sileghem, L., Vancoillie, J. and Verhelst, S. (2013). Applying design of experiments to develop a fuel independent heat transfer model for spark ignition engines. In: FISITA 2012 World Automotive Conference, Beijing, China. FISITA paper no. F2012-A07-004.

16. Turner, J.W.G., Pearson, R.J., Harrison, P., Marmont, A., Jennings, R., Verhelst, S., Vancoillie, J., Sileghem, L., Pecqueur, M., Martens, K. and Edwards, P.P. (2012). Evolutionary decarbonization of transport: a

contiguous roadmap to affordable mobility using Sustainable Organic Fuels for Transport. In: IMechE Sustainable Vehicle Technology Conference, Gaydon, UK.

17. Naganuma, K., Vancoillie, J., Verhelst, S., Sileghem, L., Turner, J.W.G., Pearson, R.J. and Martens, K. (2012). Drive cycle analysis of load control strategies for methanol fuelled ICE vehicle. In: SAE 2012 International Powertrains, Fuels & Lubricants Meeting, Malmö, Sweden, 2012. SAE paper no. 2012-01-1606.

18. Vancoillie, J., Sileghem, L. and Verhelst, S. (2013). Development and validation of a knock prediction model for methanol-fuelled SI engines. In: 2013 SAE World Congress, Detroit, MI, USA. SAE paper no. 2013-01-1312.

19. Sileghem, L., Huylebroeck, T., Van den Bulcke, A., Vancoillie, J. and Verhelst, S. (2013). Performance and emissions of a SI engine using methanol-water blends. In: 2013 SAE World Congress, Detroit, MI, USA. SAE paper no. 2013-04-08.

20. Naucler, J.D., Sileghem, L., Vancoillie, J., Nilsson, E.J.K., Verhelst, S. and Konnov, A.A. (2013). Laminar burning velocities of methanol under oxy-fuel conditions. In: European Combustion Meeting, Lund, Sweden.

21. Naganuma, K., Vancoillie, J., Sileghem, L. and Verhelst, S. (2013). Effect of load control strategies for methanol fueled vehicle on drive cycle emissions. In: JSAE Annual Congress 2013, Yokohama, Japan.

22. Sileghem, L., Casier, B., Coppens, A., Vancoillie, J. and Verhelst, S. (2014). Influence of water content in ethanol-water blends on the performance and emissions of an SI engine. In: FISITA 2014 World Automotive Conference, Maastricht, The Netherlands. FISITA paper no. F2014-CET-014.

23. Sileghem, L., Vancoillie, J. and Verhelst, S. (2014). Sensitivity analysis of a quasi-dimensional model for SI engines fuelled with gasoline-alcohol blends. In: FISITA 2014 World Automotive Conference, Maastricht, The Netherlands. FISITA paper no. F2014-CET-161.

24. Vancoillie, J., Sileghem, L. and Verhelst, S. (2014). Modeling the combustion of (m)ethanol in spark-ignition engines. In: FISITA 2014 World Automotive Conference, Maastricht, The Netherlands. FISITA paper no. F2014-CET-095.

25. Sileghem, L., Ickes, A., Wallner, T. and Verhelst, S. (2015). Experimental Investigation of a DISI Production Engine Fuelled with Methanol, Ethanol, Butanol and ISO-Stoichiometric Alcohol Blends. In: 2015 SAE World Congress, Detroit, MI, USA. SAE paper no. 2015-01-0768.

Nederlandse samenvatting –Summary in Dutch–

De energievoorziening in de transportsector is tegenwoordig nog altijd zeer sterk afhankelijk van olie. Benzine en diesel zijn fossiele brandstoffen en de verbranding ervan brengt problemen met zich mee: de CO_2-uitstoot heeft een invloed op de klimaatverandering; in grote steden met veel verkeer in het stadscentrum zijn er problemen met de luchtkwaliteit; de bevoorrading van fossiele brandstoffen kan in de problemen geraken door internationale conflicten met grote gevolgen voor de economische markten, enz. Nooit is er een groter algemeen besef geweest dat er een omschakeling moet komen naar een hernieuwbare en duurzame energievoorziening.

Naast een verminderd gebruik van fossiele brandstoffen en een lage uitstoot van schadelijke emissies, zijn er nog enkele belangrijke voorwaarden waaraan alternatieven in de transportsector moeten voldoen. Het gebruiksgemak en comfort van het voertuig mag niet drastisch verlaagd worden en de omschakeling naar een alternatief moet economisch haalbaar zijn, zeker als je weet dat de grootste groei van voertuigen verwacht wordt in de BRICS (Brazilië, Rusland, India, China en Zuid-Afrika) landen. De schaalbaarheid van een nieuwe technologie speelt hierbij een belangrijke rol. De economische haalbaarheid en schaalbaarheid zijn bv. grote hinderpalen voor de opkomende elektrische voertuigen. Het potentieel van zowel batterij-elektrische voertuigen als elektrische voertuigen met een waterstofbrandstofcel is beperkt door het gebruik van lithium, zeldzame metalen of platinum. De huidige verbrandingsmotor daarentegen is een relatief goedkope technologie waarbij de schaalbaarheid zeker bewezen is. Daarnaast heeft de verbrandingsmotor de mogelijkheid om op verschillende brandstoffen te draaien en is er nog veel potentieel voor een efficiëntere en schonere werking. Het zou dus dom zijn het kind met het badwater weg te gooien. Vandaar kunnen we stellen: verander de brandstof, niet de motor.

Alternatieve brandstoffen zijn bij voorkeur gemakkelijk en goedkoop te produceren, eenvoudig in distributie en geschikt om te gebruiken in verbrandingsmotoren. Lichte alcoholen, in het bijzonder methanol en ethanol, voldoen volledig aan deze voorwaarden. Methanol en ethanol zijn de twee kleinste en eenvoudigste alcoholmoleculen en kunnen gemaakt worden uit gemakkelijk

gevonden atomen op aarde (zuurstof, waterstof, koolstof). Methanol is bijzonder flexibel in termen van productie, het kan gesynthetiseerd worden uit verschillende bronnen zoals biomassa, afval en alternatieve fossiele brandstoffen. Verschillende onderzoekers stellen zelfs een cyclus voor waarbij methanol geproduceerd wordt uit waterstof, opgewekt via hernieuwbare elektriciteit, en CO_2 gecapteerd uit de atmosfeer. Hierbij wordt een gesloten CO_2-cyclus gevormd en wordt methanol soms omschreven als een 'electrofuel'. Methanol en ethanol zijn ook vloeibaar bij atmosfeeromstandigheden, waardoor ze op een gelijkaardige manier als benzine en diesel verdeeld en gestockeerd kunnen worden. Daarboven maken de brandstofeigenschappen methanol en ethanol uitermate geschikt voor gebruik in verbrandingsmotoren, waardoor een hoger rendement en lagere emissies kunnen bekomen worden in vergelijking met benzine. Misschien de belangrijkste eigenschap is dat deze lichte alcoholen gemengd kunnen worden met benzine waardoor een zachte overgang mogelijk is van fossiele brandstoffen naar hernieuwbare alcoholen door gebruik te maken van flex-fuel voertuigen.

Om flex-fuel verbrandingsmotoren te kunnen optimaliseren om zo het gebruik van alcoholbrandstoffen te stimuleren zijn nauwkeurige simulatiemodellen nodig. Verbrandingsmotoren worden immers steeds complexer met een hoog aantal vrijheidsgraden. De gebruikte modellen moeten de invloed van de verschillende alcohol-benzine mengsels op de processen in de motor zo correct mogelijk weergeven. Het doel van dit doctoraatsonderzoek is om een simulatietool te ontwikkelen om de werking van vonkontstekingsmotoren op alcohol-benzine mengsels te kunnen voorspellen, zowel bij normale en abnormale verbranding (klop).

Dit doctoraat start eerst met een uiteenzetting waarom alcoholbrandstoffen zo interessant zijn. Het gebruik van methanol als brandstof voor verbrandingsmotoren wordt gekaderd in de methanoleconomie waarbij methanol, naast het gebruik als brandstof, ook gebruikt wordt als grondstof voor de vervaardiging van kunststoffen, verf, enz. en als energiebuffer voor hernieuwbare energieproductie. Daarnaast wordt het concept van ternaire GEM (gasoline, ethanol en methanol) mengsels uitgelegd. In dit concept worden ternaire mengsels van benzine, ethanol en methanol gevormd met quasi dezelfde eigenschappen als binaire ethanol-benzine mengsels die gebruikt kunnen worden in de huidige flex-fuel voertuigen. Deze voertuigen kunnen rijden op zuiver benzine, E85 (een mengsel van 85 vol% ethanol en 15 vol% benzine) of een tussenliggend mengsel. Ternaire GEM mengsels zouden als 'drop-in' brandstof gebruikt kunnen worden in deze flex-fuel voertuigen aangezien ze heel gelijkaardige eigenschappen hebben als een overeenkomstig ethanol-benzine mengsel en dus onzichtbaar zouden zijn voor de ECU van de motor. Via dit concept zou het aandeel hernieuwbare brandstof kunnen stijgen door het feit dat er meer E85/flex-fuel voertuigen bestaan dan momenteel kunnen worden bediend door de E85 supply chain.

De invloed van bepaalde brandstofeigenschappen van methanol en ethanol wordt

uitgelegd en de formulering van GEM mengsels wordt uiteengezet. Verder wordt er gefocust op eigenschappen die niet lineair schalen volgens het aandeel van bepaalde componenten in een mengsel. Metingen werden uitgevoerd op twee motorproefstanden om de prestaties en de emissies van alcoholen in vergelijking met benzine te bestuderen en het concept van de ternaire GEM mengsels meer in detail te onderzoeken. Er wordt aangetoond dat het rendement op lichte alcoholen aanzienlijk beter is dan bij benzine, met bovendien een lagere uitstoot van schadelijke emissies. Daarbij wordt de grootste rendementstoename gezien voor methanol aangezien methanol de meest uitgesproken brandstofeigenschappen heeft. Voor een bepaald werkingspunt bij een motor met directe injectie was het rendement op methanol bijna 40%, meer dan 5 procentpunten hoger dan op benzine, wat resulteerde in een afname van CO_2 uitstoot van 20.7% ten opzichte van benzine. De testresultaten bevestigen ook dat de ternaire GEM mengsels kunnen gebruikt worden als een 'drop-in' brandstof voor flex-fuel voertuigen.

Om de verbranding van alcohol-benzine mengsels te kunnen simuleren zijn bepaalde submodellen nodig. Voor de normale verbranding speelt de laminaire verbrandingssnelheid een cruciale rol terwijl voor de abnormale verbranding het zelfontstekingsuitstel belangrijk is. Aangezien het de bedoeling is om via een motorsimulatiecode de werking voor een groot aantal parameters te optimaliseren is het gewenst dat de submodellen voor de laminaire verbrandingssnelheid en ontstekingsuitstel niet rekenintensief zijn. Een mogelijkheid om de laminaire verbrandingssnelheid en ontstekingsuitstel uit te rekenen is gebruik maken van chemische verbrandingsmodellen die kunnen bestaan uit duizenden componenten en reacties en dus rekenintensief zijn, zeker voor complexe mengsels. Eén van de doelstellingen van dit doctoraat was dan ook om eenvoudige mengwetten op te stellen om de laminaire verbrandingssnelheid en het ontstekingsuitstel van alcohol-benzine mengsels te kunnen berekenen uit de verbrandingssnelheid en het ontstekingsuitstel van de afzonderlijke componenten die in het verbrandingsmodel kunnen geïmplementeerd worden via éénvoudige correlaties.

Voor de laminaire verbrandingssnelheid werd eerst beroep gedaan op data uit de literatuur en gesimuleerde data om bepaalde mengwetten te valideren. In een later stadium werden metingen gedaan op een vlakke vlam brander aan de Universiteit van Lund (Zweden) om de mengwetten verder te kunnen valideren en de verbrandingssnelheid van benzine, methanol, ethanol en surrogaatbenzines te kunnen onderzoeken. Uit deze metingen werden ook nieuwe correlaties voorgesteld voor de laminaire verbrandingssnelheid van benzine en methanol om te kunnen gebruiken in de motorcycluscode. Voor het ontstekingsuitstel was er niet de mogelijkheid om zelf metingen te doen. Een model uit de literatuur werd gebruikt om ontstekingsuitstellen van methanol-benzine mengsels te berekenen en hieruit werd een mengwet opgesteld. Zowel voor de laminaire verbrandingssnelheid als voor het ontstekingsuitstel werd bevonden dat een schaling volgens de energiefractie van de componenten een aanvaardbare benadering gaf van de werkelijke waarden. Bijkomend is het belangrijk bij het

ontstekingsuitstel van alcohol-benzine mengsels dat deze schaling gebeurt met logaritmische waarden.

In een volgende fase werden de mengwetten voor laminaire verbrandingssnelheid en ontstekingsuitstel geïmplementeerd in de motorcycluscode samen met verschillende submodellen voor de turbulente verbrandingssnelheid. Deze code is gebaseerd op een bestaand model voor de vermogenscyclus, ontwikkeld in de onderzoeksgroep van de auteur, en werd in het verleden al gevalideerd voor waterstof en pure alcoholen. Motormetingen met verschillende methanol-benzine mengsels op een poortgeïnjecteerde CFR motor en een direct geïnjecteerde Hyundai motor werden gebruikt als validatie voor de normale verbranding van de motorcyluscode. Een beperkte meetset op de CFR motor werd gebruikt om de gevoeligheid van bepaalde submodellen voor verschillende methanol-benzine mengsels te onderzoeken. De resultaten toonden het belang aan van de laminaire verbrandingssnelheid, de initiële vlamontwikkeling en de schatting van de restgasfractie. Bepaalde experimentele trends werden echter niet juist gesimuleerd. Onzekerheid over de eerste vlamontwikkeling, onzekerheid over de laminaire verbrandingssnelheid bij hogere drukken en temperaturen of het onvermogen van het turbulente verbrandingsmodel om bepaalde chemische effecten te voorspellen werden geclaimd als mogelijke redenen. Verder onderzoek van o.a. de laminaire verbrandingssnelheid bij hogere temperaturen en drukken is dus nodig om de onzekerheid te verlagen. Na optimalisatie van de eerste vlamontwikkeling om dezelfde initiële verbranding te reproduceren als in de metingen werden de experimentele trends veel beter voorspeld. Dit toont aan dat een brandstofafhankelijke kalibratie van de eerste vlamkern heel effectief kan zijn om simulatieresultaten te verbeteren. Tenslotte werden verschillende modellen voor de turbulente verbrandingssnelheid getest. Hoewel de absolute waarden niet verbeterden, werd door de opname van het Lewisgetal in het turbulente verbrandingsmodel de trend van benzine naar methanol beter voorspeld.

Op de Hyundai motor werd een breder meetbereik dan op de CFR motor gebruikt om een meer algemeen beeld te krijgen van de simulaties. Eerst werden simulaties uitgevoerd met de nieuw ontwikkelde correlaties voor de laminaire verbrandingssnelheid van methanol en benzine. In het algemeen kwamen de simulaties goed overeen met de experimentale waarden. Daarnaast werden nog verschillende andere correlaties voor de laminaire verbrandingssnelheid van methanol getest samen met de nieuwe correlatie voor benzine zonder dat de oorspronkelijke kalibratie werd gewijzigd. Het was duidelijk dat deze correlaties slechter presteerden dan de nieuw ontwikkelde correlatie. Dit toonde aan dat het belangrijk is om correlaties van verschillende brandstoffen op elkaar af te stemmen als het effect van een andere brandstof onderzocht moet worden.

Ten slotte werden metingen op CFR motor gebruikt als validatie voor het submodel voor de abnormale verbranding. De voorgestelde mengwet in combinatie met het klopintegraalmodel presteerde goed ondanks de vereenvoudiging. Naast de

voorwaarde van de klopintegraal, die gelijk aan één moet worden, werd een tweede voorwaarde op basis van de onverbrande massafractie en de krukhoek bij begin van klop gebruikt om klop te identificeren. Het model was in staat om het begin van klop te voorspellen binnen de foutmarges van de metingen voor bijna alle meetpunten op methanol, benzine en een mengsel van 50 vol% methanol en 50 vol% benzine.

English summary

Energy supply in the transport sector is currently still largely dependent on oil. Gasoline and diesel are fossil fuels and the combustion of these fuels poses problems: the CO_2 emissions have an impact on climate change; there are air quality problems in large cities with lots of traffic in the city center; the supply of fossil fuels may get complicated due to international conflicts with major consequences for the economic markets, etc. Never has there been a greater general awareness that there has to be a change to a renewable and sustainable energy supply.

In addition to a decreasing use of fossil fuels and lower harmful emissions, there are other important conditions that alternatives in the transport sector have to meet. The ease of use and comfort of the vehicle should not be drastically reduced and switching to an alternative should be economically feasible, especially if you know that the largest growth of vehicles is expected in the BRICS (Brazil, Russia, India, China and South Africa) countries. The scalability of a new technology plays an important role in the feasibility. The economic feasibility and scalability are major obstacles to the emerging electric vehicles. The potential of both battery-electric vehicles and electric vehicles with a hydrogen fuel cell is limited due to the use of lithium, rare metals or platinum. The present internal combustion engine on the other hand is a relatively low-cost technology for which the scalability is definitely proven. In addition, the internal combustion engine has the ability to run on different fuels, and there is still much potential for efficiency improvement and reduction of harmful emissions. It would therefore be foolish to throw the baby out with the bath water. Hence we can say: change the fuel, not the engine.

Alternative fuels are preferably easy and inexpensive to produce, easy to distribute and suitable for use in internal combustion engines. Light alcohols, methanol and ethanol in particular, fully meet these conditions. Methanol and ethanol are the two smallest and simplest alcohol molecules and can be made from readily found atoms on the Earth (oxygen, hydrogen, carbon). Methanol is particularly flexible in terms of production, it can be synthesized from a variety of sources, such as biomass, waste or alternative fossil fuels. Several researchers even suggest a production cycle in which methanol is produced from hydrogen, generated by renewable electricity, and CO_2 captured from the atmosphere. In this way, a closed CO_2-cycle is formed and methanol is sometimes described as an ‘electrofuel’. Methanol

and ethanol are also liquid at atmospheric conditions, making it possible to distribute and store them in a similar manner as gasoline and diesel. Additionally, methanol and ethanol are excellent fuels for internal combustion engines. Due to the excellent fuel properties, higher efficiencies and lower harmful emissions compared to gasoline can be achieved. Perhaps the most important property is that these light alcohols can be blended with gasoline making it possible to have a gentle transition from fossil fuels to renewable alcohols by the use of flex-fuel vehicles.

To optimize flex-fuel internal combustion engines in order to stimulate the use of alcohol fuels, accurate simulation models are needed. Internal combustion engines are indeed becoming increasingly complex with a high number of degrees of freedom. The models have to reproduce the influence of various alcohol-gasoline blends on the processes in the engine as correctly as possible. Thus, the goal of this study is to develop a simulation tool to predict the performance of spark ignition engines fuelled with alcohol-gasoline blends, both for normal and abnormal combustion (knock).

This Ph.D. study first starts with an explanation why alcohol fuels are so interesting. The use of methanol as a fuel for internal combustion engines is framed in the methanol economy in which methanol, besides its use as fuel, is also used as a raw material for the manufacture of plastics, paints, etc. and as an energy buffer for renewable energy production. Additionally, the concept of ternary GEM (gasoline, ethanol and methanol) blends is explained. In this concept, ternary mixtures of gasoline, ethanol and methanol are formulated with almost the same properties as binary ethanol-gasoline blends that can be used in the current flex-fuel vehicles. These vehicles can run on pure gasoline, E85 (a mixture of 85 vol % ethanol and 15 vol % gasoline) or an intermediate blend. Ternary GEM blends can be used as 'drop-in' fuels in these flex-fuel vehicles because they have very similar properties as a corresponding ethanol-gasoline blend and are therefore invisible to the engine ECU. With this concept, the fraction of renewable fuel in the fuel pool can increase due to the fact that there exist more E85/flex-fuel vehicles than currently can be supplied by E85.

The influence of certain fuel properties of methanol and ethanol is explained and it is shown how to formulate GEM blends. Further, the focus is on properties that do not scale linearly with the fractions of components in a mixture. Measurements were performed on two engine test benches in order to study the performance and emissions of alcohols in comparison with gasoline, and to investigate the concept of the ternary GEM blends in more detail. It is shown that the efficiency on light alcohols is significantly better than on gasoline, with lower harmful emissions on top. The largest increase in efficiency is seen for methanol since methanol has the most pronounced fuel properties compared to gasoline. For a given operating point of an engine with direct injection, the efficiency on methanol was almost 40%, more than 5 percentage points higher than on gasoline, resulting in a decrease of

CO_2 emission of 20.7 % compared to gasoline. The test results also confirm that the ternary GEM blend can be used as a 'drop-in' fuel for flex-fuel vehicles.

In order to simulate the combustion of alcohol-gasoline blends, certain sub-models are required. For the normal combustion, the laminar burning velocity plays a crucial role while the autoignition delay time is important for the abnormal combustion. Since the aim is to optimize the engine operation for a large number of parameters via engine simulations, it is desirable that the sub-models for the laminar burning velocity and autoignition delay time are not computationally demanding. One possibility to calculate the laminar burning velocity and autoignition delay time is to use chemical kinetic models which can include thousands of components and reactions and are therefore computationally demanding, especially for complex mixtures. One of the goals of this research was therefore to develop simple mixing rules to calculate the laminar burning velocity and autoignition delay time of alcohol-gasoline mixtures from the laminar burning velocity and autoignition delay time of the individual components. To implement the laminar burning velocity and autoignition delay time of the individual components in the combustion model, simple correlations can be used.

To validate mixing rules for the laminar burning velocity, data from literature and simulated data were first used. In a later stage, measurements were done on a flat flame burner at Lund University (Sweden) to further validate the mixing rules and to investigate the laminar burning velocity of gasoline, methanol, ethanol and gasoline surrogates. With these measurements, new correlations were also proposed for the laminar burning velocity of gasoline and methanol in order to use in the engine cycle code. For the autoignition delay time, it was not possible to perform measurements. A model from literature was used to calculate autoignition delay times of methanol-gasoline blends, and this data was used to develop a mixing rule. For both the laminar burning velocity as for the autoignition delay time, it was found that scaling according to the energy fraction of the components gave an acceptable approximation of the actual values. Additionally, it was shown that it is important for the autoignition delay time of alcohol-gasoline blends that this scaling is done with logarithmic values.

In the next phase, the mixing rules for the laminar burning velocity and autoignition delay time were implemented in the engine cycle code along with several sub-models for the turbulent burning velocity. This code is based on an existing model for the power cycle of internal combustion, developed in the author's research group, and has been validated for hydrogen and pure alcohols in the past. Engine measurements on a port-injected CFR engine and a direct-injected Hyundai engine fuelled with different methanol-gasoline blends were used as validation for the normal combustion of the engine cycle code. A limited measurement set on the CFR engine has been used to investigate the sensitivity of certain sub-models for different methanol-gasoline blends. The results showed the importance of the laminar burning velocity correlation, the initial flame kernel

and the estimation of the residual gas fraction. Certain experimental trends were however not properly simulated. Uncertainty about the initial flame kernel, uncertainty about the laminar burning velocity at higher pressure and temperatures or the inability of the turbulent combustion model to adequately capture the chemical effects were claimed as possible reasons. Further investigation of, among other things, the laminar burning velocity at higher temperatures and pressures is thus necessary to lower the uncertainty. After optimization of the initial flame development in order to reproduce the same initial combustion as in the measurements, the experimental trends were much better predicted. This shows that a fuel-dependent calibration of the initial flame kernel can be very effective in order to improve simulation results. Finally, several turbulent burning velocity models were tested. Although the absolute values did not improve, the trends going from gasoline to methanol could be better reproduced when the Lewis number was included in the turbulent burning velocity model.

A broader measurement range than on the CFR engine was used on the Hyundai engine to get a more general view of the simulation output. First, simulations were done with the newly developed laminar burning velocity correlations of methanol and gasoline. In general, the simulations were in good agreement with the experimental values. In addition, several other laminar burning velocity correlations of methanol were tested together with the new correlation of gasoline without changing the initial calibration. It was clear that these correlations performed worse than the newly developed correlation. This showed that it is important to match laminar burning velocity correlations of different fuels if the effect of using a different fuel needs to be investigated.

Finally, measurements on the CFR engine were used as validation for the sub-model for the abnormal combustion. The proposed mixing rule in combination with the knock integral model performed well despite the simplification. Next to the condition of the knock integral, which has to be equal to one, a second condition has been used based on the unburned mass fraction and the crank angle at the onset of knock to identify knock. The model was able to predict almost all the knock onsets of the different operating points within the error margins of the experimental knock onsets of methanol, gasoline and a mixture of 50 vol% methanol and 50 vol% gasoline.

1 Introduction

1.1 Alternatives to fossil fuel powered engines

Fossil fuels have been consumed in large quantities since the industrial revolution. In the past decades, awareness has grown that we cannot solely depend on these fuels as energy carriers for transport applications. Shrinking oil reserves, climate change and air quality are factors that force us to look at alternatives.

Several important conditions can be put forward which should be met by alternatives:

- decrease in fossil energy use (cradle-to-grave fossil energy consumption) and greenhouse gas emissions
- very low pollutant emissions (especially important for the air quality in big cities)
- affordable without compromising driving range and comfort
- sustainable
- scalable

As a result, the ideal energy carrier for vehicles should:

- be easy to produce, from abundantly available (scalable) and renewable (sustainable) resources
- be capable of being handled, stored and distributed easily and safely
- have a high enough energy density (~ vehicle range)
- not have energy security issues because of geographic concentrations

Verhelst [1] pointed out that scalability is an important condition which is often forgotten, especially with present growth rates of the BRICS countries (BRICS = Brazil, Russia, India, China and South Africa). To have a scalable alternative, it should not rely heavily on raw materials of which reserves are limited. This may be the greatest obstacle in scaling up the production of battery electric vehicles and hydrogen fuel cell vehicles due to the constrains of lithium, rare earth metal and platinum resources [2, 3]. The internal combustion engine, on the other hand, is a proven technology, easy to produce from abundantly available, recyclable materials. One of the major advantages of the internal combustion engine is that it can run on different fuels, making it a flex-fuel powertrain, in many cases only with a change of some parameters such as ignition timing and injection duration. This gives it the potential to make the transfer from fossil fuels to renewable fuels.

Liquid alcohols, methanol and ethanol in particular, are attractive alternatives. These are the two smallest and simplest alcohol molecules, made from easily found atoms on the Earth (oxygen, nitrogen, carbon) which is an advantage from a production point of view. They are liquid and thus a very efficient way of storing, handling and distributing energy, similar to gasoline and diesel. Being liquid gives these light alcohols a high energy density, especially compared to batteries and hydrogen, see Figure 1.1 [4]. Additionally, methanol and ethanol are also miscible with gasoline enabling a soft start to an alternative transport energy economy. A possible pathway of introducing methanol into the current transportation fuel pool is presented by Turner et al. [5–7] and discussed in Section 1.2.1.

Renewable ethanol can be made from biomass such as corn or sugarcane. This is often referred to as bio-ethanol. For now, bio-ethanol has the upper hand when it comes to non-petroleum-derived transportation energy and efforts are undertaken to avoid interference with the food chain through research and development of next-generation cellulosic ethanol [8]. Methanol can be produced from a wider variety of renewable sources (e.g. gasification of wood, agricultural by-products and municipal waste) and alternative fossil fuel based feed stocks (e.g. coal and

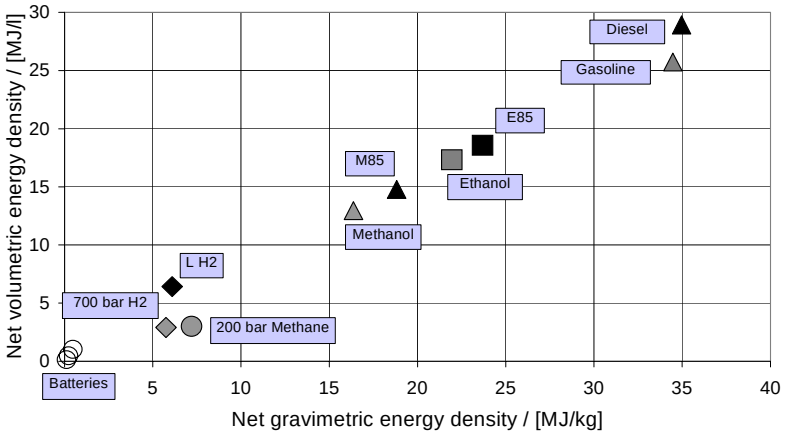

Figure 1.1: Net system volumetric and gravimetric energy densities for various on-board energy carriers [4]

natural gas). Synthetic methanol can also be produced from renewable hydrogen and atmospheric CO_2, forming a sustainable closed-carbon cycle [9]. Such synthetic fuels produced from renewable electricty (for the hydrogen production) are sometimes described as 'electrofuels' [9–15] and will be briefly discussed in the next Section.

1.1.1 Electrofuels

Biofuels such as bio-ethanol are not considered to be viable in the long term as a substitute for fossil fuels, due to the biomass limit [4]. This biomass limit is different for each country, and depends on the amount of biomass that can be grown, the amount of energy required by the country, any impact of land-use change that may arise, and limits set by any impact on the food chain [5]. It has been estimated that this limits the potential of biofuels to about 20% of the energy demand in 2050 [10].

This biomass limit can be overcome by the use of synthetic fuels made from renewable energy. These 'electrofuels' are not constrained by a production limit and could become more and more important in the future. These energy carriers are synthesized from CO_2 and water using renewable energy. In other words, CO_2 is captured and combined with renewable hydrogen to form a liquid hydrogen carrier. This results in a closed CO_2 cycle. Methanol is the most energetically efficient liquid electrofuel that can be synthesized using this approach [10]. This closed carbon production cycle of methanol is presented in Figure 1.2.

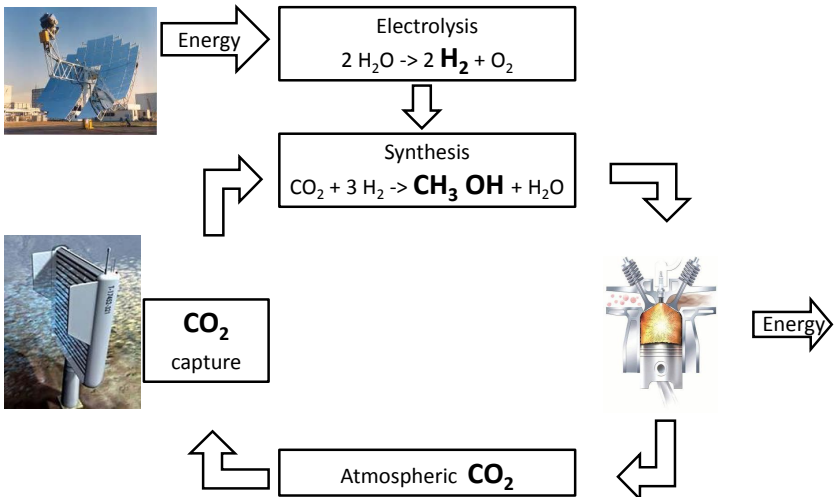

Figure 1.2: Closed carbon cycle for methanol production [9]

The methanol economy

Next to the use of methanol as a transportation fuel, synthetic methanol can also serve as energy storage to act as a buffer for renewable energy production. The intermittency of renewable energy such as solar, hydro and wind energy is a big obstacle to their large-scale use [16]. A condition to fully exploit the potential of these renewable energy sources is that there should be some kind of energy buffer on a massive scale. Synthetic methanol produced from renewable energy as presented in Figure 1.2 could be used as energy buffer when electricity production outweighs electricity demand.

Methanol is also a chemical feedstock for the manufacture of plastics, paint, etc. and can be used as a building block for making more complex hydrocarbons, facilitated by the so-called methanol-to olefins (MTO) process [17].

The use of methanol as **fuel**, **feedstock** and **energy buffer** are three main aspects of the **methanol economy** proposed by Nobel prize winner George Olah [9]. The cycle presented in Figure 1.2 forms the basis of this economy.

Synthetic methane from renewable energy can be made in a similar way [10]. Methane can already act as a large energy buffer due to the fact that in many countries there is an existing gas network that could be used for storage and subsequent re-use in the power generation and heat sectors. Pearson et al. [10] proposed the integration of the production of renewable electricity and renewable

methane for power generation back-up and use in the heat sector with the synthesis of liquid fuels for use directly in transport. This system combining the power, heat, and transport sectors is schematically represented in Figure 1.3. The renewable liquid fuels are represented by methanol, CH_3OH, and higher hydrocarbon fuels, $n(-CH_2-)$.

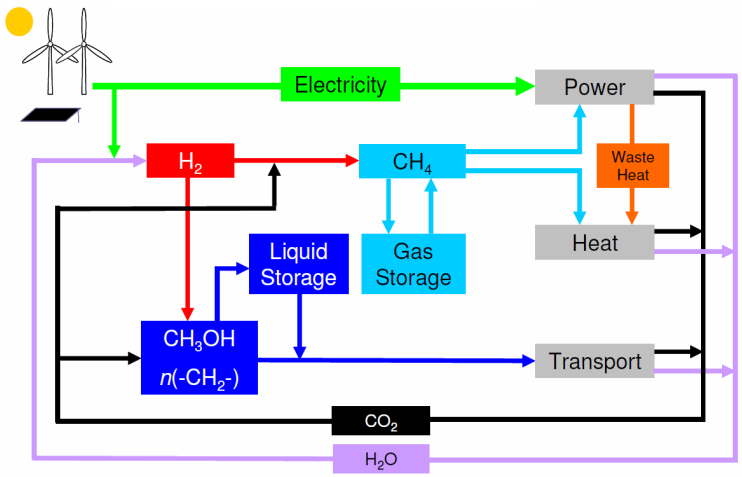

Figure 1.3: Integrated power, heat and transport system combining renewable methane and liquid fuels [10].

In the next Section, the potential of light alcohol as a fuel for internal combustion engines will be assessed.

1.2 The potential of light alcohols as a fuel for internal combustion engines

1.2.1 Spark ignition engines

The physico-chemical properties of light alcohols, discussed in more in detail in Chapter 2, make them very well suited for use in spark-ignition engines. Unusually for alternative fuels, ethanol and methanol have the potential to increase engine performance and efficiency over that achievable with gasoline. Recent work on modern multi-cylinder engines has demonstrated significant opportunities for both increasing efficiency and performance. Nakata et al. [18] used a

high compression ratio (13:1) naturally aspirated port-fuel injected spark-ignition engine and reported a full-load brake thermal efficiency at 2800 rpm of 39.6% using pure ethanol, compared with 37.9% and 31.7% using high and low-octane gasoline respectively. Brusstar et al. [19] converted a 1.9 L turbocharged diesel engine to run on pure methanol and ethanol by replacing the diesel injectors with spark plugs and fitting a port fuel injection system for the alcohol fuels. Running at the 19.5:1 compression ratio of the diesel engine, the PFI methanol variant was able to run with very high exhaust gas recirculation (EGR) fractions and increased the peak brake thermal efficiency from 40% on diesel to 42% on pure methanol while emissions of NOx, CO, and HC were extremely low operating on methanol using a conventional three-way catalyst. The work of Brusstar et al. [19] was extended by Ghent University and Karel de Grote University College [20]. Similar to Brusstar et al. [19], peak brake thermal efficiencies of 42% were obtained on methanol. Gasoline operation was not possible due to heavy knock. At part loads, the absence of throttling losses due to high levels of EGR and benefits associated with lower in-cylinder temperatures enabled relative efficiency improvements up to 20% compared to throttled operation. The high levels of EGR dilution at these loads (up to 50%) also allowed to reduce the engine-out NOx emissions to negligible levels [20]. These results demonstrate that methanol can be used in dedicated engines with diesel-like efficiencies while using cheap aftertreatment systems.

In the following Section, the potential of methanol and ethanol as blend components in gasoline, resulting in ternary gasoline-ethanol-methanol (GEM) blends as fuel for spark-ignition engines, will be discussed.

Ternary blends

Turner et al. [5–7] presented the concept of ternary blends of gasoline, ethanol and methanol in which the stoichiometric air-to-fuel ratio is controlled to be the same as that of conventional E85 (85 vol % ethanol and 15 vol % gasoline) alcohol-based fuel. In fact, starting from any binary gasoline-ethanol mixture, a ternary blend of gasoline, ethanol and methanol can be devised in which the fraction of each component is chosen to yield the same stoichiometric air to fuel ratio (for E85, this is $\sim 9.7 - 9.8 : 1$ depending on the AFR of the gasoline which can vary somewhat). E85 is a fuel which can be used in the so-called flex-fuel vehicle (FFV). These FFVs are capable of using ethanol in concentration levels of up to 85% (E85) by volume. However, despite the registration of over several million flex-fuel vehicles, representing 4% of the light duty vehicle fleet in the United States, only 1% of the total ethanol use in the USA has been in the form of E85 sales [21]. E85

has suffered both from limited availability and uncompetitive pricing on an energy basis in the USA.

It was shown by Turner et al. [5, 6] that all the possible iso-stoichiometric ternary blends starting from a binary blend of gasoline and ethanol are practically invisible for the engine control unit (ECU) of flex-fuel vehicles calibrated to run on any ethanol-gasoline blend up to E85. This opens the possibility to use these ternary blends as drop-in fuels for flex-fuel vehicles without the danger of upsetting the on-board diagnostics of the engine management system. If the methanol used is of a renewable and energy-secure nature then, for a fixed volume of ethanol in the fuel pool dependent on the biomass limit, an increased level of renewability and energy security is achieved. This overall situation is made possible by the fact that there are more E85/flex-fuel vehicles in existence than can currently be serviced by the E85 fuel supply chain. The formulation of ternary GEM blends and the properties of these blends will be discussed in Section 2.4.

Turner et al. [5, 6] tested the drop-in ability of the iso-stoichiometric gasoline-ethanol-methanol (GEM) blends in two flex-fuel vehicles. One vehicle was provided with a physical sensor for alcohol content and the other vehicle had a 'virtual' sensor. A physical sensor directly measures the alcohol concentration of the fuel relying on the electric permittivity or the resistance of the fuel, while a virtual sensor utilizes an algorithm based on the information of the other sensors of the engine to calculate the alcohol concentration. A 'virtual' sensor has the advantage that there is no additional cost in hardware. During vehicle testing, the hypothesis that iso-stoichiometric GEM blends can function as drop-in alternatives to binary ethanol-gasoline blends has been confirmed. There were only two malfunction lights when running on the binary gasoline-methanol blend with the vehicle with the 'virtual' sensor. Turner et al. [5, 6] stated that this could be due to phase separation as the vehicle was not subjected to road shocks or accelerations on the test bench and that some form of cosolvent might be necessary when methanol and gasoline are blended together. Compared to the gasoline tests on the same vehicles, there was an overall efficiency improvement of approximately 5% when using the alcohol blends. Turner et al. [5, 6] also performed cold start tests. The only fuel blend which failed the cold start test was the normal E85 blend. This is to be expected as ethanol is harder to start than gasoline or methanol, and so reducing the proportion of this component and replacing it with larger amounts of the other two would only be expected to improve the situation.

This means that there is the possibility with GEM blends to effectively extend gasoline displacement during winter months when currently, with existing commercial E85 fuels, the ethanol content is decreased to levels close to 70% in order to maintain cold startability. A year-round fixed blend ratio is therefore a

possibility. It is important to note that the tests were conducted on a vehicle and the emissions were measured at the end of the tailpipe without knowing what the ECU was actually doing. Measurements on an engine test bench and engine-out emissions would enable to better understand the effect of replacing ethanol by methanol/gasoline in the GEM-blends. This is addressed in Section 3.4 where different GEM blends are tested on engine test benches.

Next to the hypothesis, other benefits of the GEM-blends were discussed like the potential economic advantage. Turner et al. [6] showed that with wholesale prices of $3.11, $2.30 and $1.11 per US gallon for gasoline, ethanol and methanol respectively, the price of the blends can be made significantly lower than gasoline on an energy basis. With these prices, with ternary blends containing more than 25% by volume of methanol, a reduction in motoring costs could be realized just through a reduction in the relative price of the fuel versus gasoline. Since the vehicles would be expected to become more efficient when operated on the high-blend alcohol fuels, one would expect another reduction in operating costs. Another advantage is that for flex-fuel vehicles, there is no need for range anxiety, which is a major obstacle for electric vehicles, because these flex-fuel vehicles are still able to run on gasoline. The user would be able to run on a high-alcohol GEM blend, on which the vehicle would be significantly cheaper to operate but with a lower range due to the lower volumetric energy content of the alcohol fuel, or on gasoline, when he would like to travel longer distances before refueling.

1.2.2 Compression ignition engines

Low carbon number alcohols have very low cetane numbers. For methanol the number is so low that it cannot be measured directly [4]. Extrapolation of test data using additives gives a cetane number of 3 for pure methanol and a cetane number of 2 for methanol with 10% water [22]. Since the cetane number is a measure of the auto-ignitibility of a fuel, pure methanol and ethanol are found to be unsuitable for use in conventional compression-ignition engines. It can only be used in compression ignition engines if the ignition is improved. This can be done chemically with the use of an additive or another fuel blended in, or physically, e.g. preheating the intake air. It can also be used in dual fuel operation in conjunction with another fuel which is more auto-ignitable.

Another problem is the lubricity of alcohol fuels. Typical diesel fuel lubricates engine fuel pumps and injectors to remain operable. For the low viscosity of methanol and ethanol, lubricity improvers exist which could solve the problem [23].

Pure alcohols

Recently, the use of methanol and ethanol in compression-ignition engines have been investigated without adding additives to improve the ignition. This was done in the 'Sootless Diesel' project of the Advanced Combustion group of Stanford University [23]. This project aimed at understanding the available strategies for reducing soot emissions. Spray imaging and engine measurements have shown the huge potential of these light alcohols to reduce soot emissions. For spray images, the camera sensitivity required to capture the radiation of soot formation from methanol and ethanol had to be increased with a factor of nine compared to spray images of diesel fuel. Engine measurements were performed on a single-cylinder research engine with a compression ratio of 17:1. As alcohol fuels have very low cetane numbers, the intake air was heated to 125°C in order to allow consistent combustion. The engine measurements showed that with methanol and ethanol, full-load could be realized while still obviating the need for a particulate filter, even at stoichiometric air-to-fuel ratios. The levels of soot were far below the current regulation limit, especially for methanol. This opens the opportunity to use an inexpensive three-way catalyst while running at stoichiometric air-to-fuel ratios in order to reduce the other pollutant emissions. At stoichiometric operation, the combustion efficiency dropped compared to lean operation but was still almost 96%.

Light alcohols in combination with diesel ignition

In Europe, methanol is being considered as a more cost effective alternative to meeting upcoming emission legislation for the marine industry because of the advantages in distribution and storage at terminals and onboard ships compared to other possible alternative fuels such as Liquefied Natural Gas (LNG). Additionally, the conversion to dual fuel engines is significantly easier for methanol than for LNG. The Scandinavian Efficient Shipping with Low Emissions (EffShip) project investigated a number of alternative fuels and advanced methanol as the most promising one [24]. In a spin-off project of EffShip, the engines of the RoPax ferry Stena Germanica will be converted to dual fuel methanol-diesel operation. Methanol will be injected close to the top dead center and ignited by a small amount of pilot fuel (=traditional diesel fuel) resulting in a diffusion combustion of the methanol fuel [25]. Compared with current fuel used in the ferries, sulphur emissions are expected to be reduced by about 99%, NOx emission by 60%, particles by 95%, and CO_2 emissions by 25% [26]. Stena Line may convert a fleet of 40 ferries to methanol depending on the success achieved with the Stena Germanica conversion.

1.3 Scope and outline

Light alcohols are definitely interesting alternatives. The fact that they are also miscible with gasoline enables an evolution rather than a revolution to an alternative transport economy. To favor the chances of these alcohols fuels, engine models should be able to accurately simulate the power output and emissions of engines fuelled with alcohol fuels in order to optimize flex-fuel engines and fully exploit the potential of these alcohol fuels. Within the author's department, a quasi-dimensional engine model was already developed for the power cycle of spark ignition engines fuelled with hydrogen [27] and pure methanol and ethanol [28]. Quasi-dimensional models are more complex than zero-dimensional models due to the inclusion of certain geometrical parameters and a mass burning rate that is modeled instead of predefined. Compared to multi-dimensional models, which are used to study certain physical processes in detail, these models are computationally less demanding and thus the ideal choice for performing parameters studies and optimizing engine settings. The goal of the present research is to extend the validity of the quasi-dimensional model to alcohol-gasoline blends.

Chapter 2 focuses on the fuel properties of alcohol-gasoline which are relevant to internal combustion engines. Chapter 3 describes the engine test benches and the measurements carried out during this Ph.D. study. In Chapter 4, it is explained why the use of hydrous alcohol (water-alcohol mixtures) in internal combustion engines can have advantages and the effect it has on the power output and emissions is addressed with engine measurements on these hydrous alcohol fuels. Because the laminar burning velocity is a key parameter to model the combustion of fuels in spark ignition engines, Chapter 5 focuses on the laminar burning velocity of alcohol-gasoline blends and how the laminar burning velocity of complex alcohol blends can be calculated in engine cycle models using mixing rules. The engine cycle model is described in Chapter 6 and the predictive capability of the normal combustion (non-knocking operating points) is evaluated through comparison with experiments on a port fuel injection engine and a direct injection engine. In Chapter 7, a sub-model to model knock in spark ignition engines fuelled with alcohol-gasoline blends is presented and evaluated through comparison with experiments. In Chapter 8, the main findings are summarized and an outlook for future work is given.

2

Fuel properties of alcohol blends

2.1 Introduction

As explained in Chapter 1, methanol and ethanol are promising alternative fuels for internal combustion engines. Methanol and ethanol are the two simplest alcohols with well known properties. Gasoline, however, is a mixture of hundreds of hydrocarbons. There is a wide variation in composition of gasoline between market fuels (see Figure 2.1) and the composition depends also on the season to have a good startability. On a molecular level, the most distinct feature of alcohol molecules compared to gasoline is the hydroxyl functional group (-OH) which is bound to a saturated carbon atom. This hydroxyl group is responsible for the polarity of the molecules which is more pronounced in light alcohols such as methanol and ethanol than for alcohols with a higher carbon count. Several interesting physico-chemical properties of light alcohols are due to the strong inter-molecular forces, known as hydrogen bonding, caused by this polarity, e.g. high boiling points relative to the molar masses, high heats of vaporization and low vapor pressure. This is because, due to the extensive hydrogen bonding in the case of methanol, a 'quasi-super-molecule' known as a cyclic tetramer is formed in which four methanol molecules form a structure via hydrogen bonds between the individual molecules. These cyclic tetramers have an effective molecular mass of four times that of an individual molecule. Thanks to the resulting properties,

methanol and ethanol have the potential to increase engine performance and efficiency over that achievable with gasoline but it also raises cold start problems. Another negative effect of the polarity of light alcohols is the high corrosiveness which can lead to problems with material compatiblity. During his Ph.D. study, Vancoillie [28] studied the combustion of pure methanol and ethanol in internal combustion engines and gave an overview of different measures which can be taken to solve problems with material compatibility and cold start on alcohol fuels. Additionally, some misconceptions about extreme toxicity and fire safety of methanol were rebutted by Vancoillie [28].

In this Chapter, the effect of light alcohols on the performance, efficiency and emissions of internal combustion engines will be explained briefly and compared to higher carbon count alcohols. Higher carbon count alcohols, such as butanol, have been of interest due to the more gasoline-like properties. Engine measurements on butanol will be reported in Chapter 3. Secondly, as this Ph.D. study focuses on alcohol-gasoline blends, the behavior of some relevant properties of alcohol-gasoline blends that do not scale linearly with the molar content of the individual components will be discussed. Finally, more information will be given about the properties of iso-stoichiometric and iso-energetic gasoline-ethanol-methanol blends (GEM blends).

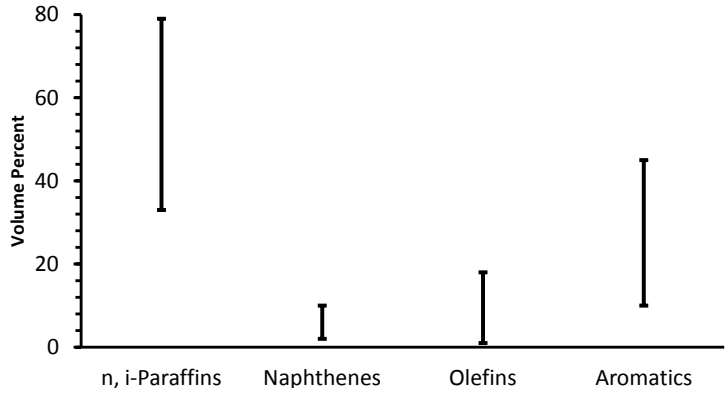

Figure 2.1: Approximate ranges of paraffins, naphthenes, aromatics, and olefins in commercial U.S. gasoline [29].

2.2 Alcohol properties relevant to internal combustion engines

Some properties of methanol and ethanol, relevant to spark-ignition engines, are shown in Table 2.1 and compared against other alternative fuels and typical gasoline. In the introduction, it was already mentioned that light alcohols have the potential to increase performance and efficiency compared to gasoline. Lower heat losses due to lower in-cylinder temperatures, higher volumetric efficiency due to higher charge cooling and lower propensity to knock are the main contributing factors to the higher performance and efficiency. The higher heat of vaporization in combination with the lower air-to-fuel ratio of alcohols leads to an increase of intake charge cooling. This potential of charge cooling can be fully exploited in direct injection engines. This cooling effect can increase the power output of internal combustion engines because of the higher volumetric efficiency due to an increased charge density but it also helps to mitigate the propensity to knock and lowers the heat losses. Lower temperatures are also expected for alcohols because of the lower adiabatic flame temperature and higher exhaust gas heat capacity. Next to the cooling effect, light alcohols also have an elevated chemical resistance to knock compared to gasoline. Methanol and ethanol have a single-stage autoignition behavior compared to the two-stage autoignition behavior with cool-flame reactions of gasoline. These cool-flame reactions can boost the high-temperature oxidation responsible for knock.

The higher burning velocity of methanol and ethanol compared to gasoline also allows increased levels of mixture dilution, e.g. external exhaust gas recirculation (EGR), which can lower throttling losses [30].

Pollutant emissions are also affected by alcohols. As alcohols have a hydroxyl group, the oxygen in the molecule can have a positive effect on the formation of noxious emissions such as unburned fuel and CO emissions [31, 32]. Due to the relatively low combustion temperature, NOx emissions normally decrease with addition of light alcohols. If additionally the level of EGR can be raised substantially with addition of methanol or ethanol, the NOx emissions can be lowered drastically [30]. Finally, soot emissions, which can be significant for direct injection engines, can decrease by using light alcohols, especially for methanol which does not have a carbon-carbon bond. The presence of oxygenates has been shown to reduce the concentration of intermediate species required for the formation of aromatic soot precursors [33].

*Table 2.1: Properties of typical gasoline, methanol, ethanol, (iso-)butanol, methane and hydrogen relevant to internal combustion engines [4, 27, 28, 34–36]. * Includes atmospheric nitrogen. NA: not available. NTP: normal temperature (293 K) and pressure (101325 Pa).*

Property	**Gasoline**	**Methanol**	**Ethanol**	**Butanol**	**Methane**	**Hydrogen**
Chemical Formula	Various	CH_3OH	C_2H_5OH	C_4H_9OH	CH_4	H_2
Oxygen Content by Mass [%]	0	49.9	34.7	21.6	0	0
Density at NTP [kg/l]	0.74	0.79	0.79	0.802	0.00065	0.00008
Lower Heating Value [MJ/kg]	42.9	20.09	26.95	33.08	50	120
Volumetric Energy Content [MJ/l]	31.7	15.9	21.3	26.5	0.033	0.010
Stoichiometric Air to Fuel Ratio [kg/kg]	14.7	6.5	9	11.2	17.6	34.2
Energy per Unit mass of air [MJ/kg]	2.92	3.09	2.99	2.95	2.83	3.51
Research Octane Number (RON)	95	109	109	113	120	130 (λ=2.5)
Motor Octane Number (MON)	85	88.6	89.7	94	120	NA
Sensitivity (RON-MON)	10	20.4	19.3	19	0	NA
Boiling point at 1 bar [°C]	25-215	65	79	108	-164	-253
Heat of vaporisation [kJ/kg]	180-350	1100	838	579	-	-
Heat of vaporisation, λ=1 [kJ/kg Air]	18.0	169.2	93.1	51.7	-	-
Reid Vapour Pressure [psi]	7	4.6	2.3	0.49	NA	NA
Mole ratio of products to reactants*	0.937	1.061	1.065	1.067	1	0.852
Ratio of triatomic to diatomic products*	0.35	0.53	0.44	0.40	0.40	0.53
Flammability Limits in Air [vol%]	1.3-7.6	6.7-36	3.3-19	1.7-10.6	5-15	4-75
Flammability Limits in Air [λ]	0.26-1.60	0.23-1.81	0.28-1.91	0.36-2.44	0.59-1.99	0.15-10.57
Minimum Ignition Energy in Air [mJ]	0.25	0.14	NA	NA	0.28	0.02
Laminar flame speed at NTP, λ=1 [cm/s]	33.0	40.0	38.6	NA	35.2	210
Specific CO_2 Emissions [g/MJ]	73.95	68.44	70.99	71.79	54.87	0.00

Table 2.2: C1-C8 alcohols

Name	C #	Chemical composition	Oxygen content [m%]	Stoichiometric Air to Fuel Ratio [kg/kg]
Methanol	1	CH_3OH	49.9	6.5
Ethanol	2	C_2H_5OH	34.7	9.0
Propanol	3	C_3H_7OH	26.6	10.4
Butanol	4	C_4H_9OH	21.6	11.2
Pentanol	5	$C_5H_{11}OH$	18.1	11.8
Hexanol	6	$C_6H_{13}OH$	15.7	12.2
Heptanol	7	$C_7H_{15}OH$	13.8	12.5
Octanol	8	$C_8H_{17}OH$	12.3	12.7

Methanol and ethanol are quite different from gasoline which makes it impossible to use these light alcohols pure or in high-level blends in the current SI engines without (small) modifications to especially the fuel system, injectors and ECU calibration. Additionally, the lower energy density of light alcohols makes the range of the vehicles drop significantly for equal fuel tank volumes (methanol has approximately half the energy density of gasoline). The fact that for higher carbon count alcohols, the distinct properties, which are most pronounced for methanol, progressively degrade towards gasoline-like values, has been the main reason why also higher alcohols such as butanol are currently investigated to be used in combination with gasoline.

Table 2.2 shows an overview of the alcohols ranging from methanol (1 carbon atom) to octanol (8 carbon atoms). When enough carbon atoms are present (> 2 carbon atoms), different isomers are possible. These are molecules with the same chemical composition, but with different structures and placement of the hydroxyl group. The isomer with a straight carbon chain and the OH-group at the end is called an n-isomer or 1-isomer. The branched isomer with the OH-group at the end of the branch is preceded by '-iso'. In the case of butanol, there is a four-carbon structure so different isomers exist based on the location of the hydroxyl group (OH group). The different structures of butanol isomers have a direct impact on the physical properties. The different isomers are called n-butanol (1-butanol), sec-butanol, tert-butanol and iso-butanol and the chemical structure is shown in Figure 2.2. Sec-butanol is not considered a potential alternative engine fuel due to its low motor octane number. Tert-butanol is not considered as an alternative fuel at higher volumetric concentrations, due to its high melting point. 1-butanol and iso-butanol have physical properties closer to gasoline and could therefore be considered a potential alternative fuel. In this study, only iso-butanol was used because of the higher octane number which is close to the octane number of methanol and ethanol. From here on, iso-butanol will be simply called butanol.

The concentration of fuel blends is usually quantified in terms of volume fraction, whereas the mole fraction of a component should provide the most meaningfuel insight into the variation of physico-chemical properties. Blends of different fuels

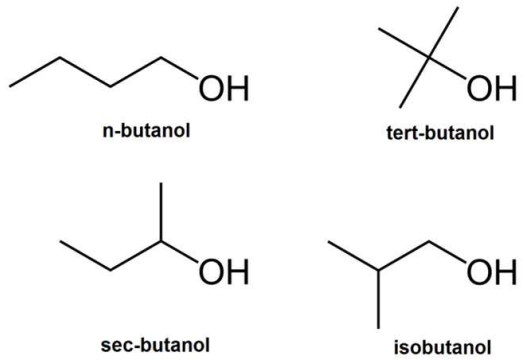

Figure 2.2: Chemical structure of butanol isomers.

for which there is a large difference in the ratio of density of the component to the molar mass of the component will exhibit a large difference in concentration expressed in terms of mole fraction and volume fraction. This is especially true for lower carbon count alcohols blended in gasoline. This is shown in Figure 2.3 in which the relationship between mole and volume fraction for alcohols blended in standard gasoline (molar mass = $107 kg/kmol$ and density = $740 kg/m^3$) is plotted. For ethanol and methanol there is a significant difference, e.g. M10 and E10 on a volumetric basis become respecitively M28 and E22 on a molar basis. For higher alcohols, there is less difference because of the higher molecular mass of these molecules.

Wallner et al. [37] has evaluated alcohols up the octanol as possible alternative fuel candidates. The authors evaluated the different alcohols on several physical and engine related properties:

- **Lower heating value:** Increasing oxygen content of the fuel almost linearly reduces the lower heating value. For methanol and ethanol, there is a reduction of respectively 53 % and 37% in mass-specific energy content. This can be reduced with longer-chain alcohols such as butanol with a LHV penalty compared to gasoline of approximately 23 % or hexanol with a respective penalty of only 16 %. However, due to their oxygen content the energy per unit mass is still significantly reduced compared to the gasoline baseline. Among the alcohol isomers, 1-structures show slightly higher lower heating values compared to their respective iso-structures.
- **Melting and boiling point:** To ensure that a fuel stays liquid regardless of region and time of the year, the melting point of the fuel cannot exceed

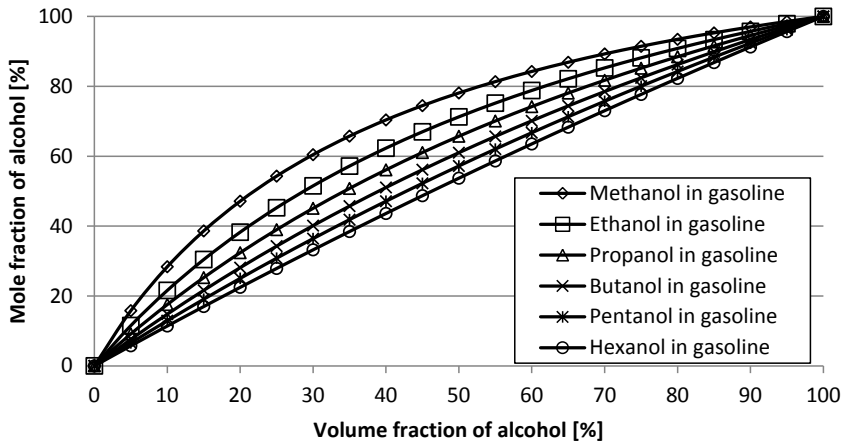

Figure 2.3: Mixtures of alcohols with gasoline: mole fraction of alcohol as a function of volume fraction.

an upper limit. Wallner et al. [37] decided to take -40°C as a realistic upper limit. They reported that there is a general trend of increasing melting temperature with longer carbon chain length. Several isomers, especially tert-isomers and higher carbon count alcohols such as hexanol and octanol, are close to or exceed the upper limit of -40°C due to the reduced intermolecular forces caused by the reduced polarity.

Similar to the trend of the melting points but even more pronounced, there is an increasing trend for the boiling point with increasing carbon count. The boiling point range starts at 65 °C for methanol up to almost 200°C for certain octanol isomers. Contrary to a single boiling point, gasoline has a distillation range. Adding a certain alcohol to gasoline results more or less in an extension of the distillation curve at the boiling point of the alcohol. Therefore the boiling point is critical in influencing the evaporative behavior, certainly when targeting higher blends levels. In contrast with methanol and ethanol, the melting point and boiling point of some higher alcohols make their use as vehicle fuel questionnable and probably only possible in low-level blends.

- **Latent heat of vaporization, vapor pressure and stoichiometric air demand:** A successful cold start depends heavily on these fuel properties. A combination of a low stoichiometric air-to-fuel ratio, high latent heat of vaporization and high vapor pressure can make it difficult to meet the right conditions. Additionally, the distillation curve has an important influence.

Alcohols are single components with a fixed boiling point. As a result, pure alcohols do not contain very volatile components that are present in gasoline to improve the startability.

In Table 2.2, the stoichiometric air-to-fuel ratio is shown for the range of C1 to C8 alcohols. As can be seen in Table 2.2, the relative oxygen content decreases with increasing carbon count which explains the increasing air-to-fuel ratio with increasing carbon count. Wallner et al. reported a clear trend of decreasing Reid Vapor Pressure with decreasing oxygen content for alcohol fuels. All tested alcohols (C2-C6) had RVP values significantly below the RVP value which is normally reported for gasoline. Methanol and ethanol have clearly a lower RVP value than gasoline, but low-level (m)ethanol-gasoline blends can have higher RVP values than gasoline because of the azeotropic behavior of these (m)ethanol-gasoline blends. This will be discussed in more detail in Section 2.3.1.

Finally, the latent heat of vaporization plays an important role during cold start. A higher heat of vaporization means more energy is needed to evaporate the fuel. Wallner et al. [37] reported that the latent heat of vaporization normalized by the amount of fuel energy delivered to the engine increases with oxygen content with a clear maximum for methanol.

- **Mixture calorific value:** The mixture calorific value is a metric for the energy content of a certain volume of stoichiometric air/fuel mixture. The mixture calorific value for gasoline is approximately $3.5 MJ/m^3$, while the values for alcohols are slightly higher with approximately $3.55 MJ/m^3$ for propanol, butanol and hexanol, $3.6 MJ/m^3$ for ethanol and almost $3.7 MJ/m^3$ for methanol [37]. Assuming constant engine efficiencies and constant volumetric efficiency for the different fuels, an advantage in mixture calorific value directly translates into an improvement in engine power output.

- **RON/MON:** The traditional measure for knock resistance is the octane number. Although the applicability of RON and MON in modern, downsized, turbo-charged engines has been widely discussed [38–41], the values are still a commonly used benchmark for fuel characterization. The Research Octane Number (RON) and Motor Octane Number (MON) decrease significantly with increasing carbon count. Iso-structures show increased knock resistance compared to their respective n-structures. It is also worth noting that Research Octane Numbers do not scale linearly when blending gasoline and alcohols. This will be discussed in more detail in Section 2.3.3.

2.3 Non-linear properties of (m)ethanol-gasoline blends

Solutions of methanol and/or ethanol in gasoline behave as non-ideal mixtures: the alcohol-alcohol interactions are different from the alcohol-gasoline or gasoline-gasoline interactions due to the polarity of the alcohol molecules and the resulting hydrogen bonding between alcohol molecules. As the blend ratio changes, certain interactions can become stronger or weaker resulting in a non-linear behavior with the molar content of the individual component. For example when the alcohol is mixed with increasing quantities of gasoline, which is a non-polar liquid, the hydrogen bonds are progressively weakened and become less extensive. In the case of methanol, the methanol molecule starts to behave as a low molecular mass component in gasoline, which is a mixture of hundreds of hydrocarbons, instead of a cyclic tetramer with four times the mass of an individual methanol molecule.

In this Section, the following properties with a non-linear behavior will be discussed: vapor pressure, distillation curve, octane number and density. Other properties such as the laminar burning velocity and the ignition delay do also have a non-linear behavior with the molar fraction of the components. The laminar burning velocity of alcohol-gasoline blends will be discussed extensively in Chapter 5 and the ignition delay will be discussed in Chapter 7 about knock modelling of alcohol-gasoline blends.

2.3.1 Vapor pressure

The most commonly used measure of vapor pressure is the Reid vapor pressure (RVP), defined as the vapor pressure measured at 37.8°C (100°F) in a chamber with a vapor-to-liquid volume ratio of 4:1. This is an indication of the presence of very light fractions that vaporize at low temperatures. Methanol and ethanol, when mixed with gasoline, have very pronounced peaks in RVP around 10 vol% alcohol fraction while this behavior diminishes with increased alcohol chain length [42]. This is shown in Figure 2.4.

This non-intuitive behavior of (m)ethanol-gasoline blends is a consequence of molecular interactions between the gasoline components and (m)ethanol. For an ideal mixture of components, the vapor pressure would follow a molar concentration weighting and the vapor pressure can be expressed by Raoult's law:

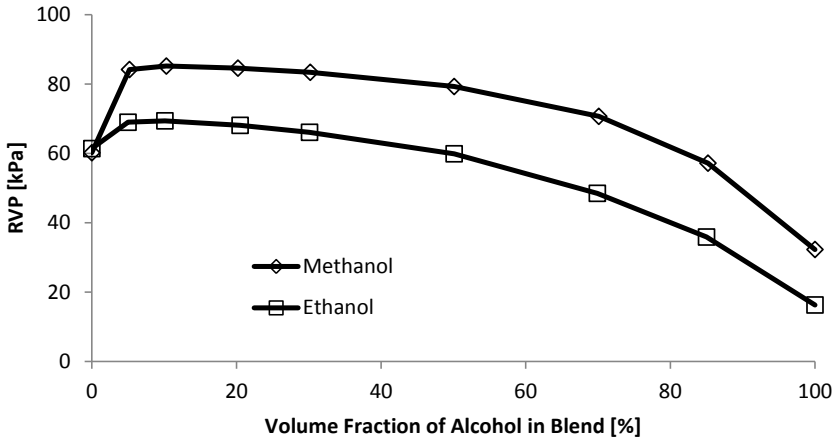

Figure 2.4: RVP of methanol-gasoline and ethanol gasoline blends [42].

$$p = \sum p_i x_i \tag{2.1}$$

where p is the vapor pressure of the mixture, p_i is the vapor pressure of compound i and x_i is the mole fraction of compound i. Solutions of methanol and/or ethanol in gasoline however behave as non-ideal mixtures. As explained earlier, when gasoline is added to alcohol with increasing quantities, the hydrogen bonds are progressively weakened and the alcohol starts to behave as a low molecular mass component and the gasoline-alcohol interactions change [42]. The non-polar hydrocarbon molecules in gasoline interfere with the intermolecular hydrogen bonding between the polar (m)ethanol molecules, and the (m)ethanol interferes with molecular interactions between the gasoline hydrocarbons [43–45]. These interferences with intermolecular bonding allow the respective molecules to more readily escape the liquid as vapor, increasing vapor pressure, and result in the formation of near-azeotropes of (m)ethanol and gasoline components. The effect of the low molecular mass component eventually falls away as more gasoline is added and the alcohol concentration drops to zero. As can be seen in Figure 2.4, the magnitude of the increase of RVP is less pronounced with ethanol addition compared to methanol addition. This is due to the lower vapor pressure and lower polarity of ethanol [42].

This behavior of the vapor pressure can influence the cold-start performance of an engine and explains how evaporative emissions using methanol and ethanol in

high level blends can be lower than those of gasoline while they can be higher using low level blends [43].

The American Petroleum Institute (API) provided an extensive dataset of vapor pressures for ethanol blends with market gasolines and blendstocks of varying volatility [46]. The RVP increase with ethanol addition to gasoline was shown to be dependent on the composition of the gasoline, with greater RVP increase observed for gasoline with lower RVP or greater saturated hydrocarbon content. It was found that the fuel components that contribute most to the vapor pressure are the most volatile components of gasoline: primarily isomers of butane and pentane. Finally, it was shown that vapor pressure increases with temperature with a greater sensitivity to temperature for the vapor pressure of ethanol-gasoline blends than for gasoline containing no ethanol [42]. Thus, for a gasoline containing no ethanol and a gasoline containing ethanol with the same RVP, the vapor pressure of the gasoline with ethanol will increase more as the temperature is increased above the RVP temperature (37.8°C). On the other hand, it will also have a lower vapor pressure at lower temperatures.

2.3.2 Distillation curve

The vaporization behavior of a fuel is important in order to ensure proper cold start and normal operation of the engine. For gasoline, the distillation curve has to meet the ASTM standard D4814. 10 vol% of the fuel must be evaporated at a temperature of 70°C (T10), 50 vol% between 77 and 121°C (T50) and 90 vol% at a maximum temperature of 190°C (T90). The gasoline must be completely evaporated at a temperature of 225°C. The inclusion of large quantities of a single component (in this case methanol or ethanol) in a blend is known to distort the distillation profile near to the boiling point of that single component. The formation of near-azeotropes can cause further distortions, as is known to be the case with methanol and ethanol. Because of the near-azeotropic behavior, the distillation does not occur as discrete segments of compounds but rather as vaporization of mixtures with gradually varying composition and with decreasing volatility [47].

In Figure 2.5 and 2.6, the near-azeotropic behavior of methanol-gasoline and ethanol-gasoline blends is visible as a more slowly rising distillation curve indicating a higher volatility than that of the base gasoline. For increasing alcohol content, this slowly rising curve expands to cover a larger portion of the distillation curve [47]. For high-level ethanol-gasoline blends, problems can arise because of the low volatility at the front end of the distillation curve for low temperatures. Because of the low volatility, the ethanol fraction in 'E85' blends is decreased to

typically 70% by volume during winter months. Other solutions could be adjusting the calibration of engine parameters or installing a second fuel tank with another fuel which would be used during cold start. A second fuel tank makes the system more complex and expensive but an additional gasoline fuel tank is already used in Brazilian flex-fuel vehicles which are running on hydrous ethanol. Vancoillie [28] has given an overview of possible engine-related changes to ensure cold start.

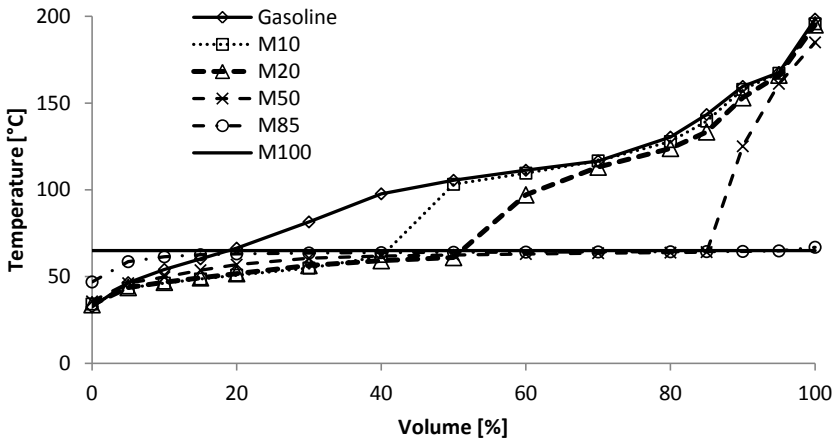

Figure 2.5: Distillation curve of methanol-gasoline blends [47].

2.3.3 RON/MON

Anderson et al. [48] studied the Research Octane Numbers (RON) and Motor Octane Numbers (MON) of gasoline-alcohol blends and found that these properties behave non-linearly on a volumetric basis but can be estimated by calculating the average of the octane numbers of the components using the mole fraction. The difference between mole fraction and volume fraction of methanol-gasoline and ethanol-gasoline blends was shown in Figure 2.3. Because the octane numbers of alcohol-gasoline blends can be estimated using mole fractions, it follows that the sensitivity, $S = RON - MON$, can also be estimated by molar weighting. Still, the behavior of the RON and MON is not completely linear with molar content as shown in Figure 2.7 [21]. Anderson et al. [21] proposed to use a non-linear term to improve the molar-weighted estimate of RON and MON values for ethanol-gasoline blends because measured RON values were up to 3 RON higher than values estimated by molar weighting. Anderson et al. [21]

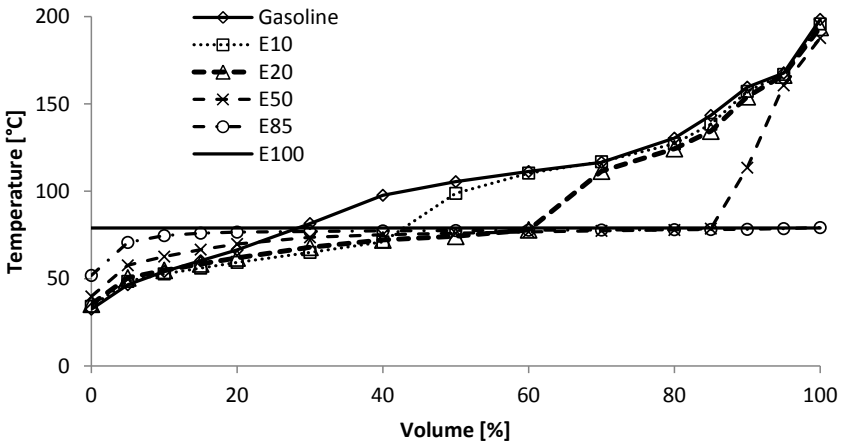

Figure 2.6: Distillation curve of ethanol-gasoline blends [47].

explained the non-linear behavior by interactions between ethanol and certain hydrocarbons.

2.3.4 Density

Due to the way liquids having different molecular size group together, the total volume of a blend of different liquid components can be different from the sum of the volumes of the components prior to mixing. The volume occupied by a number of molecules depends on the molecules that surround them. This can affect the density of alcohol-gasoline blends, especially when water addition is involved. For example, when 1 mole of water is added to a large volume of water at 25 °C, the volume increases by $18cm^3$. When 1 mole of water is added to a large volume of ethanol at 25 °C, the volume increases by only $14cm^3$ because of the higher density packing of the water molecules [49]. For most applications involving anhydrous alcohol-gasoline blends, the density can be approximated with enough accuracy using linear combinations. Turner et al. [50] measured the density of different ternary gasoline-ethanol-methanol blends, discussed in the next Section, at 20°C using a pycnometer. The measured densities were observed to be near linear combinations of individual component densities.

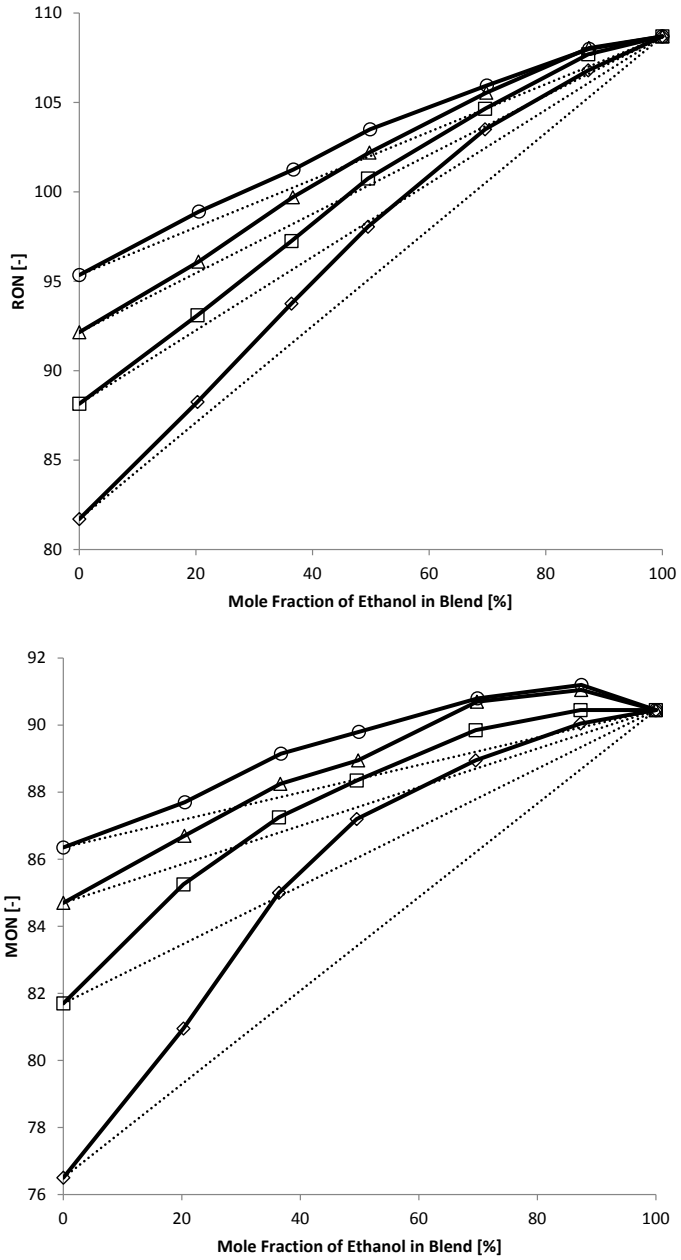

Figure 2.7: Non-linear behavior of RON and MON values of ethanol blends with different gasoline blendstocks. Measurements - symbols [21].

2.4 Ternary gasoline-ethanol-methanol blends

To have ternary blends which could have the potential to be 'drop-in' fuels for binary ethanol blends in flex fuel vehicles, two properties of the blends are absolutely necessary: the blends should have the same stoichiometric air-to-fuel ratio and volumetric energy density as the target binary blend. With identical volumetric energy densities, the opening duration of the fuel injectors can remain the same without the need to recalibrate the ECU. The stoichiometric air-to-fuel ratio condition is required to not upset the ECU with signals from the lambda sensor which are outside the expected range. First, simple expressions are derived which quantify the volume fractions of methanol, gasoline and ethanol required to generate iso-energetic ternary mixtures [51]. These mixtures have the same volumetric energy density as a target binary blend of gasoline and ethanol.

The lower heating value of a fuel blend can be calculated with the following equation:

$$LHV = \sum_{i=1}^{k} \left[\left(\frac{m_i}{m} \right) LHV_i \right] \tag{2.2}$$

with m_i/m the mass fractions of the mixture components. Turner et al. [50] found that the densities of different ternary gasoline-ethanol-methanol blends are near linear combinations of individual component densities. It can thus be assumed that the sum of the volume fractions before mixing, V_i, can be approximated by the post mixing volume, V, for ternary gasoline-ethanol-methanol blends. This is expressed as:

$$V_G + V_E + V_M = V \tag{2.3}$$

or

$$\frac{V_G}{V} + \frac{V_E}{V} + \frac{V_M}{V} = 1 \tag{2.4}$$

in which the subscripts 'G', 'E' and 'M' stand for gasoline, ethanol and methanol. Using Equation 2.4, Equation 2.2 can be re-arranged:

$$\rho LHV = \rho_G \left(\frac{V_G}{V} \right) LHV_G + \rho_E \left(\frac{V_E}{V} \right) LHV_E + \rho_M \left(\frac{V_M}{V} \right) LHV_M \tag{2.5}$$

In the previous Equation, the mass fraction was expressed as:

$$\frac{m_i}{m} = \frac{\rho_i}{\rho}\frac{V_i}{V} \tag{2.6}$$

ρLHV in Equation 2.5 is in fact the volumetric energy density of the target binary blend. Using Equation 2.4, Equation 2.5 can be re-arranged to calculate the volume fraction of gasoline or the volume fraction of methanol as a function of the volume fraction of ethanol which is needed to match the volumetric energy density of any target binary ethanol-gasoline blend. For example, the volume fraction of methanol as a function of the volume fraction of ethanol can be expressed as:

$$\frac{V_M}{V} = \frac{V_E}{V}\frac{(\rho_E LHV_E - \rho_G LHV_G)}{(\rho_G LHV_G - \rho_M LHV_M)} + \frac{(\rho_G LHV_G - \rho LHV)}{(\rho_G LHV_G - \rho_M LHV_M)} \tag{2.7}$$

Using Equation 2.7, the concept of these ternary blends is shown in Figure 2.8 for equivalent 'E85' blends. On the right side of Figure 2.8, the composition of normal E85 can be seen (85 v/v % ethanol and 15 v/v % gasoline). On the left side of Figure 2.8, the binary mixture of gasoline and methanol is shown in which all the ethanol is replaced with gasoline and methanol. This results in a M56 blend (56 v/v % methanol and 44 v/v % gasoline). In between these two blends, any iso-stoichiometric ternary blend can be determined by drawing a vertical line in Figure 2.8 and reading the blend ratios on the left axis of the Figure (for example the yellow dotted line in Figure 2.8). In Figure 2.8, the concept of iso-energetic GEM blends has been shown for equivalent 'E85' blends, but iso-energetic GEM blends can be formulated for any binary ethanol-gasoline blend. The limit case where all the ethanol is removed and substituted by methanol and gasoline can easily be calculated from Equation 2.7, i.e. when $V_E/V = 0$:

$$\frac{V_M}{V} = \frac{(\rho_G LHV_G - \rho LHV)}{(\rho_G LHV_G - \rho_M LHV_M)} \tag{2.8}$$

The possible deviation of the stoichiometric AFR from that of the target binary blend is also quantified for the iso-energetic GEM blends, see Figure 2.9. As the AFR of the blends also depends on the AFR of the gasoline which is used to formulate the blends, the AFR ratios of E85 and M56, which are assumed to be iso-energetic, are plotted in Figure 2.9 as a function of different gasolines with changing AFR while assuming the other properties of the different gasolines stay equal. The deviation between the two limiting binary GEM blends, E85 and M56, becomes larger as the AFR of gasoline increases. The deviation is 1.7 % when the AFR ratio is 14.7 for gasoline and only 0.014 % for an AFR of 14.1. These deviations should however never be a problem for the ECU.

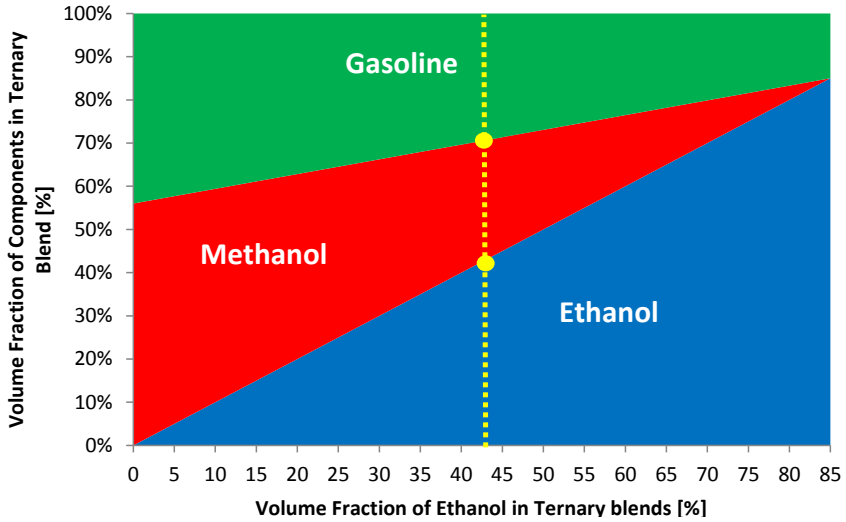

Figure 2.8: Iso-stoichiometric GEM blends equivalent to conventional E85.

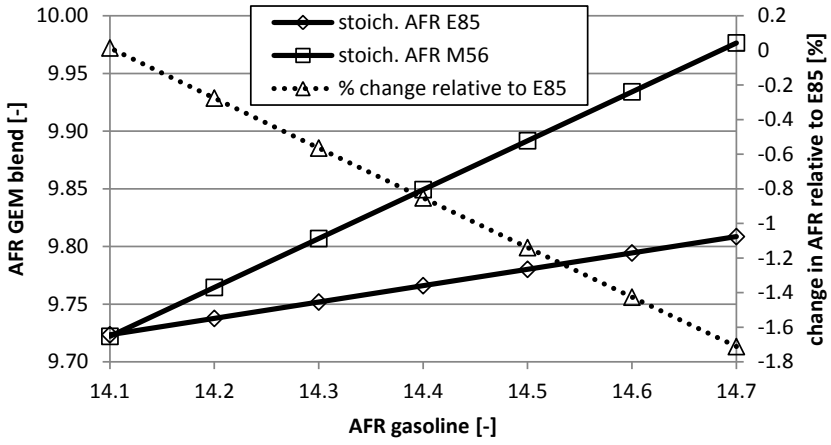

Figure 2.9: Variation of AFR of E85 and M56 as a function of the AFR of gasoline and the deviation of the AFR of M56 relative to E85.

Turner et al. [5–7] found that all the possible iso-stoichiometric and iso-energetic ternary blends starting from a binary blend of gasoline and ethanol have, beside the same AFR and identical volumetric energy content, essentially constant octane numbers and constant latent heat. The fact that these ternary blends show very few differences in physical properties opens the possibility to use these ternary blends as drop-in fuels for flex-fuel vehicles without the danger of upsetting the on-board diagnostics of the engine management system. The octane numbers of four different GEM blends, measured by Turner et al. [5], are shown in Figure 2.10. As can be seen, octane numbers do not vary much for the different blends and even the sensitivity (RON-MON) is more or less constant.

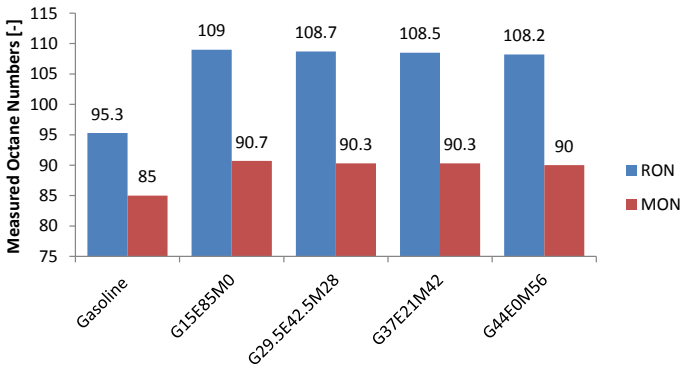

Figure 2.10: Measured Research (RON) and Motor (MON) octane numbers for each of the blends [5].

The GEM blends have the potential to be used as drop-in alternatives to binary ethanol-gasoline blends such as E85 from a combustion and control point of view but it is also important to understand their aggressivity towards materials, volatility properties, blend stability, etc. This was investigated by Turner et al. [50] for several GEM blends. As discussed in Section 2.3.2, a single component in a blend will distort the distillation profile around the boiling point of that single component, with further distortions possible due to azeotropic behavior. For different E85-equivalent GEM blends, Turner et al. [50] found that the biggest distortion for the front end of the distillation curve (low temperatures) occured for the E85 blend (without methanol) indicating low volatility. With increasing methanol content, the distillation curve approaches that of the base gasoline. This indicates that GEM blends containing higher levels of methanol will be less compromised regarding cold temperature startability. The low volatility of the binary ethanol-gasoline blend E85 is the reason that, during winter, the amount of ethanol in E85 is reduced to ensure that there is sufficient gasoline which will

vaporize during cold start.

As the alcohol content decreases in alcohol-gasoline blends, the RVP increases with a peak around 10-15 vol% (see Section 2.3.1). Increased RVP has been linked to increased evaporative emissions. Because the alcohol content decreases when GEM blends with higher methanol fractions are formulated and the vapor pressures of methanol-gasoline blends are higher than the vapor pressures of ethanol-gasoline blends, RVP increases as more methanol is added in the GEM blends. This may lead to increased evaporative emissions and overloaded carbon canister traps, especially for GEM blends with lower alcohol content, e.g. E15 [50]. Instead of standard gasoline, a reformulated blendstock for oxygenate blending or "RBOB" could be used to counteract these issues to some extent.

Qi et al. [52] investigated the blend stability of methanol-gasoline blends. At lower temperatures, a methanol-gasoline blend can become unstable and ethanol was used as a co-solvent in order to yield stable mixtures. The data of Qi et al. [52] was corrected by Turner et al. [6] and is shown in Figure 2.11. This data at -15°C shows that there is a boundary between stable and unstable mixtures and that the E85-equivalent GEM blend without ethanol, M56, would not be stable. This suggests that ethanol should always be used as a co-solvent in some concentration in order to have stable mixtures.

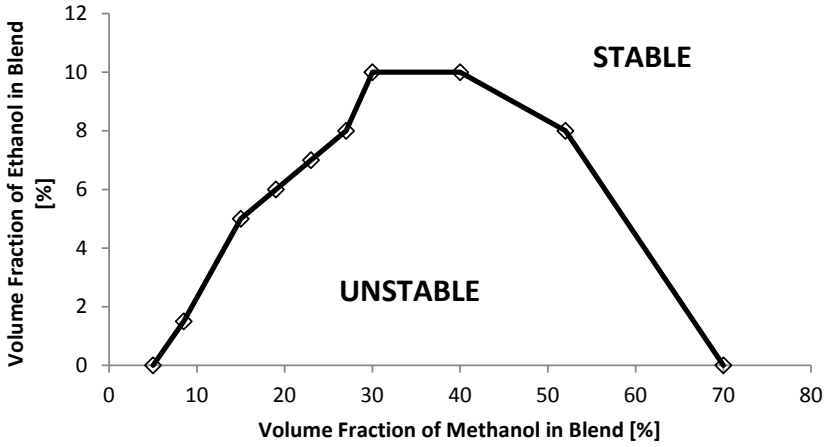

Figure 2.11: Boundary between stable and unstable region in which phase separation can occur at -15°C [52].

Finally, because methanol has a lower molar volume than ethanol, it is expected that the take up and swelling of elastomeric materials would increase for GEM

blends containing higher levels of methanol [53]. Turner et al. [50] evaluated the elastomeric material swelling properties of three different elastomers using different GEM blends and found that the blends containing higher levels of methanol indicated more severe swelling. Turner et al. stated that materials typical for M85 applications can be used with any GEM blend because none of the blends indicated more swelling than M85.

3

Engine experiments

3.1 Introduction

During this Ph.D. study, pure fuels, alcohol-gasoline blends and alcohol-water blends have been tested on engine test benches. Because only engines with port fuel injection were available at Ghent University, the author did a research stay at Argonne National Laboratory (Chicago, USA) where a direct injection spark ignition engine was available. This engine was used to investigate the potential of alcohol fuels in combination with direct fuel injection. The measurements on pure fuels and alcohol-gasoline blends will be reported in this Chapter while the measurements on alcohol-water blends will be reported in Chapter 4. Most of the measurements performed at Ghent University were done by Master students under guidance of the author as part of their Master dissertation.

Finally, at the end of this Ph.D. study, a new engine with direct injection, variable valve timing and a turbo charger was put on a test stand under the guidance of the author. This engine will be used in the future to further investigate the potential of alcohol fuels.

3.2 Experimental equipment

The main specifications of the four engines and the corresponding measurement equipment used in the current study are summarized in Table 3.1 and 3.2.

3.2.1 Test engines

Table 3.1: Engine specifications.

Engine type	Volvo	Audi	CFR	Hyundai
Cylinders	4 in-line	1	1	4 in-line
Valves	16	2	2	16
Valvetrain	DOHC	OHC	OHV	DOHC
Bore	83 mm	77.5 mm	83.06 mm	88 mm
Stroke	82.4 mm	86.4 mm	114.2 mm	97 mm
Displacement	1783 cc	407.3 cc	618.8 cc	2360 cc
CR	10.3:1	13.13:1	variable	11.3:1
Injection	PFI	PFI	PFI	DI
Induction	NA	NA	NA	NA
IVO [° ca ATDC]	VVT	-17	10	VVT
IVC [° ca ABDC]	VVT	45	29	VVT
EVO [° ca BBDC]	40	75	39	VVT
EVC [° ca ATDC]	80	10	12	VVT

Table 3.2: Measurement equipment

Engine type	Volvo	Audi	CFR	Hyundai
Cylinder pressure	Kistler	AVL	Kistler	Kistler
	6118AFD13	QC34C	701A	6118
Intake pressure	Kistler	Kistler	Kistler	Kulite
	4075A10	4075A10	4075A10	ETL-179D-190M
Exhaust pressure	Kistler	Kistler	Kistler	Kulite
	4075A20	4075A20	4075A10	EWCT-312
Fuel flow	gravimetric	gravimetric	gravimetric	coriolis flowmeter
Air flow	Bosch MAF	Bronkhorst	Bronkhorst	Flowmaxx subsonic
		F-106BZ-HD-01-V	F106AI-ABD-01-V	venturi flow meter
O_2	Maihak	Maihak	Maihak	Horiba
	Oxor-P S710	Oxor-P S710	Oxor-P S710	MEXA7100
CO,CO_2,NO_x	Maihak	Maihak	Maihak	Horiba
	Multor 610	Multor 610	Multor 610	MEXA7100
HC	-	-	-	Horiba
	-	-	-	MEXA7100
PM	-	-	-	AVL
	-	-	-	483 Micro Soot Sensor
Data acquisition	NI cDAQ	NI cDAQ	NI PXI	ETAS INCA system
				AVL IndiCom

Volvo

A Volvo four-cylinder sixteen valve naturally aspirated gasoline engine with a total swept volume of 1783 cc and a compression ratio of 10.3:1 was converted to tri-fuel operation by mounting an additional fuel rail supplying gaseous fuel (in this case, hydrogen) to 8 Teleflex GSI gas injectors (2 per cylinder), mounted on the intake manifold. Additional adjustments to allow reliable operation on hydrogen are described in [34]. Further, the Volvo engine was equipped with a fully programmable engine control unit to control ignition timing, start of injection and injection duration. Liquid fuel injectors with increased flow capacity (Racetronix 48INJL) and stainless steel fuel lines and fuel rail were installed to ensure light alcohol compatibility. The standard spark plugs were replaced by colder ones to avoid pre-ignition issues on hydrogen and methanol [54]. This engine is shown is Figure 3.3.

Audi

A first single cylinder engine used in this study is based on an Audi research DI diesel engine, see Figure 3.1. It has a swept volume of 407 cc and a compression ratio of 13.13:1. The diesel injectors were replaced by spark plugs and the engine was converted for tri-fuel operation using similar adjustments as for the Volvo 1.8L.

Figure 3.1: the Audi 1-cylinder test engine

CFR

Another single cylinder engine used in this research was based on a CFR (Cooperative Fuel Research) engine. The engine speed is held constant at 600 rpm by a synchronous generator. This research engine is specifically designed to measure the octane number of different fuels and can endure long periods of knocking operation without engine damage. It is equipped with port fuel injection for both gaseous and liquid fuels. The compression ratio can be adapted by turning a lever that displaces the cylinder head relative to the crankcase. As can be seen in Figure 3.2 the cylinder head includes four openings with a diameter of M18, which can be used to install various sensors. More information on this engine can be found in [55].

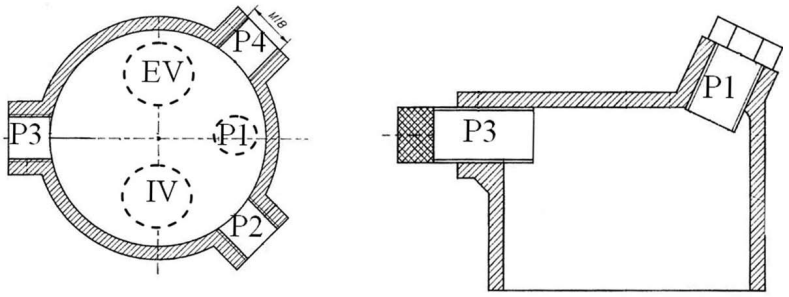

Figure 3.2: Cross-section of the CFR engine, P1: spark plug, P1-P4: sensor positions, IV: intake valve, EV: exhaust valve

Hyundai

The Hyundai 2.4L GDI engine (Theta II) is a naturally aspirated, 4-cylinder, gasoline direction injection (GDI) platform used in a range of Hyundai vehicles in the United States. The engine is equipped with an Engine Control Unit (ECU) that allows for adjustment of operational parameters such as spark timing and injection parameters. For this study, a stock ECU calibration for unleaded gasoline operation with the factory engine knock detection algorithm activated was used. All tests were run with stock, early injection resulting in homogeneous charge using a closed loop feedback to tightly control air/fuel ratio to stoichiometric conditions. This engine is shown is Figure 3.3.

Figure 3.3: The Volvo 1.8L (left) and Hyundai 2.4L GDI (right) test engines

3.2.2 Measurement equipment

Cylinder pressure measurements were done using piezo-electric pressure sensors and piezo-resistive sensors were placed in the intake and exhaust runners, close to the valves, for pegging the cylinder pressure (see Table 3.2). This was done by assuming that intake and cylinder pressure equalize at the end of the intake stroke, around bottom dead center. The time-averaged intake and exhaust gas temperatures were measured at the same position using thermocouples.

For the Hyundai 2.4L GDI engine, regulated emissions of carbon monoxide (CO), hydrocarbons (HC) and oxides of nitrogen (NO_x) of pre-catalyst emission samples (engine-out emissions) were measured using a Horiba MEXA7100. The raw emissions bench uses separate analyzers to determine the level of NO_x, HC, CO, CO_2, and O_2 in the exhaust stream. Using a heated sample line, exhaust is fed to an oven that houses a heated flame ionization detector (FID Model FIA-725A) and a heated chemiluminescent detector (CLD Model CLA-720MA) for HC and NO_x emissions measurements, respectively. CO is measured using cold analyzers (NDIR). The soot mass concentration in exhaust gas (PM emissions) is measured by using an AVL 483 Micro Soot Sensor. For the Volvo 1.8L and both single cylinder engines, the dry, engine-out exhaust gas components O_2, CO, CO_2 and NO_x were measured (O_2: Maihak Oxor-P S710, paramagnetic; CO, CO_2, NO, NO_2: Maihak Multor 610, non-dispersive infra-red).

All measurements signals were acquired and logged using the data-acquisition systems in Table 3.2. For the Hyundai engine, dynamometer data was collected for 120 seconds and cylinder pressure data for 200 engine cycles after measurements were allowed to stabilize. The dynamometer data was collected two consecutive times at each operating point.

3.2.3 Measurement methodology

General

The results presented in this work were acquired during steady state operating conditions at various engine speeds and loads. MBT (Minimum spark advance for best torque) spark timing was applied, except for knock-limited operating conditions, where borderline detonation (BLD) spark timing minus 2°ca was used. Stoichiometric operation was chosen in order to maximize the conversion rate of the commonly used three-way catalyst (TWC).

For the test engines at Ghent University, indicated quantities are normally averaged over 50 consecutive pressure cycles, in order to level out cyclic variation. The sample rate resolution of the pressure measurements was 0.25°ca in normal operation. For the knock measurements and the measurements used for validation of the simulation models, the amount of cycles was increased to 100. For knock measurements, pressures were sampled every 0.1 °ca by a crank angle encoder in order to discern the high frequency knock induced oscillations.

For the Hyundai test engine at Argonne National Laboratory, dynamometer data was collected for 120 seconds and cylinder pressure data for 200 engine cycles, sampled every 0.1 °ca. The dynamometer data was collected two consecutive times at each operating point. The basic engine map, which prescribes injection properties and ignition timing for gasoline, was adjusted for the other fuels through fuel trims and ignition advancement in order to keep stoichiometric operation.

Error analyses of the employed experimental setups have been described in previous work [27, 28, 55].

3.3 Comparison of pure fuels

First, the difference between pure alcohols and gasoline will be investigated. Measurements were performed on the Hyundai 2.4L GDI engine fuelled with

pure methanol, ethanol, gasoline and butanol. Butanol was added in the tests because butanol is often mentioned as a potential alternative fuel next to methanol and ethanol, see Section 2.2. EEE Certification gasoline was used for the measurements to be sure that there were no oxygenates in the gasoline. The measured operation points at constant torque and engine speed can be seen in Table 3.3. At high load and high rpm, it was not possible to measure on pure methanol because the stock ECU did not allow enough adjustment of the fuel trim to maintain stoichiometric operation. As a result, only 1 operation point on pure methanol was measured at 150 Nm because it was not possible to measure at the same operating conditions at speeds higher than 1500 rpm. At 50 Nm and 75 Nm, it was not possible to maintain stoichiometric operation at 3000 rpm when using pure methanol.

Table 3.3: Measurement points for the Hyundai engine

	Hyundai 2.4L
rpm	1500 - 2000 - 2500 - 3000
Torque [Nm]	50 - 75 - 150
BMEP [bar]	2.66 - 4 - 8

3.3.1 Efficiency

First, the efficiencies on pure methanol, ethanol, butanol and gasoline operation are compared for a range of engine speeds. Figure 3.4 shows the brake thermal efficiency for the different fuels at different loads and a range of engine speeds. Notice that at high load and high rpm, it was not possible to measure on pure methanol. In Figure 3.4a and 3.4b, every operating point could be achieved with MBT timing as there was no knock at these lower loads. The efficiency of the different fuels behaves in a similar way as a function of engine speed. In Figure 3.4c, the curve is different for gasoline because at 1500, 2000 and 2500 the ignition timing for gasoline could not be advanced until MBT timing was achieved but BLD spark timing minus 2°ca was used to avoid knock. Starting with the non-knock-limited operating points, it is clear that methanol has the superior efficiency. Jung et al. [56] compared E85 to gasoline in an alternating back-to-back manner and quantified the effects which resulted in the higher brake thermal efficiency of E85. Approximately half of the improvement could be attributed to the way the heating value is measured in a combustion bomb. The remaining difference was mostly due to lower heat transfer losses. Differences in pumping work and emissions accounted for only a small fraction. When measuring the heating value in a combustion bomb, the heat of vaporization of the fuel

detracts from the heat release while this is not the case for the heat released during combustion in a SI engine because the fuel is already evaporated before combustion. This effect on the efficiency can be accounted for by recalculating the efficiency using the sum of the heating value and the heat of vaporization instead of only the heating value that is measured in a combustion bomb. In Figure 3.5, the 'corrected' brake thermal efficiency for a fixed torque of 75 Nm is shown. As seen on the Figure, the efficiencies of the different fuels are lower and closer to each other. This is because of the higher heat of vaporization of the alcohol fuels compared to gasoline. More than half of the improvement for methanol can be attributed to this effect. For ethanol and butanol, almost the entire increase in efficiency can be attributed to this effect at 1500 rpm. Further optimization of the direct injection of the alcohol fuels is probably needed to fully use the charge cooling potential in flex-fuel engines. Besides the greater charge cooling potential, alcohol fuels can have lower in-cylinder heat transfer losses due to the lower adiabatic flame temperature. The adiabatic flame temperature increase is a function of the heat released per mole and the molar specific heat of the combustion products. With the same method used by Jung et al. [56] to take the effect of the heat of vaporization on the heat release into account, it was found that the heat released per mole of combustion products for methanol, ethanol and butanol is lower than for gasoline. This is shown in Table 3.4. In Table 3.4, the fraction of triatomic molecules in the combustion products is also shown. Because of the higher proportion of triatomic molecules compared to gasoline, the specific heat at high temperatures is slightly higher.

Table 3.4: Heat release per mole of combustion products and percentage of triatomic molecules in combustion products for gasoline, methanol, ethanol and butanol

	Gasoline EEE	**Methanol**	**Ethanol**	**Butanol**
Heat released per mole of combustion products [MJ/mole]	0.0800	0.0782	0.0783	0.0787
Decrease compared to gasoline [%]	0%	2.23%	2.19%	1.72%
Percentage of triatomic molecules in combustion products [%]	25.8%	34.6%	30.6%	28.4%
Increase compared to gasoline [%]	0%	34%	19%	10%

Methanol and ethanol also have the potential of broadening the EGR working range due to the higher burning velocity. A shorter burn duration due to higher burning velocities can also have a positive impact on the efficiency [57] because of the more isochoric combustion. However, an increase in combustion rate results in higher pressure rise, higher cylinder temperature, and hence, higher heat transfer loss [58]. As a result, it is expected that the effect of the higher burning velocity on the thermal efficiency is almost negligible.

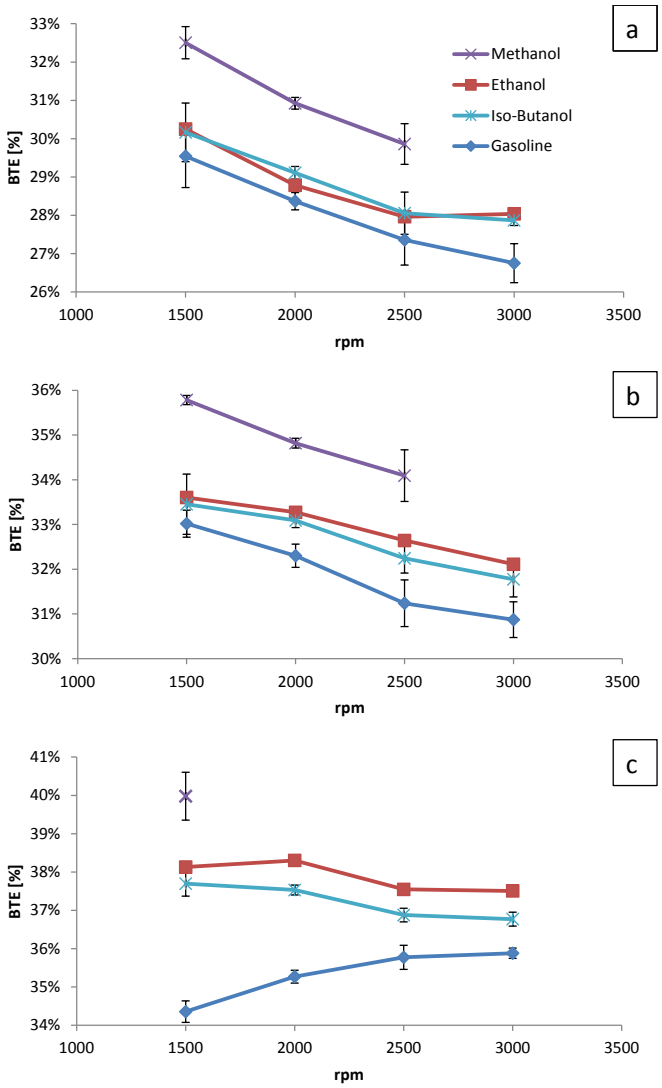

Figure 3.4: Brake thermal efficiency as a function of engine speed for different fixed brake torques of 50 Nm (a), 75 Nm (b) and 150 Nm (c).

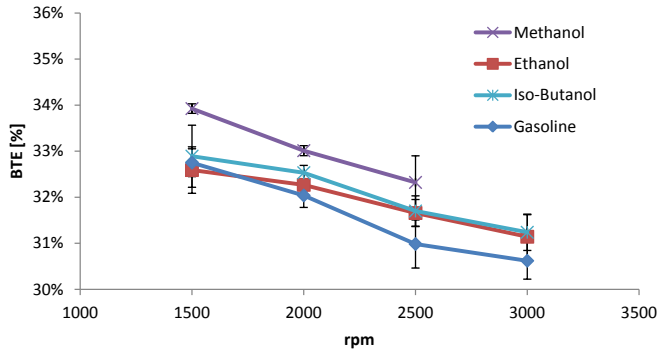

Figure 3.5: Corrected brake thermal efficiency as a function of engine speed for a fixed brake torque of 75 Nm.

As most of the properties of ethanol and butanol (see Table 2.1) are in between those of methanol and gasoline, it was expected that the efficiency of ethanol and butanol would be in between the efficiency of methanol and gasoline as can be seen in Figure 3.4. For most operating points, it seems that there is a slightly better efficiency (based on the LHV) in the case of ethanol compared to butanol. The increase in brake thermal efficiency of the three alcohol fuels becomes significant at the operating points where gasoline is knock-limited. All alcohol fuels could be run at 150 Nm without being knock-limited. For methanol, there was an improvement of 2.7 percentage points on average compared to gasoline for the non-knock-limited operating points at 50 and 75 Nm but for the knock-limited case at 150 Nm and 1500 rpm this difference increased to 5.6 percentage points with the brake thermal efficiency of methanol reaching almost 40%. This means that with the trend of downsizing and also downspeeding of spark ignition engines, there is a big efficiency improvement possible with these alcohol fuels.

Efficiency is closely related to the CO_2 emissions. As can be seen in Table 2.1 in Section 2.2, the specific CO_2 emissions are the lowest for methanol, followed by ethanol, butanol and gasoline. Even if the efficiency of the four different fuels was the same, methanol, ethanol and butanol would emit lower CO_2 emissions than gasoline. Together with the increased efficiency, it is clear that a large CO_2 emission reduction is possible as is shown in Figure 3.6. Figure 3.6 shows the CO_2 emissions of the different fuels for the different fixed torques as a function of engine speed. As expected, the biggest drop in CO_2 emissions is at 150 Nm and 1500 rpm in the case of methanol. There is a decrease of 20.7% compared to gasoline. These emissions are only engine out CO_2 emissions. If you take into account that methanol, ethanol and butanol can be produced from renewable

resources, the well to wheel CO_2 emissions would decrease even more compared to gasoline.

Based on the properties of methanol, ethanol and butanol (high heat of vaporization and low air to fuel ratio) and given the fact that the efficiency for these alcohol fuels is higher than the efficiency of gasoline, one could expect that the exhaust temperature would be the lowest for methanol, followed by ethanol and butanol and the highest for gasoline. In Figure 3.7, the exhaust temperature for the four fuels is shown for a torque of 75 Nm as a function of the engine speed. As expected, the exhaust temperature of gasoline is the highest with a 20-30 K increase compared to the alcohol fuels. The exhaust temperatures of methanol, ethanol and butanol are on the other hand very similar. The temperature can change due to several factors. For example, the exhaust temperature depends on the amount of fuel, air and dilution (internal EGR) in the cylinder. Because of the different properties of the fuels, the throttle position was not the same at the same load for every fuel and the interaction of the fuel spray with the air could have an effect on the gas dynamics changing the amount of dilution. Another possible reason is that the spray of the direct fuel injection is not yet optimized to take full advantage of the possible charge cooling of these fuels. As a result, a relatively big fraction of the vaporization heat could be taken from the cylinder walls and piston.

3.3.2 Emissions

In this section, the trends of emissions of NO_x, CO, UHC and PM are shown and discussed for the pure fuels. In Figure 3.8, the NO_x emissions are shown for the four different fuels at a fixed load of 75 Nm and a range of engine speeds. The highest NO_x emissions are clearly on gasoline and the lowest NO_x emissions are on methanol. The NO_x emissions of ethanol and butanol are in between gasoline and methanol. The lower combustion temperature of the alcohol fuels is responsible for the lower NO_x emissions since most NO_x is produced by the thermal mechanism which is very dependent on temperature. The lower NO_x emissions at lower engine speeds might be caused by elevated levels of internal EGR given the vacuum in the intake due to throttling at lower engine speeds. It is remarkable that the maximum difference in NO_x emissions between the three alcohol fuels is around 3.8 g/kWh and that the difference between butanol and gasoline is 6.15 g/kWh on average. In other words, the NO_x emissions of the three alcohol fuels do not differ a lot while there is a big increase for the gasoline NO_x emissions. This could be linked to the very similar exhaust temperatures of the alcohol fuels as discussed earlier (see Section 3.3.1) as the NO_x mechanism is very dependent on temperature.

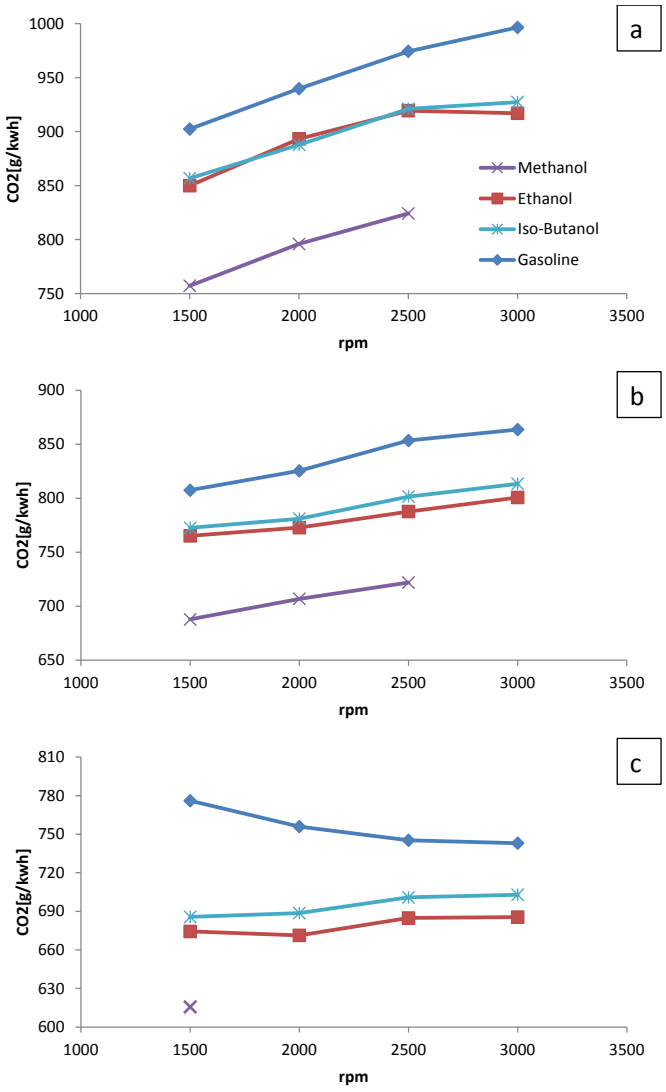

Figure 3.6: CO2 emissions as a function of engine speed for different fixed brake torques of 50 Nm (a), 75 Nm (b) and 150 Nm (c).

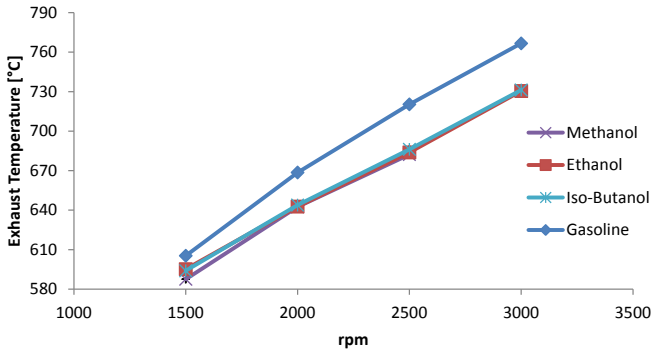

Figure 3.7: Exhaust temperature as a function of engine speed for a fixed brake torque of 75 Nm.

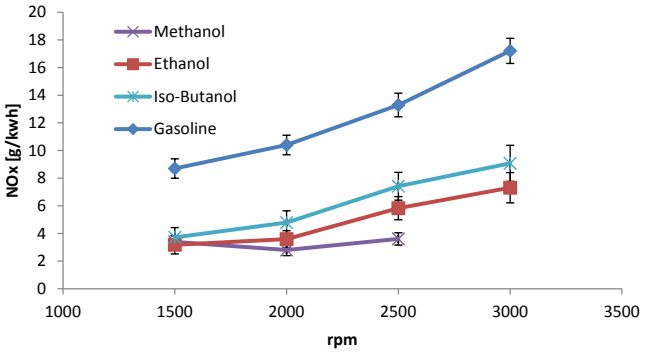

Figure 3.8: NOx emissions as a function of engine speed for a fixed brake torque of 75 Nm.

The engine-out CO and UHC emissions for the different fuels are compared in Figure 3.10 and Figure 3.11 respectively for a load of 75 Nm. Emissions of unburned fuel were measured using flame ionization detectors. It has been reported that using the flame ionization detector technique might lead to an underestimation of the total unburned hydrocarbons of alcohol fuels. The reason for this is that oxygenated species are commonly found in the exhaust gases of alcohol engines but the reaction time for oxygenated hydrocarbons is impracticably long for flame ionization detectors and thus realistic values are not possible. However, the UHC can be corrected using a response factor. The corrected UHC emissions are calculated using the uncorrected UHC measurement from the FID measurement and a response factor unique to each fuel. Response factors for ethanol and butanol were calculated from the study done by Wallner [59]. Wallner developed a correlation for response factors based on emissions measurement on ethanol-gasoline and butanol-gasoline blends performed with a standard raw emissions bench with FID as well as with an emissions bench with Fourier transform infrared spectroscopy (FTIR). This correlation is solely based on volumetric alcohol content and carbon count of the alcohol fuel used for blending. This correlation was also tested for data of methanol-gasoline blends measured by Yanju et al. [60] which included operating conditions for blend levels of 10 vol%, 20 vol% and 85 vol% at various speeds and loads but no satisfying agreement was found. As a result, for the response factors of methanol, data from the study of Yanju et al. [60] was used instead of the correlation developed by Wallner et al. [59]. In Figure 3.9, the response factors derived from the data are shown together with a fitted trend line which made it possible to estimate the response factor at 100% methanol. The equation of the trendline was also used to calculate the response factor for the M56 GEM fuel to correct the UHC emissions of M56 in Section 3.4.2. The data provided by Yanju et al. [60] was the only data available in literature. When interpreting the corrected UHC emissions results, it is important to keep in mind that the methanol response factors were based on a very limited set of data which has not been evaluated by other measurements. In Figure 3.11a, the uncorrected UHC emissions are shown and in Figure 3.11b, the UHC emissions are corrected with response factors calculated as discussed earlier. The CO and UHC emissions of alcohol fuels could be lower than gasoline due to the oxygenated nature of alcohols which might cause a more complete combustion [61]. In Figure 3.10, it seems that gasoline has the highest CO emissions while there is no clear trend for methanol, ethanol and butanol. When looking at the uncorrected UHC emissions of the different fuels in Figure 3.11a, there seems to be a clear trend. Methanol has the lowest UHC emissions, followed by ethanol, butanol and gasoline. This trend could be explained by the increasing oxygen content of the alcohol fuels. For the corrected emissions in Figure 3.11b, this trend is still present for gasoline, ethanol and butanol but the trend is less pronounced.

However, for methanol, it seems that the correction made by the response factor could be overestimated as the trend of ethanol, butanol and gasoline as a function of engine speed behaves in a more or less similar way while for methanol the decrease with increasing engine speed is much steeper. As mentioned earlier, the response factors for methanol are calculated with a very limited data set of emission measurements. More validation of the difference between the actual unburned fuel and UHC emissions measured with the FID technique is therefore needed.

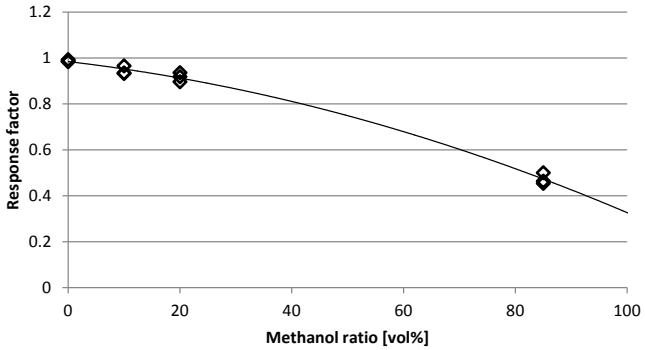

Figure 3.9: Response factor for UHC emissions of methanol

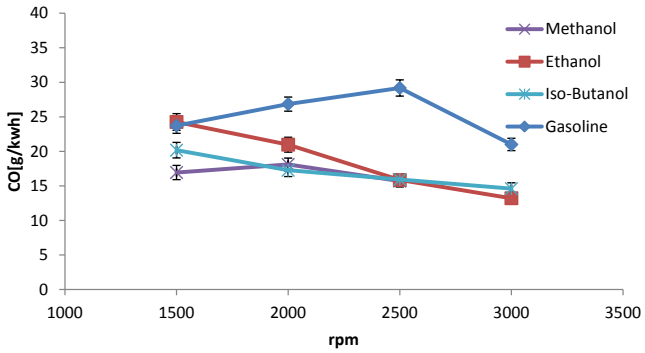

Figure 3.10: CO emissions as a function of engine speed for a fixed brake torque of 75 Nm.

Finally, in Figure 3.12 the PM emissions are shown as a function of engine speed for a fixed torque of 75 Nm. Because of the oxygenated nature of alcohols, it is expected that the PM emissions will be lower. Additionally, it is often assumed that a methanol engine is free from particle emissions because there

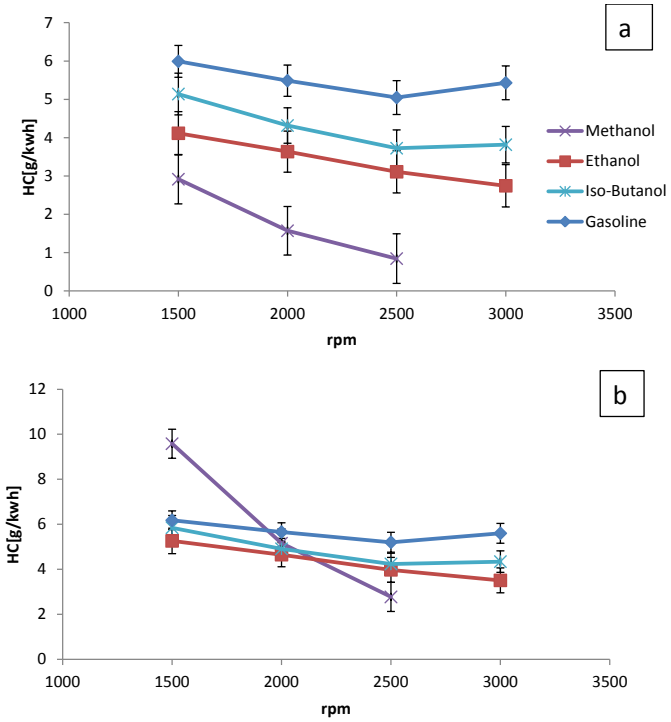

Figure 3.11: Uncorrected UHC (a) and corrected UHC emissions (b) as a function of engine speed for a fixed brake torque of 75 Nm.

is no carbon-carbon bond in the molecule of methanol. However, during the combustion, soot precursors such as benzene, pyrene, etc. with carbon-carbon bonds can be formed. In Figure 3.12, gasoline clearly has the highest soot emissions while the trend is not completely clear for the three alcohol fuels. At lower rpm, butanol has the highest PM emissions while at higher rpm, it has the lowest emissions. This trend is not seen at the other load points, but for all the load points, it is clear that gasoline has higher soot emissions than the alcohol fuels.

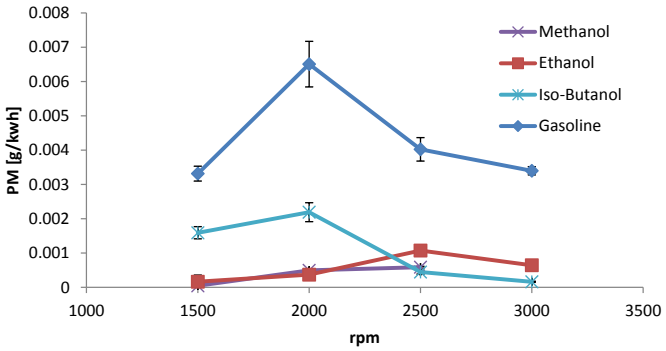

Figure 3.12: PM emissions as a function of engine speed for a fixed brake torque of 75 Nm.

3.4 Ternary gasoline-ethanol-methanol (GEM) blends

In the next section, the hypothesis that iso-stoichiometric/iso-energetic ternary blends can be used as drop-in fuels for spark-ignited flex-fuel engines is studied. The performance of different GEM blends will be evaluated and compared to some results on methanol, ethanol and gasoline on the Volvo 1.8L engine and Hyundai 2.4L. Secondly, the pollutant emissions of the GEM blends will be discussed and finally, the knock limit of the GEM blends will be compared to the knock limit of methanol, ethanol and two different gasolines with a RON of 95 and 98 on the single cylinder Audi engine.

The measured operation points on GEM blends at constant torque and engine speed can be seen in Table 3.5 for the measurements done on the Volvo 1.8L and in Table 3.3 for the the measurements done on the Hyundai 2.4L.

Table 3.5: Measurement points on GEM blends for the Volvo engine

	Volvo 1.8L
rpm	1500 - 2000 - 2500 - 3000 - 3500
Torque [Nm]	40 - 80
BMEP [bar]	2.82 - 5.63

3.4.1 Efficiency

Volvo 1.8L

On the Volvo 1.8L engine, four different GEM blends were investigated. The composition and the properties of the blends are shown in Table 3.6. There are two binary blends: Blend A representing normal E85 and the iso-stoichiometric methanol-gasoline Blend D with 57 v/v % methanol. This methanol-gasoline blend has 1 v/v % methanol more than in the study of Turner et al. [15] because of the AFR of the gasoline used here. The two other blends are ternary blends of which the ethanol content is halved each time starting from E85.

Figure 3.13 shows the brake thermal efficiency for all blends at a load of 40 Nm (2.82 bar BMEP) for a range of engine speeds. The hypothesis that all iso-stoichiometric blends have similar BTE is confirmed as all values fall within the experimental uncertainty. This statement is valid for all loads tested. Figure

Table 3.6: Properties of the GEM blends

	Blend A	Blend B	Blend C	Blend D
	E85	G29.5E42.5M28	G37E21M42	M57
Oxygen content [m%]	23.34	22.74	22.38	22.54
Gravimetric LHV [MJ/kg]	29.22	29.48	29.66	29.53
AFR_{stoich} [kg/kg]	9.72	9.76	9.8	9.73
Δh_{vap} [kJ/kg]	762.4	762.7	761.5	770.8
α (#H/#C in fuel)	2.83	2.86	2.87	2.9
Specific CO_2 emission [g/MJ]	71.69	71.56	71.49	71.41

3.14 displays the comparison with gasoline, methanol, ethanol and a mean value for the GEM blends for 40 and 80 Nm. This mean value is representative for all mixture compositions as the differences between the GEM blends are within the experimental uncertainty. When compared to gasoline, it is clear that the GEM blends show significant efficiency gains. The mean value for the GEM blends is similar to the BTE of pure ethanol. Pure methanol clearly still has superior performance as explained in Section 3.3.1 when comparing the pure fuels. In Figure 3.14, the efficiencies of all the fuels increase as the delivered torque increases. As a result of the increasing torque, the mechanical efficiency increases strongly. With an increasing torque, the flow losses increase because of the larger flow, but the pumping losses decrease due to a larger throttle position. The increase in mechanical efficiency and indicated efficiency results in the increase of the brake thermal efficiency with higher torque outputs. The BTE of the fuels tested for this study can be seen to show little sensitivity to the engine speed. There seems to be a small drop with increasing engine speed. On the one hand, the increasing air flow with engine speed causes higher flow losses but on the other hand, as seen from the TP curve in Figure 3.15, the throttle opening has to be increased with engine speed to keep the torque output constant, which decreases the throttling losses. Both effects seem to almost cancel each other out but the net effect is a decrease in BTE. Additionally, friction also increases with increasing speed reducing the BTE at higher engine speeds.

The BSFC does - as expected after the discussion on BTE - not depend on mixture composition as seen on Figure 3.16 because of the similar LHV of the four GEM blends. The BSFC is still considered as the main disadvantage of fuels containing alcohols due to their decreased LHV. While the GEM blends display similar BTE as pure ethanol, their BSFC is less penalized as for pure methanol. This can be derived from Figure 3.17 in which a comparison of the BSFC of gasoline, methanol, ethanol and a mean value for the GEM blends for 40 and 80 Nm is shown.

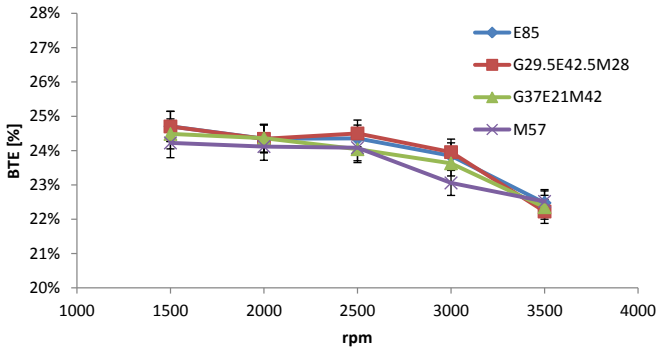

Figure 3.13: Brake thermal efficiency of GEM blends as a function of engine speed for a fixed brake torque of 40 Nm (2.82 bar BMEP).

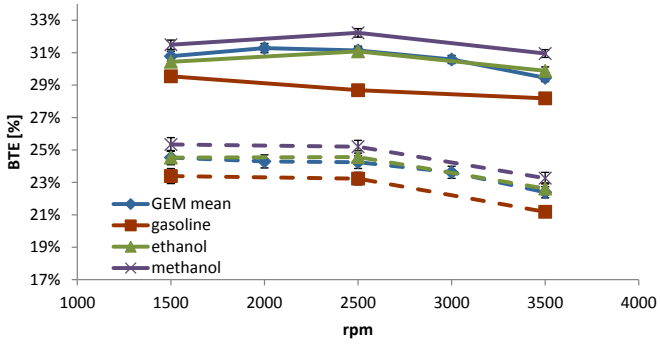

Figure 3.14: Brake thermal efficiency as a function of engine speed for different fixed brake torques of 40 Nm (- - -) and 80 Nm (-).

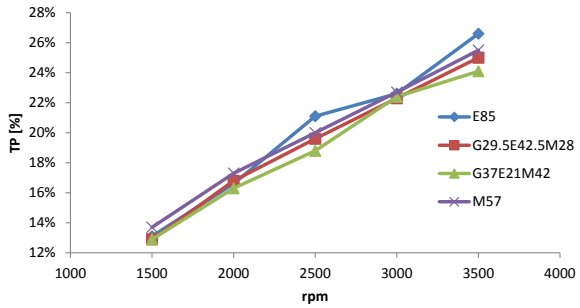

Figure 3.15: Throttle position of GEM blends as a function of engine speed for a fixed brake torque of 40 Nm (2.82 bar BMEP).

Despite the better efficiency on GEM blends, this engine will consume 32% more GEM fuel on a volume basis than when it is running on gasoline. This difference will be smaller for modern highly downsized and pressure charged engines with direct injection in which the properties of alcohols will have greater benefits.

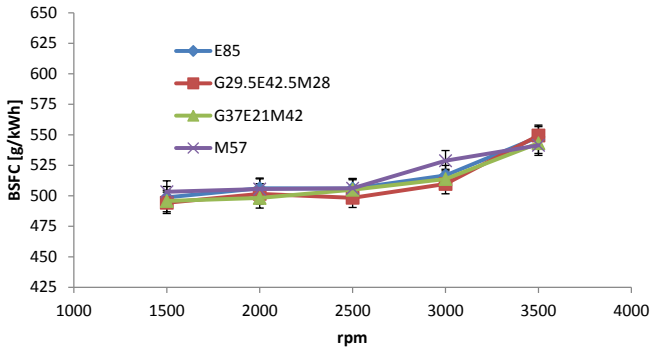

Figure 3.16: Brake specific fuel consumption of GEM blends as a function of engine speed for a fixed brake torque of 40 Nm (2.82 bar BMEP).

In Figure 3.18, the volumetric efficiency is shown at a load of 40 Nm for the four different GEM blends. The volumetric efficiency is defined as:

$$\eta_v = \frac{\dot{m}_{fuel+air}}{\dot{m}_{theoretically}} \tag{3.1}$$

with $\dot{m}_{fuel+air}$ the actual mass flow of fuel and air entering the cylinders during

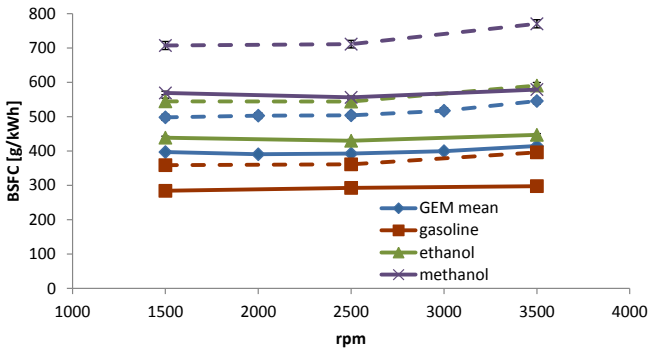

Figure 3.17: Brake specific fuel consumption as a function of engine speed for different fixed brake torques of 40 Nm (- - -) and 80 Nm (-).

the intake stroke and $\dot{m}_{theoretically}$ the theoretical mass flow that could enter the cylinders under the atmospheric conditions during the measurements. All the possible ternary blends have essentially identical volumetric energy content and constant latent heat. As a result of the similar efficiencies of the GEM blends, the volumetric efficiency is largely unaffected by the blend composition for all measuring points. An increase of the volumetric efficiency with engine speed for a fixed torque is explained by the drop in BTE with engine speed. More mixture is needed for the same torque output. It is expected that every parameter can stay equal within the control systems of the engine. This is also reflected in the throttle position and the MBT ignition timing for a specified load, as can be seen in Figure 3.15 and Figure 3.19. MBT-timing is set manually and, as a result, slight deviations can occur in the measurements. Selected MBT timing for almost all blends are similar with a maximum deviation of 1 °ca. Due to the identical properties of the GEM blends, resulting in almost identical performance and efficiencies, the exhaust temperatures of the different blends are quasi equal, see Figure 3.20. This can be important for turbocharged engines to make sure that the turbine inlet temperature does not exceed the maximum allowed temperature of the materials.

The CoV of the IMEP as a function of engine speed is shown in Figure 3.21. All CoV values are low enough (lower than 3%) to have reproducible results.

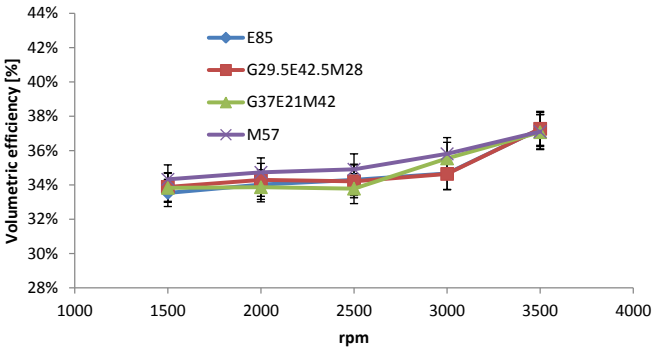

Figure 3.18: Volumetric efficiency of GEM blends as a function of engine speed for a fixed brake torque of 40 Nm (2.82 bar BMEP).

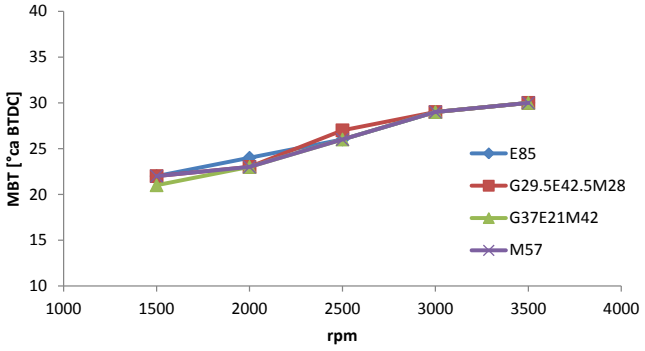

Figure 3.19: MBT of GEM blends as a function of engine speed for a fixed brake torque of 40 Nm (2.82 bar BMEP).

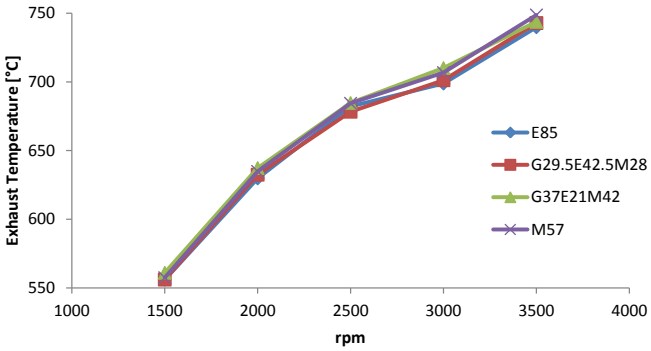

Figure 3.20: Exhaust temperatures of GEM blends as a function of engine speed for a fixed brake torque of 40 Nm (2.82 bar BMEP).

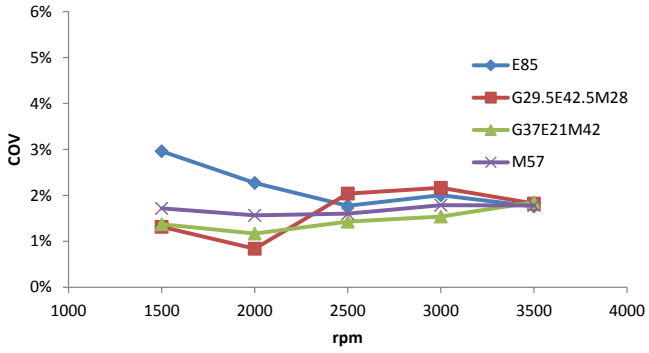

Figure 3.21: Coefficient of variation of the IMEP of GEM blends as a function of engine speed for a fixed brake torque of 40 Nm (2.82 bar BMEP).

Hyundai 2.4L GDI: E85 vs. M56

In this section, we will zoom in on the difference between two iso-energetic GEM blends as measured on the Hyundai engine with direct injection: E85 and M56. M56 is the iso-energetic blend with the maximum fraction of methanol starting from E85. Because of different gasoline used to formulate the GEM blends, the composition of the binary methanol-gasoline blends has changed compared to the previous Section (M56 vs. M57). Every other GEM blend that would be stoichiometric to E85 would have properties between these two blends. As a result, it is expected that the results of every other GEM blend starting from E85 would be between the results of the binary blends tested in this study. First, measurements were done for E85 at fixed loads of 50, 75 and 150 Nm for a range of engine speeds. All parameters regarding injection (start of injection and injection pressure) and ignition were kept the same for the measurements on M56. Only very small adjustments of the throttle valve were allowed to have the same torque output with M56 as with E85. The ECU data and high-speed cylinder pressure data was used to investigate if there could be a significant difference between the combustion behavior of these two blends with very similar properties. In Figure 3.22, the brake thermal efficiency for E85 and M56 is shown at different loads and a range of engine speeds. The only significant difference can be seen for a fixed torque of 150 Nm. In Figure 3.22C, it is clear that at an engine speed of 2500 the error bars do not overlap. For 50 and 75 Nm, the brake thermal efficiencies are very close with overlapping error bars for each operating point.

The difference in injection duration between E85 and M56 is shown in Figure 3.23. It can be seen that for 50 Nm and 75 Nm, only for one operating point, the difference is bigger than 1%. For 150 Nm, the differences are larger but still only 2.7% at maximum.

As the difference at 150 Nm is the biggest, the combustion characteristics calculated from the in-cylinder pressure data of the AVL IndiModul system were investigated for this load. In Figure 3.24 and Figure 3.25, the crank angle at 5% mass fraction burned and the duration of 10-90% mass fraction burned are shown respectively. The main combustion (10-90% mass fraction burned) is similar for both fuels with a slightly slower combustion for M56. This could be explained by the slower laminar burning velocity of M56 compared to E85. In Chapter 5, laminar burning velocities of alcohol-gasoline blends are studied in more detail. As will be explained in Chapter 5, the laminar burning velocity of alcohol-gasoline blends can be calculated out of the laminar burning velocity of the components using a mixing rule. With a mixing rule based on energy fraction, it can be calculated that the laminar burning velocity of M56 at atmospheric pressure and 298 K is 4.4 % slower than the laminar burning velocity of E85 which gives an

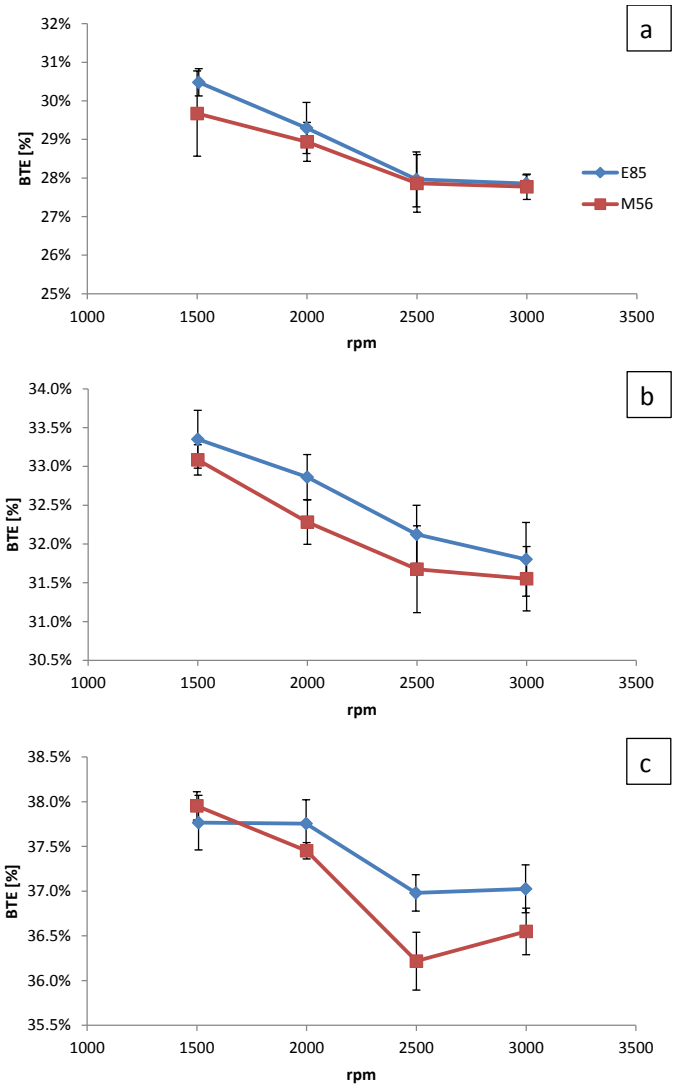

Figure 3.22: Brake thermal efficiency as a function of engine speed for different fixed brake torques of 50 Nm (a), 75 Nm (b) and 150 Nm (c).

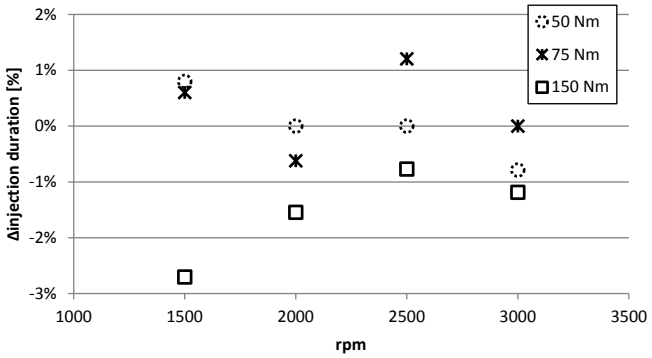

Figure 3.23: Difference in injection duration of M56 compared to E85 as a function of engine speed for different fixed brake torques of 50 Nm, 75 Nm and 150 Nm.

indication for the slower combustion of M56. The 10-90% mass fraction burned duration of M56 increases with ± 0.8°ca. The biggest difference can be seen for the crank angle at 5% mass fraction burned at 2500 rpm, which could explain the difference in brake thermal efficiency for this operating point. As the fuel-air mixture is never 100% homogeneous in a DI engine, the start of the combustion process could also be influenced by small inhomogeneities due to different spray behavior which could lead to different interaction with the incoming air in the combustion chamber.

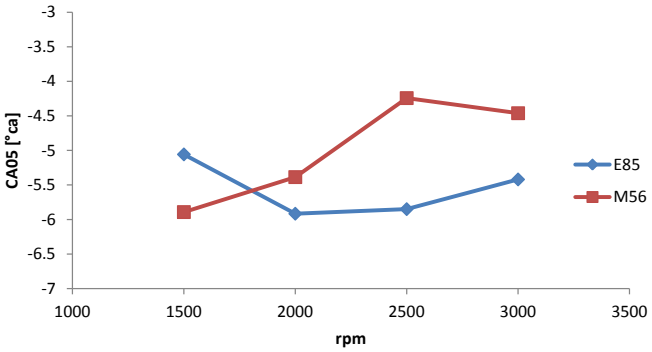

Figure 3.24: CA05 as a function of engine speed for a fixed brake torque of 75 Nm.

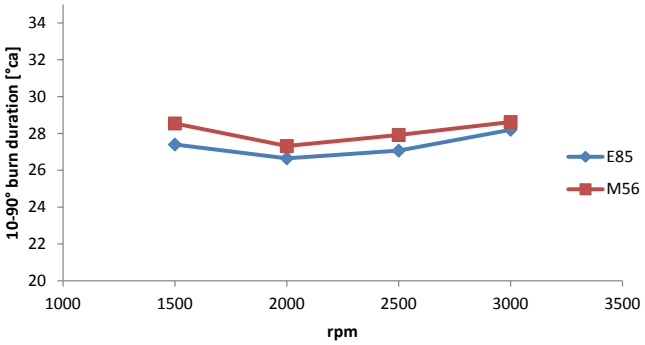

Figure 3.25: duration of 10-90% mass fraction burned as a function of engine speed for a fixed brake torque of 75 Nm.

3.4.2 Emissions

Volvo 1.8L

Figure 3.26 compares the engine-out NOx emissions for the four GEM blends measured on the Volvo 1.8L engine at a load of 40 Nm. As can be seen, the highest NOx emissions are on gasoline and the lowest NOx emissions are on methanol. All the NOx emissions on the GEM blends are somewhere between gasoline and methanol. The lower combustion temperatures of the alcohol fuels are responsible for the lower NOx emissions since most NOx is produced by the thermal mechanism which is very dependent on temperature. The lower NOx emissions at lower engine speeds might be caused by elevated levels of internal EGR since the vacuum in the intake due to throttling is quite considerable at this load of 40 Nm. For the GEM blends it is remarkable that there is an increase in NOx emission with increased gasoline content in the mixture. This variation with gasoline content and thus total alcohol concentration for all other measurements could be ascribed to the slight variation in flame temperature. The engine-out CO emissions for the different blends are compared in Figure 3.27 for a load of 40 Nm. All GEM fuels gave more or less the same CO emissions considering the error bars. According to some authors, due to the oxygenated nature of alcohols which might cause a more complete combustion, the CO emissions of alcohol fuels should be lower than gasoline [61]. Thus, it is expected that the CO emissions of the blends are higher than the CO emissions of pure methanol and lower than gasoline. This trend could not be seen in the measurements. Both gasoline and methanol gave similar CO emissions. It is not possible to conclude that the CO emissions are

actually lower or higher for the blends because the error bars overlap and the fact that slight deviations from stoichiometric operation might have a bigger influence on the CO emissions than the fuel type.

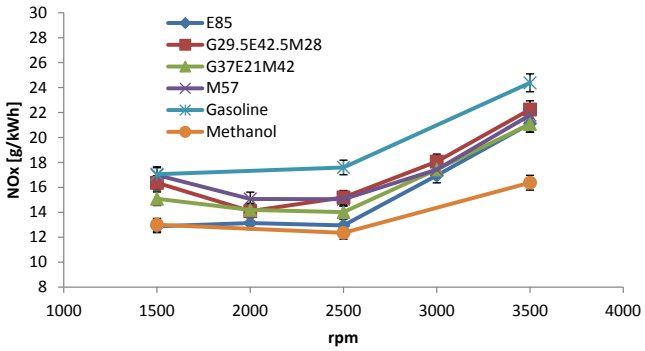

Figure 3.26: NOx emissions as a function of engine speed for a fixed brake torque of 40 Nm (2.82 bar BMEP).

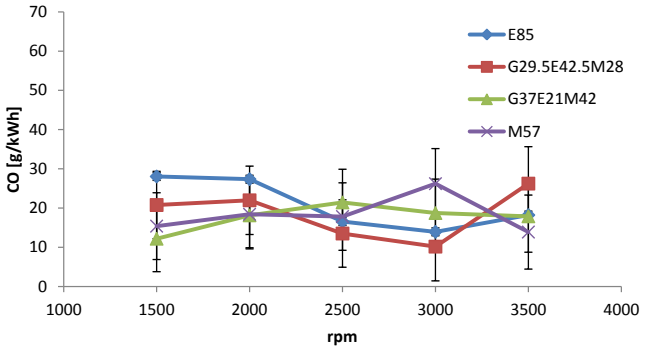

Figure 3.27: CO emissions of GEM blends as a function of engine speed for a fixed brake torque of 40 Nm (2.82 bar BMEP).

Hyundai 2.4L GDI: E85 vs. M56

Finally, in Figure 3.28, Figure 3.29 and Figure 3.30, the engine-out NOx, CO and UHC emissions of E85 and M56 for a fixed torque of 75 Nm are shown as a function of engine speed. There are slightly better engine out emissions for E85 although the error bars overlap for most points and the differences are small

compared to M56 for the whole engine speed range. The emissions of both E85 and M56 are close to the emissions of pure ethanol. E85 (85 v/v % ethanol) is close to pure ethanol which explains this behavior.

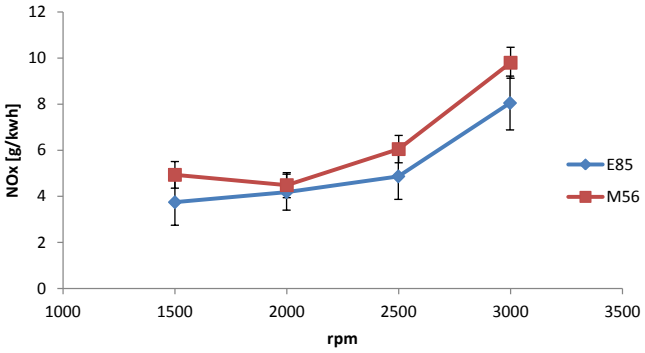

Figure 3.28: NOx emissions as a function of engine speed for a fixed brake torque of 75 Nm.

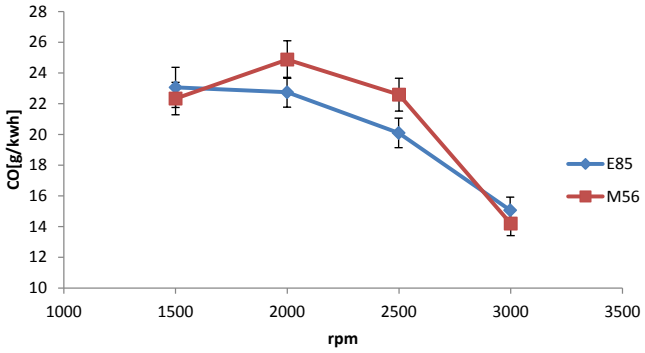

Figure 3.29: CO emissions as a function of engine speed for a fixed brake torque of 75 Nm.

3.4.3 Knock behavior

Audi single cylinder

GEM blends should have a bigger advantage over gasoline in modern pressure charged engines because these fuels suppress knock more than gasoline. For the

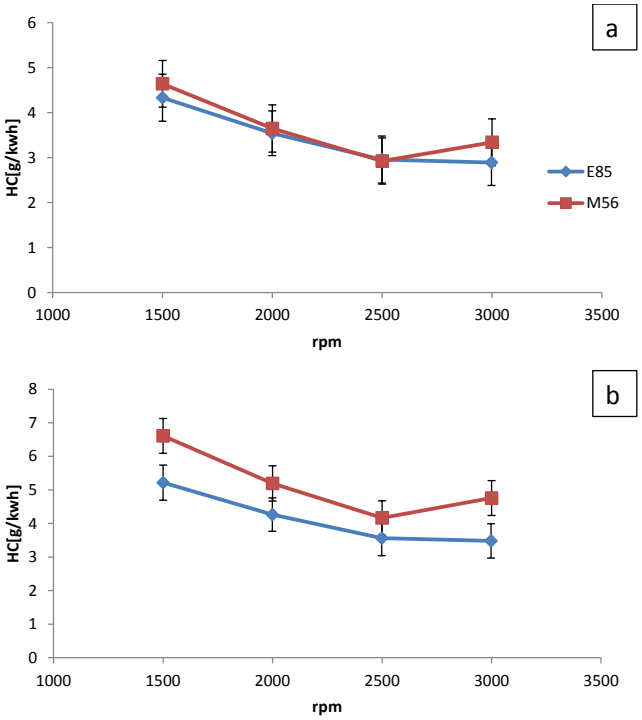

Figure 3.30: Uncorrected UHC (a) and corrected UHC emissions (b) as a function of engine speed for a fixed brake torque of 75 Nm

Volvo 1.8L and Hyundai 2.4L engine, no knock occurred during the measurements on the different GEM blends and MBT timing could be set for every load and engine speed. Turner et al. [5] investigated the octane numbers of the GEM blends and found that the octane numbers as well as the sensitivity of the GEM blends was quasi constant. As a result, it is expected that the different GEM fuels have the same knock behavior. To investigate the statement that all such blends exhibit quasi constant RON and MON, all blends and components (pure methanol, ethanol and gasoline) are tested on the single cylinder Audi engine with a compression ratio of 13.13:1. The properties of this test engine are listed in Table 3.1. At an operating point of 25 Nm (BMEP = 7.713 bar) and 2000 rpm, ignition timing is advanced until an intermediate knocking condition is obtained. This intermediate knocking condition is assessed by audible signals and the third derivative of the pressure signal [62]. Next to the gasoline with RON 95, which was used to make the blends, a gasoline with RON 98 was also used. The results of this experiment are shown in Figure 3.31. As can be seen, all blends have similar knocking behavior resulting in the same ignition timing before knock occurs. The ternary blends display the same ignition timing as pure ethanol. The equivalent 'E85' GEM blends are close to pure ethanol which explains this behavior. Methanol still has superior knock resistance mainly because of the additional cooling effect due to its latent heat of vaporization combined with the lower AFR. Finally, all alcohol containing mixtures score significantly better than the two gasolines tested in this engine.

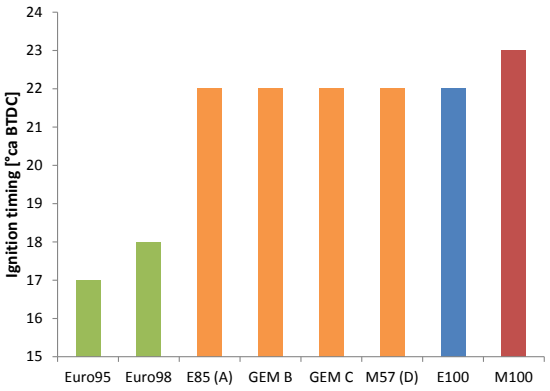

Figure 3.31: Knock limited spark advance of all GEM blends and components.

3.5 Conclusion

The performance and engine-out emissions (NOx, CO, HC and PM) of methanol, ethanol and butanol were examined on the Hyundai 2.4L GDI engine and compared with those on neat gasoline. It was shown that the brake thermal efficiency when running on alcohol fuels is significantly better than with gasoline while emitting fewer emissions. It was clear that methanol was superior both in the case of efficiency and emissions. In a knock limited case for gasoline, the brake thermal efficiency on methanol of almost 40% was more than 5 percentage points better than on gasoline which resulted in a decrease in CO_2 emissions of 20.7 % compared to gasoline. Additionally, measurements were done on both the Hyundai 2.4L GDI engine and the Volvo 1.8L engine with iso-stoichiometric/iso-energetic GEM blends to investigate the hypothesis that GEM blends can be used as drop-in fuels for spark-ignited flex-fuel engines. Confirmation of similar BTE, volumetric efficiency, BSFC and knock behavior was reported for the tested operating points. Only NOx formation displayed small variations with mixture composition. The comparison with gasoline was made to emphasize the potential for efficiency improvements and emission reduction. Special attention was given to the injection duration and the combustion analysis based on the in-cylinder pressure measurements for the measurements performed on the Hyundai 2.4L GDI engine. The engine test results confirmed that, from an engine control point of view, the iso-stoichiometric/iso-energetic methanol-gasoline blend can indeed be used as a 'drop-in' fuel in flex-fuel vehicles.

4

Hydrous alcohol blends

4.1 Introduction

As explained in Chapter 2, methanol and ethanol are polar molecules. Due to their polarity, alcohols such as methanol and ethanol are miscible with water and can also absorb water from the atmosphere.

Most of the production processes for alcohols result in a crude alcohol containing residual gases and a significant amount of water. Thus, distillation becomes an inevitable step to obtain high grade alcohol. The dehydration step accounts for an important part of the overall cost of production, both in investment and in exploitation. Therefore it would be interesting, from an economical point of view, to use hydrous alcohol and reduce or avoid the dehydration process. A second incentive to investigate hydrous alcohol is the potential of increasing the efficiency by means of the cooling effect of water. Several publications [63–65] pointed out that hydrous ethanol (up to 7 wt% water content) can be used as an efficient fuel.

Figure 4.1 gives an example of the energy needed to get anhydrous ethanol produced from corn.

The full circle in Figure 4.1 represents the total energy output for a unit of corn (ethanol, oil and gluten) [66]. The energy that remains after accounting for all

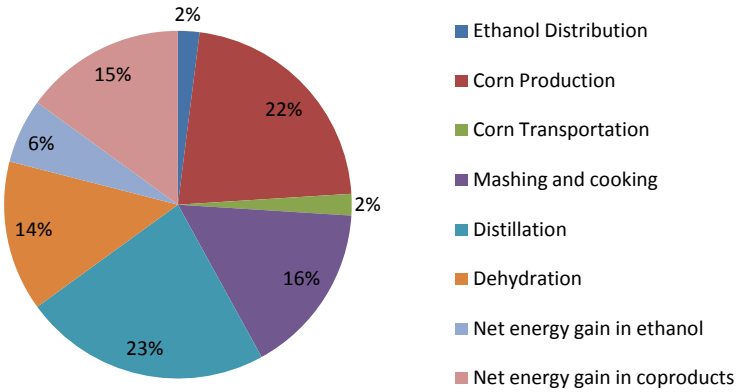

Figure 4.1: Net energy balance for ethanol produced from corn [66].

the energy consumption is the net energy gain, which has two components: net energy in the ethanol and net energy in the coproducts. Conventional distillation is used for the first part of the dehydration process to reduces the water content from 12 wt% to the azeotropic value of 4.37 wt% and accounts for 23 % of the total energy output. As water and ethanol form an azeotropic mixture at 95.63 wt% ethanol/4.37 wt% water, the last water content is removed through an energy intensive dehydration process. The azeotropic ethanol-water blend is dehydrated up to more than 99 wt% purity through an expensive and time-consuming process using additives (toluene or benzene) to absorb the greater part of the remaining water. This step accounts for as much as 14 % of the total energy output. Such a process is needed because an azeotropic mixture is a mixture of liquids in such a way that its components cannot be altered by simple distillation. When an azeotrope is boiled, the vapor it produces has the same constituents as the liquid. In Figure 4.2 the energy (referred to the Lower Heating Value of ethanol) required to obtain a specific purity is plotted. It is clear that the curve has a very steep slope for purities over 90 % because of the azeotropic mixture and therefore the energy costs increase dramatically once high grade ethanol is required.

These energy requirements determine a significant part of the total ethanol production cost. Distillation efficiencies are still improving thanks to optimization of process and installation, e.g. distillation step integration and more efficient heat utilization [67–69]. Another important efficiency gain is feasible through material development where molecular zeolite sieves present a valuable and energy efficient alternative when used in Pressure Swing Adsorption [70–72]. Nevertheless, all the

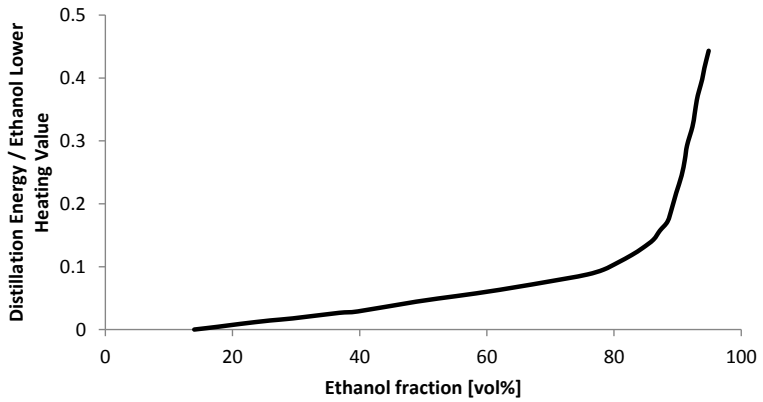

Figure 4.2: Production energy required as a function of purity [66].

processes needed for distillation increase the process energy intensity, well-to-tank CO_2 emissions (depending on the energy source used), and capital cost [73, 74]. It is clear that using hydrous ethanol directly as fuel (or as blending component with gasoline [65]) would imply a substantial economic advantage over fully dried ethanol.

Mack et al. [75] reported that direct utilization of 35% ethanol in-water mixtures reduces water separation cost to only 3% of the energy of ethanol and co-products (versus 37% for producing pure ethanol), and improves the net energy gain of ethanol and co-products (the energy that remains after accounting for all the energy consumption) from 21% to 55%. Although this mixture is probably not exploitable in existing production SI engines due to ignition limitations, numerical simulations of a HCCI engine predict the possibility of operation on this blend [66]. Mack et al. [75] tested this statement experimentally and reported a stable HCCI operation up to 40 wt% water.

Brazil has been a frontrunner regarding alcohol usage as fossil fuel alternative in production vehicles. Depending on ethanol supply, minimum mandatory blending percentages of 18 to 25 % ethanol in gasoline are instructed. Higher alcohol content blends are also marketed (e.g. the well-known E85) as is the hydrous ethanol, presented as E100. This blend can contain up to 7.4 % water content.

The cost increase for methanol of high purity is less dramatic than with ethanol due to the formation of a zeotropic instead of an azeotropic mixture and simple distillation is sufficient to fully dry it. For a quantification of the distillation cost, various parameters such as water content of the crude methanol must be taken into account. The water content itself highly depends on the production process. When,

for example, methanol is formed with renewable hydrogen and atmospheric CO_2, the reaction is theoretically:

$$CO_2 + 3H_2 \rightarrow CH_3OH + H_2O \tag{4.1}$$

Per mole of methanol, there is a mole of water.

Although a minimum level of distillation is mostly required in order to eliminate possible dissolved volatile gases from other production processes of methanol and therefore stabilize the methanol for safe transport, crude methanol distillation requires energy and thus contributes to the cost of methanol production.

Earlier research for hydrous methanol mostly covers the blending of hydrous methanol and gasoline. The major issue encountered when blending water, methanol and gasoline is phase separation, the dispersion of the blend in an aqueous and an organic liquid phase. Cold start problems, a fluctuating knock resistance and a suboptimal mapping are the main disadvantages related to phase separation in a vehicle's fuel tank. Phase separation of hydrous alcohol blends will be discussed in more detail in Section 4.2.1.

When using hydrous alcohol as a fuel, special attention should also be paid to corrosion. In general, corrosion is often caused by ionic impurities such as chloride ions and acetic acid with chloride ions being the most aggressive single contaminant in ethanol that contains water [76]. It has also been documented that a combination of three contaminants (chloride ion, acetic acid, and ethyl acetate) produces a synergistic effect in hydrous ethanol, and corrosion is many times greater than that by any single contaminant [77]. Also wet corrosion can be caused by the water present in the alcoholic fuel, which oxidizes most metals [78]. Ethanol and methanol are electrically conductive. Corrosion behaviors that are dependent on conductive fluid behavior, such as electrochemical and galvanic corrosion, can be enhanced by an increase of the alcohol fuel's electrical conductivity due to absorbed water and contaminants [76]. However, corrosion is not an insurmountable obstacle. In Brazil, there are already millions of flex-fuel vehicles on the market that can run on hydrous ethanol.

4.2 Hydrous alcohol fuels

4.2.1 Water tolerance of alcohol-gasoline blends

An important aspect of the storage of fuels is that the fuel must be stable. Contrary to methanol and ethanol, gasoline is not miscible with water. As a result,

blend stability and by extension water tolerance are important factors for hydrous alcohol-gasoline blends. The water tolerance in blends is the amount of water (volume percent) that a blend can dissolve before separating into two phases at equilibrium. Skinner et al. [79] pointed out that the tendency of water induced phase separation is a function of the amount of water, the type of alcohol, the temperature and the alcohol/gasoline ratio. Qi et al. [52] produced critical phase separation temperatures for a range of methanol/gasoline blends as a function of water content, see Figure 4.3. The critical phase separation temperature of methanol-gasoline blends increases with the amount of water present in the blend. Additionally, they stated that the addition of ethanol will reduce the phase separation temperature. Donnelly et al. [80] concluded that, when as little as 0.1 vol% water is added to a M20 blend, phase separation can occur at a temperature of 20 °C. Because of this very small water tolerance of the methanol-gasoline blend, water contamination during the methanol transport and storage has to be avoided.

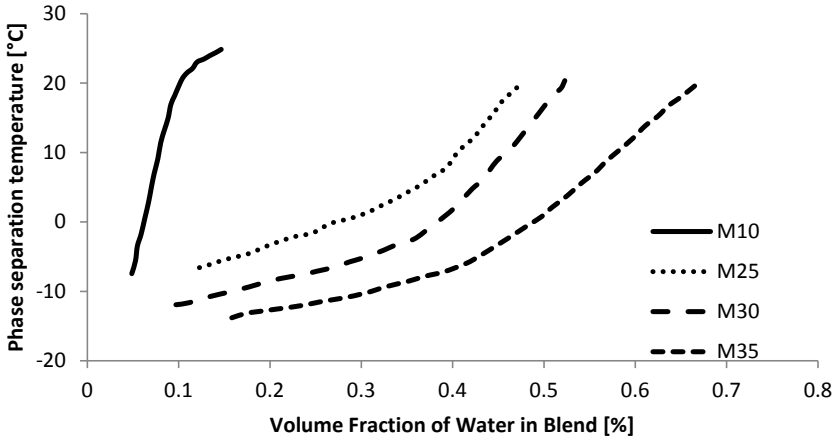

Figure 4.3: Effect of water on the phase separation temperature of methanol-gasoline blends [52].

In this study, the software Aspen was used to get insights into the phase separation process of alcohol-gasoline blends. In Aspen the UNIFAC-LiquidLiquid model was used to get qualitative results of phase separation for gasoline-alcohol-water blends. For gasoline, a toluene reference fuel (blend of iso-octane, n-heptane and toluene) was used as representation of a real gasoline because a real gasoline was not included in the Aspen libraries. In Figure 4.4, the results are shown. The alcohol in the gasoline-alcohol-water blends is a mixture of methanol and ethanol going from 100% methanol to 100 % ethanol as can be seen in the Figure. Under

the lines, the blend is unstable and phase separation is expected. As expected from the literature, blends with a high fraction of alcohol are more water tolerant and addition of ethanol will reduce the chance of phase separation [52].

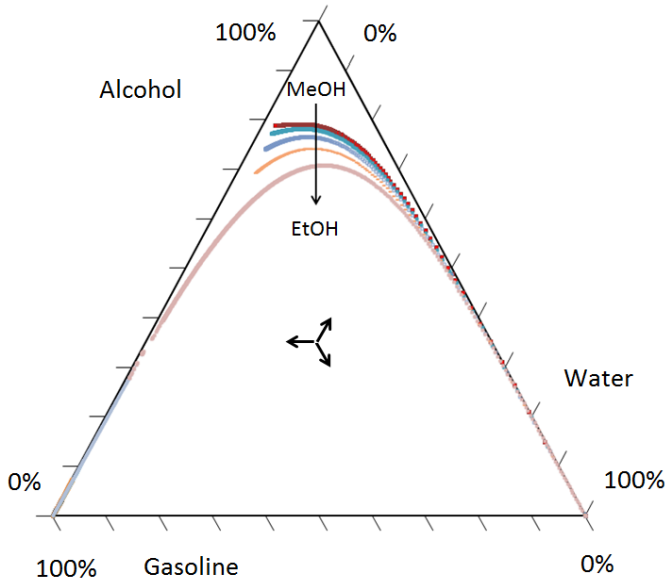

Figure 4.4: Phase diagram of alcohol/water/gasoline mixtures.

4.2.2 Influence of water in a SI engine

When water is added to a fuel blend, the fraction of water can be seen as an extra dilution. After the water has evaporated, it displaces a volume which otherwise could be taken by an air-fuel mixture. As is the case with external exhaust gas recirculation (EGR), adding higher fractions of dilution can render the combustion unstable. There will thus be an upper limit of water percentage that can be added to a fuel blend. The effect of water addition has several similarities to the effect of adding EGR.

In Figure 4.5, the relationship between mole and volume fraction for hydrous methanol and hydrous ethanol is plotted, similar to Figure 2.3. This relationship can be important to keep in mind: adding a small volume of water to methanol or ethanol can result in a significant change in the molar composition, e.g. in ethanol, 10% water by volume represents a mole fraction of 26%.

Engine measurements on hydrous alcohol fuels are very limited in literature. This

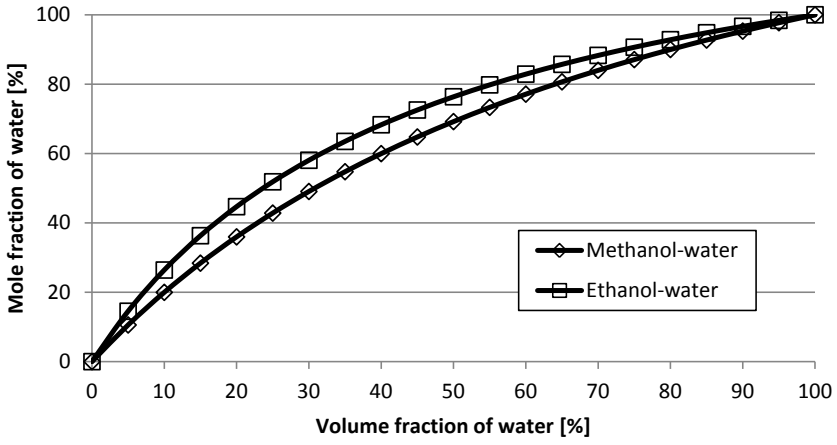

Figure 4.5: Mixtures of water with methanol or ethanol: mole fraction of water as a function of volume fraction.

is the reason why measurements on hydrous methanol and hydrous ethanol have been performed in this study. These measurements are discussed in Section 4.3. The following differences with regard to the efficiency are expected when water is added:

1. Water has a higher latent heat of vaporization and a higher specific heat capacity than methanol, ethanol or gasoline (heat of vaporzation of water is 2257 kJ/kg vs. 1100 kJ/kg for methanol). Because the stoichiometric air quantity also decreases with water addition in the fuel blend, the latent heat of vaporization per kg air increases significantly and this leads to an even bigger cooling effect of the intake charge. For fuel blends with low water fractions, a higher power output resulting from the higher volumetric efficiency can be expected. For fuel blends with higher water fractions the power output will decrease because of the lower Lower Heating Value of the fuel. This can also be seen as a higher degree of dilution which displaces more and more volume. The higher specific heat capacity of the water vapor results also in a more isothermal compression and thus the compression work decreases which has a positive effect on the efficiency.

2. Elevated knock resistance because of the larger cooling effect and the water vapor dilution which both contribute to lower in-cylinder temperatures.

3. The water vapor dilution of the air-fuel mixture yields a lower laminar

burning velocity and lower adiabatic flame temperature. Because of the lower laminar burning velocity, the combustion process takes more time to complete and is less isochoric. A less isochoric combustion yields a lower efficiency. The longer combustion duration should be reflected in a more advanced ignition timing. A lower adiabatic flame temperature and the lower in-cylinder temperatures reduce heat losses contributing to a higher efficiency.

Water dilution also has an effect on the emissions. The next effects can be expected:

1. Concerning NOx emissions, there are 3 important factors: presence of oxygen, high temperatures and residence time at high temperatures. Due to the longer combustion process, the end gases have a longer residence time at high combustion temperatures. This effect will increase NOx emission. However, because of the water dilution combined with the higher specific heat capacity, the in-cylinder temperatures will decrease. This, in combination with the lower adiabatic flame temperature should lead to a decrease of NOx emissions. The water addition thus seems to induce two counteracting effects on NOx formation. Because temperature dependence is thought to be more important than residence time dependence, it is expected that NOx emissions will decrease with higher water content.

2. Because of the water dilution, the combustion process is expected to be less complete and the flame is expected to be more susceptible to flame extinction. Moreover, condensing water vapor can enlarge the quench layer. From this it can be expected that unburned fuel emissions and CO emission will increase.

3. CO_2 emissions are highly dependent on the carbon molar weight fraction of the fuel molecule. Because water vapor does not change the basic combustion reagents (fuel and air), the CO_2 emissions will not differ significantly when the efficiency is similar. On the other hand, the lower temperatures obtained with the combustion of methanol-water blends can reduce the dissociation reactions (CO_2 to CO) resulting in slightly higher CO_2 emissions before the three-way catalyst. Because dissociation reactions are of minor importance compared to the efficiency dependence, it is expected that CO_2 emissions will follow the same trend as the efficiency.

4.3 Water-(m)ethanol blends

In this Section, a comparison of different alcohol-water blends on the Volvo 1.8L engine will be discussed. The correct calculation of the properties of the blends is very important to make the correct conclusions. First of all, the blends have to be made correctly. The blends were made on a volume basis but blending e.g. 0.9 l of methanol and 0.1 l of water does not yield 1 l. Due to differences in the way liquids having different molecular sizes 'pack' together, the final volume is about 1.8% smaller. Depending on the methanol fraction, the deviation can rise to 4%. In this study, the volume fraction is always the volume percentage before mixing. The measurements on hydrous alcohol fuels were done by Master students under guidance of the author as part of their Master dissertation [1].

4.3.1 Efficiency

Methanol-water

The Volvo engine was fuelled with three different methanol-water blends (2.5% v/v, 5% v/v and 10% v/v water).

The efficiencies on pure methanol, gasoline and the three different methanol-water blends are compared at a torque of 40 Nm for a range of engine speeds. Figure 4.6 shows the brake thermal efficiency as a function of engine speed. The efficiency does not differ significantly for all fuel blends, which is remarkable for a methanol-water blend with 10% v/v or 19.97 mole% of water.

It is hard to see a clear trend with the addition of water as all differences fall within the experimental uncertainty. However, at lower rpm, pure methanol seems to have a higher efficiency and at higher rpm, the methanol-water blends seem to have higher efficiencies. This is somewhat clearer when a contour plot of the efficiencies as a function of the engine speed and engine load in BMEP is shown, see Figure 4.7. A possible reason for this trend is that the lower laminar burning velocity of methanol-water blends has less influence on the actual burning velocity at higher engine speeds because of the higher turbulence at high speeds.

[1] Because the engine test benches typically were changed slightly every year and the fact that every year different students operated the engine test bench, some measurements on the same fuel changed a little from year to year. Determining the minimum ignition timing for maximum torque is something that is set by hand and can differ from person to person. This can lead to small differences for the same fuel between different Sections.

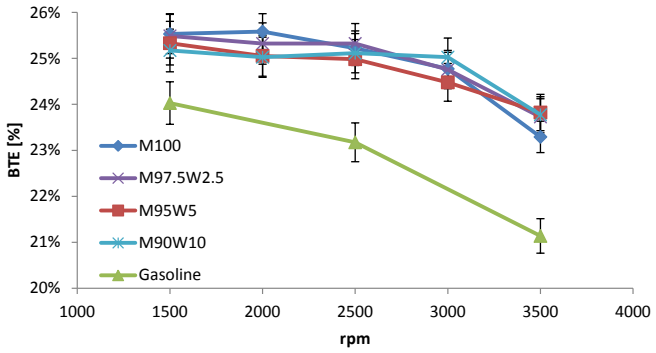

Figure 4.6: Brake thermal efficiency at 40 Nm

In Figure 4.8, the volumetric efficiency is shown at a load of 80Nm. In Figure 4.9, the throttle position for the different fuels is shown and as can be seen, there is no big difference between the throttle positions of the different fuels. As a result, the difference in the volumetric efficiency is mainly caused by the cooling effect of the different methanol-water blends. From Figure 4.8, it is clear that the higher heat of vaporization of the water-methanol blends has a bigger cooling effect on the intake charge resulting in a higher volumetric efficiency.

Ethanol-water

The Volvo engine was also fuelled with pure ethanol and three different ethanol-water blends (5% v/v, 10% v/v and 20% v/v water). The first blend is chosen at 5% v/v so the energy intensive dehydration process could be excluded, see Section 4.1. The third blend is chosen at 20% v/v because in Figure 4.2, the exponential increase in distillation energy begins here. The second blend is chosen in between the two other blends to be able to optimally observe the evolution with increasing water content in the blends.

In Figure 4.10, the brake thermal efficiency of the ethanol-water blends is shown at a load of 40 Nm and various engine speeds. There are no significant differences between all ethanol-water blends, which is remarkable for a blend with 10% v/v (26.44 mole%) and even 20% v/v (44.72 mole%) of water. If we compare this with gasoline (Euro 95), we see a 1-2%pt improvement for the ethanol blends. Despite the fact that all differences between the ethanol-water blends fall within the experimental uncertainty, it is still possible to observe a certain trend with the addition of water. This trend is similar to the trend seen for methanol-water blends. At lower speed, pure ethanol seems to have a higher efficiency than the

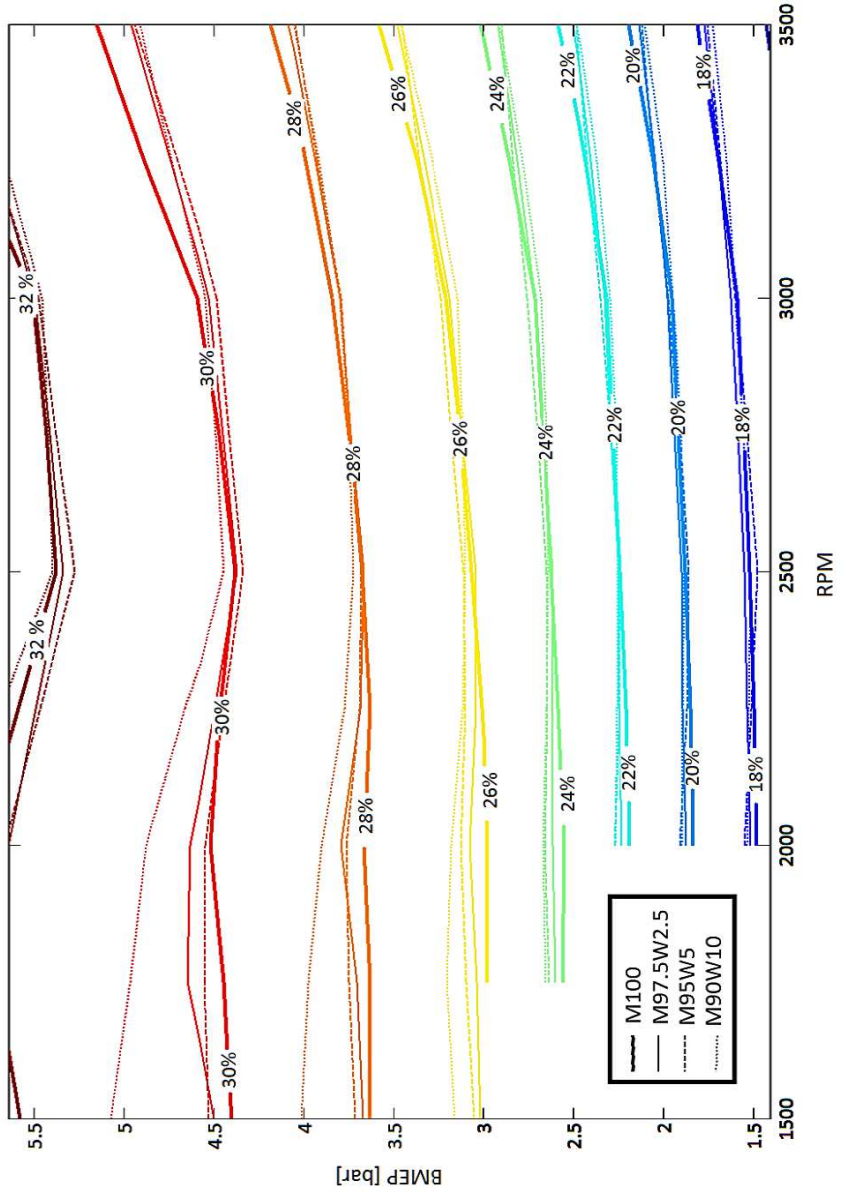

Figure 4.7: Contour plot of the brake thermal efficiency as a function of engine speed and BMEP

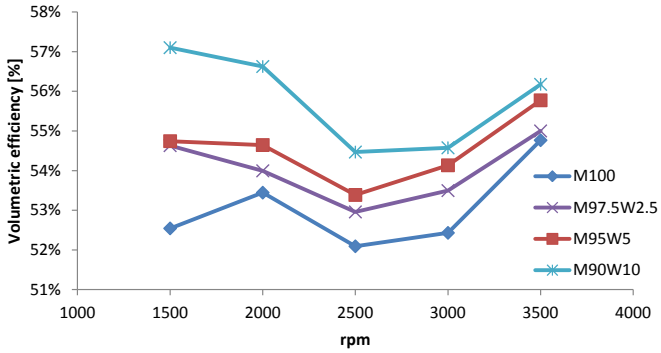

Figure 4.8: Volumetric Efficiency at 80Nm

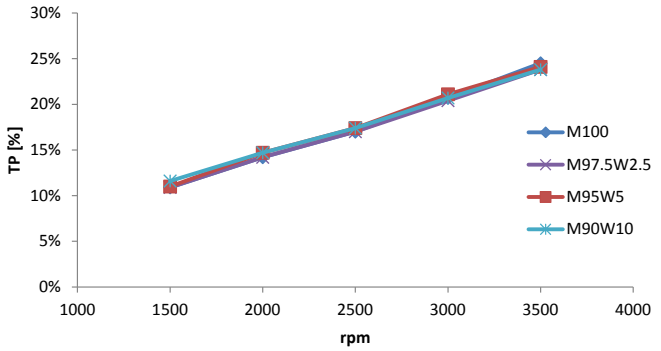

Figure 4.9: Throttle position at 80Nm

other blends, while at higher speed the ethanol-water blends seems to have higher efficiency than the pure ethanol.

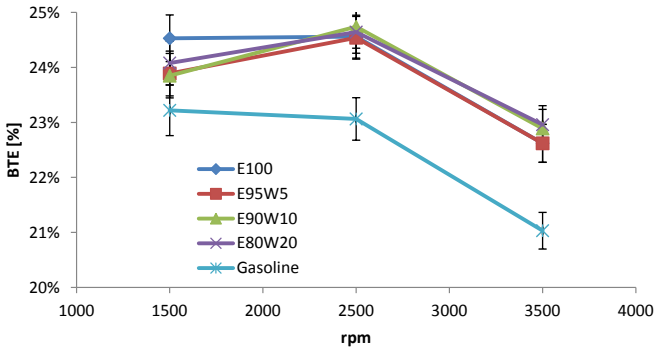

Figure 4.10: Brake thermal efficiency at 40 Nm

The same results and trends were also found for the higher load of 80 Nm (see Figure 4.11). As the load increases, the efficiencies increase too and are a significant 5-7%pt higher than at the 40 Nm part load. The reason for this improvement is the increase in mechanical and indicated efficiency with increasing load.

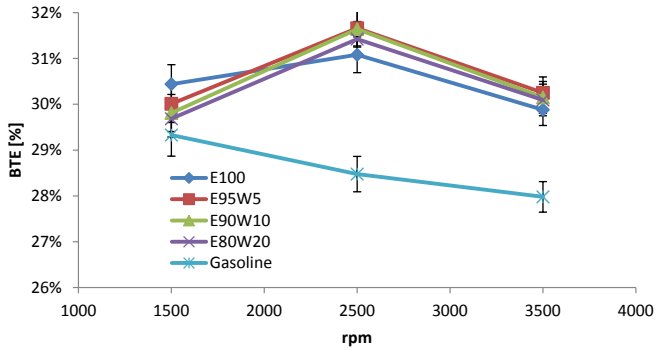

Figure 4.11: Brake thermal efficiency at 80 Nm

The addition of water to the ethanol decreases the LHV (Lower Heating Value) of the blend. This means more fuel will have to be injected to maintain the same load with the ethanol-water blends, which results in a significant increase of the BSFC (Figure 4.12). For the same fuel tank, the driving range will be shorter with increasing water content. This effect will be slightly counteracted by the rearrangement of the water and ethanol molecules, so that the blend will occupy

less volume than the sum of volumes of the 2 components.

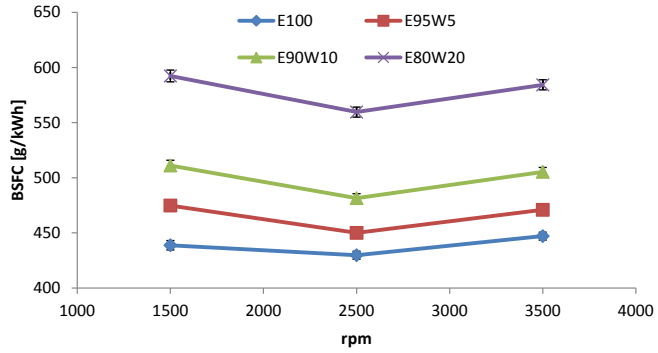

Figure 4.12: Brake Specific Fuel Consumption at 80 Nm

In Figure 4.13, the volumetric efficiency is shown at the higher load of 80 Nm. The difference in the volumetric efficiency is mainly caused by the cooling effect of the different ethanol-water blends. From Figure 4.13, it is clear that the higher heat of vaporization of the water-ethanol blends has a bigger cooling effect on the intake charge resulting in a higher volumetric efficiency.

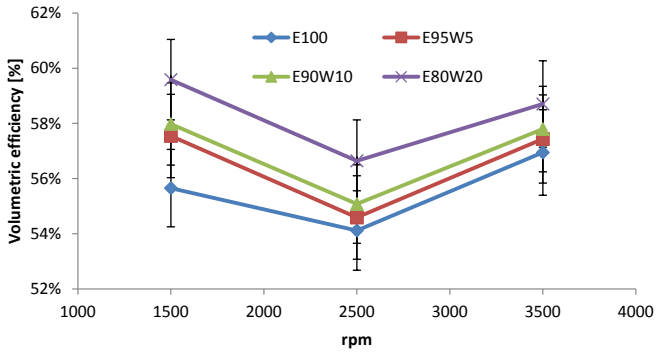

Figure 4.13: Volumetric efficiency at 80 Nm

4.3.2 Emissions

Methanol-water

Figure 4.14 compares the engine-out NOx-emissions for pure methanol and the different water-methanol blends at a load of 40 Nm. The lower adiabatic flame

temperature and cooler in-cylinder temperature due to the larger cooling effect and the water dilution explain the lower NOx-emissions on methanol-water blends compared to on pure methanol. At 2500 rpm there is a deviation from the trend. As NOx-emissions are strongly influenced by the ignition timing, this can be explained as we look at the setting for MBT-timing for these measurements. MBT-timing is set by hand and, as a result, slight deviations can occur in the measurements. Figure 4.15 shows the MBT-timing for the measurements at 40 Nm and from this figure it is clear the ignition timing has a big influence on the NOx-emissions. For example, it looks like the MBT-timing at 2500 rpm for pure methanol can be advanced a few degrees. This late timing results in lower NOx-emissions at this point.

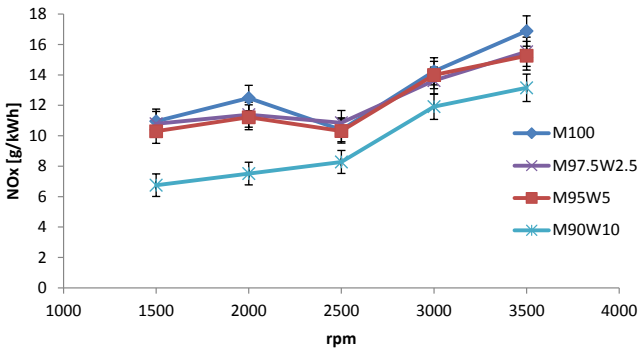

Figure 4.14: NOx-emissions at 40 Nm

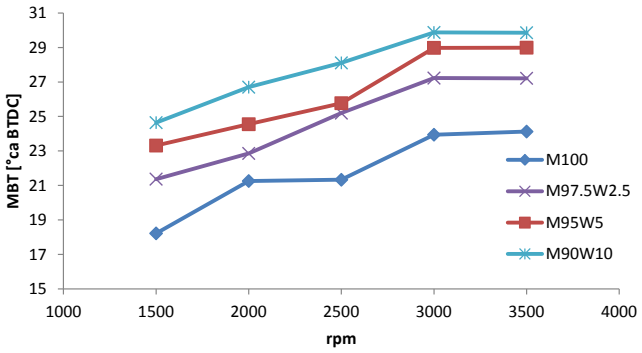

Figure 4.15: MBT-timing at 40 Nm

The engine-out CO emissions are compared in Figure 4.16 for a load of 40 Nm and in Figure 4.17 for a load of 80 Nm. From the properties of methanol-water blends, it is expected the CO emissions of the blends are higher than the CO emissions of

pure methanol. This trend can be seen in both figures, especially at lower engine speeds. However, it is not possible to conclude that the CO emissions are actually higher for the blends because the error bars overlap.

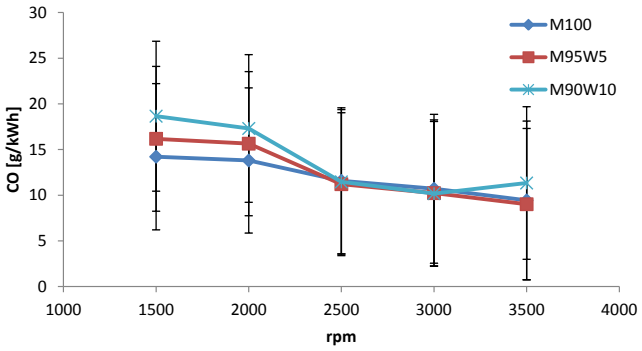

Figure 4.16: CO-emissions at 40 Nm

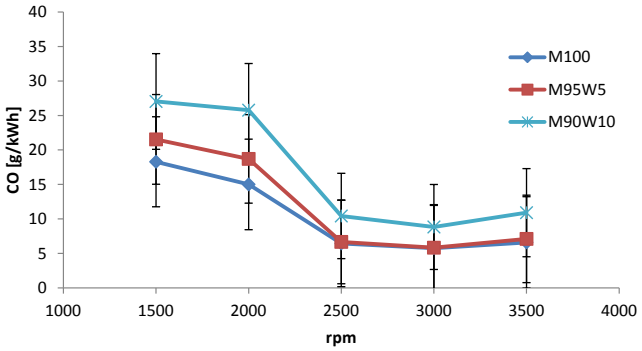

Figure 4.17: CO-emissions at 80 Nm

Ethanol-water

Figure 4.18 shows the engine-out NOx-emissions for the various ethanol-water blends at the load of 80 Nm. The same conclusions can be drawn as for methanol-water blends.

In Figure 4.19 we see the CO-emissions of the various ethanol-water blends at the load of 40 Nm. As expected the emissions of the water containing blends are slightly higher than with the pure ethanol, because of the less complete combustion. This is also confirmed for the higher 80 Nm load. Nevertheless,

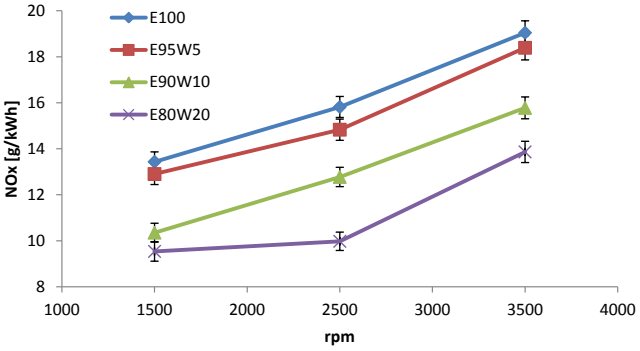

Figure 4.18: NOx-emissions at 80 Nm

all differences fall within the experimental uncertainties so it is not possible to be certain of this trend.

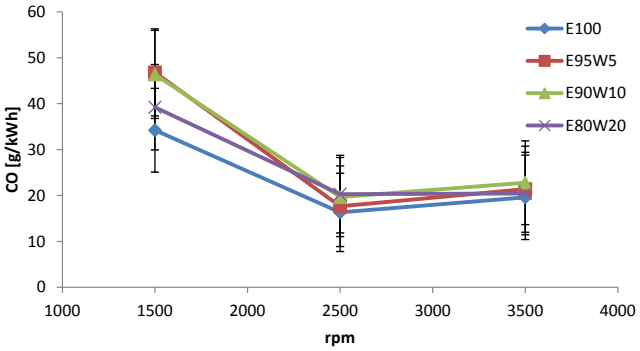

Figure 4.19: CO-emissions at 40 Nm

4.4 Conclusion

The present Chapter gave insights into the advantages that could exist with alcohol-water blends. Using alcohol-water blends as fuel for internal combustion engines could have an economic advantage compared to anhydrous alcohol because the alcohol does not have to be fully dried in the production process. The cost reduction in production comprises both the costs of investment and exploitation. This study compared the brake thermal efficiencies and engine-out emissions from a production-type four-cylinder SI gasoline engine running on

methanol-water blends and ethanol-water blends. Methanol-water blends of 2.5% v/v, 5% v/v and 10% v/v water and ethanol-water blends with 5% v/v, 10% v/v and 20% v/v were tested. It was shown that the brake thermal efficiency does not differ significantly for all fuels and is still higher than the efficiency of gasoline. NOx emissions were reduced substantially for the fuels with higher water content because of the lower temperatures in the cylinders due to the water addition in the fuel.

5

Laminar burning velocity of alcohol blends

5.1 Introduction

When combustion takes place in the flamelet regime, which is assumed by most of the turbulent combustion models [28], the flame is assumed to propagate locally at the (stretched) laminar flame speed. Consequently, one of the key parameters to model the combustion of fuels in spark ignition engines is the laminar burning velocity of the fuel.

Contrary to methanol and ethanol, gasoline does not consist out of one molecule but is a complex fuel mixture, with a wide variation in composition between commercial gasolines (for example the composition depends on the season, for startability) and as a result there is no fixed laminar burning velocity for gasoline. Because of the complexity of gasoline and because of the varying composition of gasoline, gasoline surrogates are often used in experiments and in calculations. The term surrogate gasoline refers to a simpler representation of a fully-blended fuel [29]. The most common gasoline surrogates are iso-octane or binary mixtures of iso-octane and n-heptane, the primary reference fuels (PRF's) for determining octane ratings for spark ignition engine fuels. Several studies concerned the

laminar burning velocity of iso-octane, n-heptane and mixtures of these two fuels [81–90]. However, Pitz et al. [29] came to a consensus that next to iso-octane and n-heptane, toluene should be included in any gasoline surrogate. N-heptane and iso-octane represent the normal-alkanes and iso-alkanes in gasoline and were chosen since they are the primary reference fuel components and toluene was chosen to represent the aromatic fraction because it is the most abundant aromatic in gasoline. The laminar burning velocity of toluene has not been investigated as extensively as iso-octane and n-heptane with only few measurements having been presented [91–96]. For a "real" gasoline, even fewer measurements have been reported [88, 97–99]. When investigating if a particular surrogate is good enough to predict the behavior of gasoline, comparison has to be made with a real gasoline. However, such comparison is lacking in literature and laminar burning velocity measurements of a "real" gasoline are needed.

For blends of alcohols and gasoline, it would be interesting to know how the laminar burning velocity behaves when the blend ratio or the blend's components are changed. Knowledge on the behavior of the laminar burning velocity of alcohol blends could allow better and faster optimization of an engine fuelled with (complex) blends of alcohols and gasoline (e.g. binary ethanol-gasoline blends, ternary GEM blends as discussed in Section 2.4 or even quaternary or more complex blends). These alcohol blends can differ a lot from each other: low-level, medium-level or high-level blends are possible and the alcohol component can differ as well (methanol, ethanol, butanol,... are possible alternatives). One way to obtain the laminar burning velocity is through experiments. However, measurements of the laminar burning velocity are mostly limited in pressure and temperature and are compromised by the effects of flame stretch and instabilities as discussed in Appendix A.2. Computationally, these effects can be avoided by calculating one-dimensional, planar adiabatic flames using chemical oxidation mechanisms. The velocity of these flames is the laminar burning velocity by definition. Thus kinetic models can be used to calculate the laminar burning velocity over a range of conditions used in practical applications. Computer simulations where combustion chemistry is involved, e.g. CFD study of the combustion in an internal combustion engine, are computationally demanding. As a result, to calculate the laminar burning velocities, they rely in many cases on reduced kinetic models or correlations which give the laminar burning velocity in terms of pressure, temperature and composition of the unburned mixture, to have faster computation times.

The problem with complex fuel blends is that the kinetic models become very large and complex, with long calculation times as result, and that in many cases no models exist for blends of different fuels. A possible solution would be to have accurate mixing rules for the laminar burning velocity which can determine

the laminar burning velocity of fuel blends out of the burning velocity of the fuel components without being computationally too demanding. Developing a mixing rule for the laminar burning velocity is not straightforward because the combustion reaction is a complex phenomenon. To evaluate mixing rules, it is important to know what exactly determines the burning velocity. Burning velocities are mostly governed by flame temperature, activation energy, and, to a certain extent, the transport properties [93]. There is thus a kinetic, a thermal and a transport effect. Depending on the fuel which is blended in the mixture, an enhanced reactivity can be expected, which is the case for example with hydrogen [100]. A lower or higher adiabatic flame temperature, responsible for the thermal effect, can lead to another mixture reactivity, even assuming the same underlying reaction mechanism. Furthermore, depending on the diffusivities of the blend components, there can be a modification of the mixture concentration in the flame structure [101]. The inherent difficulty in the development of a mixing rule is that various thermal and chemical effects may not be separable for certain fuel blends because of possible thermo-kinetic couplings. For this reason, mixing rules are not expected to be linear in the fuel blend composition for certain fuel blends [93].

This Chapter is devoted to investigate the difference between the laminar burning velocity of methanol, ethanol and gasoline. First an overview of mixing rules found in the literature is provided in Section 5.2. As one of the goals is to find a mixing rule for alcohol-gasoline blends, evaluation of these mixing rules is needed. However, accurate laminar burning velocity measurements of alcohol blends were lacking in literature, especially at higher temperature and pressure. Consequently, these mixing rules are first tested on a limited dataset of experimental laminar burning velocities of ethanol-hydrocarbon blends at atmospheric pressure found in literature but additional values for the laminar burning velocity of alcohol-hydrocarbon mixtures were simulated with chemical kinetic models to evaluate the mixing rules at higher pressure and temperature (see Section 5.4). In a later stage, measurements performed on the heat flux setup of Lund University during a research stay in Lund, Sweden, are used to further validate mixing rules for alcohol-gasoline blends, see Section 5.6. Because measurements were performed at different temperatures, these measurements could also be used to study the temperature dependence of the laminar burning velocity of methanol, ethanol and gasoline. Additionally, because gasoline surrogates are often used to reproduce the properties of gasoline, the gasoline surrogates iso-octane, n-heptane and toluene were measured as well on the heat flux setup. In Section 5.6, it will be investaged if a mixture of these surrogates can reproduce the laminar burning velocity of gasoline.

5.2 Mixing rules for the laminar burning velocity

The following mixing rules for the laminar burning velocity of fuel blends were found in literature:

1) Mixing rule based on mole fraction, mass fraction or energy fraction of the fuels' components [102].

$$u_{l,blend}(\phi) = \sum_{i=1}^{n} \gamma_i u_{l,i}(\phi) \tag{5.1}$$

In the previous expression γ_i is either the mole fraction, mass fraction or energy fraction of the fuel components. The energy fraction can be calculated as follows:

$$\gamma_i = \frac{\Delta cH_i^{\circ}.x_i}{\sum_{i=1}^{n} \Delta cH_i^{\circ}.x_i} \tag{5.2}$$

ΔcH_i° is the heat of combustion of the mixture components. x_i is the mole fraction of the fuel components.

2) Mixing rule based on Le Chatelier's rule [103].

$$u_{l,blend}(\phi) = \frac{1}{\sum_{i=1}^{n} \frac{x_i}{u_{l,i}(\phi)}} \tag{5.3}$$

x_i is the mole fraction of the fuel components. Le Chatelier [104] first proposed a similar empirical mixing rule for predicting the flammability limit of lean fuel-air mixtures:

$$LFL_{blend} = \frac{1}{\sum_{i=1}^{n} \frac{x_i}{LFL_i}} \tag{5.4}$$

where x_i is the mole fraction of the i^{th} component and LFL_i is the lower or lean flammable limit of the i^{th} component in volume percent. Benedetto et al. [103] used Le Chatelier's rule to predict the laminar burning velocity of hydrogen-methane blends and found a good agreement for lean and stoichiometric

conditions but for rich mixtures there were more significant differences between the simulation results obtained with the detailed reaction scheme GRI-Mech version 3.0 [105] and the values predicted by Le Chatelier's rule.

3) Mixing rule developed by Hirasawa et al. [93].

Hirasawa et al. [93] found for ethylene/n-butane, ethylene/toluene and n-butane/toluene mixtures that the flame temperature has the dominant influence on the burning velocity of the fuel blends at atmospheric pressure and that the kinetic coupling hardly affects the burning velocities of these fuel mixtures. An empirical mixing rule, depending on a mole fraction weighted average of the burning velocities and flame temperatures was developed. The adiabatic flame temperature of a pure fuel ($T_{f,i}$) can be expressed by:

$$T_{f,i} - T_u = \Delta T_i = \frac{Q_i}{n_i c_{p,i}} \tag{5.5}$$

Q is the heat release per mole of fuel. n is the total number of moles of the products (including diluents) per mole of fuel. c_p is the mean molar specific heat of the products and T_u is the unburned gas temperature. In the same way, the flame temperature of a fuel blend can be expressed by:

$$T_{f,blend} - T_{u,blend} = \Delta T_{blend} = \frac{Q_{blend}}{n_{blend} c_{p,blend}} \tag{5.6}$$

$$Q_{blend} = \sum_{i=1}^{n} x_i Q_i \tag{5.7}$$

x_i is the mole fraction of the fuel component. Assuming that the total amount of moles of the combustion products and diluents is:

$$n_{blend} = \sum_{i=1}^{n} x_i n_i \tag{5.8}$$

the adiabatic flame temperature of the fuel blend can be calculated with:

$$\Delta T_{blend} = \sum_{i=1}^{n} \frac{x_i n_i \Delta T_i}{n_{blend}} \tag{5.9}$$

Law et al. [106] gave an expression for u_l with non-unity Lewis number Le as a function of the unburned gas density ρ_u, the thermal conductivity λ, a collision frequency B_c, the activation temperature T_a and the Zeldovich number Ze:

$$\rho_u u_l = \left[\frac{Le(\frac{\lambda}{c_p})B_c}{Ze} \right]^{\frac{1}{2}} exp\left(-\frac{T_a}{2T_f} \right) \tag{5.10}$$

By rearrangement of this expression and compressing most of it into an "activation temperature" $\tilde{T}_a$, the burning velocity of the fuel constituents and the fuel blend can be expressed as:

$$u_{l,i} = exp\left(-\frac{\tilde{T}_{a,i}}{T_{f,i}} \right) \tag{5.11}$$

and

$$u_{l,blend} = exp\left(-\frac{\tilde{T}_{a,blend}}{T_{f,blend}} \right) \tag{5.12}$$

Assuming $\tilde{T}_{a,blend}$ can be expressed in the same way as ΔT_{blend}, $u_{l,blend}$ can be calculated:

$$\tilde{T}_{a,blend} = \sum_{i=1}^{n} \frac{x_i n_i \tilde{T}_{a,i}}{n_{blend}} = -\sum_{i=1}^{n} \frac{x_i n_i T_{f,i} \ln(u_{l,i})}{n_{blend}} \tag{5.13}$$

Finally, the expression for laminar burning velocity becomes:

$$u_{l,blend} = \prod_{i=1}^{n} u_{l,i}^{\beta_i} \tag{5.14}$$

$$\beta_i = \frac{x_i n_i T_{f,i}}{n_{blend} T_{f,blend}} \tag{5.15}$$

The mixing rule developed by Hirasawa et al. [93] predicted the measurements very accurately for atmospheric laminar burning velocities of ethylene/n-butane, ethylene/toluene, and n-butane/toluene mixtures. In the same way, Ji et al. [107] found that the laminar burning velocity of n-dodecane/toluene and

n-dodecane/methylcyclohexane mixtures at atmospheric pressure can be predicted using the laminar burning velocities and adiabatic flame temperatures of the components. It was found that although the initial fuel consumption pathways of n-dodecane, toluene and methyl-cyclohexane and the resulting intermediates and radicals may be different for each neat component, the propagation of flames of binary fuels is mostly sensitive to the flame temperature through its influence on the main branching reaction $H + O_2 \rightarrow OH + O$. Kinetic couplings appeared to have minor effect on flame propagation.

On the other hand, there may be fuel blends for which chemical kinetic interactions have the biggest influence, e.g. hydrogen/methane mixtures [100, 101, 108]. There have been a lot of measurements of the laminar burning velocity of fuels in combination with hydrogen. The reason is that because of the strong reactivity of hydrogen, an addition of hydrogen enhances flame propagation and extends the flammability limits of fuel/air mixtures. Therefore, it has the potential to promote combustion efficiency and reduce pollutant and greenhouse gas emissions [100]. The effects of hydrogen addition have been studied extensively using different methods and different fuels such as methane, ethylene, acetylene, propane, n-butane, iso-octane, carbon monoxide and natural gas [101, 109–114]. Yu et al. [115] found that the increase of burning velocity with hydrogen addition can be approximately linearly correlated with R_H. R_H being the ratio of the amount of hydrogen plus the stoichiometric amount of air needed for its oxidation, to the amount of fuel plus the remaining air left for its oxidation:

$$R_H = \frac{C_H + \frac{C_H}{(\frac{C_H}{C_A})_{st}}}{C_F + \left[C_A - \frac{C_H}{(\frac{C_H}{C_A})_{st}}\right]} \tag{5.16}$$

C_F, C_A and C_H are the mole concentrations of the fuel, air and hydrogen addition. Tang et al. [101] found the same linear correlation for n-butane with hydrogen addition. With a sensitivity analysis, they showed that the kinetic effect is the most prominent, followed by the thermal effect, with the diffusion effect being minimal. Wu et al. [100] did the same for the laminar burning velocities of mixtures of ethane, ethylene, acetylene and carbon monoxide with a small amount of hydrogen addition at atmospheric and elevated pressures. It was found that the approximately linear correlation also largely applies to ethane, ethylene, and acetylene at atmospheric as well as elevated pressures and that in most cases hydrogen addition enhances the burning velocity mainly through the modification of the activation temperature rather than the flame temperature. The linear correlation did not hold for carbon monoxide due to the strong catalytic effect

of hydrogen on the oxidation of carbon monoxide. In Section 5.4, different mixing rules will be tested for alcohol-hydrocarbon blends. At the end of Section 5.4, the same mixing rules will be briefly evaluated for a hydrogen-methane mixture.

5.3 Kinetic modeling

In the Sections 5.4 and 5.6, simulation results of the laminar burning velocity, calculated with two different chemical oxidation mechanisms, are used, on the one hand, as validation data for mixing rules at higher temperature and pressure and, on the other hand, to compare with experimental results measured on the heat flux setup (see Section 5.5). The following two mechanisms are used: the model of Andrae [116] and the model of Mehl et al. [117]. These models are commonly used in CFD and engine simulations to calculate the laminar burning velocity. The model of Andrae [116] is a semi-detailed mechanism containing 150 species and 759 reactions. It consists of a detailed description of toluene and ethanol oxidation and skeletal mechanisms of iso-octane and n-heptane. The model of Mehl et al. [117] is a reduced version of a detailed chemical kinetic mechanism for the simulation of gasoline surrogate mixtures. This reduced version was made for engine numerical applications and considers 312 species. The original detailed model has been assembled from existing Lawrence Livermore National Laboratory mechanisms for n-heptane, iso-octane [118], toluene and C5-C6 olefins [119] and validated using experimental data from shock tubes, stirred reactors and rapid compression machines. For the modeling of adiabatic premixed flames, the one-dimensional chemical kinetics code CHEM1D was used [120]. This code was developed at Eindhoven University of Technology and employs the EGLIB complex transport model, including multi-component transport and thermal diffusion. In each case, the solution was calculated using the exponential differencing technique in a grid consisting of 200 points, with most of the detail centered at the inner flame layer. Radiation was neglected, and solver convergence was confirmed by ensuring that all residuals were below 10^{-10} and the laminar burning velocity had reached a stable value.

5.4 Testing mixing rules on literature data

To validate mixing rules, an accurate determination of the laminar burning velocity of the fuel components and the laminar burning velocity of the fuel blends is needed. Unfortunately, there are few measurements of fuel blends (with the

exception for fuels with hydrogen addition) and there can be doubt on the accuracy of the measurements when measurements on different setups are compared [121]. In the literature few measurements of relevant fuel blends are reported. Hirasawa et al. [93] measured the laminar burning velocity of binary blends of ethylene+n-butene, ethylene+toluene and n-butane+toluene. Dirrenberger et al. [99] did measurements on mixtures of 15 % v/v ethanol with gasoline and a toluene reference fuel (mixture of iso-octane, n-heptane and toluene). Van Lipzig et al. [82] considered binary and ternary mixtures of n-heptane, iso-octane and ethanol, Broustail et al. [122] performed measurements with mixtures of butanol and ethanol with iso-octane and Gülder et al. [123] measured the laminar burning velocity of iso-octane+methanol and iso-octane+ethanol mixtures. This is the reason why the decision was made to do additional measurements of the laminar burning velocity of (m)ethanol-hydrocarbon blends during this Ph.D. study. These measurements are reported in Section 5.6 and will also be used to validate the mixing rules.

In the following, different mixing rules are first tested and evaluated for laminar burning velocity measurements of ethanol-hydrocarbon blends at atmospheric pressure from literature. Secondly, as laminar burning velocity measurements of alcohol-hydrocarbon blends at higher temperature and pressure are lacking in literature, the mixing rules are evaluated for the laminar burning velocity of ethanol-hydrocarbon blends at higher pressure and temperature using simulation results from chemical kinetic models.

5.4.1 Laminar burning velocity at atmospheric pressure

In the first stage of evaluating mixing rules, measurements performed by van Lipzig et al. [82] were used because these measurements were performed using the heat flux method on a flat flame burner resulting in a reported accuracy of $+/-1cm/s$. This setup is the same setup as was used during this Ph.D. study to perform measurements of the laminar burning velocity. Van Lipzig et al. [82] measured the laminar burning velocity of ethanol, iso-octane, n-heptane and mixtures of 50% v/v ethanol+ 50% v/v n-heptane, 50% v/v ethanol+ 50% v/v iso-octane and 1/3 v/v ethanol + 1/3 v/v n-heptane + 1/3 v/v iso-octane. The measured laminar burning velocities of the 50% v/v ethanol+ 50% v/v n-heptane mixture at 338K and atmospheric pressure are compared with calculated values using different mixing rules in Figures 5.1 (mole, mass and energy fraction mixing rule) and 5.2 (Hirasawa et al. mixing rule and Le Chatelier's mixing rule). Calculations were made for equivalence ratios of 0.7 to 1.3 but in Figures 5.1 and 5.2 the minimum equivalence ratio is 0.9 for the clarity of the Figure and because

the difference in laminar burning velocity in the 0.7-0.8 range was $2cm/s$ at its maximum. In Figure 5.1, the best agreement is seen for the energy fraction mixing rule and in Figure 5.2, the Hirasawa et al. mixing rule reproduces the measured laminar burning velocity better than Le Chatelier's mixing rule. It is clear that the mole and mass fractions mixing rules and Le Chatelier's mixing rule do not predict the measured laminar burning velocity of this binary mixture of ethanol and n-heptane for $\phi > 1$ accurately enough although the maximum difference between the measurements and the calculated laminar burning velocities is only 2 cm/s.

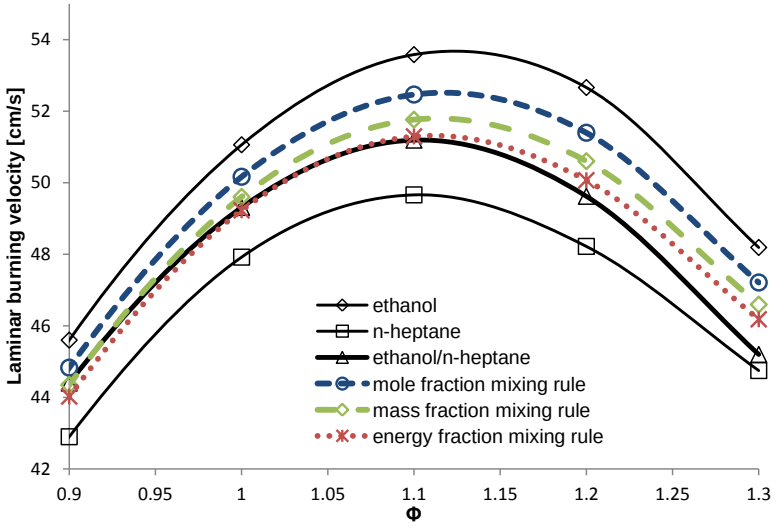

Figure 5.1: u_l of ethanol, n-heptane and ethanol/n-heptane blend (1/2;1/2) as a function of ϕ (p = 1 bar, T_u = 338 K) and u_l of ethanol/n-heptane blend calculated with the mole, mass and energy fraction mixing rule.

Hirasawa et al. [93] validated their mixing rule only for binary mixtures of ethylene, n-butane or toluene. In Figure 5.3 the laminar burning velocity of the ternary mixture of 1/3 v/v ethanol + 1/3 v/v n-heptane + 1/3 v/v iso-octane at 338K and atmospheric pressure is compared to the values predicted with the energy fraction mixing rule and the Hirasawa et al. mixing rule. Again, the burning velocities can be estimated well with these two rules. The maximum error with the Hirasawa et al. mixing rule is 1.23 cm/s and with the energy fraction mixing rule 1.36 cm/s. However, this is still outside the reported accuracy of +/- 1cm/s [82].

To get an overall view of predictive capabilities of the different mixing rules, the root mean square errors (RMSE) of the different mixing rules are shown in Table 5.1 for all the laminar burning velocity measurements of ethanol-hydrocarbon

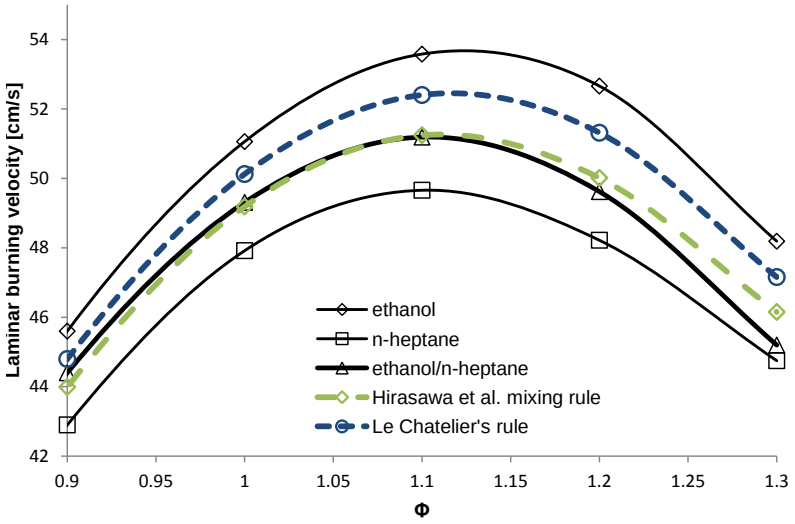

Figure 5.2: u_l of ethanol, n-heptane and ethanol/n-heptane blend (1/2;1/2) as a function of ϕ (p = 1 bar, T_u = 338 K) and u_l of ethanol/n-heptane blend calculated with the Hirasawa et al. mixing rule and Le Chatelier's rule.

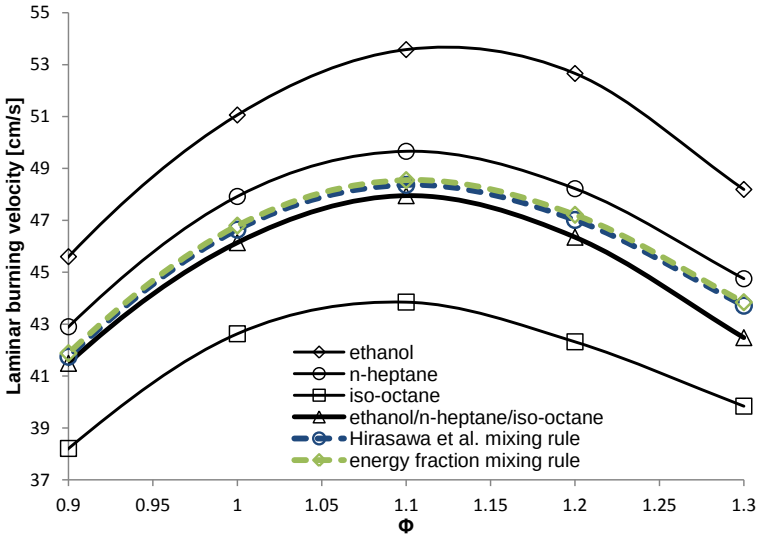

Figure 5.3: u_l of ethanol, n-heptane, iso-octane and ethanol/n-heptane/iso-octane blend (1/3;1/3;1/3) as a function of ϕ (p = 1 bar, T_u = 338 K) and u_l of ethanol/n-heptane/iso-octane blend calculated with the energy fraction mixing rule and the Hirasawa et al. mixing rule.

Table 5.1: Root mean square error for the laminar burning velocities calculated with different mixing rules. EH = ethanol/n-heptane, EO = ethanol/iso-octane, EHO = ethanol/n-heptane/iso-octane

RMSE [cm/s]	**EH**		**EO**		**EHO**		**mean error**
	298 K	**338 K**	**298 K**	**338 K**	**298 K**	**338 K**	
Mole fraction	0.75	1.20	2.07	3.21	1.75	2.46	1.94
Mass fraction	0.37	0.77	0.90	1.58	0.98	1.26	0.99
Energy fraction	0.30	0.63	0.26	0.67	0.69	0.73	0.55
Hirasawa et al.	0.31	0.63	0.14	0.47	0.62	0.60	0.47
Le Chatelier's rule	0.71	1.15	1.85	2.90	1.58	2.22	1.77

blends at 298K and 338K performed by van Lipzig et al. [82]. It is clear that the best agreement is seen for the Hirasawa et al. mixing rule and the energy fraction mixing rule. This gives a first indication that the flame temperature is the dominant factor for the laminar burning velocity of these ethanol-hydrocarbon blends, similar to what was found by Hirasawa et al. [93]. Actually, it is not very surprising that the energy mixing rule gives similar results as the Hirasawa et al. mixing rule because it is based on the mole fraction and the heat of combustion of the fuel components which also can be said of the flame temperature, the dominant factor in the Hirasawa et al. mixing rule.

5.4.2 Laminar burning velocity of multi-component fuels at higher pressures and temperatures

The next goal was to investigate if the results of the previous Section can be extended to higher pressures and temperatures, and multi-component mixtures. Because gasoline blended with an alternative fuel such as methanol or ethanol is in fact a binary blend of a multi-component fuel and a pure fuel, it should be investigated if the mixing rules also work for blends of multi-component fuels. In the literature, such measurements of multi-component fuel blends at higher pressure and temperature are not reported yet. Therefore, the chemical kinetic model of Andrae et al. [116] was used to calculate laminar burning velocities of a toluene reference fuel (TRF), ethanol and blends of ethanol and the TRF at higher temperature and pressure (600 K and 40 bar). This model was chosen because it is one of the few kinetic models for ethanol-hydrocarbon fuels that was also validated with laminar burning velocities collected at elevated temperature and pressure and because it includes a detailed reaction mechanism for ethanol. A toluene reference fuel (69% v/v iso-octane, 14% v/v n-heptane and 17% v/v toluene) was chosen to represent a gasoline and the composition of the iso-octane/n-heptane/toluene blend was chosen based on the results in [124] where the laminar burning velocities of

this blend compared well with measurements of the laminar burning velocity of a real gasoline performed by Zhao et al. [97]. In Figure 5.4 the laminar burning velocity of E75 (75% v/v ethanol and 25% v/v TRF) and E20 (20% v/v ethanol and 80% v/v TRF) at 600 K and 40 bar is calculated with different mixing rules and again, it is clear that the mole fraction mixing rule is not the right approach to predict the laminar burning velocity of multi-component fuels. Notice also the large difference in burning velocity between the TRF and ethanol.

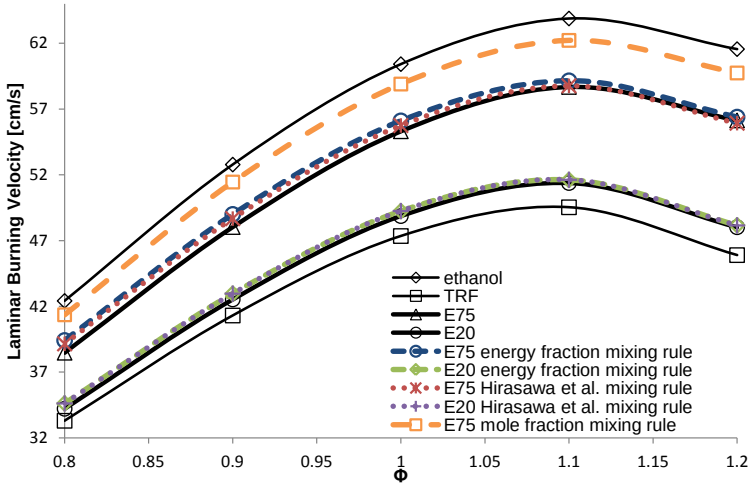

Figure 5.4: u_l of ethanol, TRF, E75 and E20 as a function of ϕ (p = 40 bar, T_u = 600 K) and u_l of E75 and E20 calculated with the mole fraction mixing rule, the Hirasawa et al. mixing rule and the energy fraction mixing rule.

As can been seen in Figure 5.4, the energy fraction mixing rule and the Hirasawa et al. mixing rule give excellent agreement with the calculations from the chemical kinetic model with the best results for the Hirasawa et al. mixing rule especially for higher ethanol fraction.

For the different fuels and range of equivalence ratios employed in this study, both the results with the energy mixing rule and the Hirasawa et al. mixing rule indicate that these mixing rules can be used to predict the laminar burning velocity of multi-component fuel blends at higher temperature and pressure. The best results are achieved with the Hirasawa et al. mixing rule while the energy mixing rule has the greater simplicity as advantage. Given the fact that the energy fraction mixing rule and the Hirasawa et al. mixing rule, which are both based on the mole fraction and the heat of combustion, give the best results, it is worth to investigate if Le Chatelier's rule could not be used if the energy fraction is used instead of the mole fraction:

$$u_{l,blend}(\phi) = \frac{1}{\sum_{i=1}^{n} \frac{\gamma_i}{u_{l,i}(\phi)}} \tag{5.17}$$

with γ_i the energy fraction instead of the mole fraction. In Figure 5.5, the energy fraction mixing rule, the Hirasawa et al. mixing rule and Le Chatelier's mixing rule based on energy fraction are compared for E75 at 600 K and 40 bar. In Figure 5.6, all the different mixing rules are compared for E75 at 600 K and 1 bar. Here, the differences are more noticeable because the laminar burning velocities of pure ethanol and the TRF are more different from each other. As can be seen, the mixing rules all overpredict the laminar burning velocity with the smallest overprediction for Le Chatelier's mixing rule based on energy fraction. The root mean square errors (at 600 K and 1 bar) of the energy fraction mixing rule, the Hirasawa et al. mixing rule and Le Chatelier's rule are respectively 4.51, 3.15 and 1.70 cm/s. Thus, the agreement is best for Le Chatelier's mixing rule using the energy fraction when data of the kinetic model of Andrae [124] is used. The same was found when the measurements of van Lipzig et al. were compared (not shown here).

The evaluation using calculated laminar burning velocities with the model of Andrae [124] was repeated for a second chemical kinetic mechanism used for simulation of gasoline surrogate mixtures developed by Mehl et al. [117]. This chemical kinetic model was used to calculate the laminar burning velocity of a binary ethanol/n-heptane (70% v/v ethanol and 30% v/v n-heptane) blend at 600 K and 1 bar. The results are shown in Figure 5.7. For the clarity of the Figure, only the laminar burning velocities of the blend and the predictions by the mixing rules are shown. There is a small overprediction with the least overprediction for Le Chatelier's rule and the largest overprediction for the energy fraction mixing rule. However, notice that the differences are very small.

The laminar burning velocity of fuel blends for which chemical kinetic interactions have the biggest influence, e.g. hydrogen/methane mixtures, cannot be predicted with the previous mixing rules, which is clear from Figure 5.8. Calculations of the laminar burning velocity of a mixture of 70% v/v H_2 and 30% v/v CH_4 were done with the GRI-Mech 3.0 mechanism [105]. In Figure 5.8, different mixing rules are tested but the deviations from the simulated laminar burning velocities of the H_2-CH_4 mixture are large.

Summary

Different mixing rules to predict the laminar burning velocity of fuel blends were tested and compared with each other. Mixing rules are not expected to be linear

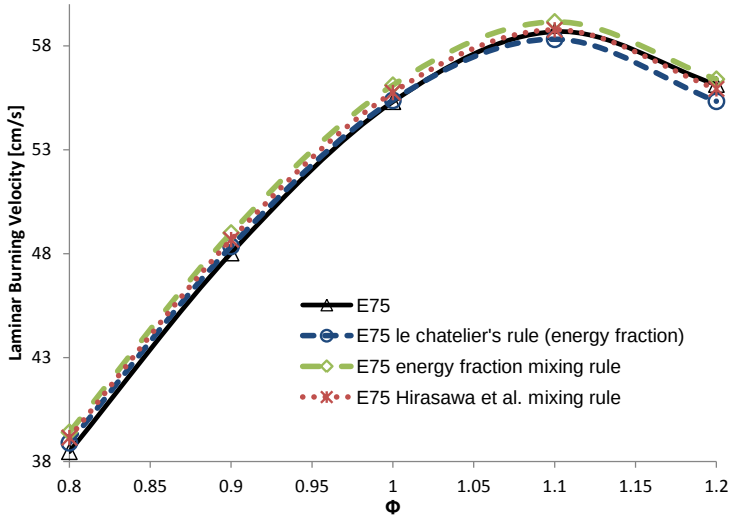

Figure 5.5: u_l of E75 as a function of ϕ (p = 40 bar, T_u = 600 K) and u_l of E75 calculated with different mixing rules

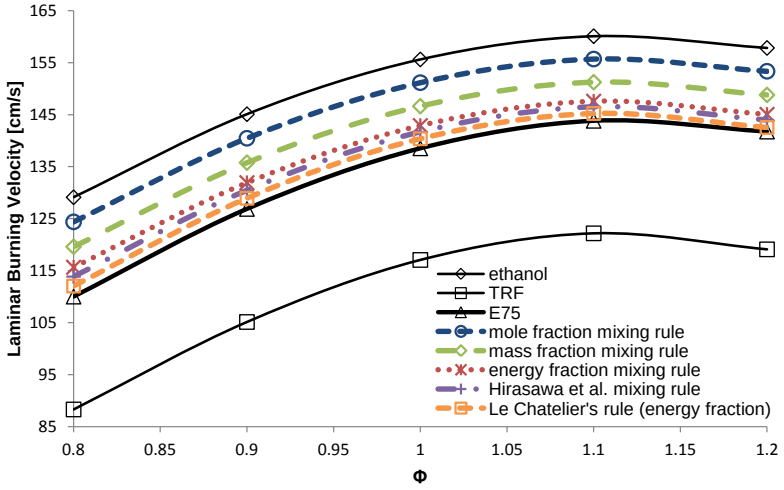

Figure 5.6: u_l of E75 as a function of ϕ (p = 1 bar, T_u = 600 K) and u_l of E75 calculated with different mixing rules

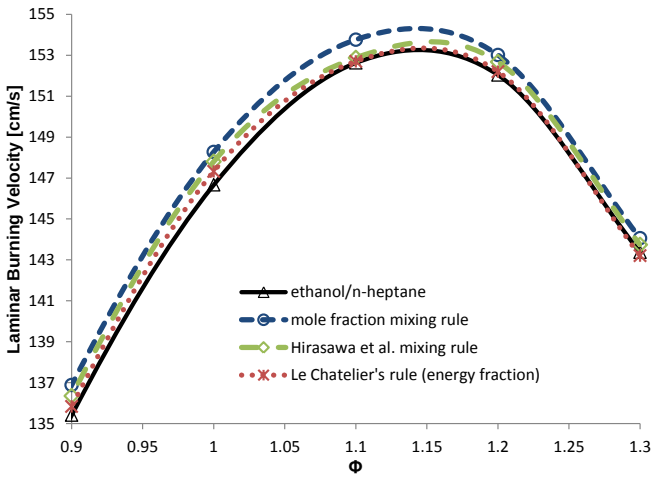

Figure 5.7: u_l of ethanol/n-heptane (LLNL mechanism) as a function of ϕ (p = 1 bar, T_u = 600 K) and u_l calculated with different mixing rules

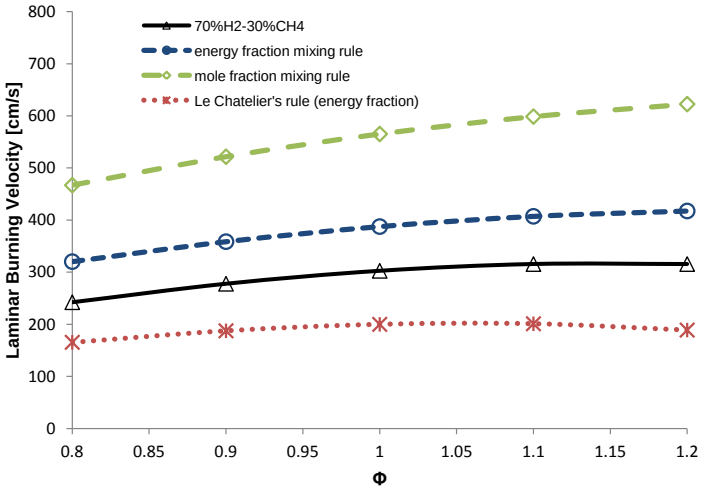

Figure 5.8: u_l of 70% H_2 and 30% CH_4 as a function of ϕ (p = 1bar, T_u = 600 K) and u_l calculated with different mixing rules

in the fuel blend composition, proven by the poor predictions of the mole fraction and mass fraction mixing rules. The energy fraction mixing rule, the mixing rule developed by Hirasawa et al. and Le Chatelier's rule based on energy fraction gave the best results, indicating that the flame temperature is the dominant factor for laminar burning velocity of ethanol-hydrocarbon mixtures. These three mixing rules performed very well for binary, ternary and multi-component fuels and for 'binary' blends of fuels which are a blend of components, even at higher temperature and pressure. It was also shown that these mixing rules do not work for hydrogen-methane blends.

5.5 Heat flux setup

Published data of the laminar burning velocity are not always consistent with one another and the spread of the measured values often exceeds the reported experimental uncertainty, even for fuels which have been investigated thoroughly like iso-octane and n-heptane. Galmiche et al. [90] showed that there are significant discrepancies between all the correlations for the laminar burning velocity of iso-octane/air mixtures and that the differences are mainly due to the different experimental setups and methodologies for data postprocessing. Laminar burning velocity measurements can still be improved and the influence of temperature, pressure and diluents on the laminar burning velocity has to be investigated in further detail.

To investigate the difference between the laminar burning velocity of methanol, ethanol, gasoline and the gasoline surrogates iso-octane, n-heptane and toluene and to validate mixing rules for these alcohol-gasoline blends, accurate measurements are needed. This is the reason why a research stay at Lund University, Sweden, was planned during the Ph.D. study. At Lund University, a flat flame adiabatic burner could be used to measure the laminar burning velocity using the heat flux method. Measurements of laminar burning velocities of iso-octane, n-heptane, ethanol and methanol have previously been performed by van Lipzig et al. [82] and Vancoillie et al. [125] using the same heat flux setup as in the present work. Recently, Dirrenberger et. al [99] also measured the laminar burning velocity of a commercial gasoline, iso-octane, n-heptane, toluene, ethanol and ethanol blends with gasoline and a toluene reference fuel using the heat flux method on a different setup. The results by Dirrenberger et al. [99] are however systematically lower than what was reported by van Lipzig et al. [82] by a few cm/s. This discrepancy is larger than the stated experimental error.

Due to the differences between the results of Dirrenberger et al. [99] and van Lipzig et al. [82], laminar burning velocities of the different fuels were revisited in the present study, and in addition a wider temperature range was covered (298-358 K). The experimental setup has been subject to some improvements since the measurements of van Lipzig et al. [82] and the new results are therefore considered more reliable. The heat flux setup and the error assessment are discussed in the following. The measurements will be discussed in Section 5.6.

5.5.1 Experimental setup

The heat flux method for the stabilization of premixed laminar flames on a flat flame burner has been proposed by de Goey et al. [126] and further developed by van Maaren and de Goey [127]. This method was extensively used for measuring laminar burning velocities of gaseous fuels [127, 128]. A detailed description of the method and associated experimental uncertainties for gaseous [129, 130] and liquid [82, 131] fuels have been published previously. Important features of the method are, therefore, only shortly outlined in the following. The present experimental rig is similar to that used by van Lipzig et al. [82] and Vancoillie et al. [125]. The experimental setup for the adiabatic flame stabilization using the heat flux method is shown in Figure 5.9. The heat flux burner has two major parts: a burner head with a heating jacket supplied with thermostatic water to keep the temperature of the burner plate constant at 368K and a plenum chamber with a separate temperature control system supplied with water. This control system enables to set a temperature of the fresh gas mixture from 298 to 358 K. A burner plate of 2 mm thickness perforated with small holes (0.5 mm in diameter) is attached to the burner outlet. The heating jacket keeps the burner plate edges at a certain temperature higher than the initial gas temperature, thus warming the (unburned) flow of gases. Conductive heat transfer of the flame to the burner plate cools the gas flow on its turn. When the flow rate of the gas mixture is changed, an appropriate value of the gas velocity can be found to nullify the net heat flux. In this case, the radial temperature distribution in the burner plate is uniform and equal to the temperature of the heating jacket. A theoretical analysis of the heat flux method has been given by de Goey and van Maaren [126, 127] where it was shown that the temperature profile of the burner plate can be approximated by a parabolic function:

$$T_p(r) = T_c - \frac{q}{4\kappa_p h} r^2 = T_c + Cr^2 \tag{5.18}$$

Where $T_p(r)$ is the mean temperature of the perforated plate (averaged over the burner thickness) at radial position r. T_c is the thickness averaged temperature of the perforated plate at the center of the plate ($r = 0$). h is the thickness of the perforated plate ($h = 2$ mm). κ_p is the heat conductivity of the plate, and q is the net heat flux (the difference between the heat flux from the flame to the plate and the heat flux from the plate to the unburned mixture).

A series of thermocouples attached to the burner plate allow for measuring the temperature distribution at different radial positions. A polynomial fit is performed to find the heat flux constant C in Equation 5.18. Close to C = 0, the heat flux constant C can be well-approximated by a linear fit. This was the case for all flames

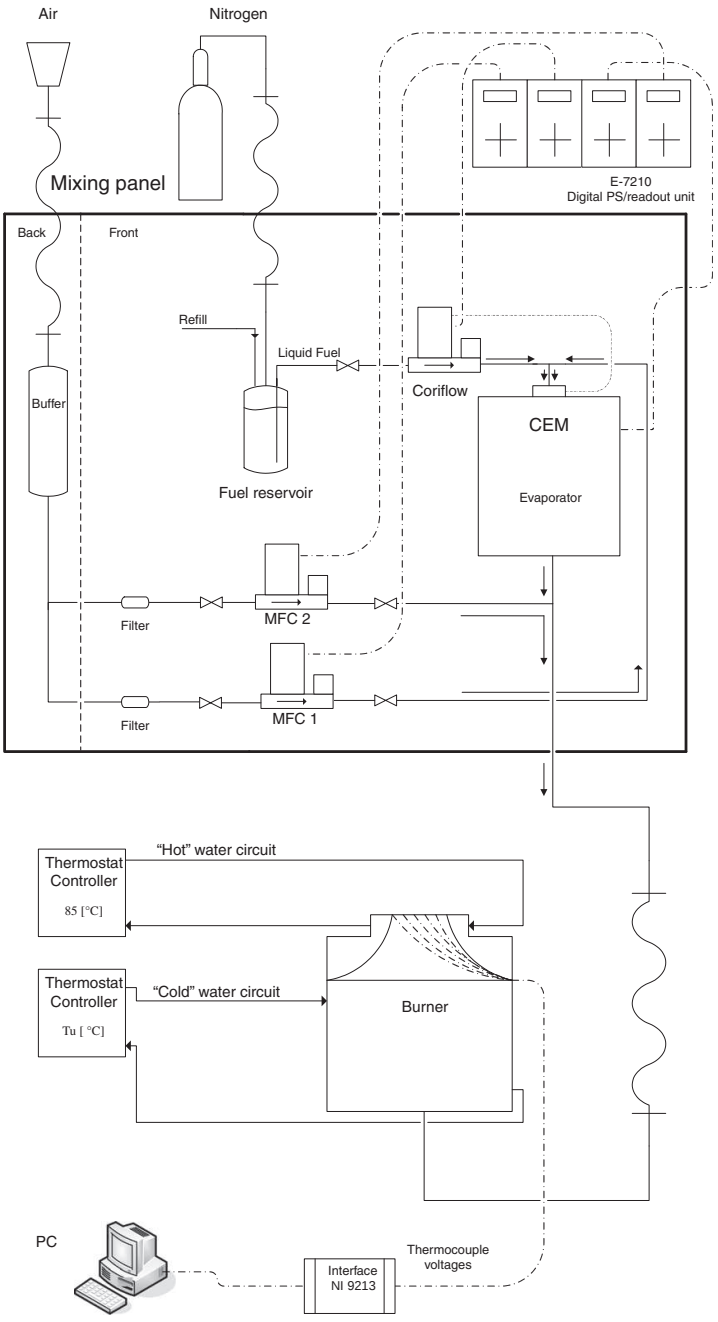

Figure 5.9: Heat flux setup for liquid fuels.

considered in this study. The interpolated flow velocity at which the net heat flux was zero is shown to be the adiabatic flame burning velocity of the unburned gas mixture [126, 127].

A mixing panel shown in Figure 5.9 was used to provide a controlled flow of the vaporized fuel and air, at the required equivalence ratio. The key part of this mixing panel is the CORI-FLOW liquid mass-flow controller (MFC) connected to the controlled evaporator mixer (CEM), both from Bronkhorst B.V. The liquid fuel flow from the fuel reservoir, pressurized by nitrogen, is metered by the CORI-FLOW MFC and fed to the CEM. Part of the air flow controlled by the gas MFC-1 is used as a carrier gas to facilitate vaporization at temperatures up to $473K$. Another part of the air flow controlled by the gas MFC-2 and mixed downstream is varied to provide the required mixture composition. For the measurements reported in this study, the tube connecting the controlled evaporator mixer to the plenum chamber of the burner was a heated tube to avoid condensation of the fuel in the way to the plenum chamber.

5.5.2 Error assessment

Three major sources of experimental uncertainties for gaseous fuels pertinent to the heat flux method were identified as:

- Irregular thermocouple placement in the burner plate.
- Inaccuracy in the mass-flow control.
- Temperature of the unburned mixture.

A detailed analysis of these uncertainties was performed earlier [129, 130] and showed that the overall accuracy of the burning velocity measurements in mixtures near stoichiometry could be better than ±0.8 cm/s and the relative accuracy of the equivalence ratio was found to be typically below 1.5% [131].

Additional possible sources of experimental uncertainties associated with liquid fuels are the following:

- Variable flow ratio of the air between MFC-1 and MFC-2.
- Influence of the CEM operating temperature.
- Dissolution of nitrogen in the liquid fuel.

- Fuel purity.
- Influence of the temperature of the heated tube between the evaporator and the burner.
- Stability of the CORI-FLOW operation.

The first four additional sources were assessed experimentally as described in ref [131], and relevant procedures were repeated for the present installation [82]. It was shown that the ratio of the flows via MFC-1 (carrier gas for the CEM) and MFC-2 does not affect the measured burning velocity within the expected accuracy of the measurements. No influence of the CEM operating temperature was observed when it was set well above boiling temperatures of the fuels. The purity of the fuels, delivered in sealed bottles, was better than 99.5 % for iso-octane, 99 % for n-heptane, 99.9 % for toluene, methanol and ethanol and the refilling time was very short to avoid impurities in the fuel.

In contrast to the work of van Lipzig et al. [82] and Vancoillie et al. [125], the gas mixture was transported from evaporator to burner through a heated tube. Although no droplets were observed during the measurements without the heated tube, a comparison of results obtained with and without heated tube strongly suggested that some condensation did occur without it, especially for toluene and gasoline. For instance in the measurements on toluene without the heated tube, the burning velocities for rich mixtures were too high indicating that the fuel-air mixture was probably leaner than set because of condensation. From this experience we conclude that one of the reasons that the laminar burning velocities measured by van Lipzig et al. [82] and Vancoillie et al. [125] using the same heat flux setup as in the present work are systematically higher than the present measurements by a few cm/s can possibly be a result of condensation and thus leaner gas mixtures than expected. For the stability of the CORI-FLOW operation, it was found that vibrations of the water heaters to control the temperature of the fuel/air mixture had an influence resulting in unstable laminar burning velocity measurements, especially at lower flows. After eliminating the vibrations of the water heaters, stable operation was observed for all equivalence ratios and temperatures. Both of the described changes, installation of heated tube and elimination of vibrations, are expected to decrease the uncertainty in mixture composition and thus give a more reliable result for the laminar burning velocities. Condensation of the fuel in the tube between the evaporator and the burner is more likely to happen for rich equivalence ratios resulting in an overestimation of the laminar burning velocity. If because of vibrations, the actual fuel rate is different than set, the laminar burning velocity is influenced which can lead to over- or underestimation of the true laminar burning velocity. Another

experimental difficulty associated with the heat flux method is related to the important assumption of the symmetry of the temperature distribution in the burner plate, described by Equation 5.18. In fact all previous studies employing this method rely on point-wise temperature measurements using thermocouples or a thermographic phosphor technique [132]. Some scatter in the thermocouple readings were attributed to the different depth of their placement in the burner plate holes [130]. Bosschaart and de Goey proposed a linear correction to compensate for this effect that reduced residual deviation of the thermocouple reading from the expected parabolic profile to less than 0.5 K [130]. However, if for some reasons the thermal conductivity on the edges of the burner plate is not uniform there could be systematic deviations from the symmetry that may lead to systematic errors in the burning velocity measurements. Then switching off one of the most affected thermocouples may lead to significant deviation in the approximated temperature profile as observed by van Lipzig et al. [82]. This deviation, though not significant, was actually observed by Bosschaart and de Goey [130]: even after correction the residuals are not zero for zero value of the parabolic coefficient C (see Equation 5.18). Moreover, lack of expected symmetry was recently found employing a thermographic technique [133] where the complete burner plate surface was covered by a phosphor. One may conclude that the measurements of van Lipzig et al. [82] were probably affected by the non-symmetry effect that was manifested in significant over-evaluation of the burning velocities obtained in that study. Previous work on liquid fuels estimates the overall accuracy of the heat flux method due to these uncertainties to be better than ±1 cm/s [82, 125]. While the same type of error estimation is used for the uncertainty in the mass-flow control, a different method has been used to estimate the error due to the thermocouples. The new method calculates the error due to the polynomial fit of the temperature distribution as a function of the radial placement of the thermocouples. To calculate this error, the standard deviation of the polynomial fit on the thermocouples readings is divided by the slope of the linear fit to find the flow velocity at which the net heat flux was zero. This way, the error on the burning velocity made by the error of the polynomial fit is also taken into account. This is demonstrated in Figure 5.10. In this Figure, the black vertical error bars are the standard deviations of the polynomial fits on the thermocouple readings and the red horizontal error bar represents the corresponding error on the burning velocity. With this method, the overall accuracy of the measurements presented in this work is commonly better than ±1 cm/s. Only for mixtures with an equivalence ratio of 1.3, the error was larger (maximum ±1.4 cm/s) as a result of the slope of the linear fit to find C = 0 being smaller. Because for these rich mixtures, the flame structure is too unstable near the velocity of the laminar burning velocity, extrapolation from lower burning velocities is used. As a result, the standard deviation of the polynomial fit on the thermocouple readings is larger.

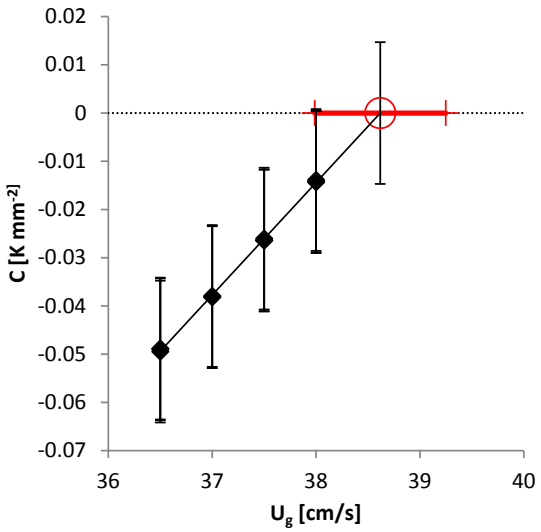

Figure 5.10: Heat flux constant C as a function of the unburned gas velocity U_g (T_0 = 318 K, and p = 1). The horizontal red line is the error on the burning velocity made by the error of the polynomial fit.

5.6 Experimental results

The goal of the research stay at Lund University was first, to provide accurate experimental laminar burning velocity data for a (well characterized) gasoline, methanol, ethanol and the gasoline surrogate components iso-octane, n-heptane and toluene (+alcohol-hydrocarbon blends and a toluene reference fuel) and compare the experimental data with numerical simulations, previous data from the same setup [82] and data from the literature; second, to further validate the mixing rules tested in Section 5.4; third, to investigate the temperature dependence of the laminar burning velocities; and fourth, to try to find a gasoline surrogate of iso-octane, n-heptane and toluene that can match the laminar burning velocity of the studied gasoline.

To investigate the temperature dependence, the power exponent of the temperature dependence, as presented in most laminar burning velocity correlations, will be used. The correlation describing the effect of initial temperature on the burning velocity is:

$$u_l = u_{l0} \left(\frac{T_u}{T_{u0}} \right)^{\alpha} \tag{5.19}$$

where u_l is the laminar burning velocity and T_u is the unburned mixture temperature, and has been used in this or equivalent form since the 1950s, e.g. [134]. The subscript 0 refers to the values at reference conditions (usually 298 K and 1 bar). α represents the power exponent of the temperature dependence. The temperature dependence can be assessed by plotting the laminar burning velocities as a function of the temperature using log-log scales. The slope of the measurements represents the power exponent of the temperature dependence and can be compared to the power exponents used in correlations for laminar burning velocity.

In the following Sections, first the "pure" fuels gasoline (Section 5.6.1), iso-octane, n-heptane and toluene (Section 5.6.2), and methanol and ethanol (Section 5.6.3) are compared with measurements from literature and simulations of kinetic models. Additionally, the temperature dependence of these fuels will be investigated. In Section 5.6.4, a toluene reference fuel will be formulated to match the laminar burning velocity of gasoline and measurements of this TRF will be shown. Finally in Section 5.6.5, measurements of alcohol-hydrocarbon blends will be discussed and mixing rules will be evaluated using these measurements.

Measurements of the laminar burning velocity of the different fuels at different initial temperatures are summarized in Appendix B together with the detailed composition of the gasoline.

5.6.1 Gasoline

Laminar burning velocities have been measured for a gasoline (Exxon 708629-60) without oxygenates at 298 K, 318 K, 328 K, 338 K, 348 K and 358 K. The gasoline has been analyzed and was found to be composed of 10.37% v/v n-alkanes, 40.2% v/v iso-alkanes, 34.39% v/v aromatics, 9.39% naphthenes and 5.65% v/v olefins. The detailed composition of the gasoline can be found in Appendix B.2. Figure 5.11 compares the measurements at 358K with the data found in literature for commercial gasolines. There is a good agreement both with the data of Dirrenberger et al. [99], who used the same method to measure the laminar burning velocity, and with the data of Zhao et al. [97] (at 353K) who used the stagnation jet-wall flame configuration and Particle Image Velocimetry. It is expected that the differences are influenced by the composition of the gasoline. The gasoline used by Dirrenberger et al. [99] was provided by TOTAL (ref. IFPEN: TAE 7000) and contained oxygenated compounds which could explain the higher burning velocities around equivalence ratio 1.0-1.1 if the oxygenated compounds were alcohols.

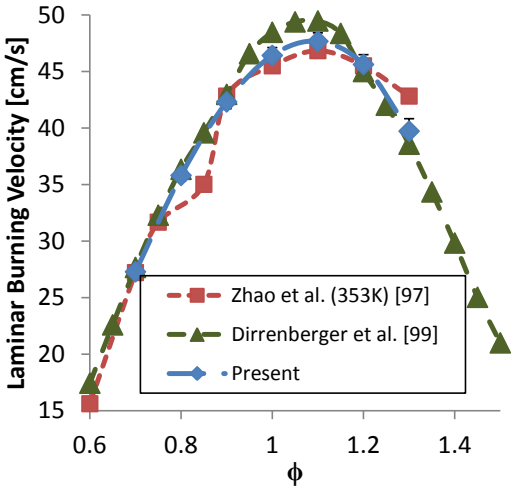

Figure 5.11: Laminar burning velocities of gasoline-air mixtures at 358 K.

Measured laminar burning velocities of gasoline-air flames at atmospheric pressure and different initial temperatures are shown in Figure 5.12 using log-log scales. Apart from the experimental data represented by symbols, lines are included to show the best fits to Eq. 5.19. In Figure 5.13, the derived power exponents α are compared to the power exponent of other correlations used for the laminar burning velocity of gasoline in simulation programs. In comparison to the present measurements, the correlation by Metghalchi and Keck [85] and the correlation used in GT-Power [135], the industry standard for engine simulations, use higher α values. The correlation used in GT-Power is based on the publication of Takashi et al. [136]. The correlation by Gülder [137] is based on laminar burning velocity measurements of iso-octane and is sometimes used in simulations to calculate the burning velocities of gasoline [138]. This correlation has α values that are lower than the results of the present study imply, and does not include the effect of the equivalence ratio on the power exponent. Metghalchi and Keck and Gülder both used closed vessels and spherical flames to measure the laminar burning velocity but did not take flame stretch and instabilities into consideration. Failing to perform stretch corrections for the spherical flames inside these closed vessels can lead to over- or underestimation of the true laminar burning velocity depending upon the sign of the Markstein number resulting in different α exponents [81]. We can conclude that none of the correlations is able to reproduce the temperature dependence, with a minimum around the equivalence ratio at peak burning velocity, measured for this gasoline.

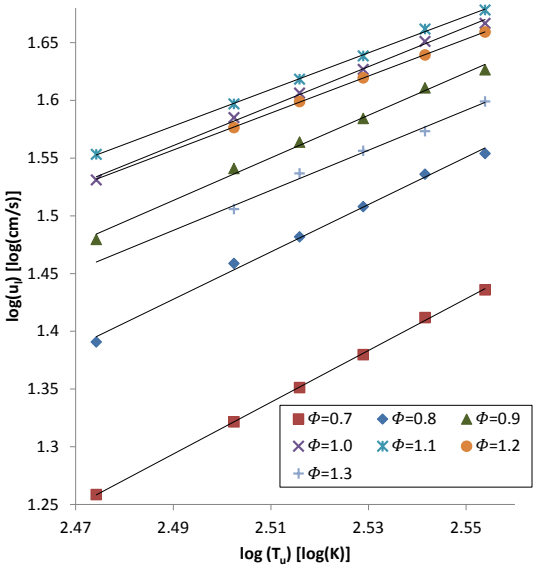

Figure 5.12: Log-log plot of laminar burning velocities of gasoline-air flames at atmospheric pressure and different initial temperatures. Symbols, experiments; lines, linear fits.

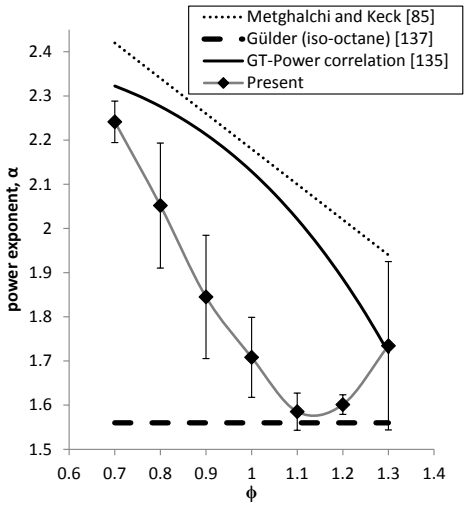

Figure 5.13: Comparison between the power exponent α from measurements and the power exponent α used in correlations of the burning velocity of gasoline.

5.6.2 Gasoline surrogate components: iso-octane, n-heptane and toluene

Laminar burning velocities have been measured for the gasoline surrogate components iso-octane, n-heptane and toluene at 298 K, 318 K, 328 K, 338 K and 358 K. In Figure 5.14, 5.15 and 5.16, there is a comparison between the present measurements and data from literature at respectively 298 K and 358 K. For the clarity of the Figures, only selected data from the literature is included. For iso-octane at 298 K, there is again a good agreement with the measurements of Dirrenberger et al. [99] who used the same method. The measurements are a few cm/s lower than the previous measurements on the same setup performed by van Lipzig et al. [82]. At 358 K, there is a very good agreement with the measurements of Dirrenberger et al. [99]. The measurements of Bradley et al. [81] who used spherically expanding flames to measure flame speeds compare well for rich mixtures but are higher for lean mixtures.

For n-heptane and toluene, the same trend as for iso-octane is seen. There is a good agreement with the measurements of Dirrenberger et al. [99] and there are some differences when comparing to other data. For n-heptane at 298 K, the measurements of Dirrenberger et al. are almost the same and there is also a good agreement with the measurements of Huang et al. [86] and Davis et al. [89]. Only for toluene at 298 K, the difference between the measurements of Dirrenberger et al. and the present measurements is more marked. Dirrenberger et al. did measurements at 298 K, 358 K and 398 K and as a result, it is possible to compare the temperature dependence of the present measurements and the measurements performed by Dirrenberger et al.

On Figure 5.17, the laminar burning velocities are shown as a function of the temperature on log-log scales, only for a few equivalence ratios for the clarity of the Figure. It is clear from Figure 5.17, that the measurements of Dirrenberger et al. follow more or less the same trend as the present measurements for 358 K and 398 K but deviate for 298 K. Based on this it seems likely that the laminar burning velocities of toluene at 298 K measured by Dirrenberger et al. are too high compared to the other measurements.

In Figure 5.18, 5.19 and 5.20, a comparison is made between two chemical oxidation mechanisms (see Section 5.3) and the present measurements of iso-octane, n-heptane and toluene at 298 K and 358 K. For toluene and iso-octane, the model of Mehl et al. [117] predicts the laminar burning velocities better, especially for lean mixtures. For iso-octane, the model overpredicts the measurements but the qualitative dependence of the equivalence ratio is covered better than with the model of Andrae [116] which underpredicts the laminar

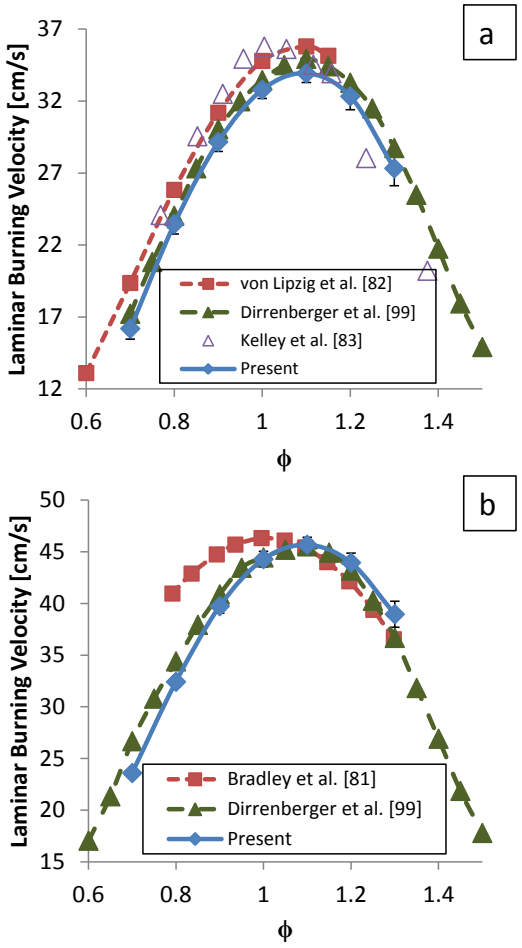

Figure 5.14: Laminar burning velocities of iso-octane-air mixtures at 298 K (a) and 358 K (b).

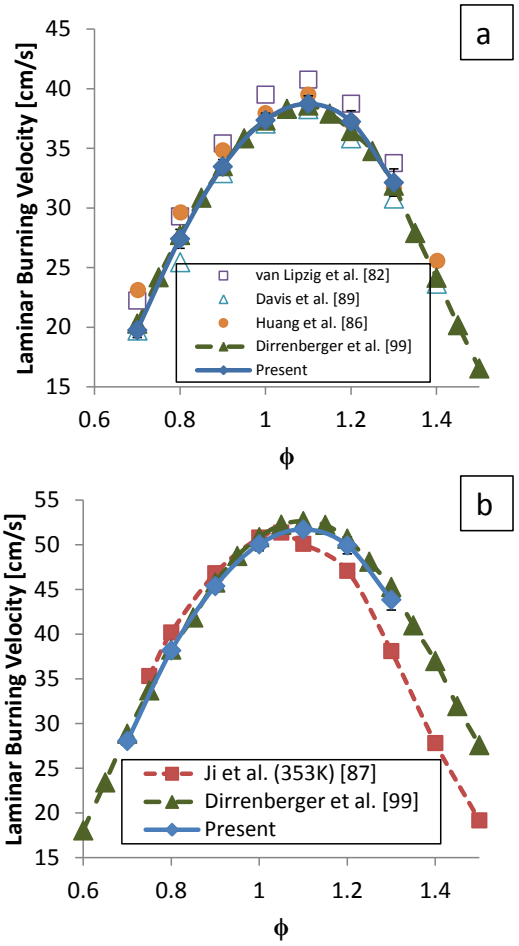

Figure 5.15: Laminar burning velocities of n-heptane-air mixtures at 298 K (a) and 358 K (b).

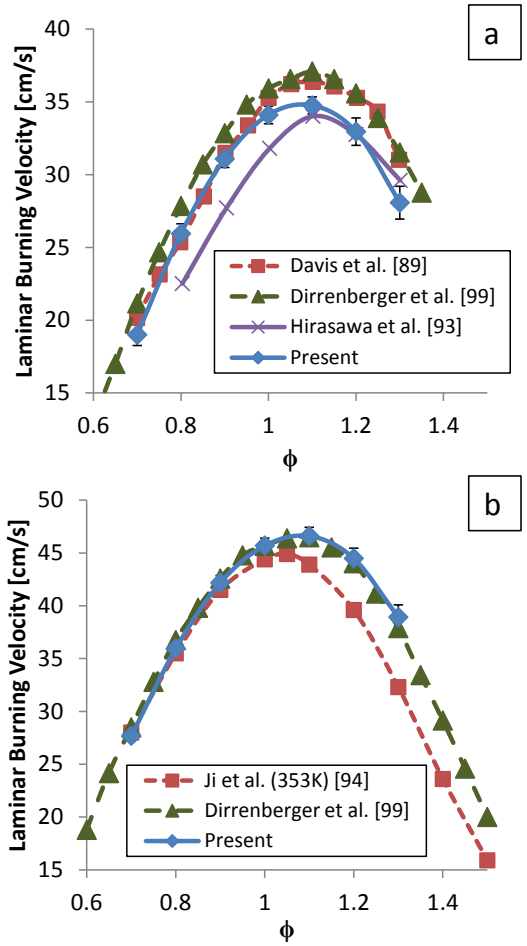

Figure 5.16: Laminar burning velocities of toluene-air mixtures at 298 K (a) and 358 K (b).

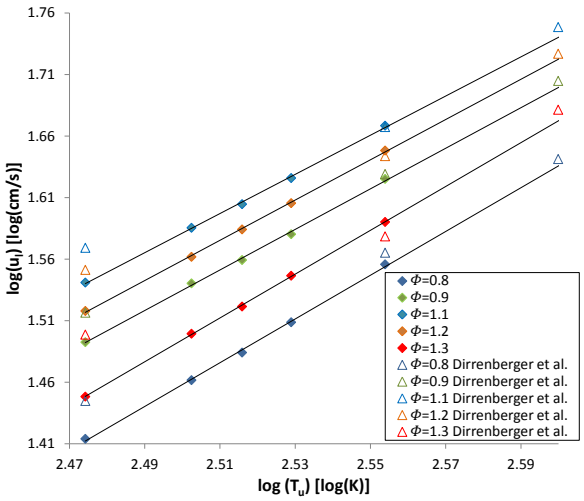

Figure 5.17: Log-log plot of laminar burning velocities of toluene-air flames at atmospheric pressure and different initial temperatures. Diamonds, present experiments; Triangles, measurements [99].; lines, linear fits of present measurements.

burning velocities for lean mixtures and overpredicts the laminar burning velocity for equivalence ratios in the region of 1.1-1.2. For n-heptane, both models cover the dependence of the equivalence ratio in a good way but both models overpredict the laminar burning velocity. Here, the better agreement is for the model of Andrae.

In Figure 5.21, the derived power exponents α of iso-octane are shown and compared to the power exponents of correlations for the laminar burning velocity of iso-octane/air mixtures and to the power exponents derived from the simulations with the model of Mehl et al. There is again a minimum around the equivalence ratio of peak burning velocity which is covered by none of the correlations. The correlation of Metghalchi and Keck [85] and the correlation of Galmiche et al. [90] predict a linear decrease of α as a function of the equivalence ratio whereas the correlation of Gülder [137] does not include the effect of the equivalence ratio on the power exponent. The minimum around the equivalence ratio of peak burning velocity is well covered by the model of Mehl et al. and there is a good agreement for equivalence ratios from 0.8 to 1.2. In Figure 5.22, the derived power exponents α of iso-octane, n-heptane and toluene are shown together. All three fuels have a minimum around the equivalence ratio of peak burning velocity.

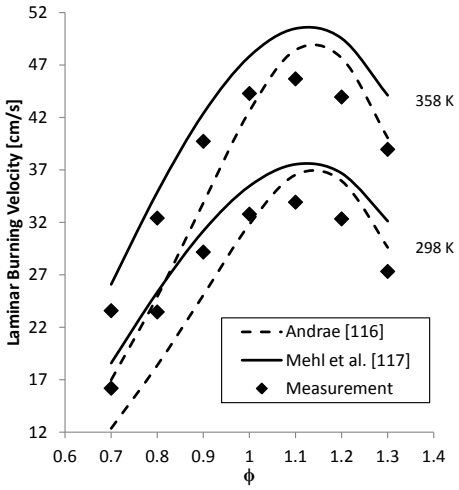

Figure 5.18: Comparison between kinetic models and laminar burning velocity of iso-octane-air mixtures at 298 K and 358 K.

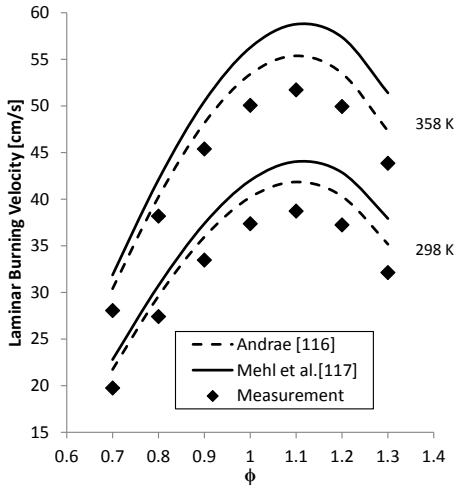

Figure 5.19: Comparison between kinetic models and laminar burning velocity of n-heptane-air mixtures at 298 K and 358 K.

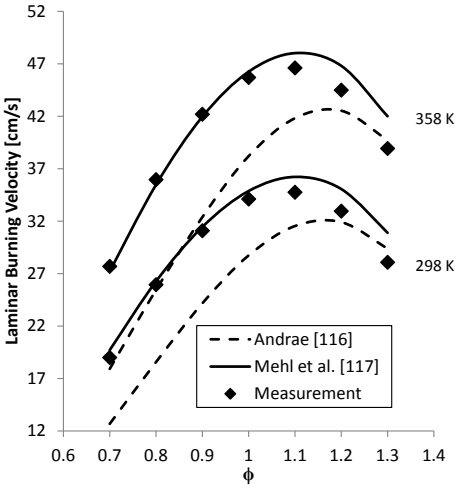

Figure 5.20: Comparison between kinetic models and laminar burning velocity of toluene-air mixtures at 298 K and 358 K.

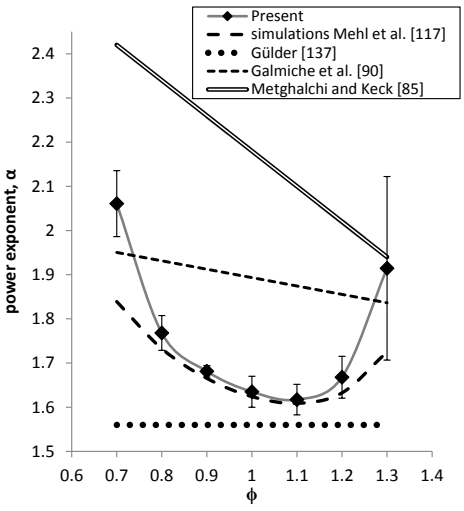

Figure 5.21: Comparison between the power exponent α of iso-octane from measurements and the power exponent α derived from the model of Mehl et al. and used in correlations of the burning velocity of iso-octane.

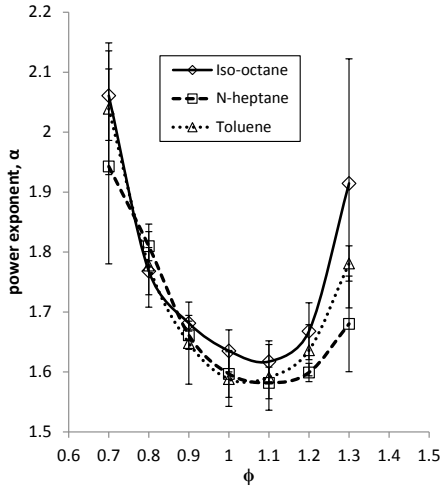

Figure 5.22: Power exponent α of iso-octane, n-heptane and toluene from measurements

5.6.3 Methanol and ethanol

In this section, the measurements of the laminar burning velocity of methanol and ethanol will be discussed. For both fuels, the laminar burning velocity has been measured at 298K, 318K, 328K, 338K and 358K. Due to limitations in the experimental setup, measurements on methanol performed on the same setup by Vancoillie et al. [125] were limited to equivalence ratios below 1.1 and equal to 1.5. However, in the present work the whole range of equivalence ratios from 0.7 to 1.5 was reached by using a fuel mass flow controller with a higher upper limit. Figure 5.23 compares the measurements for methanol at 298K, 318K and 338K with the data found in the literature. As described before, the results of Vancoillie et al. [125], done on a similar setup, are slightly higher than the measurements done in this study. Further, it is clear that there are still large deviations with the other data in the literature. At 298K, deviations with the measurements of Gibbs and Calcote (G&C) [139] are large but it has been shown that the measurement methods of Gibbs and Calcote produced unreliable results [140, 141]. For the measurements of Metghalchi and Keck (M&K) [85], the agreement is good for lean mixtures. Metghalchi and Keck did not take flame stretch and instabilities into consideration in their closed vessel studies. Failing to perform stretch corrections for the spherical flames can lead to over- or underestimation of the true laminar burning velocity, depending upon the sign of the Markstein number. At 318K, the

laminar burning velocities of Egolfopoulos et al. [142] are higher than the present measurements for equivalence ratios from 1 to 1.3. Egolfopoulos et al. did take flame stretch effects into account but because of the typically small strain rate in their flames (about 100 s-1), they used a linear extrapolation to zero stretch. This linear extrapolation has recently been reported to lead to overestimations of the burning velocity by 5-10% [142, 143]. At 338K, measurements were compared to those of Veloo et al. [144] at 343K. Veloo et al. recently repeated the measurements by Egolfopoulos et al. [142] on methanol-air flames under a restricted set of conditions. They used the counterflow twin-flame burner in combination with a particle image velocimetry method. The unstretched laminar burning velocity was derived using a nonlinear extrapolation approach based on direct numerical simulations of the experiments. This led to an improved accuracy of the measured burning velocity compared to the linear extrapolation employed by Egolfopoulos et al. [142]. From Figure 5.23 it is clear that the effect of the equivalence ratio on the laminar burning velocity agrees well with the present measurements, although the measurements were done at a different temperature.

In Figure 5.24, the measurements for ethanol at 298K and 358K are compared with the data found in the literature. For ethanol, the scatter between the different measurements is already less than for methanol. The measurements of Konnov et al. [131], van Lipzig et al. [82] and Dirrenberger et al. [99] were all done with the same measurement method, i.e. the heat flux method. The measurements done by Dirrenberger et al. compare very well at 358K, especially at lean and rich mixtures, but are slightly higher at 298K. The measurements of Konnov et al. [131] report lower laminar burning velocities for leaner mixtures of ethanol. For rich mixtures, the agreement is better but the burning velocities are slightly higher. Van Lipzig et al. [82] stated that the differences between his measurements and the measurements of Konnov et al. [131] were due to erroneous readings from the edge thermocouple that affected temperature measurements but when we compare the present measurements with the measurements of Konnov et al., there seems also to be a small shift of the curve to higher equivalence ratios, both for 298K and 358K. A possible cause for this shift could be fuel condensation. Special attention was paid to prevent fuel condensation during this study by installing a heated tube between the evaporator and the burner. Note also that the correspondence with the recent data sets of Bradley et al. [145] is reasonable although these authors gathered their data with a completely different measurement method.

In Figure 5.25, both the present data and the data of Vancoillie et al. [125] are plotted as a function of the temperature on a log-log scale. The slope of the measurements represents the power exponent of the temperature dependence. As can be seen, there is a clear linear behavior for the present measurements on methanol while for the measurements of Vancoillie et al. [125], there seems to

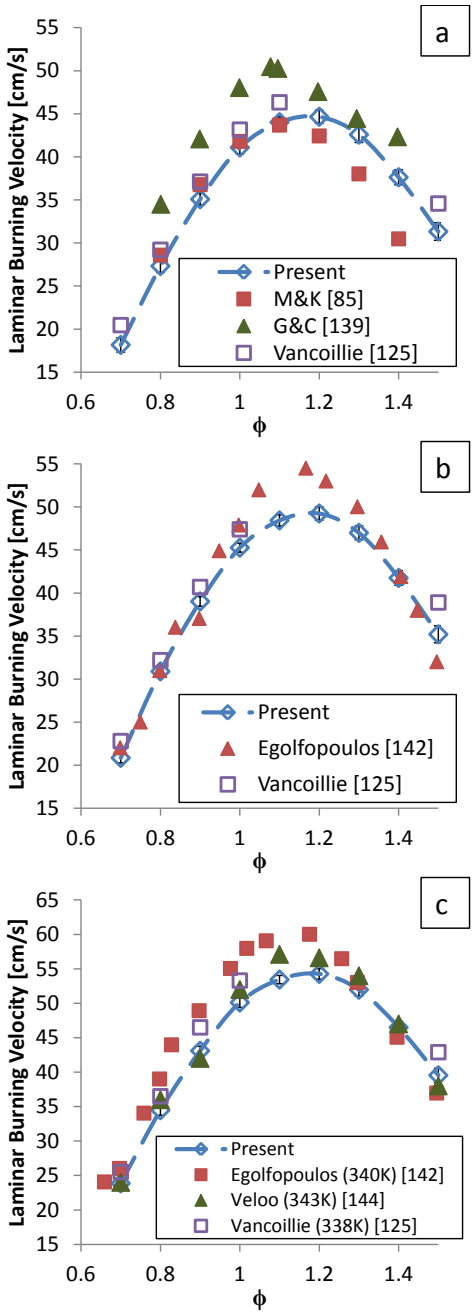

Figure 5.23: Laminar burning velocities of methanol-air mixtures at 298 K (a), 318 K (b) and 338 K (c).

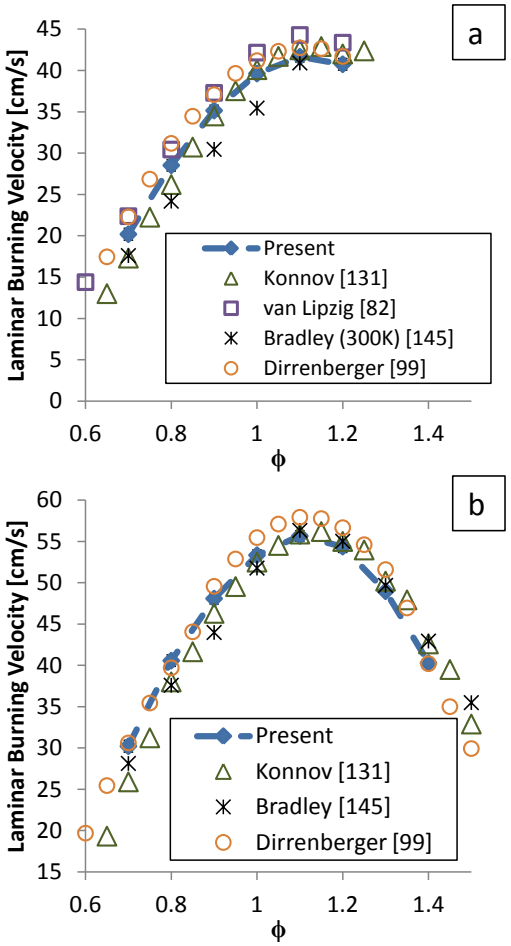

Figure 5.24: Laminar burning velocities of ethanol-air mixtures at 298 K (a) and 358 K (b).

be larger random devations, although these deviations are still small, from the expected linear trend. It is clear that the changes to the setup (heated tube, stability of the CORI-FLOW) result in more stable and reliable results. In Figure 5.26, the power exponents α, derived from the present measurements on methanol, are compared with the power exponents found by Vancoillie et al. [125]. Around stoichiometry, there is still a good agreement. In Figure 5.26, the power exponents derived from modeling results using the mechanism by Li et al. [146] are also shown. This mechanism also produces a minimum for slightly rich mixtures and it agrees very well with the measurements of Vancoillie et al. [125], especially for lean mixtures. For the present measurements, the agreement is good around equivalence ratios of 1-1.3 but the deviations are larger for lean mixtures. More details about the modeling can be found in [125].

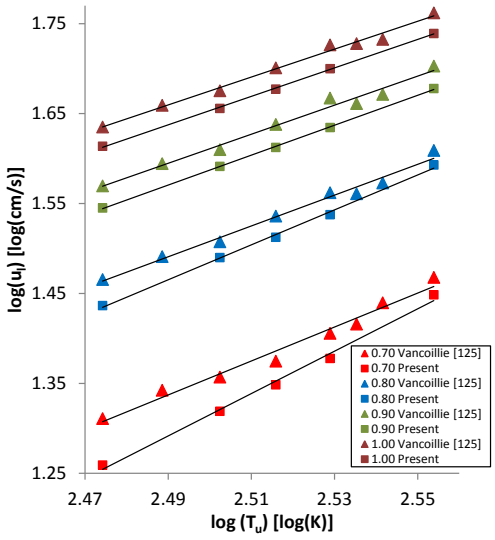

Figure 5.25: Log-log plot of laminar burning velocities of methanol-air flames at atmospheric pressure and different initial temperatures. Squares, present experiments; Triangles, Vancoillie [125].

In Figure 5.27, the laminar burning velocities of ethanol are shown as a function of the temperature on log-log scales. The difference in temperature dependence between the present measurements and the measurements of Dirrenberger et al. [99] and Konnov et al. [131] corresponds also to the difference in deviations between the laminar burning velocities at different temperatures. In Figure 5.28, the power exponents, derived from the present measurements, the data of

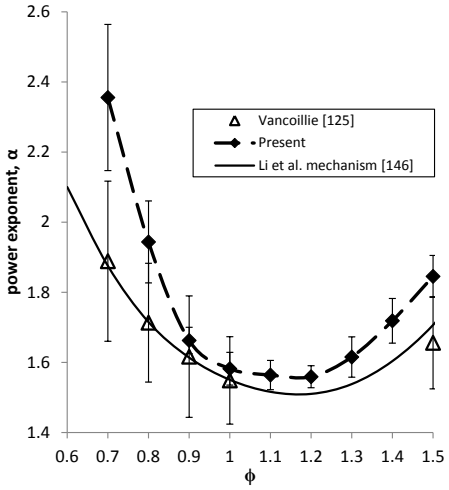

Figure 5.26: Comparison between the power exponent α of methanol from measurements and the power exponent α derived from the mechanism of Li et al. [146].

Dirrenberger et al. [99] and the data of Konnov et al. [131], are compared. The shape of the curve for power exponents for the present measurements is consistent with the previous measurements on the same setup [125], the minimum is around the equivalence ratio of peak burning velocity. This is also reflected in the measurements of Konnov et al. [131], while the shape of the power exponents derived from the measurements of Dirrenberger et al. [99] is very different. The power exponent of Dirrenberger et al. [99] was derived from measurements at only three different temperatures which is less accurate and could be the cause of the different shape. In Figure 5.28, calculated power exponents using the Konnov mechanism [147] were added. The power exponents agree well with the present experimental data especially for rich mixtures. The power exponents derived from the data of Konnov et al. [131] indicate the trend to level off with increasing equivalence ratio. This effect was also predicted in methane-air flames [148]. This cannot be seen in the present measurements and it seems that the experimental trend follows the simulations by the Konnov mechanism; therefore, further measurements of the laminar burning velocity of rich mixtures are desirable.

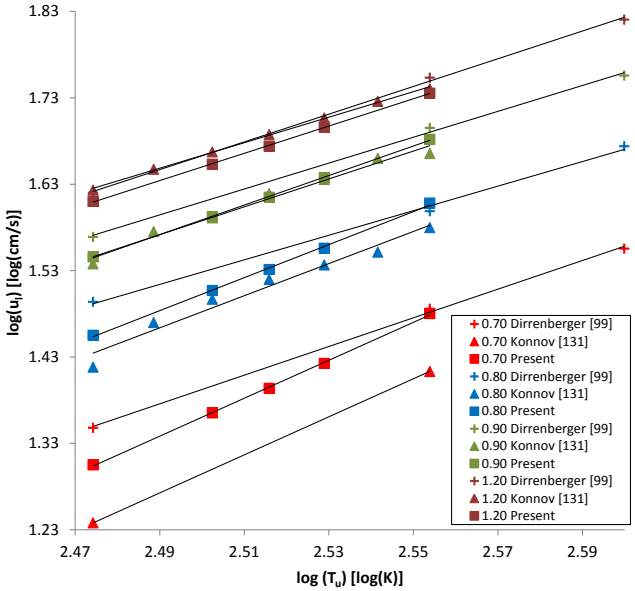

Figure 5.27: Log-log plot of laminar burning velocities of ethanol-air flames at atmospheric pressure and different initial temperatures. Squares, present experiments; Triangles, Konnov [147]; Crosses, Dirrenberger [99].

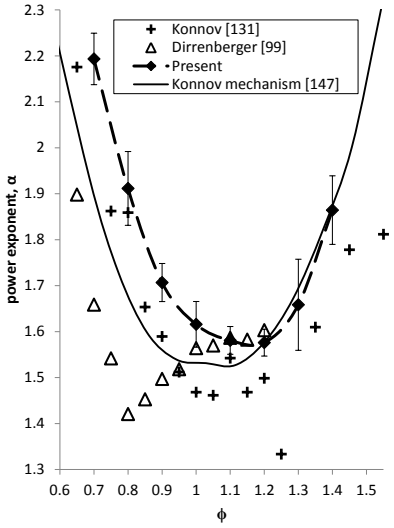

Figure 5.28: Comparison between the power exponent α of ethanol from measurements and the power exponent α derived from the Konnov mechanism [147].

5.6.4 Can a toluene reference fuel match the laminar burning velocity of gasoline?

Measurements of a toluene reference fuel (iso-octane, n-heptane and toluene) have been performed to see if a toluene reference fuel can be used to match the laminar burning velocity of a commercial gasoline. Therefore, a correct mixing ratio of the mixture of iso-octane, n-heptane and toluene has to be found. Dependent on the specific property that the surrogate should be able to predict, the method to find the correct mixing ratio of the different fuels will be different. For some applications the toluene reference mixture is formulated to match the commercial gasoline regarding either C/H ratio, molecular mass, lower heating value, boiling point, density or auto-ignition properties such as the research octane number or the motor octane number [149]. In the present study the composition of the toluene reference fuel was based on the laminar burning velocities of the pure fuels iso-octane, n-heptane and toluene and the laminar burning velocities of the gasoline at different temperatures. A simple mixing rule for the laminar burning velocity was applied to predict which mixture of iso-octane, n-heptane and toluene could have a similar laminar burning velocity of gasoline for the whole temperature range. In Section 5.4, it was found that three mixing rules gave very good results for ethanol-hydrocarbon mixtures: a mixing rule based on the energy fraction of the components, a mixing rule proposed by Hirasawa et al. [93] and a mixing rule using the principle of Le Chatelier's flame theory. These mixing rules can be used to calculate the mixture of iso-octane, n-heptane and toluene that could match the laminar burning velocity of gasoline. For the fuels used in this study, the differences between the results of the different mixing rules are small and here, the energy fraction mixing rule was used, see Equation 5.1 and 5.2.

By changing the fraction of the components in the mixing rule, it was found that a mixture of 1/3 iso-octane, 1/3 n-heptane and 1/3 toluene on volume basis could have a similar laminar burning velocity and this mixture had the advantage that it was easy to blend on volume basis decreasing the chances for errors. In Figure 5.29, a comparison between the laminar burning velocities of gasoline, iso-octane, n-heptane, toluene and the toluene reference fuel is shown. It is clear that for lean mixtures, a combination of iso-octane and n-heptane could be sufficient to reproduce the laminar burning velocity of gasoline but that the same fuel blend will not be able to reproduce the laminar burning velocities for rich mixtures because of the aromatics in gasoline. This was also found by Jerzembeck et al. [88]. They found that the laminar burning velocity for lean mixtures of a commercial gasoline can be matched by a PRF mixture with a research octane number of 87 but deviations were observed for stoichiometric and rich mixtures. To cover a bigger equivalence ratio range, a TRF is needed. From Figure 5.29, one can conclude

that the mixture of 1/3 iso-octane, 1/3 n-heptane and 1/3 toluene on volume basis is capable of matching the laminar burning velocity of gasoline and that the energy fraction mixing rule is accurate enough to predict the laminar burning velocity of toluene reference fuels although the differences between all the fuels are relatively small.

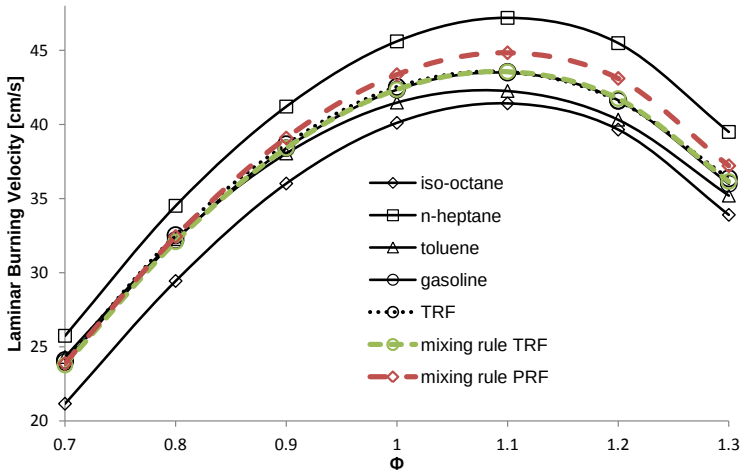

Figure 5.29: Comparison between the laminar burning velocity of iso-octane, n-heptane, toluene, gasoline and the toluene reference fuel at 338 K together with the prediction of the energy fraction mixing rule.

In Figure 5.30, the laminar burning velocity of gasoline is shown for different temperatures together with the laminar burning velocity of the TRF and the predictions made by the energy fraction mixing rule based on the burning velocities of iso-octane, n-heptane and toluene. From this Figure we can conclude that for these laminar burning velocities at atmospheric pressure, this mixture of iso-octane, n-heptane and toluene is able to reproduce the laminar burning velocity and the temperature dependence of the commercial gasoline. The power exponents of the toluene reference fuel and the gasoline are compared in Figure 5.31. For most of the equivalence ratios, both fuels have similar temperature dependence. Although the laminar burning velocities of this toluene reference fuel are in correspondence with the laminar burning velocities of the studied gasoline, this mixture of iso-octane, n-heptane and toluene will not be able to predict all fuel properties, engine characteristics or laboratory data of this gasoline such as ignition delay, evaporation characteristics, emissions, etc. Therefore, specific surrogates should be used to emulate specific properties.

One can ask the question if the laminar burning velocity of gasoline could be

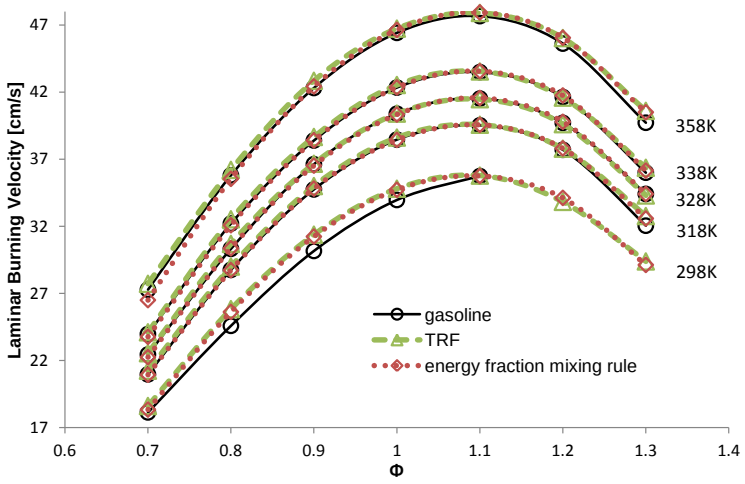

Figure 5.30: The laminar burning velocity of gasoline and the toluene reference fuel at 298 K, 318 K, 328 K, 338 K and 358 K together with the predictions of the energy fraction mixing rule

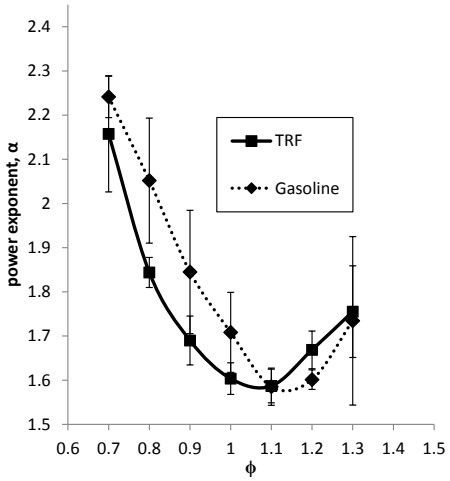

Figure 5.31: Comparison between the power exponent α of gasoline and the power exponent α of the toluene reference fuel.

predicted based on the composition of the gasoline. In this study, the composition of the TRF that matched the laminar burning velocity of the used gasoline was determined using a mixing rule resulting in a very good agreement. In the study of Mannaa et al. [150], laminar burning velocities were measured of several toluene reference fuels and three gasoline fuels of 70, 85 and 95 RON (FACE J, C and F) at the initial temperature of 358 K and pressures up to 0.6 MPa using a constant-volume spherical vessel. Three TRF's were found to successfully emulate the burning rate characteristics of the gasoline fuels associated with these RONs under the various experimental conditions investigated. In Figure 5.32, the composition of the different gasolines and matching TRF's is shown. The composition of the gasolines measured by Mannaa et al. [150] was not specified but the composition of these gasolines was taken from a report of the non-profit organization Coordinating Research Council [151]. As can be seen in Figure 5.32, as a first guideline to compose a TRF that could match the laminar burning velocity of the gasoline, the fraction of iso-octane, n-heptane and toluene in the TRF could be taken the same as the fraction iso-alkanes, n-alkanes and aromatics in the given gasoline.

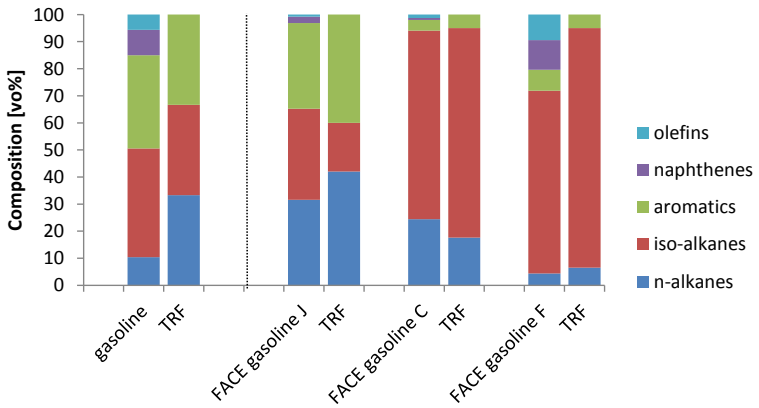

Figure 5.32: Comparison of the composition of the best matching TRF and the gasoline used in the experiments. Laminar burning velocity measurements of FACE gasoline and matching TRF's are measured by Mannaa et al. [150].

5.6.5 Validating mixing rules for blends of methanol, ethanol, iso-octane and n-heptane

To further validate the mixing rules tested in Section 5.4, measurements have been done on different fuel blends: ethanol/iso-octane (25% v/v liquid, 50% v/v and 75% v/v ethanol), methanol/iso-octane (75% v/v methanol) and a mixture of methanol, ethanol, iso-octane and n-heptane (25% v/v each). For the binary mixtures, the measurements have been limited to alcohol/iso-octane mixtures because the difference in laminar burning velocity between iso-octane and the light alcohols is bigger compared to n-heptane. The measurements on methanol/iso-octane could not be extended to lower methanol blends because of phase separation. Methanol/iso-octane mixtures with 75% v/v methanol were found to be the practical lower limit. In Figure 5.33, the measurements for all ethanol/iso-octane blends are shown at 338K and in Figure 5.34, a comparison of different mixing rules is made for ethanol/iso-octane with 50% v/v ethanol. As expected, the laminar burning velocities of the fuel blends are in between the laminar burning velocities of the pure fuels. The energy fraction mixing rule, the Hirasawa et al. mixing rule and Le Chatelier's mixing rule based on energy fraction are used in this Section because these three mixing rules gave the best agreement when tested on literature data and simulation data, see Section 5.4. In Figure 5.34, the best prediction is obtained with Le Chatelier rule based on energy fraction, especially for richer mixtures, in agreement with what was found for ethanol-hydrocarbon mixtures in Section 5.4. Mixing rules based on mole or mass fraction were also evaluated in Section 5.4 and it was concluded that they gave less accurate predictions. An example of this applied to the present study can be seen in Figure 5.35, where the laminar burning velocity is plotted for different equivalence ratios as a function of either energy fraction of ethanol or mole fraction of ethanol. From Figure 5.35 we can conclude that predicting the laminar burning velocity with a linear interpolation based on the mole fraction is not a good option. Predicting the laminar burning velocity of ethanol-hydrocarbon blends based on the energy fraction is a better option with only a slight overprediction which can also be seen in Figure 5.34.

In Figure 5.36, different mixing rules are tested for methanol/iso-octane. Here, the energy fraction mixing rule gives the best prediction and the Hirasawa et al. mixing rule and Le Chatelier mixing rule underpredict the measurements. The laminar burning velocity of methanol/iso-octane is again in between the laminar burning velocity of iso-octane and methanol.

A quaternary mixture with both ethanol and methanol was measured because complex mixtures with more than one alcohol component could play an important

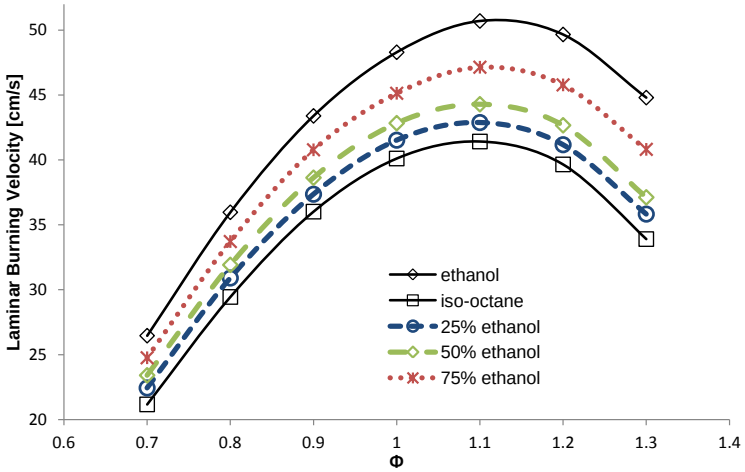

Figure 5.33: The laminar burning velocity of iso-octane, ethanol and ethanol/iso-octane blends (25% v/v, 50% v/v and 75% v/v ethanol) at 338K.

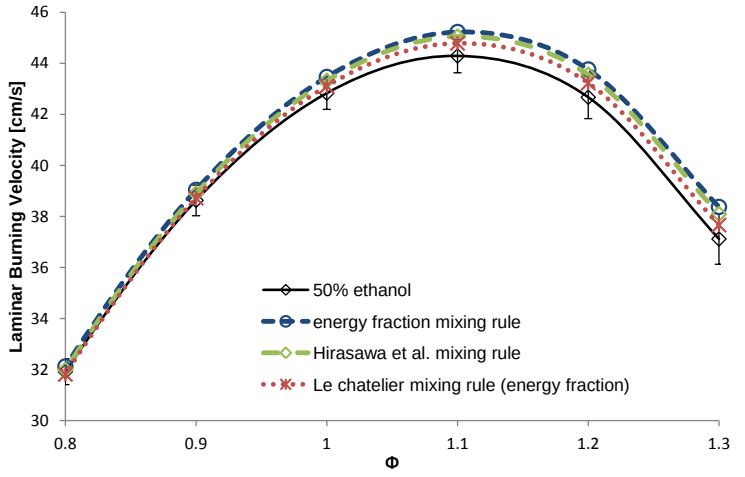

Figure 5.34: The laminar burning velocity ethanol/iso-octane (50% v/v ethanol) at 338K together with the predictions of different mixing rules.

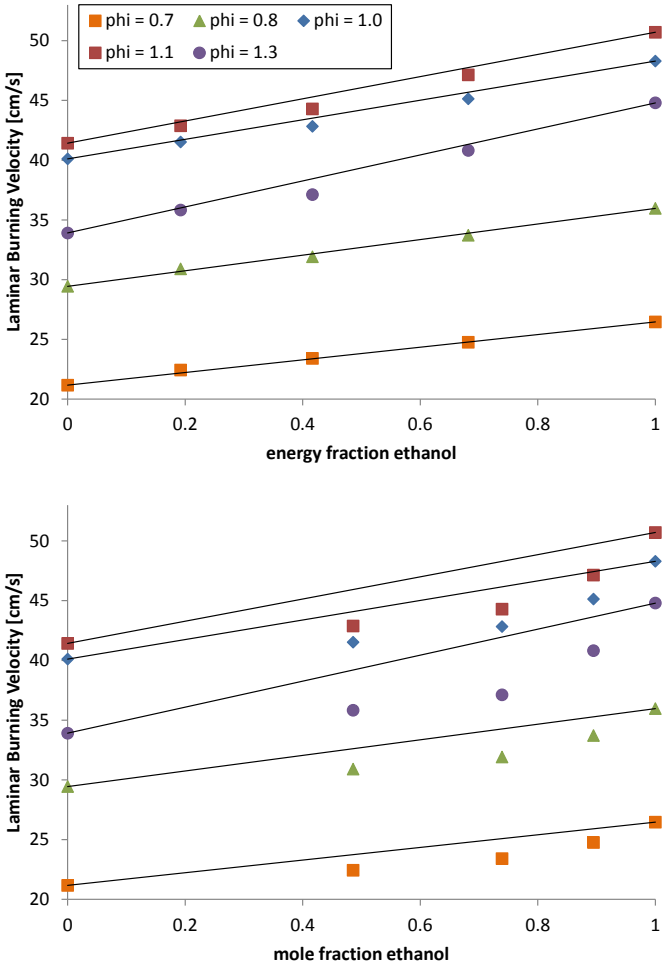

Figure 5.35: The laminar burning velocity of iso-octane, ethanol and ethanol/iso-octane blends (25% v/v, 50% v/v and 75% v/v ethanol) at 338K as a function of either energy fraction of ethanol or mole fraction of ethanol. Symbols: experimental data.

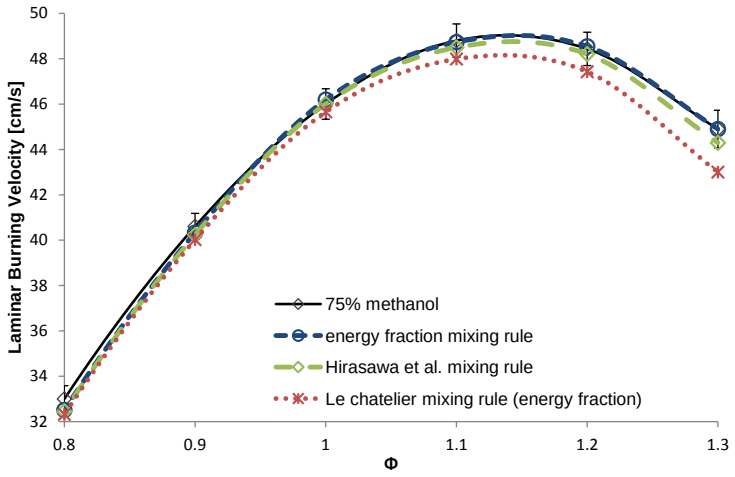

Figure 5.36: The laminar burning velocity methanol/iso-octane (75% v/v methanol) at 338K together with the predictions of the different mixing rules.

role in the future, see Section 2.4. The burning velocities of the pure components and the mixtures are shown in Figure 5.37 at 338K. In Figure 5.38, the laminar burning velocity of the mixture is shown together with the predictions of different mixing rules and with the predictions of a linear interpolation based on the mole fraction. Again, it is clear that the mole fraction is not the right choice to calculate the laminar burning velocity of fuel blends out of the laminar burning velocities of the pure components. A mole fraction mixing rule should thus not be used in engine simulation models. The three mixing rules give similar results with the best agreement for the energy fraction mixing rule. Based on these results and the fact that there are also small errors in the laminar burning velocity of the pure fuels, we can conclude that these three mixing rules give accurate predictions for laminar burning velocities of blends with methanol and ethanol. These mixing rules can be invaluable as a way to calculate this property in a computationally efficient way in simulation programs.

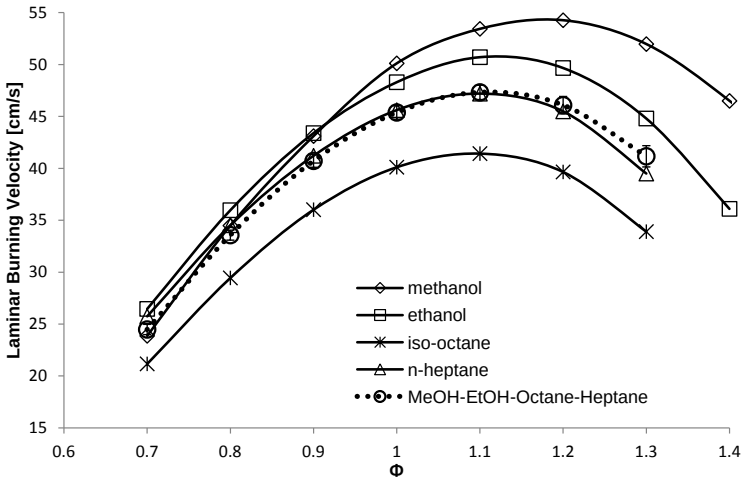

Figure 5.37: The laminar burning velocity of iso-octane, n-heptane, methanol, ethanol and their quaternary mixture (25% v/v each) at 338K.

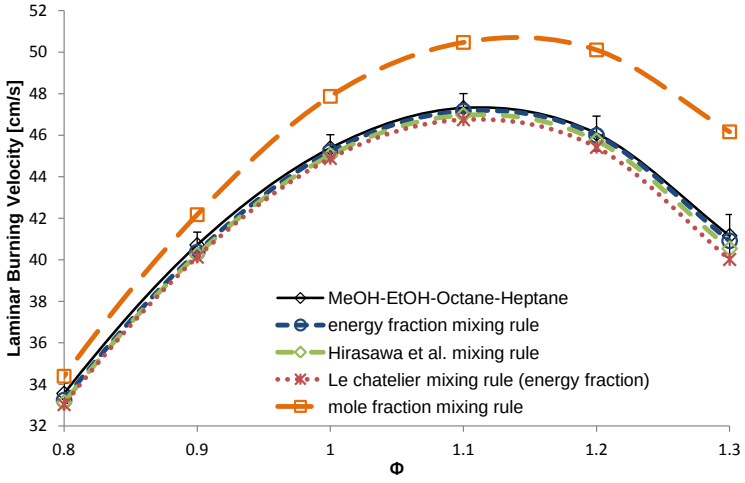

Figure 5.38: The laminar burning velocity methanol/ethanol/iso-octane/n-heptane mixture (25% v/v each) at 338K together with the predictions of the different mixing rules.

Summary

Measurements of the laminar burning velocity have been done for gasoline, iso-octane, n-heptane, toluene, methanol, ethanol, a toluene reference fuel and binary and quaternary alcohol-hydrocarbon mixtures for a wide range of temperatures at atmospheric pressure using the heat flux method on a perforated plate burner. The temperature dependence of the laminar burning velocity as a function of the equivalence ratio has been shown for the different fuels. All fuels have the temperature dependence with a minimum around the equivalence ratio of peak burning velocity. The temperature dependence of gasoline has been compared to current correlations for gasoline but none of the correlations captured the temperature dependence of gasoline with a minimum around the equivalence ratio of peak burning velocity. A mixing rule based on the energy fraction has been used to calculate the composition of a mixture of iso-octane, n-heptane and toluene that could represent the laminar burning velocity of the gasoline studied. Based on the energy fraction mixing rule, it was found that a mixture of 1/3 iso-octane, 1/3 n-heptane and 1/3 toluene should be close to the laminar burning velocity of the gasoline. Measurements of this toluene reference fuel reproduced the laminar burning velocity of the gasoline very well. The measurements of different fuels have been compared to data from the literature and to simulations of kinetic models. The agreement with the measurements of Dirrenberger et al. (who used the same method to measure the laminar burning velocity) was very good. For the kinetic mechanisms, none of the models could reproduce the laminar burning velocity of all the fuels. Additionally, different mixing rules for the prediction of the laminar burning velocity of alcohol-hydrocarbon blends were validated. The energy fraction mixing rule, the mixing rule developed by Hirasawa et al. and Le Chatelier's rule based on energy fraction gave very good results, both for mixtures with methanol and ethanol. Le Chatelier's rule gave slightly better results for the ethanol blends while the energy fraction mixing rule gave better results for methanol blends. Mixing rules are not expected to be linear in the fuel blend composition, proven by the poor predictions of the mole fraction mixing rule. Keeping in mind the uncertainties of both the laminar burning velocity of the mixture and the laminar burning velocity of the pure fuels, it can be concluded that the three proposed mixing rules can be used in simulation models to calculate the laminar burning velocity with acceptable accuracy. However, further experimental validation is needed at higher temperatures and pressures.

6

Quasi-dimensional simulation model

6.1 Introduction

The aim of the current study is to develop a predictive quasi-dimensional simulation tool for parameter studies and optimization of spark-ignition engines fuelled with alcohol-gasoline blends. Quasi-dimensional (QD) models are characterized by a predictive expression for the mass burning rate and the inclusion of geometrical parameters in the form of a thin, spherical flame front interface separating burned from the unburned gases [152].

Based on the ratio of chemical to turbulent time or length scales, different regimes can be distinguished in turbulent premixed combustion [153]. Vancoillie [28] used a flame regime diagram to identify the effects of the different properties of light alcohols on the turbulent combustion and concluded that the flamelet-like behavior is predominant for engines fuelled with pure methanol, ethanol or gasoline. As a result, turbulent burning velocity models that assume flamelet behavior to be valid will thus be used in the simulation framework for the entire range of operating conditions and alcohol-gasoline blends.

The following Sections describe how the simulation code is integrated in a commercial gas dynamics software to simulate the open part of the engine cycle.

Next, the global model structure and governing equations as well as various submodels are discussed. Finally, several laminar burning velocity (u_l) and turbulent burning velocity (u_t) correlations are implemented and tested in the QD code for measurements done on two different engines: the CFR engine with port fuel injection and the Hyundai GDI engine with direct injection.

6.2 Predictive model for the power cycle

6.2.1 The GUEST code

The main goal is to develop an engine simulation tool for alcohol-gasoline blends. The employed code builds on a QD simulation tool developed within the Transport Technology research group within the author's department: the Ghent University Engine Simulation Tool or GUEST code.

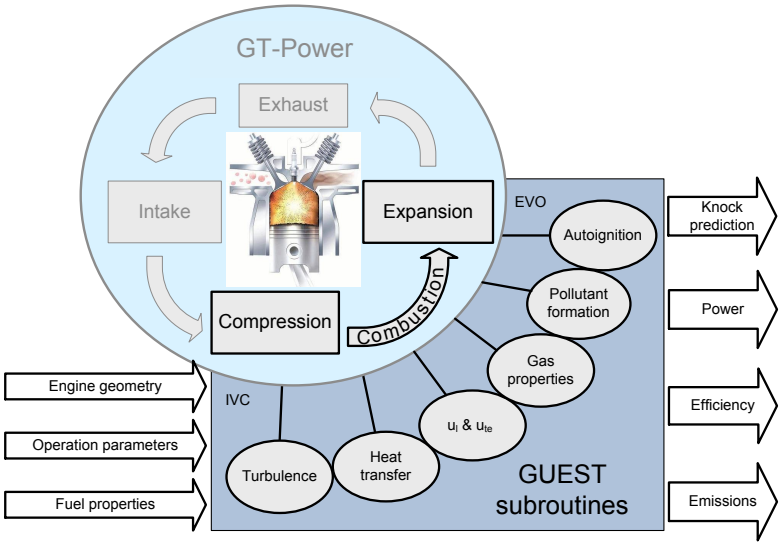

Figure 6.1: Schematic overview of the integration of GUEST (Ghent University Engine Simulation Tool) and GT-Power

Originally, the GUEST code is a simulation code for the closed part of the engine cycle, inspired by a complete cycle model developed by Vandevoorde [154] and Ph.D. research devoted to the ignition process and the earliest stages of combustion [155]. The GUEST code was further developed as an engine simulation tool for the power cycle of hydrogen-fuelled SI engines in the Ph.D. study of Verhelst [27] and for (m)ethanol-fuelled SI engines in the Ph.D. study of Vancoillie [28]. In the Ph.D. study of Vancoillie [28], the burning velocity routines forming the core of GUEST were integrated within the commercial engine performance simulation software GT-Power [135], as shown in Figure 6.1. This software is part of GT-SUITE, which is one of the leading engine and vehicle simulation tools. This was done because the GUEST code had some shortcomings, the most important being the lack of an accurate estimation for trapped conditions. An accurate

estimation of the trapped conditions could be made with the gas dynamics routines in GT-Power, which are based on 1D fluid dynamics representing flow and heat transfer in piping and other flow components of the engine system (e.g. valves, manifolds, turbines, resonators). Vancoillie [28] integrated the GUEST code into the GT-Power software using the user routines. These can substitute the default GT-Power models for certain parts of the simulation (e.g. computation of wall heat transfer computation, laminar burning velocity, etc.). User subroutines are placed in a separate Fortran library that is called whenever necessary. Within the current work, the GUEST subroutines for turbulence, laminar and turbulent burning velocity have been integrated as user subroutines. The gas property libraries of GT-Power have been supplemented with data for methanol and ethanol.

Some restrictions of the integration of the GUEST code in GT-Power are pointed out by Vancoillie [28]: the user is bound to the entrainment framework as implemented in GT-Power with no direct control of the way τ_b is calculated (see 6.2.3) and blowby can only be modeled by removing a certain amount of mass in equal proportions from the burned and the unburned zone. The external cylinder model feature in GT-Power can solve most of these restrictions. When using the external cylinder model, the user has to program every submodel and has, as a result, complete control over the combustion, heat transfer, energy equations, mass and species conservation.

6.2.2 Assumptions and governing equations

To simplify the energy conservation equations during the power cycle, some basic assumptions are used, common to most QD engine models [152, 156]. The assumptions made in the GUEST code were already explained in [27] and [28] and are repeated here for the clarity of the text.

- All gases behave as ideal, but not perfect gases i.e. the specific heat capacities are temperature dependent.
- During the entire cycle, the pressure in the cylinder is uniform.
- During compression and expansion the temperature and gas composition are uniform throughout the cylinder.
- During combustion, separate, uniform temperatures and gas compositions are assumed for the unburned and burned zone.
- The burned and unburned zones are separated by an infinitely thin (spherical) flame front with the origin at the spark plug.

- There is no heat exchange between the burned and unburned zone.
- Unburned gas is assumed to have a fixed composition.
- Burned gas composition is maintained in chemical equilibrium.

The basic equation for the engine model is derived from the conservation of energy applied to the cylinder volume:

$$dE = -\delta Q - \delta W + \sum_i h_i dm_i \tag{6.1}$$

Here, E is the internal energy of the cylinder gas mixture, Q the heat exchange of the cylinder contents with the environment (walls) where $Q > 0$ for heat loss from gas to wall, W the work where $W > 0$ for work delivered by the cylinder charge, h_i the specific enthalpy of in- or outflowing gas, and dm_i the mass flow into (+) or out of (−) the cylinder. The work δW can be expressed as $p\,dV$, where p is the pressure and V the cylinder volume. Using the assumptions stated above, Equation 6.1 can be further simplified to the expressions for the rate of temperature and pressure change [27, 28].

In the following Sections, the sub-models used in the simulation framework will be explained.

6.2.3 Mass burning rate

Fully developed turbulent combustion

The turbulent combustion model used in this work is based on the entrainment framework. In the entrainment models, there is a combustion process consisting of the entrainment into the flame front, with a velocity u_e, of turbulent eddies of characteristic size l_e. These eddies then burn inwards from the peripheral ignition sites to be consumed in a time $\tau = l_e/u_l$. This can be expressed as follows:

- first, unburned mass is entrained at a rate $\dot{m}_e$ given by

$$\dot{m}_e = \rho_u A_f u_{te} \tag{6.2}$$

  where A_f is the mean flame front surface area, $\dot{m}_e$ is the entrained mass and u_{te} is the turbulent entrainment velocity.

- then, the mass entrained into the flame front is supposed to burn with a rate proportional to the mass of entrained unburned gas, with a time constant τ_b:

$$\dot{m}_b = \frac{m_e - m_b}{\tau_b} \tag{6.3}$$

  where m_b is the mass of burned gas.

These entrainment equations form the basis of a lot of combustion models (e.g. [27, 157–160]) with differences arising from the choice of l_e and u_e [27].

In GT-Power the burn-up is postulated to take place at the laminar burning velocity over a length scale typical of the microscale of turbulence, the Taylor microscale λ_T [135]. Therefore, the time constant τ_b related to the combustion of entrained mass is given by:

$$\tau_b = \frac{\lambda_T}{u_l} \tag{6.4}$$

The laminar burning velocity u_l is computed using correlations which are a function of fuel, ϕ, temperature, pressure and the amount of residual gases/EGR. Correlations for gasoline and methanol will be discussed in Section 6.3.2. Assuming isotropic turbulence, the Taylor microscale λ_T can be calculated from Λ and Re_t, using a calibration constant C_3 to relate the Taylor microscale to the integral scale:

$$\lambda_T = \frac{C_3 \Lambda}{\sqrt{Re_t}} \tag{6.5}$$

$$Re_t = \frac{u' \Lambda}{\nu_u} \tag{6.6}$$

As mentioned by Verhelst [27], the entrainment framework is used as a mathematical representation of the effects of a finite turbulent flame thickness δ_t. The turbulent entrainment velocity u_{te} from Equation 6.2 is obtained from the turbulent burning velocity correlations described in Section 6.3.1.

Turbulent flame development

Turbulent combustion initially proceeds in a quasi-laminar fashion. When the flame kernel becomes larger than the smallest turbulent eddy, the flame front will

be wrinkled. Subsequently, the flame front will gradually become more wrinkled as it experiences a growing spectrum of turbulent length scales.

Most turbulent combustion models need an explicit expression to relate the developing turbulent burning velocity u_{tk} to the fully developed value u_t. Verhelst [27] identified several flame development models in the literature [161–164]. However, none of these flame development models take fuel properties into account. Therefore, the standard flame development model in GT-Power has been used for most of the simulations. This model takes some fuel properties into account by using the flame thickness (here defined as the ratio of the burned mixture kinematic viscosity and the laminar burning velocity) and a stretch factor H. This flame development model was developed by Wahiduzzaman et al. [159] and is in fact an extended version of the model proposed by Morel et al. [165]. Until the turbulent combustion is fully developed, the developing turbulent burning velocity u_{tk} is used instead and expressed as:

$$u_{tk} = u_t \left(1 - \frac{1}{1 + C_k \frac{r_f^2}{\Lambda^2}} \right) \tag{6.7}$$

with C_k a calibration factor, r_f the flame radius and Λ the integral turbulent length scale. In the model of Morel et al. [165], C_k is just a constant (= calibration constant for the flame development C_1) while in the extended version proposed by Wahiduzzaman et al. [159] C_k is equal to:

$$C_k = \frac{C_1}{1 + 6H} \left(1 - e^{-4.81 r^2} \right) (1.228 + 0.385 r) \tag{6.8}$$

In Equation 6.8, r is the ratio of turbulence length scale to flame thickness, H is a stretch factor and C_1 is again a calibration constant for the flame development. The stretch factor H is a function of the flame thickness, the laminar burning velocity and the burned and unburned mixture density. More information can be found in Wahiduzzaman et al. [159].

Ignition

The ignition of the cylinder charge is usually not modelled in detail. The ignition kernel, which initialises the start of combustion at or shortly after the ignition timing, is often ascribed a certain mass or volume as discussed in a review by Verhelst and Sheppard [152].

In this study, the diameter of the initial flame kernel was assumed to be $1mm$ at the time of ignition as a starting point: $2r_f = 1mm$. This diameter is comparable with the spark gap width. As the ignition process is dependent on local parameters around the spark plug [166] such initialisation is quite arbitrary. As a result, in a later stage, this initial flame kernel will be adjusted/calibrated depending on the fuel.

6.2.4 Heat transfer

In Equation 6.1, the instantaneous heat transfer between the cylinder charge and combustion chamber walls is needed. The instantaneous heat transfer in SI engines can be expressed as [55]:

$$\frac{\mathrm{d}Q}{\mathrm{d}t} = hA(T - T_{wall}) \tag{6.9}$$

Where h is the average convection coefficient, A is the wall surface area, T is the bulk gas temperature and T_{wall} is the wall temperature averaged over the heat transfer surface. The heat loss due to radiation is assumed to be negligible. In GT-Power, Equation 6.9 is solved separately for the burned and unburned gas zone. Also, different wall temperatures can be set for the piston, head and liner surfaces.

A good overview of the different models for evaluating the heat transfer coefficient h and associated assumptions can be found in the Ph.D. study of Demuynck [55]. In GT-Power, various models are implemented including the flow heat transfer model of Morel et al. [167], the model of Hohenberg et al. [168] and several variations on the Woschni correlation [169].

In his Ph.D. thesis on the development of a fuel-independent heat transfer correlation, Demuynck investigated the performance of existing heat transfer models for methanol-fuelled engines [55]. This work showed that, if properly calibrated, the Woschni correlation could accurately reproduce the heat flux trace at a certain operating point. Throughout this work, the Woschni model which was already implemented in GT-Power was employed. The assumptions for gas properties used by Woschni are strictly only valid for air, but have been confirmed by Demuynck to lead to negligible errors for methanol-air mixtures [55]. More information on the Woschni model can be found in [55].

6.2.5 Turbulence

In QD models, a turbulence sub-model is used to provide data characterizing in-cylinder turbulence, usually rms turbulent velocity u' and integral length scale

Λ. Defining and measuring turbulence in engines is not straightforward due to cyclic variations and bulk flow movements such as swirl, tumble and squish [27, 156].

Turbulence model used for the CFR engine

An empirical turbulence model was implemented in the code for simulations of the CFR engine, see Section 6.5. This model was based on measurements of the turbulent flow field in a CFR engine performed by Lancaster [170]:

- The integral length scale is assumed constant and equal to one-fifth of the TDC clearance height h_{TDC}.

$$\Lambda = \frac{1}{5} h_{TDC} \tag{6.10}$$

- u' linearly decreases with crank angle according to:

$$u' = u'_{TDC}\left(1 - 0.5\frac{\theta - 360}{45}\right) \tag{6.11}$$

  Where u'_{TDC} is the rms turbulent velocity at TDC, taken to be 0.75 times the mean piston speed. θ is the crank angle (360 at TDC of compression).

GT-Power turbulence model

Because no measurements of the turbulence flow field could be done on the Hyundai engine and no measurements were reported in literature as was the case for the CFR engine [170], it was decided to use the default turbulence model in GT-Power for simulations of the Hyundai GDI engine, see Section 6.6. This model is based on the in-cylinder flow model proposed by Morel et al. [167]. In this model the combustion chamber is divided in the 4 flow regions defined in Figure 6.2: the center, head, piston cup and squish region. u' and Λ are modeled in each region by a $k-\varepsilon$ model. More information about this model can be found in [167].

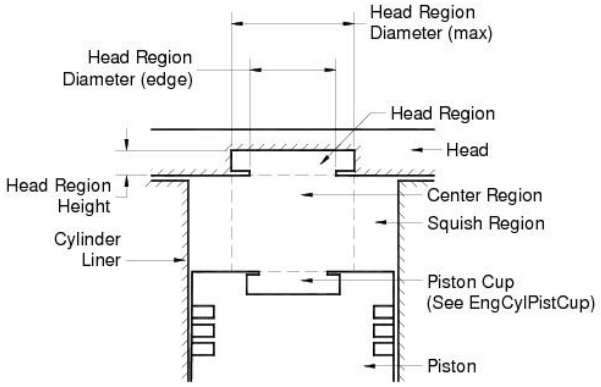

Figure 6.2: Flow regions in the turbulence model of GT-Power [135]

6.2.6 Direct injection

Vancoillie [28] pointed out that, when extending the code to direct-injection, the following three physical phenomena could be important to take into account in the simulation framework: fuel impingement on the wall, turbulence generation by injection, and mixture inhomogeneity.

Marriott et al. [171] reported that a description of cylinder wall wetting and subsequent fuel evaporation is particularly important for fuels with a high latent heat of vaporization such as light alcohols in order to not overestimate the volumetric efficiency. It was indeed found necessary to use an evaporation model for the simulations of the Hyundai GDI engine, see Section 6.6.1.

Fuel injection will influence the in-cylinder bulk flow movements and turbulence. The $k-\varepsilon$ formulation of GT-Power takes this into account by considering the kinetic energy generation by injection [135].

Finally, late injection in DISI engines can lead to mixture stratification. Changes in the laminar burning velocity associated with inhomogeneous fuel-air equivalence ratio ϕ will, among others things, change the combustion rate. A radial distribution of the entrained equivalence ratio [135], an averaged u_l based on a normal ϕ distribution [172] or even a non-homogeneous distribution based on a spray model similar to diesel spray models [173] are proposed to handle mixture inhomogeneity. However, no measurements with late injection with the purpose of mixture stratification have been performed during this study, so no model was implemented in the GUEST code to deal with mixture inhomogeneity.

6.3 Turbulent and laminar burning velocity implementation

As explained in Section 6.2.3, expressions for the turbulent burning velocity and the laminar burning velocity are necessary to close all the equations in the simulation framework. In the next Sections, several models for the turbulent combustion will be explained and the choice to develop new correlations for the laminar burning velocity of gasoline and methanol will be motivated.

6.3.1 Turbulent burning velocity models

Numerous models and correlations exist to predict the turbulent burning velocity and unfortunately no single model has emerged as the most accurate or most widely applicable. In the Ph.D. research of Verhelst [27] and Vancoillie [28], a selection was made of models that have been widely demonstrated and used in simulation of SI engines or other combustion applications. Based on the results of Verhelst [27] and Vancoillie [28], three models have been selected to be used in this study: the Damköhler model, the model of Bradley et al. [161] and the model of Zimont/Lipatnikov [164, 174]. A description of these models is repeated here for clarity.

Damköhler and derivatives

A large number of models assume the sole effect of turbulence to be flame front wrinkling leading to an increased flame area. Thus, the burning velocity ratio u_t/u_l is assumed to be equal to the flame surface area ratio A_t/A_l, where A_t is the wrinkled surface area and A_l is the mean, smooth flame surface area. Damköhler related this area ratio to the rms turbulent velocity divided by the laminar burning velocity:

$$\frac{A_t}{A_l} \sim \frac{u'}{u_l} \Rightarrow u_t \sim u' \tag{6.12}$$

This expression is claimed to be valid for large u'/u_l. In many engine models the expression is changed to $u_t \sim u' + u_l$ to recover the laminar burning velocity when $u' \to 0$.

Bradley et al.

Bradley et al. collected all known experimental values of turbulent burning velocities and searched for correlations on a theoretical basis using dimensionless terms describing the data set [161]. They developed a correlation in terms of the Lewis number Le and the Karlovitz stretch factor Ka, representing the dimensionless flow field strain.

$$u_t/u' = 0.88(KaLe)^{-0.3} \tag{6.13}$$

where Ka was taken as $Ka = 0.157(u'/u_l)^2 Re_t^{-0.5}$. The dependence of u_t/u' on the product $KaLe$ originated from the consideration of the effect of flame stretch on u_t, starting from the linear relation between flame speed and flame stretch for the local laminar flame (Eq. A.5 in Appendix A.2.1). More recently Bradley et al. [175] developed a correlation for u_t/u' as a function of the Karlovitz stretch factor Ka and the Markstein number Ma based on spherical explosions and twin kernel implosions in a fan-stirred bomb of ethanol-air mixtures for a wide range of ϕ, p and u'.

The correlation was recently further validated using measurements of seven different fuels [176, 177]. Compared to the $KaLe$ correlation (Eq. 6.13), the new correlation fits the dataset better, but is less easily implemented in an engine code due to the lack of data for Markstein numbers Ma at engine-like conditions. It might be interesting to develop a correlation for Ma for use in engine cycle simulation, but for now, Equation 6.13 will be used.

Figure 6.3 compares the Lewis number of methanol-air, ethanol-air, iso-octane-air and methane-air mixtures at 5 bar and 350 K. Iso-octane was used to represent gasoline. For mixtures with $\lambda < 0.9$ and $\lambda > 1.1$, the Lewis number Le is calculated by taking the mass diffusivity of the deficient reactant in nitrogen using the expression of Fuller et al. in [178] to simplify the calculation. Between 0.9 and 1.1, an interpolation was used as can be seen in Figure 6.3.

The deficient reactant is oxygen in rich conditions. For lean conditions this is the fuel. The Lewis number of rich mixtures of iso-octane, methanol and ethanol is less than unity, indicating thermo-diffusional instability (see Appendix A.2.2). Notice the big difference between the Lewis numbers of iso-octane and methanol/ethanol for lean mixtures due to the bulkier molecule of iso-octane.

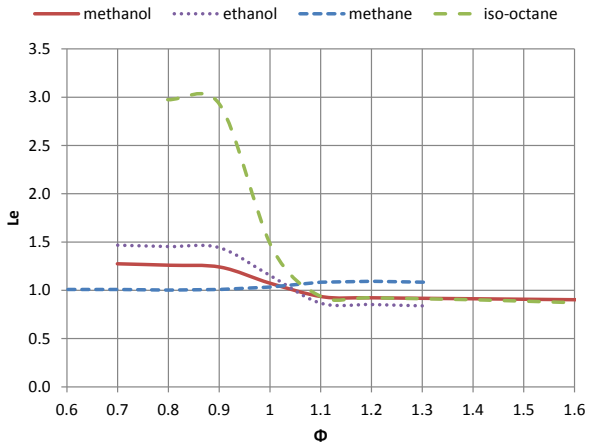

Figure 6.3: Calculated Lewis numbers for various fuels at 0.5 MPa, 360 K. Rich methanol- and ethanol-air mixtures are thermo-diffusively unstable [179].

Zimont/Lipatnikov

Zimont proposed a method to calculate the turbulent combustion in multidimensional computations based on separately modeling the behavior of the mean flame brush thickness (mainly controlled by large scale eddies) and the mass burning rate (mainly controlled by small scale eddies) [164, 174]. This reflects the regime of intermediate steady flame propagation as relevant to many practical applications, characterized by an almost constant turbulent burning velocity and an increasing flame width [174].

Lipatnikov and Chomiak comprehensively reviewed and validated the model and show substantial experimental evidence for the regime of growing flame brush thickness [164].

For the turbulent burning velocity u_t, Zimont suggested the following model:

$$u_t = Au' Da^{1/4} = Au' \left(\frac{\Lambda}{u' \tau_l} \right)^{1/4} \tag{6.14}$$

where τ_l is a chemical time scale and A is a calibration constant with a suggested value of 0.5. The chemical time scale is based on the laminar flame thickness, using the molecular heat diffusivity D_t as the relevant diffusivity: $\tau_l = \delta_l / u_l = D_t / u_l^2$. The extended model of Lipatnikov and Chomiak with this expression for

u_t has been validated against measurements in fan-stirred bombs, SI engines and several experimental databases [164].

Model implementation

The turbulent burning velocity models are slightly adapted for use in the engine cycle code. This adaptation includes a term u_n to ensure the stretched laminar burning velocity u_n appears when $u' \to 0$ and a calibration factor C_2. Stretched laminar burning velocity data of air-fuel mixtures at the instantaneous pressure and temperature imply the need for either a library of stretched flamelets or a model for the effect of stretch. As of today, there are insufficient data on stretch-free burning velocities at engine conditions, for any fuel. No stretch model has been implemented in the code as of yet and correlations for the unstretched laminar burning velocity are used, partly because of a lack of reliable data regarding the effect of stretch on alcohol-gasoline flames at engine-like conditions. In the following formulations, u_n is thus equal to u_l.

- Damköhler:
$$u_t = C_2 u' + u_n \tag{6.15}$$
- Bradley $KaLe$:
$$u_t = 0.88 C_2 u' (KaLe)^{-0.3} + u_n \tag{6.16}$$
- Zimont:
$$u_t = C_2 u' Da^{1/4} + u_n \tag{6.17}$$

6.3.2 Laminar burning velocity correlations

A convenient way to implement laminar burning velocity data in a quasi-dimensional engine cycle code is by using a correlation which gives the laminar burning velocity in terms of pressure, temperature and composition of the unburned mixture. If the effect of fuel blend composition or the effect of additional components has to be determined, it would be useful to have simple mixing rules that can predict the laminar burning velocity of the blends out of the correlations of the pure fuels with a good accuracy and without being computationally too demanding, see Section 5.2.

For this study, it was decided that the laminar burning velocity correlation of gasoline as well as of methanol should be derived from the same source to be able

to compare the influence of temperature, pressure and diluent factors of the two correlations. Therefore two new correlations were developed. Both the laminar burning velocities of methanol and gasoline have been determined using the heat flux method on a flat flame adiabatic burner, discussed in Section 5.6. The same gasoline, that was used during the laminar burning velocity measurements on the flat flame burner, was used for the experiments on the CFR engine (Section 6.5) which are used as data for the validation of the combustion model. The same gasoline could not be sent to Argonne National Laboratory in Chicago, USA. Therefore, a certification gasoline (gasoline EEE of Haltermann Solutions) was used for the experiments on the Hyundai GDI engine (Section 6.6). The form of the developed correlation is given by:

$$u_l = u_{l0}\left(\frac{T_u}{T_0}\right)^{\alpha}\left(\frac{p}{p_0}\right)^{\beta}(1-\gamma f) \tag{6.18}$$

Where u_{l0} and α are third order polynomials of ϕ fitted to the measurements done on the flat flame adiabatic burner. Because the difference in pressure and EGR dependency of the laminar burning velocity of methanol and gasoline have not been studied in detail recently, it was decided to take the same expression for β and γ for both the correlations. The difference between the pressure and EGR dependency of methanol and gasoline (or iso-octane in many cases) reported in several sources in literature could be the result of faulty measurements, e.g. Gülder did not take flame stretch and instabilities into account [137]. As a result, β is a first order function of ϕ taken from the recent study performed by Galmiche et al. [90] in which the pressure dependency of iso-octane was investigated and γ is a constant equal to 2.1 based on the measurements of Metghalchi and Keck [85] and found in many laminar burning velocity correlations. For both methanol and gasoline, the same expression is taken for β:

$$\beta = -0.24 + 0.27(\phi - 1.07) \tag{6.19}$$

For methanol, u_{l0} and α are given by:

$$u_{l0} = -70.58 + 127\phi + 34.85\phi^2 - 50.48\phi^3 \tag{6.20}$$

$$\alpha = 10.78 - 21.36\phi + 15.94\phi^2 - 3.78\phi^3 \tag{6.21}$$

and for gasoline:

$$u_{l0} = 7.32 - 94.40\phi + 240.46\phi^2 - 119.33\phi^3 \tag{6.22}$$

$$\alpha = 1.26 + 7.21\phi - 11.8\phi^2 + 5.03\phi^3 \tag{6.23}$$

These correlations are validated for an equivalence ratio from 0.7 to 1.3 for gasoline and from 0.7 to 1.5 for methanol. The reference conditions in Equation 6.18 are $p_0 = 1bar$ and $T_0 = 298K$. Several other correlations of methanol and gasoline have been implemented to compare to the newly developed correlations. More information about these correlations will be given in the concerning Sections.

6.4 Model build-up

6.4.1 Three Pressure Analysis and stand-alone cylinder model

As the main focus of the current work was to evaluate the combustion model, the employed engine model is limited to the closed part of the engine cycle (IVC to EVO). To validate the engine model for the closed part of the cycle, the 'cyl' and 'engine' templates of GT-Power were used to construct a stand-alone cylinder model (see Figure 6.4).

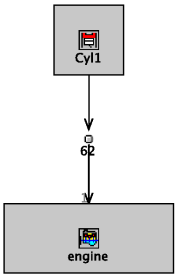

Figure 6.4: Stand-alone cylinder model for power cycle simulation in GT-Power

In order to be able to validate such a stand-alone cylinder model for a specific engine, beside the engine geometry, the operating conditions (engine speed, spark timing, equivalence ratio, etc.), surface temperatures, the trapped conditions and initial turbulence conditions are needed. Estimations of the surface temperatures of cylinder head, liner and piston are needed for the wall heat transfer calculation. Values recommended in the GT-Power manual [135] are used for these temperatures. Regarding the trapped conditions, the initial conditions for mass fractions of air and fuel are obtained from the air and fuel flow measurements. On the other hand, the level of internal EGR as well as the initial turbulence conditions have to be calculated using a Three Pressure Analysis (TPA) in the GT-Power software before the stand-alone cylinder model can be used to perform predictive calculations. To perform a TPA in GT-Power, three different pressure measurements are required from the cylinder of interest. Two of these measurements are port pressures (intake and exhaust) and the third is cylinder pressure. The main purpose of this type of simulation is to analyze the measurements in order to obtain a single combustion burn rate for each operating condition. This 'experimental' burn rate is required to calibrate the predictive combustion model and can be used to compare the simulations with the experimental burn rates.

A TPA starts with performing a 'reverse run' using the same QD framework and submodels as discussed earlier, where the cylinder pressure is input and the mass burning rate output. In a reverse run, the amount of fuel that is transferred from unburned to burned zone is iterated within each time step to make the cylinder pressure match the measured value. This TPA also enables some input data consistency checks. These include measures such as cumulative burn rate during compression, unrealistic temperature at IVC, pressure trace smoothness and the lower heating value (LHV) multiplier.

The LHV multiplier is perhaps the single most important consistency measure. During a burn rate analysis, there will always be some cumulative error causing the predicted total amount of burned fuel to differ from the real available fuel mass in the cylinder. The LHV multiplier is defined as:

$$\text{LHV multiplier} = \frac{\text{predicted total burned fuel mass}}{\text{experimental total burned fuel mass}} \tag{6.24}$$

It represents the ratio by which the fuel LHV should be adjusted so that the predicted cumulative energy matches the fuel energy when performing an in-cylinder energy balance. The model can be tuned (heat transfer multipliers, evaporation model for DI engines) in order to have the LHV multiplier close to 1 ($+/-5\%$) and similar volumetric efficiencies, intake and exhaust temperatures as measured.

6.4.2 Calibration of the predictive model

Before the code can be used to simulate a certain engine, a single set of calibration constants must be determined for the heat transfer, flame development (C_1 in Eqs. 6.7 or 6.8) and turbulent combustion model (C_2, C_3 in Eqs. 6.15, 6.16, 6.17 and 6.5). The heat transfer multipliers are calibrated for all simulations during the Three Pressure Analysis, based on correspondence between the measured and predicted cylinder pressure, the exhaust and inlet temperatures and the volumetric efficiency. For the simulations on the CFR engine (see Section 6.5), the heat transfer multiplier has a separate value during compression, combustion and expansion similar to what was done by Vancoillie [28] in order to match the pressure trace accurately and to get an S-shaped burn rate profile. For the simulations done on the Hyundai GDI engine (see Section 6.6), a single value for the heat transfer multiplier has been used, as is proposed by GT-Power [135].

The calibration factors of the combustion model (C_1, C_2 and C_3) are calibrated using the predictive combustion model and cannot be calibrated independently.

For example, the C_1 cannot be simply calibrated against measured ignition delay, because the flame development model will also affect the main combustion duration. The flame development constant C_1 is usually calibrated first in order to get a reasonable correspondence for the ignition delay. Secondly, C_2 and C_3 are adjusted simultaneously in order to get a reasonable agreement with the experimental burn rate. Increasing C_2 increases the mass entrainment rate, while increasing coefficient C_3 decreases the mass burning rate by lengthening the burn-up time. Finally, the three constants of the predictive combustion models are simultaneously optimized by minimizing the root mean square error (RMSE) between the measured and predicted normalized burn rate using the Direct Optimizer embedded in GT-Power [135].

6.5 Validation of simulation model on the CFR engine

As a first step to analyze the combustion model's predictive capabilities on alcohol-gasoline blends, a series of measurements were done on the port fuel injected single cylinder CFR engine, described in Section 3.2.1. The main characteristics of this engine are summarized in Table 3.1. The measurements comprise variable fuel/air equivalence ratio ϕ and methanol-gasoline ratios. Measurements were done for M0, M20, M40, M60, M80 and M100 at lambda equal to 1, 1.2 and 0.8. Ignition timing was fixed at 12° BTDC, the compression ratio was fixed at 7 and the throttle was turned open with 10° resulting in an IMEP range from 5.68 to 7 bar with a maximum difference of 0.4 bar IMEP between gasoline and methanol for the operating points with lambda equal to 1.2. The compression ratio was chosen very low because the gasoline used for the engine measurements (Exxon 708629-60) was prone to knock. In order to allow an accurate comparison, all measurements were performed on the same day and all parameters were fixed except for the injection duration and the fuel composition. For each operation point, three measurements were done. First the engine was set to a fixed value and the first measurement was done when all the measured values such as exhaust temperature, oil temperature, air flow, etc. did not change anymore. Then, with an interval of a few minutes, a second and third measurement was done. The values shown on the Figures are the mean values of the three measurements. The errors bars used in the Figures are two times the standard deviation of the three measurements to give an idea on the spread of the different measurements.

In the literature, a lot of different models for QD simulations of internal combustion engines can be found and a lot of new laminar burning velocity correlations, which become more and more complex, are being developed. However, the sensitivity of the added complexity of these new models and correlations is rarely tested. This is why the following procedure was taken in order to investigate the combustion model's predictive capabilities on alcohol-gasoline blends for the CFR engine:

1. A sensitivity analysis of the simulation model was done for the following parameters: the initial spark size, the residual gas fraction, the rms turbulent velocity u' and the integral turbulent length scale Λ.
    - The initial spark size was chosen because this determines the initial flame kernel. Using the same spark plug with the same ignition energy could result in a different initial flame kernel for different

fuels because of different fuel properties (ignition energy, flame temperature, burning velocity).

- The residual gas fraction was chosen because this is an input that is calculated with the Three Pressure Analysis as described in the previous section. This sensitivity analysis can give an idea of the accuracy which is needed from the gas dynamics model.
- Finally, the rms turbulent velocity u' and the integral turbulent length scale Λ were chosen because no experimental data was recorded for the turbulence in the engine. As a result, the combustion model relies on a turbulence model from the literature [170].

This sensitivity analysis was done to investigate if the uncertainties of these parameters do not outweigh the uncertainty on for example the laminar or turbulent burning velocity.

2. A comparison of different laminar burning velocity correlations of pure gasoline was performed. This was done in order to investigate how the newly developed correlation for gasoline (see Section 6.3.2) performs compared to other correlations for the laminar burning velocity of gasoline or iso-octane from the literature.

3. The effect of changing the laminar burning velocity correlation of methanol was investigated for methanol-gasoline blends using the mixing rule based on energy fraction. The pressure, temperature and residual gas fraction dependence of the laminar burning velocity of methanol has been changed to see the effect of the uncertainty on these factors found in laminar burning velocity correlations. In this way, it can be decided how accurate the behavior of the laminar burning velocity needs to be known for accurate predictions of the combustion in internal combustion engines.

4. Finally, the effect of different turbulent burning velocity models and the flame initialization has been investigated for the full range of methanol-gasoline blends.

For points 1, 2 and 3 explained above, the standard combustion model of GT-Power was used together with the newly developed laminar burning velocity correlations mentioned in Section 6.3.2. The standard combustion model in GT-Power is based on the combustion model of Damköhler extended with the flame development model of Wahiduzzaman et al. [159].

6.5.1 Sensitivity analysis of the simulation model.

In this section, four input parameters of the simulation model will be changed to investigate the sensitivity of the following output parameters to these inputs:

- ignition delay (ID): 0-2% mass fraction burned
- duration of 10-90% mass fraction burned (MFB10-90)
- 0-50% mass fraction burned (MFB50)
- maximum pressure (max P)
- crank angle between ignition and maximum pressure (0-ca max P)
- maximum temperature (max T)

These parameters were chosen because they are a good representation for the combustion and pressure trace. The following inputs will be changed:

- initial spark size (spark kernel diameter)
- the residual gas fraction
- rms turbulent velocity u'
- integral turbulent length scale Λ

The different parameters have been varied in a range that represents a possible variation due to uncertainty on their value (see Table 6.1).

Table 6.1: Parameter values for power cycle sensitivity analysis

Parameter	**Base value**	Δ
initial flame kernel radius	$0.5mm$	$+0.5mm$
$EGR\%$	$7-9\%$	$+3\%$
u'	$\sim 2m/s$	$+1m/s$
Λ	$\sim 0.0038m$	$+0.001m$

The sensitivity of the six parameters used in the previous section is expressed as follows:

$$Sensitivity = \frac{\frac{y(x_0)-y(x_0+\Delta x)}{y(x_0)}}{\frac{x_0-(x_0+\Delta x)}{x_0}} \tag{6.25}$$

A negative value means an opposite change of output y with respect to the varied input parameter x. Large absolute numbers mean a strong influence of this parameter. However, these numbers have to be interpreted carefully because large or small numbers for the initial x_0 could have a strong effect on the sensitivity value for the same relative change in y. For example if instead of the residual gas fraction, the percentage of fresh gases in the cylinder charge was used to investigate the influence of the ratio of residuals to fresh gases, the denominator of the sensitivity equation would be a lot smaller because the initial x_0 value would be bigger.

This sensitivity analysis was done for the stoichiometric, lean and rich operation points on gasoline. The laminar burning velocity was calculated with the new laminar burning velocity correlation and the calibration factors of the simulation model were optimized by minimizing the burn rate RMS error between the measurement at stoichiometry and the simulation. In the bar graphs in Figure 6.5, the sensitivity of the 6 output parameters is shown. As can be seen in Figure 6.5a, the flame kernel size has a big influence on the ID and less on the MFB10-90. Changing the initial flame kernel does not change the fully developed combustion (MFB10-90) significantly. A change in the ID only has a small effect on the MFB10-90 while triggering a similar (absolute) change in the MFB50. This will be shown later in this study (see Section 6.5.4) when the flame initialization will be used to control the ignition delay to be the same as the measured ignition delay. The second parameter that has been varied is the residual gas fraction. It has been increased with 3%. This has a significant effect on all the parameters presented here (see Figure 6.5b). As a result, the residual gas fraction has to be estimated as precisely as possible. That is why a Three Pressure Analysis in GT-Power has been used in this study to calculate the residual gas fraction in the cylinder for each measurement as accurately as possible. A good gas dynamics model is thus crucial for accurate prediction of the combustion process. Turbulence quantities for the CFR engine are calculated using a very simple turbulence model based on measurements done in a similar engine, see Section 6.2.5. The integral length scale Λ is kept constant at 1/5 of the minimum clearance height, and the rms turbulent velocity u' linearly decreases. Confirmation of this turbulence model was not possible during this study. Based on the fact that the study of the effects of engine variables on turbulence in the CFR engine dates back to 1976 [170], one can assume that there could be a significant difference between the simple model and the reality. A change in these parameters has a significant effect as can be

seen in Figure 6.5c and 6.5d. Notwithstanding this uncertainty, it is expected that this turbulence model can be used for the simulations of the CFR engine because throttle position, rpm and ignition timing remain the same for all measurements.

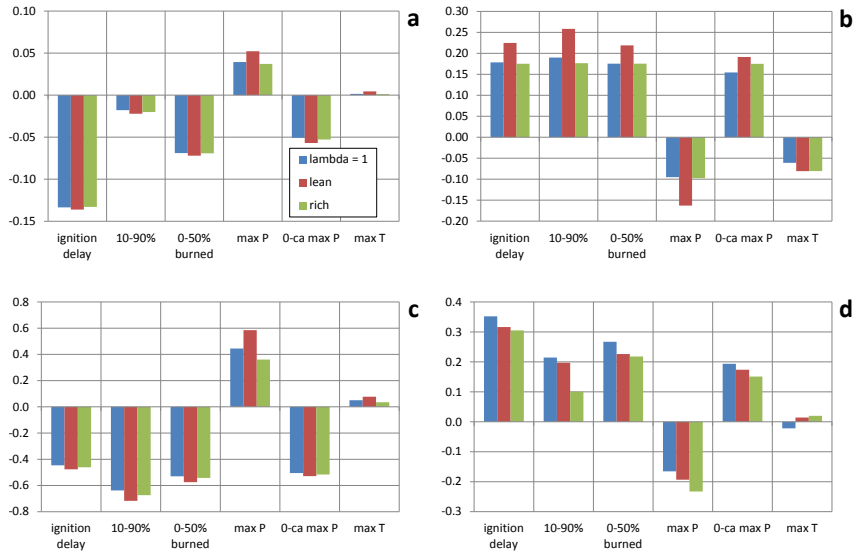

Figure 6.5: Sensitivity for a change of a: the initial kernel radius; b: the residual gas percentage; c: the rms turbulent velocity; d: the integral length scale.

6.5.2 Comparison of laminar burning velocity correlations of pure gasoline

A comparison of four different laminar burning velocity correlations of gasoline was made: the newly developed correlation based on the measurements on a flat flame burner, the standard laminar burning velocity correlation for gasoline in the simulation program GT-Power [135, 136], the correlation of Gülder [137] and the correlation of Metghalchi & Keck [85]. As there is no standard composition of gasoline, often correlations of surrogates of gasoline are used instead of a real gasoline e.g. the correlation of Gülder [137] is based on laminar burning velocity measurements of iso-octane.

The form of the four equations is the same:

$$u_l = u_{l0}\left(\frac{T_u}{T_0}\right)^{\alpha}\left(\frac{p}{p_0}\right)^{\beta}(1-\gamma f) \tag{6.26}$$

In each of the correlations, u_{l0}, α and β are different as shown in Table 6.2.

Table 6.2: u_{l0}, α and β of laminar burning velocity correlations for gasoline/iso-octane

Correlation	u_{l0}	α	β
Present	$7.32-94.40\phi+240.46\phi^2-119.33\phi^3$	$1.26+7.21\phi-11.8\phi^2+5.03\phi^3$	$-0.24+0.27(\phi-1.07)$
GT-Power	$0.35-0.549(\phi-1.1)^2$	$2.4-0.271\phi^{3.51}$	$-0.357+0.14\phi^{2.77}$
Gülder	$0.5924\phi^{-0.326}\exp(-4.48(\phi-1.075)^2)$	1.56	−0.22
Metghalchi & Keck	$0.01(27.58-78.34(\phi-1.13)^2$	$2.18-0.8(\phi-1)$	$-0.16+0.22(\phi-1)$

γ is a constant equal to 2.1. Only in the GT-Power correlation, the correction term to account for the residual gases is different. Instead of $(1-2.1f)$, the correction term is $(1-2.06f^{0.77})$. Additionally, a dilution exponent multiplier can be applied in GT-Power to adjust the value of 0.77 but this was never used during this study. Originally, the dependency of the residual gas fraction or EGR fraction was not present in the correlation of Gülder but this was added to the correlation for this study.

Figure 6.6 highlights the main differences between the different laminar burning velocity correlations as a function of equivalence ratio. It is clear from this Figure that the correlations for the laminar burning velocity of gasoline have different values for u_{l0}, α and β. As can be seen in Figure 6.6a, the GT-Power correlation has a flatter trend than the others and the correlation of Gülder in particular has higher values for the laminar burning velocity at $358K$ and $1bar$ than the newly developed correlation. Gülder measured the flame arrival time during contained explosions in a spherical vessel using flame ionization probes and derived the burning velocity from this without taking flame stretch and instabilities into consideration. This can be the cause of the higher laminar burning velocity values of the correlation of Gülder.

In Figure 6.6b, the power exponents α of the temperature dependency are compared. As explained in Section 5.6, the power exponent α has a minimum around the equivalence ratio of peak burning velocity which is covered by the newly developed correlation but not by one of the other correlations. The correlation of Metghalchi & Keck predicts a linear decrease of α as a function of the equivalence ratio whereas the correlation of Gülder does not include the effect of the equivalence ratio on the power exponent. The correlation of Gülder does not include the effect of the equivalence ratio on the power exponent β of the pressure dependency either as shown in Figure 6.6c. The other correlations include an increase of β as a function of the equivalence ratio. The biggest increase can be seen for the GT-power correlation.

For each correlation, the calibration factors of the simulation model were optimized by minimizing the burn rate RMS error between the measurement

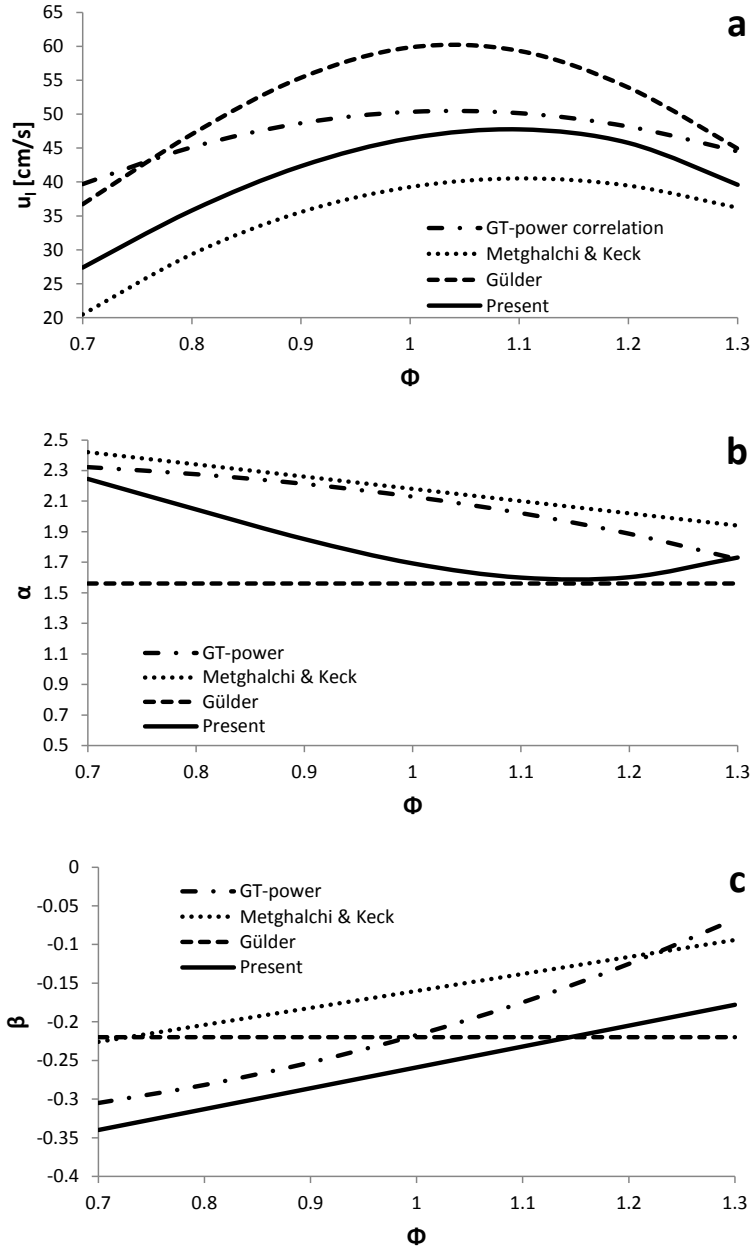

Figure 6.6: u_l (a), power exponent α (b) and power exponent β (c) as a function of ϕ as predicted by several correlations (1bar, 358K).

at stoichiometry and the simulation. In the bar graphs in Figure 6.7, the error between the simulations and the experimental measurements are shown for stoichiometric, lean and rich operation for the same 6 output parameters as in the previous section: the ignition delay (ID), duration of 10-90% mass fraction burned (MFB10-90), 0-50% mass fraction burned (MFB50), the maximum pressure (max P), crank angle between ignition and maximum pressure (0-ca max P) and the maximum temperature (max T). As can be seen on the bar graphs, none of the four correlations outperforms the others dramatically. Note that although it was calibrated for the stoichiometric operating point, the error of the ignition delay is rather high. Only for rich operation with the correlation of Gülder, the errors are clearly larger than when using the other correlations. This can be explained looking at the power exponents α and β of the laminar burning velocity correlations, in other words, the temperature and pressure dependence of the correlations (see Figure 6.6). The predictive model is calibrated for the engine running at an equivalence ratio equal to 1. Going from an equivalence ratio of 1 to 1.25 (lambda equal to 0.8), the power exponents α and β of the other correlations go more or less in the same direction (decrease for α and increase for β) resulting in lower laminar burning velocities than when they stay the same as is the case for the correlation of Gülder. This results in an additional overestimation of the burn rate when using the correlation of Gülder. The best agreements are obtained for the newly developed correlation and the standard correlation used in GT-Power. As can be seen on the graphs, the error on the ignition delay and 10-90% mass fraction burned has a significant influence on the maximum pressure and the crank angle between ignition and maximum pressure. E.g. the more these two burn rate parameters are underpredicted, the more the maximum pressure is overpredicted. We can conclude that in this framework the newly developed correlation performs equally or better than the older correlations. In the next sections this correlation will be used in conjunction with the newly developed correlation for methanol.

6.5.3 The effect of changing the pressure, temperature and residual gas fraction dependence of the laminar burning velocity correlation

In this section, the effect of changing several factors of the laminar burning velocity correlation of methanol will be investigated for methanol-gasoline blends. The pressure, temperature and residual gas fraction dependence of the laminar burning velocity of methanol has been changed to see how much the uncertainty on these factors found in laminar burning velocity correlations can influence the outcome of the simulations. This can show how accurately the behavior of the laminar burning velocity needs to be known for accurate predictions. With the

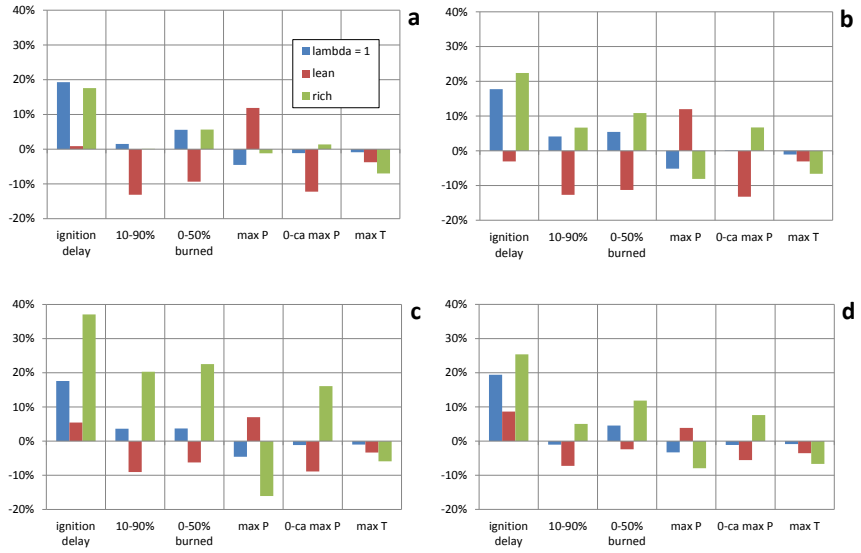

Figure 6.7: Simulation error with different laminar burning velocity correlations for gasoline. a: present correlation; b: correlation of GT-Power; c: correlation of Gülder; d: correlation of Metghalchi and Keck.

results from this study, further experimental needs for laminar burning velocity measurements can be formulated. To calculate the laminar burning velocity of methanol-gasoline blends, the mixing rule based on energy fraction has been used. As concluded from Section 5.6, this mixing rule gives very accurate predictions for the laminar burning velocity of methanol-gasoline blends.

The simulation model is again calibrated for stoichiometric operation on gasoline. The influence of the initial flame kernel and the residual gas fraction are again shown in this section, together with the effect of changing the temperature power exponent α, the pressure power exponent β and the value of the residual gas factor $(1-\gamma f)$ in the laminar burning velocity correlation of methanol. Only the correlation of methanol has been changed to see how this influences the outcome for methanol-gasoline blends. The influence of changing the parameters of the laminar burning velocity correlation of methanol should become clearer going from gasoline to pure methanol.

In Figure 6.8, 6.9 and 6.10, the results from the burn rate analysis of the Three Pressure Analysis in GT-Power are shown together with the predicted values for the stoichiometric, lean and rich operation points. On the same Figures, the results of the simulations are shown in which the parameters are changed as in Table 6.3.

Table 6.3: Parameter values for power cycle sensitivity analysis - gasoline-methanol blends

Parameter	**Base value**	Δ
initial flame kernel radius	$0.5mm$	$+0.5mm$
$EGR\%$	$7-9\%$	$+3\%$
α	see corr. MeOH (Eq. 6.18 and 6.21)	+0.07
β	see corr. MeOH (Eq. 6.18 and 6.19)	+0.05
$(1-\gamma f)$	see corr. MeOH (Eq. 6.18)	−0.03

The temperature dependence has been changed with 0.07 based on the experimental error of the measurements performed on the flat flame burner (see Section 5.6). Note that this change is very small compared to the differences seen between the temperature exponent α of other laminar burning velocity correlations of methanol and the current correlation. For example the difference between the temperature power exponent of the current correlation and the methanol correlation proposed by Metghalchi and Keck [85] is 0.6 at stoichiometry which is large compared to the value of 0.07 used in this study. The pressure and residual gas fraction dependence have been varied based on values of the pressure and residual gas fraction dependence seen in other existing correlations for the laminar burning velocity of methanol [121]. These changes are again conservative compared to some other correlations.

As can be seen in Figure 6.8a, for all blends the ignition delay at stoichiometric operation is overestimated by the predictive model when the model is calibrated by minimizing the burn rate RMS error of gasoline at stoichiometric operation. Secondly, the experimental ignition delay calculated with the Three Pressure Analysis decreases more than the predicted ignition delay when increasing the methanol concentration in the blend. As seen on the Figure, changing the initial flame kernel and residual gas fraction has a significant influence on the ignition delay. When changing the temperature, pressure or residual gas fraction dependency of the methanol laminar burning velocity correlation, the biggest change is seen for pure methanol, as expected. If all the parameters regarding the laminar burning velocity were changed at once, this could have a significant effect. E.g. with the change of the pressure dependence as was done in this study, the correct trend in the ignition delay could be reproduced. As a result, one of the reasons as to why the decrease of the experimental ignition delay with methanol addition cannot be predicted by the predictive model could be that the temperature, pressure or residual gas fraction dependencies of the laminar burning velocity correlations are not well captured for higher pressure and temperature as in internal combustion engines. Further research should help to decrease the

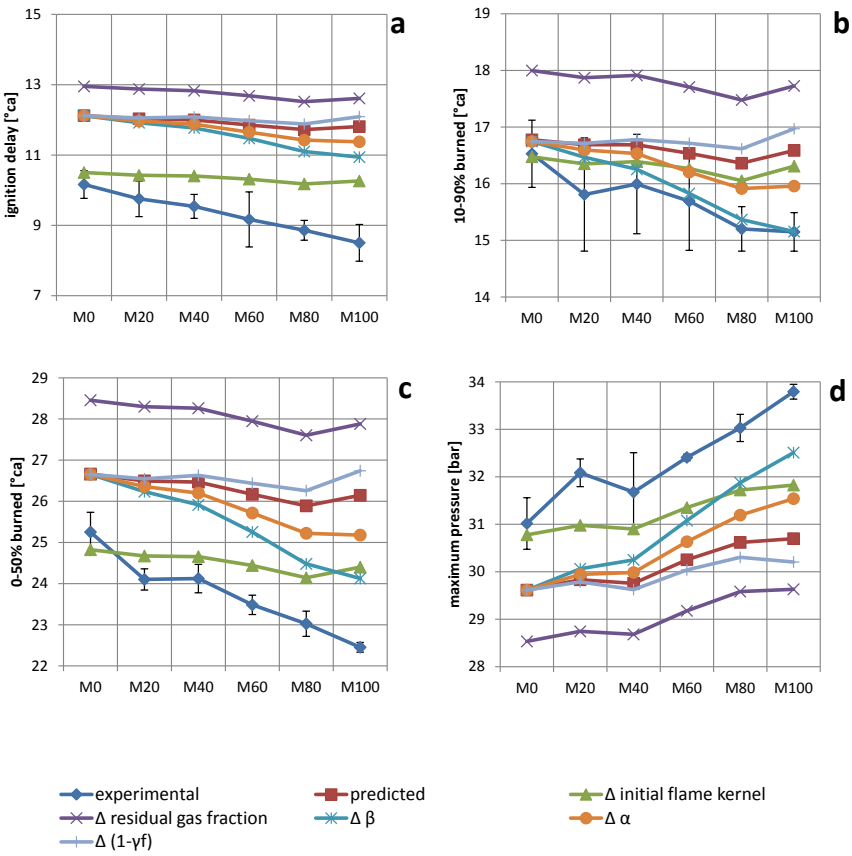

Figure 6.8: Ignition delay (a), 10-90% mass fraction burned (b), 0-50% mass fraction burned (c) and maximum pressure (d) of the stoichiometric mixtures.

uncertainty of these inputs. The biggest difference is seen when the pressure dependence is changed. The relative change of the pressure dependence is however bigger than the change done for the temperature dependence. The uncertainty on the temperature dependence was measured experimentally as described previously and is lower than the uncertainty on the pressure dependence which was taken from the comparison of different correlations. Another reason could be that the flame kernel growth model should be adapted for alcohol fuels. At last, there is still uncertainty about the initial flame kernel. In this simulation model, the initial flame kernel is defined by the spark size which had a 0.5 mm radius as starting point. As methanol has a lower minimal ignition energy and higher laminar burning velocity, one could assume that for the same ignition energy input, a larger value should be taken for the initial flame kernel for methanol in this simulation framework. This will be investigated in Section 6.5.4.

In Figure 6.8b, the $10-90\%$ mass fraction burned is shown for stoichiometric operation. As can be seen on the Figure, the predictive model overpredicts the burn rate by $1.5°ca$ for methanol while the prediction for gasoline is very good. The trend with increasing alcohol content is again not captured enough. There is again a significant change when the residual gas fraction is changed. The effect of changing the initial flame kernel is much smaller compared to the effect it had on the ignition delay. Due to the change in initial flame kernel, the ignition delay changes as in Figure 6.8a and this causes the small change in the 10-90% mass fraction burned because of slightly different temperatures and pressures throughout the flame propagation. As the flame is more and more developed and because the turbulence flow model does not change going from gasoline to methanol, the difference in burn rate between the fuels is mostly due to the difference in laminar burning velocity. The effect of changing the parameters of the methanol laminar burning velocity correlation can be seen in Figure 6.8b. The correct trend could again be reproduced by changing the parameters of the methanol correlation e.g. the pressure dependency in this case. Additionally, one should note that there exist turbulent burning velocity models that take fuel properties into account. This could also have an important influence when simulating the burn rate of fuel blends and will be investigated in Section 6.5.4.

In Figure 6.8c, the $0-50\%$ mass fraction burned is shown. The influence of the ignition delay on MFB50 can be seen in this Figure and the same conclusions can be drawn as for the ignition delay. The trend is again best captured in the case where the pressure dependency of the methanol laminar burning velocity correlation is tested. This can also be seen in the maximum pressure data, shown in Figure 6.8d.

For the lean mixtures (see Figure 6.9), more or less the same conclusions can be

drawn as for the stoichiometric mixtures. The model does not predict a decrease in ignition delay going from pure gasoline to pure methanol. Possible reasons are again uncertainty about the initial flame kernel and the laminar burning velocity at higher pressure and temperature or the inability of the turbulent combustion model to adequately capture the chemical effects. As a result, the ignition delay is overpredicted for blends with a high methanol content. For rich mixtures (see Figure 6.10a), the ignition delay is overpredicted for all the fuels used in this study but the decreasing trend is better captured. This could be explained by the fact that the developed laminar burning velocity correlations rely on the measured data of methanol and gasoline at atmospheric pressure. For rich mixtures, the difference in the measured laminar burning velocity on the flat flame adiabatic burner between methanol and gasoline is significantly larger than for lean or stoichiometric mixtures. Contrary to the lean and stoichiometric mixtures used in this study, the simulated laminar burning velocity of the rich mixtures increases significantly going from gasoline to methanol resulting in higher u_t values. Further research should investigate the laminar burning velocity at higher pressures and temperatures. The better prediction of the ignition delay for rich mixtures also results in a better prediction for the maximum pressure, as can be seen in Figure 6.10b.

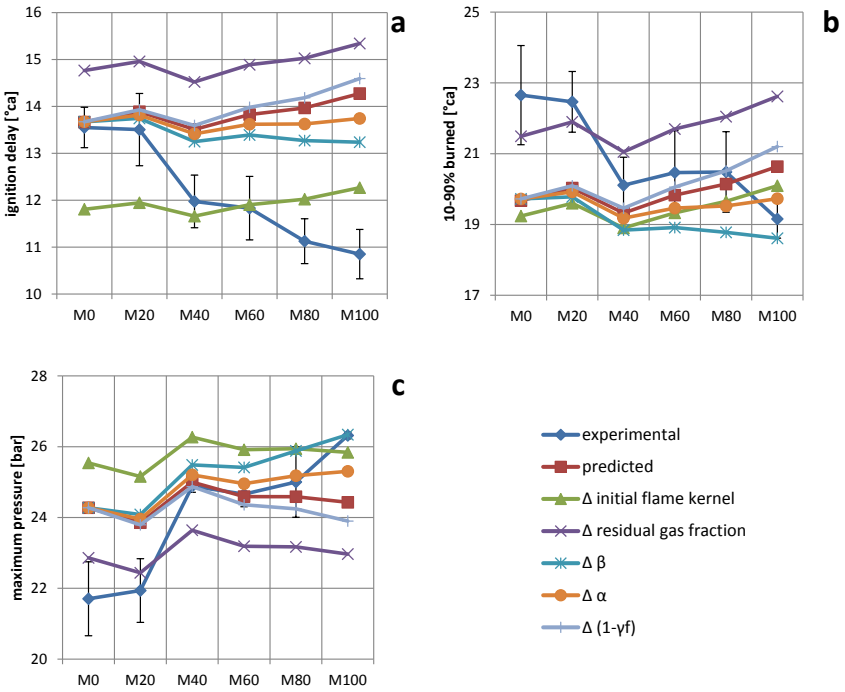

Figure 6.9: Ignition delay (a), 10-90% mass fraction burned (b) and maximum pressure (c) of the lean mixtures.

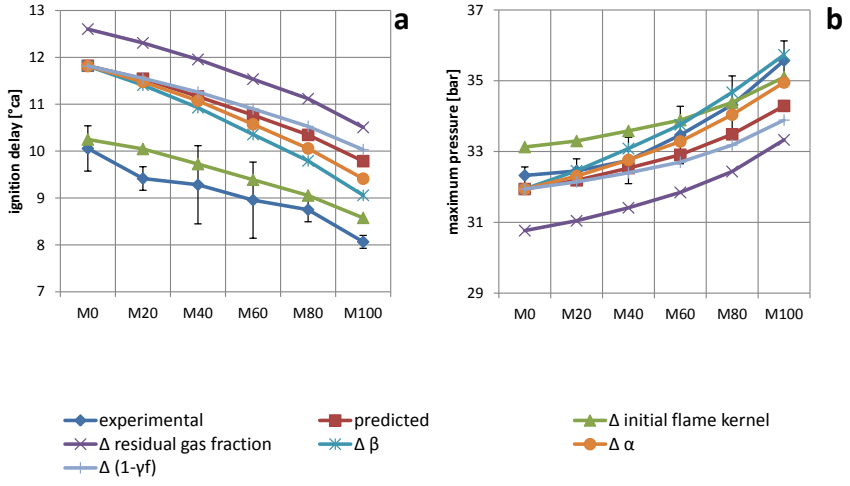

Figure 6.10: Ignition delay (a) and maximum pressure (b) of the rich mixtures.

6.5.4 Effect of the flame initialization and turbulent burning velocity model

Effect of the flame initialization

One of the conclusions of the previous section is that the trend of the ignition delay is not well predicted by the simulation model. In this section, it is investigated how the optimization of the ignition delay by tuning the initial flame kernel (= spark size) can influence the outcome of the simulation. The spark size/initial flame kernel is now seen as an additional calibration factor. First, the original calibration factors and the spark size are together optimized by minimizing the burn rate RMS error of the measurements on gasoline at stoichiometric operation and then for each measurement the spark size is changed to have the same ignition delay as in the measurements. In Figure 6.11, the spark size diameter is shown after optimization in order to simulate the same ignition delay as the experimental ignition delay. As expected from the previous sections, there is a steeper increase for stoichiometric and lean mixtures going from gasoline to methanol than there is for rich mixtures. The experimental trend of the ignition delay of rich mixtures of this dataset was already captured without this optimization. The spark size for rich mixtures stays relatively constant. It is notable that the spark size for lean mixtures follows the same trend as the stoichiometric mixtures but that all values are lower.

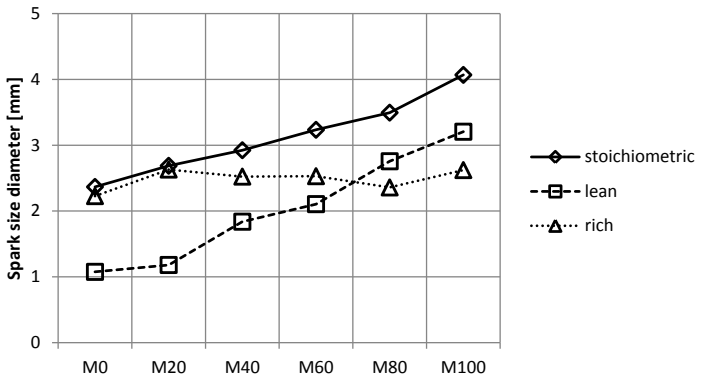

Figure 6.11: Spark size diameter for ignition delay optimization.

When the ignition delay is optimized to have the same value as the ID derived from the measurements, it is easier to evaluate the predictive capabilities regarding the other parameters. In Figure 6.12, MFB10-90, pmax and MFB50 for the stoichiometric mixtures are shown for the simulations with optimized ignition delay. For MFB10-90, the trend is very similar to the simulations without the

ignition delay optimization. There is a small change in the MFB10-90 because of slightly altered temperatures and pressures. The main burn duration is hardly affected, so the change in ID only results in a very small shift of the trend. The agreement with the experimental maximum pressure and the MFB50 is much better due to the optimized ignition delay. This results in smaller burn rate RMS errors for the methanol-gasoline blends. This can be seen in Figure 6.13. It is clear that the agreement is much better for the fuel with high methanol content. Only for pure gasoline the error is larger because originally the model was calibrated to have a minimum error.

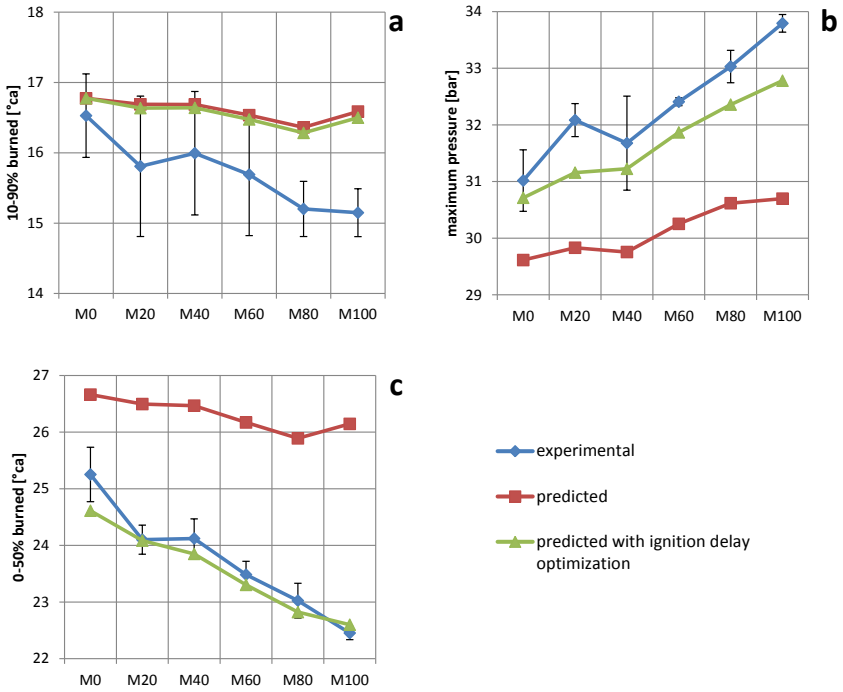

Figure 6.12: 10-90% mass fraction burned (a), maximum pressure (b) and 0-50% mass fraction burned (c) of the stoichiometric mixtures with ignition delay optimization.

Turbulent combustion initially proceeds in a quasi-laminar fashion. The flame front will wrinkle when the flame kernel becomes larger than the smallest turbulent eddy and will gradually become more wrinkled as it experiences a growing spectrum of turbulent length scales. Verhelst [27] and Vancoillie [28] identified several flame development models in the literature to relate the developing turbulent burning velocity to the fully developed burning velocity value. However, none of the flame development models take fuel properties into account. Thus,

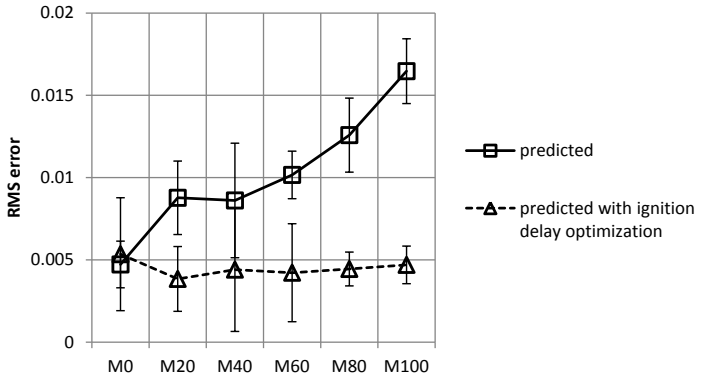

Figure 6.13: Burn rate RMS error of the stoichiometric mixtures with ignition delay optimization

changing the flame development model does not result in a different trend for the ignition delay. A flame development model or initial flame model (to initialize the flame kernel) that is better at capturing the fuel properties could be a solution.

Comparison of different turbulent burning velocity models

In the previous sections, the combustion model proposed by Wahiduzzaman et al. [159] was used. This is the standard combustion model in the simulation program GT-Power. This combustion model comprises of the turbulent burning velocity model of Damköhler together with an extended version of the flame development model of Morel et al. [165]. The Damköhler model assumes that the sole effect of turbulence is to wrinkle the flame front leading to an increased flame area resulting in $u_t \sim u'$. Contrary to the Damköhler model, the model of Bradley et al. and the model of Zimont/Liptnikov take fuel properties into account as explained in Section 6.3.1. These models are fuel dependent because this was needed to reproduce experimental trends seen for turbulent burning velocity measurements. The model of Bradley et al. has the following fuel properties: the Lewis number together with the laminar burning velocity and the kinematic viscosity of the unburned mixtures, all contained in the Karlovitz number. The model of Zimont/Lipatnikov has the laminar burning velocity and thermal diffusivity of the unburned mixture, contained in the Damköhler number. The thermal diffusivity of the unburned mixtures is also used in the model of Bradley et al. The thermal diffusivity is used in the Lewis number together with the diffusivity of the deficient reactant. The Lewis number *Le* is calculated by taking

the mass diffusivity of the deficient reactant in nitrogen using the expression of Fuller et al. from [178]. For the methanol-gasoline blends used in this study, the mass diffusivity of iso-octane was used for gasoline and the mass diffusivity of the blends was calculated out of the value of iso-octane and methanol on a molar basis. As the turbulent burning velocity model of Bradley et al. takes more fuel properties into account than the model of Zimont/Lipatnikov, it could be expected that it will reproduce the experimental trends better. This does not mean the absolute values will be closer to the experimental data. The flame development model used for this comparison is the model of Morel et al. [165]. This model is very similar but simpler than the model of Wahiduzzaman et al. [159], which was used in the previous sections, and therefore easier to implement in the GT-Power Fortran code. Due to the different flame development model, the calibration is different and other values are expected from the simulations done with the Damköhler model (which is the same as in the previous sections). For every turbulent flame model, the simulation is again calibrated for gasoline at stoichiometric operation. This calibration is used to simulate the whole range of methanol-gasoline operating points.

In Figures 6.15, 6.16 and 6.17, the simulation results of the different turbulent burning velocity models are shown for the stoichiometric, lean and rich mixtures together with the experimental data. KaLe refers to the model of Bradley et al. For the Damköhler model, it is clear that the trends are equal to the trends seen in the previous section but that the values differ due to the different flame development model and corresponding calibrations. For stoichiometric mixtures, the ID, the MFB10-90 and MFB50 do not change much going from gasoline to methanol. For lean mixtures, there is even a sligthly increasing trend which is opposite to the experimental trend and for the rich mixtures, the trend is well captured. Because the turbulent burning velocity model of Damköhler is proportional to u', the change in the combustion process is due to the laminar burning velocity, see Eq. 6.15. This means that the laminar burning velocity for stoichiometric mixtures does not change much going from gasoline to methanol in the case of stoichiometric mixtures, decreases slightly for lean mixtures and increases for rich mixtures. This can be seen in Figure 6.14. Here, the maximum laminar burning velocity during combustion is plotted. The increase for rich mixtures is very clear while for lean mixtures, one can notice a slight decrease. The reason for this is that the difference in the measured laminar burning velocity on the flat flame adiabatic burner between methanol and gasoline is significantly larger for rich mixtures than for lean or stoichiometric mixtures. The smaller difference for lean mixtures together with the lower in-cylinder temperatures in the case of methanol and smaller temperature dependence for methanol compared to gasoline (1.86 for methanol and 1.98 for gasoline for λ = 1.2) means the laminar burning velocities

decrease slightly for the lean methanol mixtures.

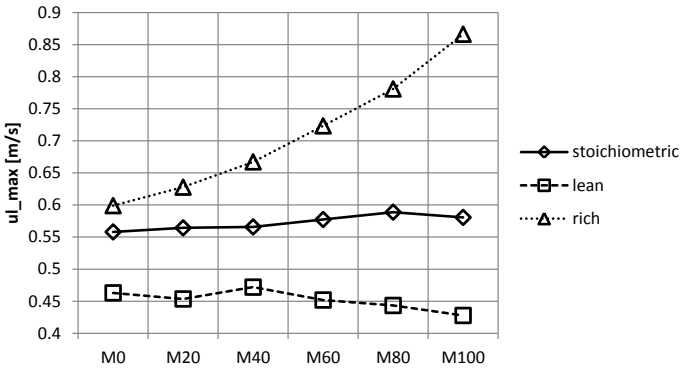

Figure 6.14: Maximum laminar burning velocity during combustion for simulation with the turbulent burning velocity model of Damköhler.

Comparing the results obtained with the turbulent burning velocity model of Zimont with the results of the Damköhler model, it is clear that the absolute values differ but more or less the same trends can be seen. For lean mixtures, the opposite trend compared to the experimental data is seen as is the case for the Damköhler model. This was expected as the model of Zimont takes the laminar burning velocity into account while there is a decrease in the simulated value of the laminar burning velocity going from gasoline to methanol, see Figure 6.14. Contrary to the model of Zimont, the turbulent burning velocity model of Bradley et al. takes also the Lewis number *Le* into account. The difference between the Lewis number of methanol and the Lewis number of iso-octane, which is used to represent gasoline, was shown in Figure 6.3 in Section 6.3.1. For rich mixtures ($\phi < 1.1$), there is no difference between the Lewis numbers of the different fuels. The deficient reactant is oxygen for both fuels. The difference between the Lewis numbers increases for stoichiometric mixtures and certainly for lean mixtures because the deficient reactant changes from oxygen to iso-octane (in the case of gasoline) and methanol. This behavior helps to explain the trends seen in Figures 6.15, 6.16 and 6.17 for the KaLe model. Because of the difference in Lewis number between methanol and iso-octane for stoichiometric and especially lean mixtures, the decreasing trend of the ID, MFB10-90 and MFB50 is better captured resulting in a better prediction of the trend seen for the maximum pressure. Especially for lean mixtures, the behavior is predicted better. However, the absolute values of the lean mixtures prediction are worse than for the other combustion models. For rich mixtures, the absolute values for the ID and MFB10-90 are also worse than the prediction of the Damköhler and Zimont model but the trend is more or less the same. This was expected due to the Lewis numbers of iso-octane and methanol for rich mixtures

being the same.

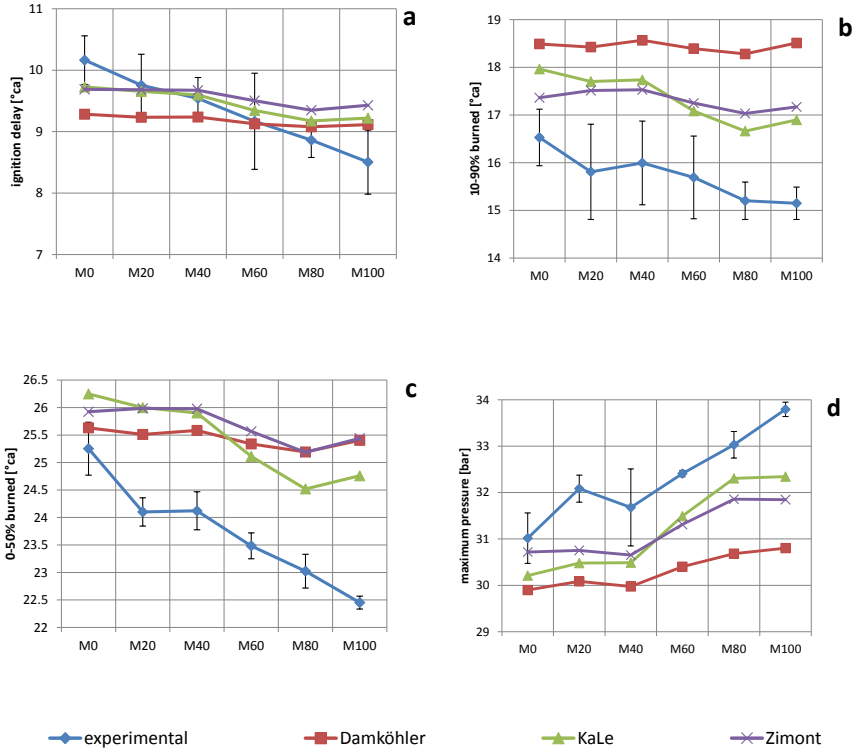

Figure 6.15: Ignition delay (a), 10-90% mass fraction burned (b), 0-50% mass fraction burned (c) and maximum pressure (d) of stoichiometric mixtures predicted by different turbulent burning velocity models.

Summary

The predictive capabilities of the simulation framework were tested for measurements on the CFR engine. Limited measurements were performed on methanol-gasoline blends for a fixed ignition timing, fixed throttle position and a fixed engine speed. The predictive performance of the newly developed laminar burning velocity correlations of gasoline and methanol together with a mixing rule was assessed. A comparison of 4 different laminar burning velocity correlations of gasoline was made from which it was shown that the newly developed correlation of gasoline performed equally or better than the older correlations. The sensitivity

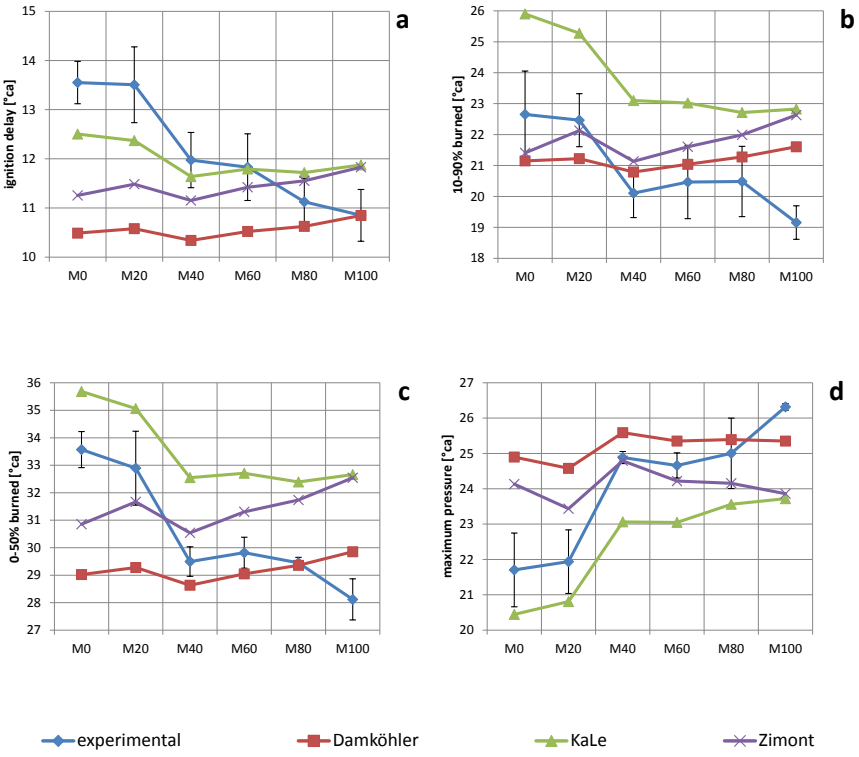

Figure 6.16: Ignition delay (a), 10-90% mass fraction burned (b), 0-50% mass fraction burned (c) and maximum pressure (d) of lean mixtures predicted by different turbulent burning velocity models.

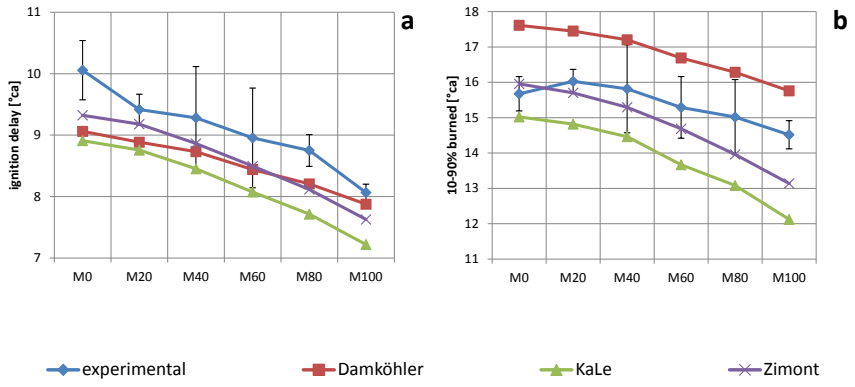

Figure 6.17: Ignition delay (a) and 10-90% mass fraction burned (b) of rich mixtures predicted by different turbulent burning velocity models.

was investigated for fuel blends going from pure gasoline to pure methanol. The results showed the importance of the laminar burning velocity correlation, the initial flame kernel and the estimation of the residual gas fraction. The experimental trends of the ID, MFB10-90, 0-CA50 and maximum pressure could not be reproduced in the simulations for lean and stoichiometric mixtures while the agreement was better for rich mixtures. **Uncertainty about the initial flame kernel**, **uncertainty about the laminar burning velocity at higher pressure and temperatures** or **the inability of the turbulent combustion model to adequately capture the chemical effects** were claimed as possible reasons. It could be seen that after changing some parameters of the laminar burning velocity correlation of methanol, the experimental trend could be reproduced. Further study of the laminar burning velocity at higher temperatures and pressures is thus needed to lower the uncertainty of these parameters. Because the initial flame kernel had a big influence on the ignition delay, it was decided to adjust this initial flame kernel depending on the operating point. After optimizing the initial flame kernel to reproduce the same ignition delay as in the measurements, the trends in burn rate and peak pressures were much better reproduced. As a result, it can be concluded that a flame kernel (growth) model that properly accounts for fuel effects could be very effective to improve the simulation results. Current predictive combustion simulations could benefit from an initial flame kernel size multiplier (or a spark size multiplier). Finally, different turbulent burning velocity models were tested. Although the absolute values did not give significantly better results, the model of Bradley et al. reproduced the trend going from gasoline to methanol much better due to the inclusion of the Lewis number.

6.6 Validation of simulation model on the Hyundai GDI engine

To further validate the combustion models' predictive capabilities on alcohol-gasoline blends over a broader working range, measurements were done on the direct injection 4 cylinder Hyundai engine at Argonne National Laboratory, Chicago, USA. This engine is described in Section 3.2.1 and the main characteristics are summarized in Table 3.1. Similar to the validation measurements on the CFR engine, for each operation point, three measurements were done. First the engine was set to a fixed value and the first measurement was done when all the measured values such as exhaust temperature, oil temperature, air flow, etc. did not change anymore. Then, with an interval of a few minutes, a second and third measurement was done. The values shown on the Figures are the mean values of the three measurements, except as mentioned otherwise. In Table 6.4, the measurements matrix is shown. This matrix was measured for gasoline, M50 and methanol. Due to limitations of the ECU, the lambda of measurement 5, 14 and 15 could not be set rich enough for methanol. The lambda that was used instead is shown between brackets for these measurements. For the same reason, measurement 7 was not measured for methanol.

Table 6.4: Measurement matrix on the Hyundai GDI engine

Measurement number	rpm	TP [%]	λ	IT [$^\circ ca$ BTDC]
1	1500	12	1	34
2	1500	12	1	37
3	1500	12	1	31
4	1500	12	1.1	34
5	1500	12	0.9 (0.97)	34
6	1500	12	1.05	34
7	1500	12	0.95	34
8	2000	12	1	40
9	1500	15	1	24
10	1500	18	1	20
11	1500	18	1	23
12	1500	18	1	17
13	1500	18	1.1	20
14	1500	18	0.9 (1.05)	20
15	2000	18	1 (1.05)	30
16	2500	18	1	35

The following procedure was taken in order to investigate the combustion model's

predictive capabilities on alcohol-gasoline blends for the Hyundai engine:

1. For the validation of the CFR engine, the two newly developed laminar burning velocity correlations were used. These correlations were both based on the laminar burning velocity measurements that were done on the flat flame burner, ergo both the correlations are derived from the same source. As the simulations on the Hyundai engine cover a broader working range and thus give a broader image of the predictive capabilities, it has been investigated what the effect of using a correlation from another source is. The correlation of gasoline was still the new correlation while several methanol correlations have been tested with the model calibration done on gasoline. This will show how important it is to match laminar burning velocity correlations of different fuels.

2. The predictive capabilities of the model has also been tested with the standard laminar burning velocity correlations in GT-Power and compared to the simulations done with the newly developed correlations.

3. Finally, the effect of different turbulent velocity models and the flame initialization has been investigated.

For points 1 and 2 explained above, the standard combustion model of GT-Power was used together with the laminar burning velocity correlations mentioned in Section 6.3.2. The standard combustion model in GT-Power is a derivate of the combustion model of Damköhler together with the flame development model of Wahiduzzaman et al. [159].

Similar to the simulations on the CFR engine, the model will be calibrated on one measurement performed with gasoline and this calibration will be used for the whole operating range and methanol blends. This calibration was always done for measurement point 9 because this measurement is located in the center of the measurement matrix (see Table 6.4).

6.6.1 Calibration of the breathing cylce with direct injection

Because the Hyundai engine has direct injection compared to the port fuel injection of the CFR engine, the Three Pressure Analysis has additional calibration factors for the injector which can be changed depending on the fuel. It was chosen to use a sequential injector with imposed air-fuel ratio. With this injector, the air-fuel ratio could be entered while other factors could be adjusted to reproduce the

correct experimental data. For the injector, the vaporized fluid fraction needed to be estimated. This is the mass fraction of the injected liquid that will vaporize immediately upon injection. For a typical port-injected gasoline engine, a normal value is 0.3. However, it was found necessary to add an additional cylinder evaporation model to control the evaporation of fuel in the cylinder in order to have the same volumetric efficiency as in the experiments. This model is used to define evaporation details of the remainder of the liquid fluid. Two factors of this model were selected as additional calibration factors: the 50% Evaporation Duration and Fraction of Vaporization Heat Taken from Walls. In the evaporation model, the 50% Evaporation Duration represents the crank angle duration required to evaporate 50% of the liquid at $600K$ with the engine running at $4000rpm$. With these three factors (vaporized fluid fraction, 50% evaporation duration and vaporization heat taken from the walls), the Three Pressure Analyse could reproduce the correct temperatures, volumetric efficiency and flow rates while the LHV multiplier was close enough to 1 (within 5%). The value of the vaporized fluid fraction was chosen very small (3%), the 50% evaporation duration was set at 60 $^{\circ}ca$ and the vaporization heat taken from the walls was set at 75%. The vaporization heat taken from the walls had to be taken very large to not overpredict the volumetric efficiency of methanol indicating wall impingement.

6.6.2 The effect of different methanol laminar burning velocity correlations

The effect of changing the laminar burning velocity of methanol

First, the results will be shown using the two new laminar burning velocity correlations of gasoline and methanol. The laminar burning velocity of M50 is again calculated with the mixing rule based on energy fraction. In Figure 6.18, the ignition delay ID (0-2% mass fraction burned), duration of 10-75% mass fraction burned MFB10-75, crank angle at 50% mass fraction burned CA50 and the maximum pressure are plotted. Contrary to the simulation results on the CFR, the MFB10-75 is shown instead of the MFB10-90. This is because a single value for the heat transfer multiplier has been used for the simulations on the Hyundai engine compared to three different values for the heat transfer multiplier on the CFR engine, as explained in Section 6.4.2. Using a single value for the heat transfer multiplier should normally be sufficient for the calibration of the model and this also helped to limit the amount of calibration factors (additional calibration factors were added for the direct injection). Because only a single value is used, this could occasionally lead to a long tail on the burn rate profile resulting in large differences in the MFB10-90 between several cases. This could lead to an

misinterpretation of the simulations for some test results. Because of the broader measurement range performed on the Hyundai engine, the simulated values are shown versus the experimental data to give a general view of the simulation results. Perfect predictions should result in a straight line passing through the origin with the slope of the line equal to 1. This line is represented by a full black line. The dotted lines give an impression of the deviation from the perfect simulation. For the ID, MFB75 and CA50, the dotted lines deviate 2°*ca* and for the maximum pressure, the deviation is 3 bar. Because the turbulence model could not be validated with experimental data, the biggest errors are expected for the operating points with higher engine speeds than 1500 rpm (the model was calibrated at this engine speed). On the Figures, the operating points at 2000 and 2500 rpm are shown using open symbols. As seen in Figure 6.18, the simulated values agree well with the experimental values. In general, the largest deviations can be seen for methanol which is clear from Figure 6.18b and c. As we look at Figure 6.18a and d, we can conclude that the trend going from gasoline to methanol is again not well captured for the ignition delay and as a result also for the maximum pressure. The ignition delay for gasoline is underpredicted for most operating points while for M50 the agreement is good and for pure methanol, it is overpredicted. The opposite is true for the maximum pressure. A similar trend was also seen for the simulations done on the CFR engine (see Section 6.5). For the MFB10-75 and CA50, the trend is less clear from these Figures.

If we zoom in at the operating points with a throttle opening of 12%, the predictive capabilities for different air-fuel ratios can be evaluated for gasoline, M50 and methanol. Figure 6.19 shows the predicted values of the ID and MFB10-75 as a function of λ for gasoline, M50 and methanol. For each operating point, three measurements were done with a few minutes between each measurement. On the Figures, the experimental data of each measurement is shown resulting in three data points for each case. This was not done for the simulation results of the CFR engine to not overload the Figures. Contrary to the measurement done on the CFR, where only the injection duration and the fuel was changed between different operating point, more parameters (such as throttle position, engine speed, valve timing, ignition timing) were changed between different operating points on the Hyundai engine. Additionally, the stock ECU was adjusting the injection and variable valve timing constantly in a closed loop control which was not possible with the CFR engine. This is probably the cause of the slightly bigger deviations between different measurements.

As can be seen in Figure 6.19, the experimental trend for the ignition delay seen for the variations of lambda is not fully captured by the simulation results for gasoline and M50. For methanol, the trend between lambda equal to 0.97 and 1.1 is well captured. However, it could not be investigated if this would be the

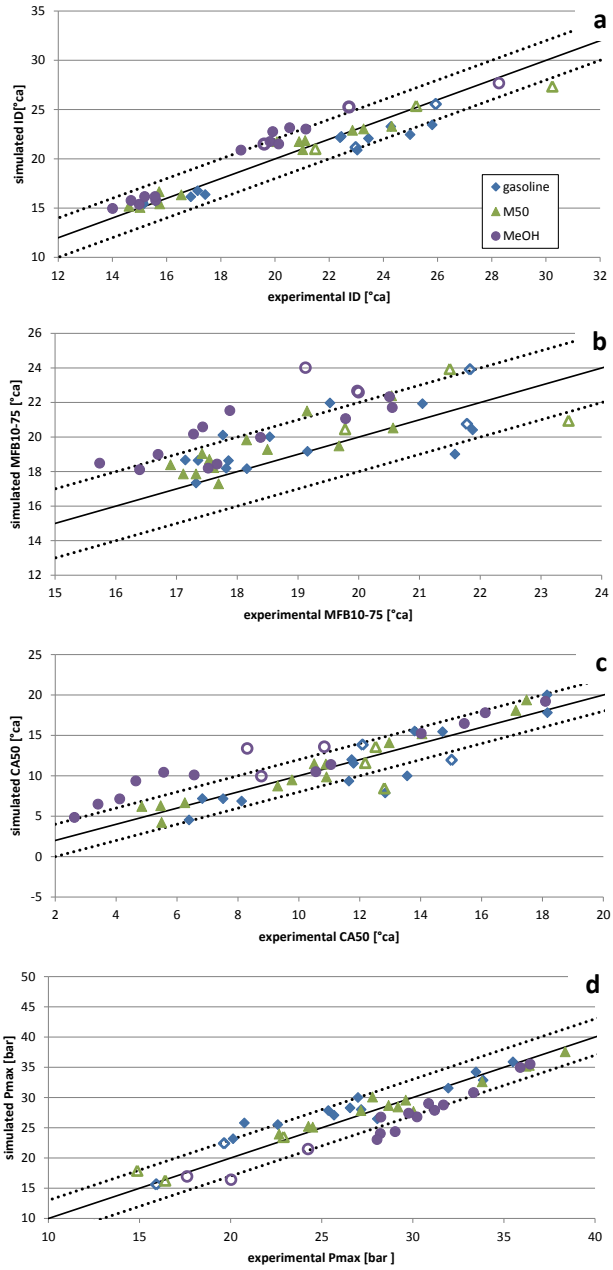

Figure 6.18: Ignition delay (a), 10-75% mass fraction burned (b), Crank angle at 50% mass fraction burned (c) and maximum pressure (d) simulated with new laminar burning velocity correlations of gasoline and methanol.

case for even richer mixtures because the ECU did not allow enough adjustment to run the engine richer than $\lambda = 0.97$. It can again be seen that the trend of the ID going from gasoline to methanol is not well predicted (underprediction for gasoline, overprediction for methanol). More or less the same conclusions can be drawn for the MFB10-75 of gasoline, M50 and methanol shown in Figure 6.19. As mentioned in Section 6.5, the cause of the deviation of the simulation results compared to the experimental data could be the uncertainty of the laminar burning velocity at engine-like conditions, the turbulent burning velocity model that does not capture all the fuel effects, the uncertainty of the flame initialization or a combination of the previous three causes. Additionally, for the Hyundai engine, there can be an extra uncertainty of fuel inhomogeneity due to the direct injection of the fuel. In Section 6.6.3, the effect of the flame initialization and the effect of different turbulent burning velocity models will be studied for a broader working range compared to the CFR engine.

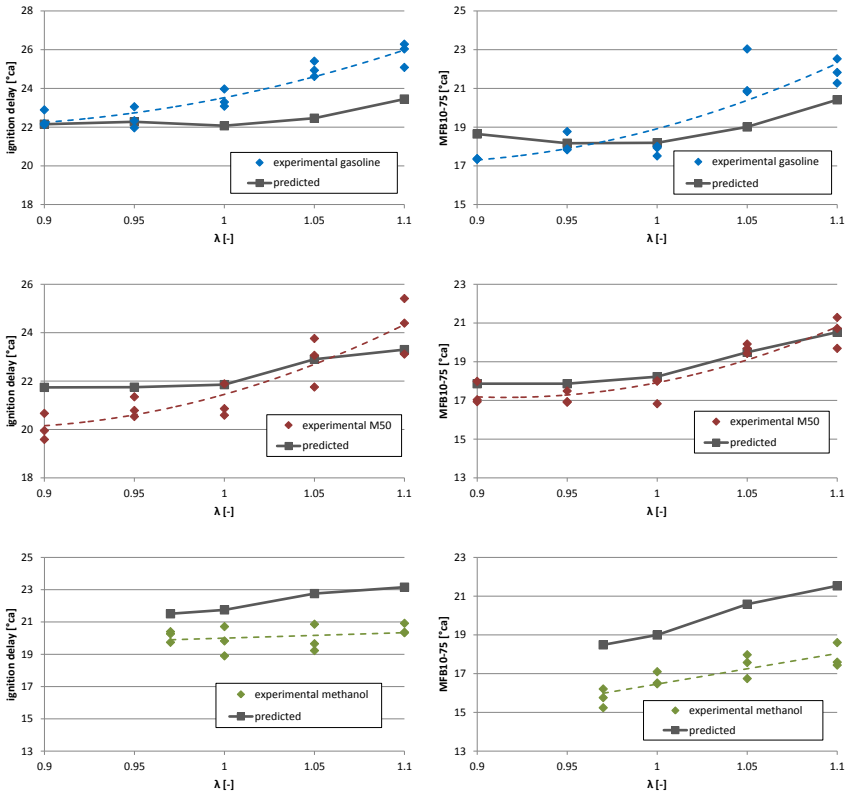

Figure 6.19: Ignition delay (left) and 10-75% mass fraction burned (right) simulated with new laminar burning velocity correlations of gasoline and methanol.

Table 6.5: Root mean square error of the ID, MFB10-75, CA50 and maximum pressure simulated with different laminar burning velocity correlations of methanol.

RMSE	ID [°ca]	MFB10-75 [°ca]	CA50 [°ca]	max P [bar]
Sileghem	1.69	2.52	2.88	3.01
Gülder	2.59	3.63	6.59	7.91
GT-power	2.00	4.04	6.24	8.41
Vancoillie	1.84	4.45	6.33	8.37

Using the newly developed laminar burning velocity correlations of gasoline and methanol, the simulated values agree rather well with the experimental values as seen in Figure 6.18. Both correlations are based on measurements performed on the same flat flame burner. However, it is also possible to use a different laminar burning velocity correlation for one of the fuels. In Figure 6.20, it is investigated what the impact is on the results when the laminar burning velocity correlations of gasoline and methanol are not matched (not from the same source). In this Figure, the standard correlation of GT-Power for methanol [135], the correlation of Gülder [123, 180] and the correlation developed by Vancoillie [121] are used next to the new correlation for methanol while the calibration of the simulation model is always the same calibration done with the new correlation of gasoline. From Figure 6.20, it is clear that the calibration of the simulation program is far from the optimal calibration that could be chosen for the three other laminar burning velocity correlations. The burning rate is overpredicted resulting in lower values for the ID, MFB10-75 and CA50 and a large overprediction of the maximum pressure. This can also be seen in Table 6.5 where the root means square errors (RMSE) of the simulation results are shown for the different laminar burning velocity correlations of methanol. It is clear that the error is similar for the ignition delay but that the newly developed correlation outperforms the other correlations especially for the maximum pressure. This result shows that it is important to match the laminar burning velocity correlations of different fuels if the effect of using another fuel than normal (in this case methanol instead of gasoline) needs to be investigated. Using properly matched laminar burning velocity correlations for different fuels can lead to an improvement of simulations results if for example an engine calibrated to run on gasoline needs to be converted to flex-fuel operation.

GT-Power laminar burning velocity correlations vs. new laminar burning velocity correlations

In the previous Section, it was pointed out that the laminar burning velocity correlations of different fuels should be matched in order to have more accurate simulations. In this Section, the standard correlations in GT-Power will be

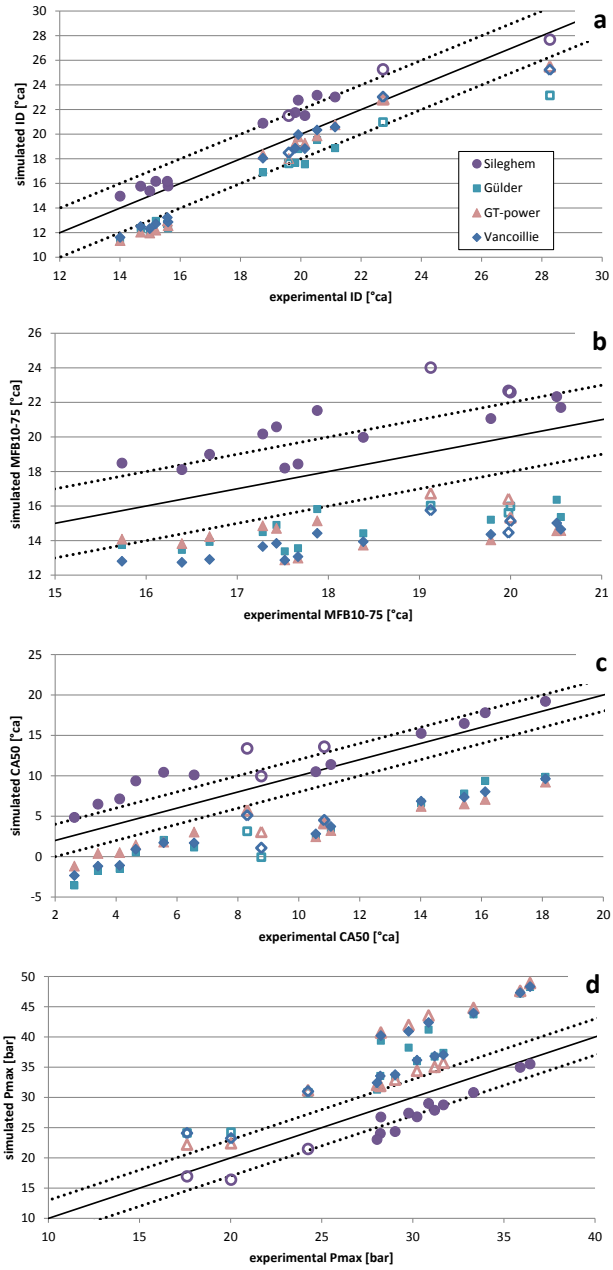

Figure 6.20: Ignition delay (a), 10-75% mass fraction burned (b), Crank angle at 50% mass fraction burned (c) and maximum pressure (d) simulated with different laminar burning velocity correlations of methanol.

evaluated and compared to the new correlation for the laminar burning velocity of gasoline and methanol (Figure 6.18). As no mixing rule for the laminar burning velocity is programmed in GT-Power, only the results of gasoline and methanol will be shown. The simulation model was calibrated for gasoline (using the GT-Power correlation) and the same calibration was used for methanol similar to what was done in the previous sections. In Figure 6.21, the ID, MFB10-75, CA50 and maximum pressure are shown for the simulations done with the GT-Power correlations. Compared to Figure 6.18, the results of the ID are similar. Looking at the MFB10-75, a slightly larger scatter of the results can be noticed, especially for methanol. There seems to be a number of operating points for which the simulated values are overpredicted and a part for which the simulations underpredict the experimental data. Closer inspection pointed out that the cases with a throttle opening of 12% have higher simulated results while the cases with a throttle opening of 18% are underpredicted by the simulation program. This was not the case using the new laminar burning velocity correlations, see Figure 6.18. This difference continues in the values of CA50 and maximum pressure where two distinct regions can be noticed: a region of underpredicted and overpredicted values for CA50 and the maximum pressure. Further, the simulated trends for changing lambda values (not shown here) are not different to the trends seen in Figure 6.19 for simulations with the new laminar burning velocity correlations. With all these results, it appears that the newly developed correlations are better in capturing the effect of changing engine loads (different engine conditions = different temperature, pressure or residual gases) than the correlations used in GT-Power.

6.6.3 Effect of the flame initialization and turbulent burning velocity model

Effect of the flame initialization

In Section 6.5.4, the ignition delay was optimized to have the same value as the ID derived from the measurements on the CFR engine. This resulted in very good predictions for MFB50 and the maximum pressure while only small changes were seen for MFB10-90. In this Section, the same method was used for the measurement on the Hyundai engine and the results are plotted in Figure 6.22. The spark size/initial flame kernel is again seen as an additional calibration factor. The original calibration factors and the spark size are optimized together by minimizing the burn rate RMS error of the measurements on gasoline and then for each measurement the spark size is changed to have an identical ignition delay as was measured experimentally. The MFB10-75, CA50 and maximum pressure for these

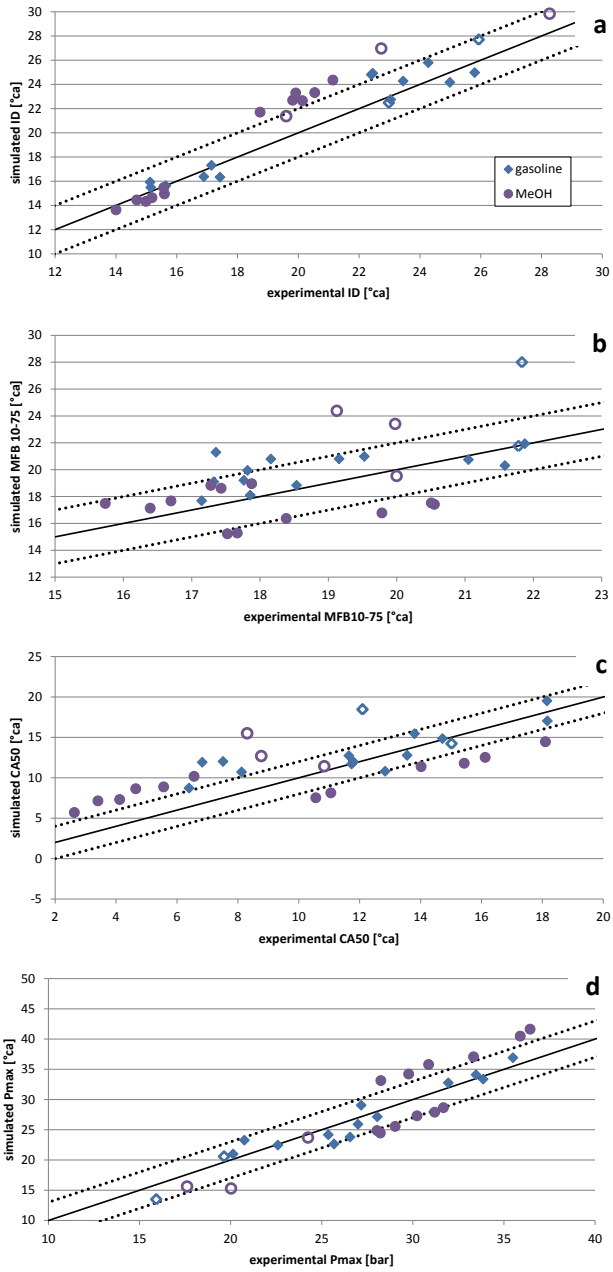

Figure 6.21: Ignition delay (a), 10-75% mass fraction burned (b), Crank angle at 50% mass fraction burned (c) and maximum pressure (d) simulated with the standard laminar burning velocity correlations in GT-Power.

simulations are presented in Figure 6.22. The adjusted calibration constants have a larger effect on the fully developed combustion (MFB10-75) for the Hyundai engine than which was seen for the CFR engine. For the CFR engine, only one throttle postion and engine speed was used for the different measuring points while for the Hyundai engine, different operating points are investigated with changing loads, changing valve timing, etc. resulting in different turbulence values from the turbulence model. This is the reason why the prediction for the fully developed combustion changes more for some operating points when adjusting the calibration factors. As seen in Figure 6.22, there is a slightly better agreement for the MFB10-75 compared to the simulations without the optimization of the ignition delay. Similar to the results on the CFR engine, the agreement between the experimental values of CA50 and the maximum pressure and the simulated results is very good. For the maximum pressure, all simulated values are between the two dotted lines which present a deviation of 3 bar. This result shows that the flame initialization (or spark size diameter) as an additional calibration factor can be very effective.

Comparison of different turbulent burning velocity models

Finally, different turbulent burning velocity models will be compared to investigate if models which take fuel properties into account can lead to better predictions. Again, the model of Damköhler will be compared to the model of Bradley et al. and the model of Zimont/Lipatnikov (see Section 6.3.1). Similar to the simulation done on the CFR with different turbulent burning velocity models, the flame development model used for this comparison is the model of Morel et al. [165] (not the extended model of Morel). For every turbulent flame model, the simulation is again calibrated for gasoline at stoichiometric operation. This calibration is used to simulate the whole range of methanol-gasoline operating points. In this Section, only the ignition delay and MFB10-75 will be shown. The results of CA50 and the maximum pressure are determined by the ignition delay and the fully developed combustion and can, as a result, be deduced from the ID and MFB10-75.

In Figure 6.23, Figure 6.24 and Figure 6.25, the simulation results of the different turbulent burning velocity models are shown. KaLe refers to the model of Bradley et al. For the results obtained with the Damköhler model, there is a good agreement with the results of the standard GT-Power models (Damköhler model coupled with an extended version of the flame development model of Morel et al. [165]) for the ID. The scatter seen for the MFB10-75 is similar to the scatter seen in Figure 6.18 but there is a stronger overprediction of the experimental data. For the KaLe and Zimont model, the simulation results of the ID and MFB10-75 seem, in general, very similar to each other. Both overpredict the

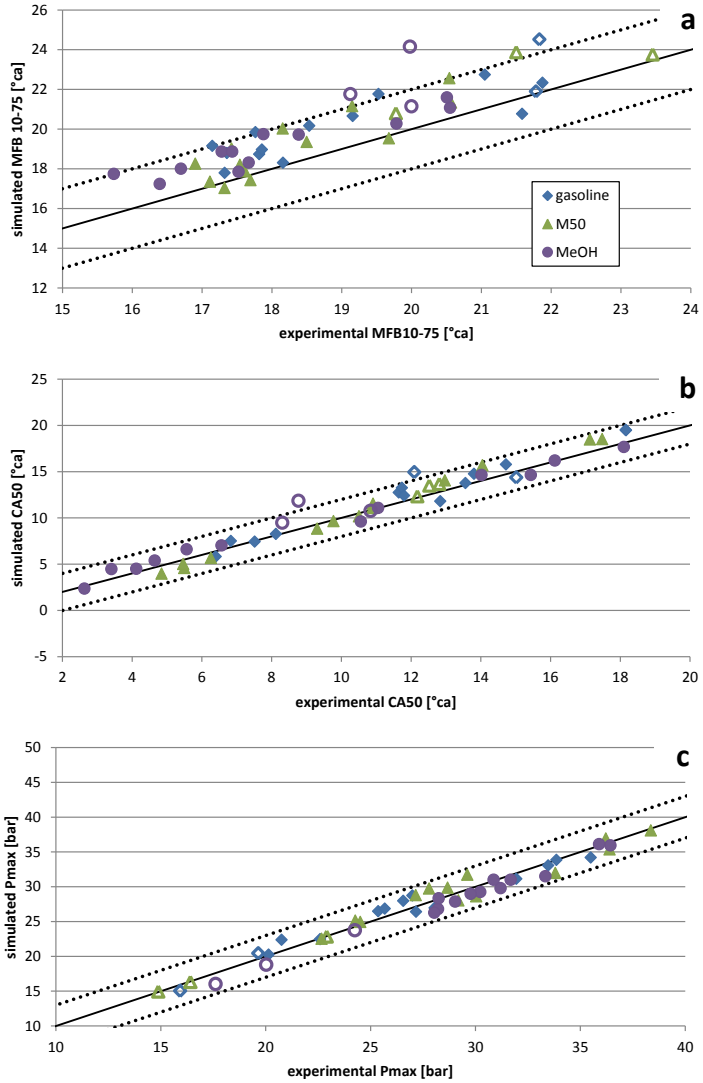

Figure 6.22: 10-75% mass fraction burned (a), Crank angle at 50% mass fraction burned (b) and maximum pressure (c) simulated with ignition delay optimization.

ID but the agreement is still acceptible while there is a very large scatter for the results of the MFB10-75. Compared to the Damköhler model, the agreement is worse, especially for operating points with higher engine speed (the non-filled data points). For the engine model of the Hyundai engine, the $k-\varepsilon$ turbulence model of GT-Power was used. Because the default turbulent combustion model in GT-Power is of the Damköhler type, the turbulence routines are possibly tuned for best performance with this model.

To detect any difference between the KaLe and Zimont turbulent combustion model, we zoomed in at the operating points with a throttle opening of 12%. These results are plotted in Figure 6.26 as a function of lambda for the three different combustion models. As expected, the trends of the Damköhler combustion model are very similar to the trends seen in Figure 6.19. Only the absolute values for the MFB10-75 are significantly higher which could be expected from the results in Figure 6.23. The Zimont combustion model gives very similar trends to the Damkohler model which was also seen in Section 6.5.4. The KaLe combustion model follows the experimental trend of the ignition delay better than the Damköhler and Zimont model, especially for gasoline, but there is a larger overestimation of the MFB10-75 for lean mixtures in the case of gasoline. The large change in Lewis number of iso-octane, used to calculate the Lewis number of gasoline, for lean mixtures (see Figure 6.3 in Section 6.3.1) can be accounted for this larger error. Althought the trend going from gasoline to methanol is better predicted for the KaLe model, this model suffers from large errors.

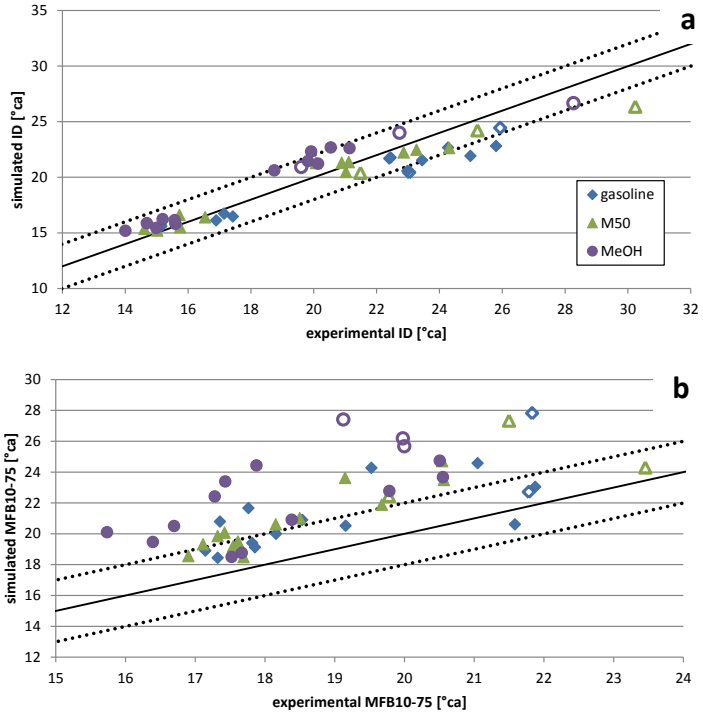

Figure 6.23: Ignition delay (a) and 10-75% mass fraction burned (b) simulated with the turbulent burning velocity model of Damköhler.

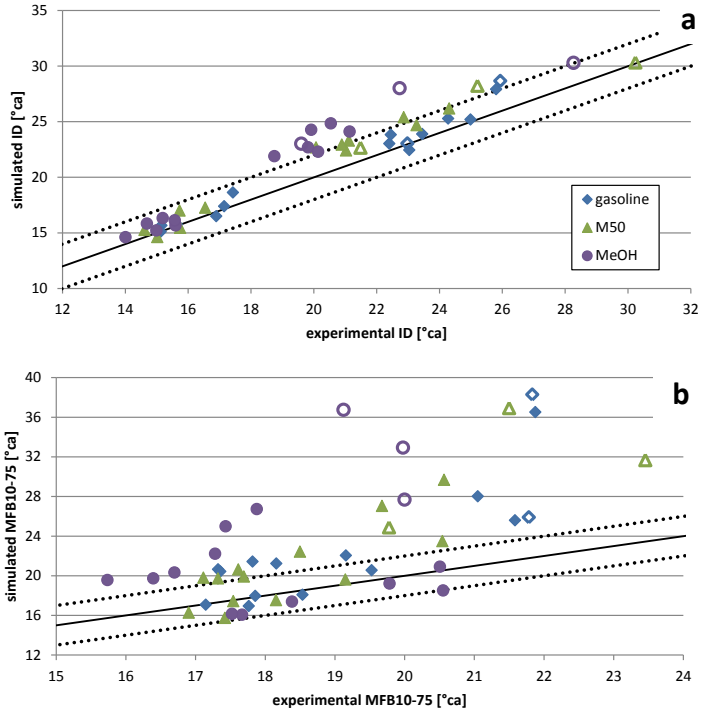

Figure 6.24: Ignition delay (a) and 10-75% mass fraction burned (b) simulated with the turbulent burning velocity model of Bradley et al. [161].

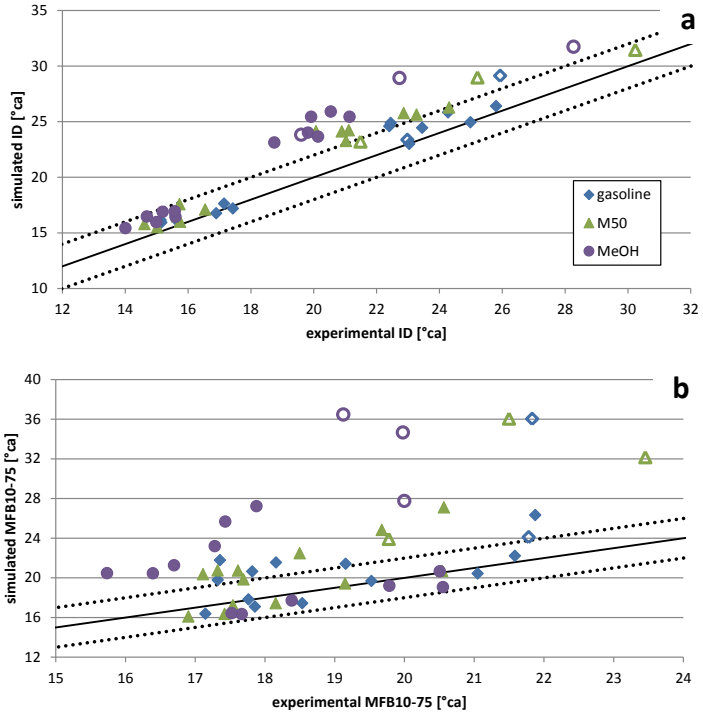

Figure 6.25: Ignition delay (a) and 10-75% mass fraction burned (b) simulated with the turbulent burning velocity model of Zimont.

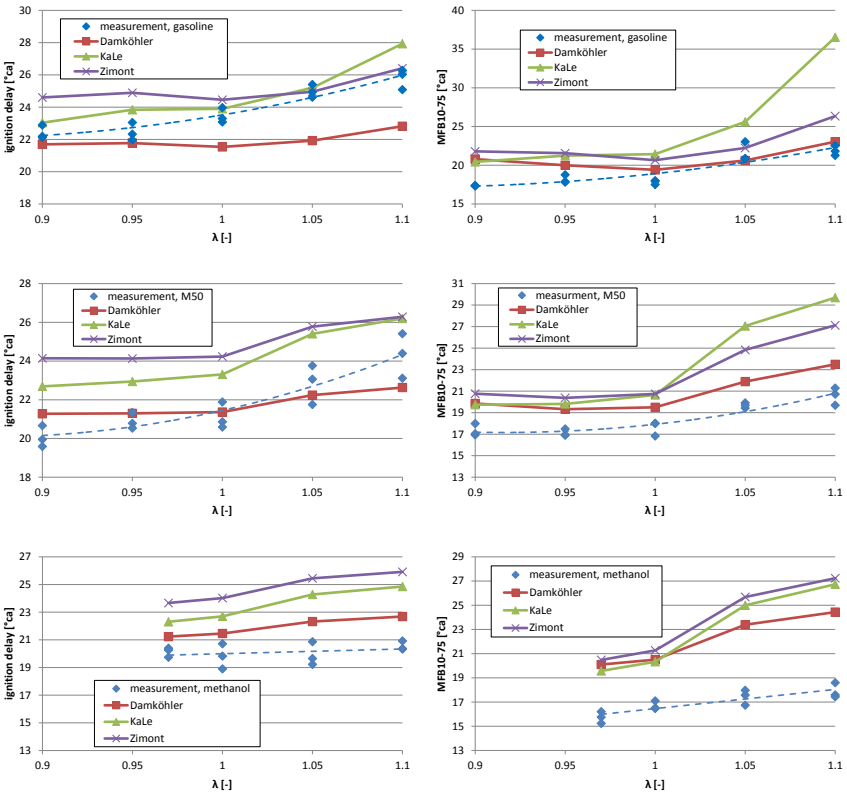

Figure 6.26: Ignition delay (left) and 10-75% mass fraction burned (right) simulated with different turbulent burning velocity models.

Summary

The predictive capabilities of the simulation framework were tested for measurements on the direct injected Hyundai engine. A broader measurement range than on the CFR engine was used to get a more general view of the simulation output. First, simulations were again performed with the standard combustion model of GT-Power in combination with the newly developed laminar burning velocity correlations of methanol and gasoline. In general, the simulations agreed well with the experimental values. Similar to what was found for the CFR engine, the trend going from gasoline to methanol was not fully captured. Additionally, the results were plotted as a function of λ and only for methanol, the trend was captured although the λ range was limited in the case of methanol. Several other laminar burning velocity correlations of methanol were tested without changing the original calibration that was performed with the newly developed correlation of gasoline. It was clear that the newly developed correlation of methanol outperformed the other correlations. This shows that it is important to match laminar burning velocity correlations of different fuels if the effect of using another fuel than normal (gasoline) needs to be investigated. After this result, both the standard laminar burning velocity correlations of gasoline and methanol in GT-Power were tested (with a new calibration) and compared to the results of the newly developed correlations. The newly developed correlation performed better in capturing the effects of changing engine loads (different temperatures, pressures, residual gas fractions) implying that the dependence on temperature, pressure or EGR is better represented by the new correlations.

Finally, the influence of the flame initialization and turbulent burning velocity models was investigated in the same way as on the CFR engine. It was again shown that changing the flame kernel depending on the fuel and on the operating point could be very effective to improve the simulations. Further it was shown that the trends going from gasoline to methanol could be better captured by the model of Bradley et al. due to the inclusion of the Lewis number but that this model can suffer from large errors compared to the experimental data.

7 Knock prediction

7.1 Introduction

Combustion knock is one of the major factors limiting the efficiency of spark ignition engines. It is caused by autoigniting pockets of unburned gas [57]. High local pressures and pressure waves across the combustion chamber, caused by the rapid energy release associated with knock, can lead to mechanical and thermal damage to the engine. Light alcohols, such as methanol and ethanol, are interesting fuels with elevated knock resistance. Methanol and ethanol have an elevated chemical resistance to autoignition, which is reflected in their high octane number (ON = 109) [35]. This is due to the single-stage autoignition behavior of alcohols. Gasoline has a two-stage autoignition behavior. This means that, at temperatures below 900 K, a cool-flame reaction can occur. This reaction promotes the main autoignition at high temperatures. At higher temperatures, the pre-cool flame delay gets progressively shorter until the cool-flame is no longer present [35]. As autoignition in engines takes place at unburned mixture temperatures of 800-900K, it is the prime reason for the reduced delay time of gasoline compared to alcohols [181]. Additionally, the larger cooling effect of light alcohols compared to gasoline further reduces the tendency to knock. In directly injected E85 engines the knock inhibiting effect of vaporization cooling has been shown to be comparable to the chemical effect [182]. Finally, the increased (laminar) burning velocity of light

alcohols helps to suppress knock as more end gas is burned before it can reach autoignition conditions [18, 121]. As there is a renewed interest in alcohols as alternative fuel, an accurate predictive knock model for alcohols fuels would be of great value to engine designers.

The objective of this chapter is to develop such a model for (m)ethanol-gasoline blends using a simple mixing rule for the ignition delay of alcohol-gasoline blends. The model will be calibrated on pure gasoline (stoichiometric operation) and on pure methanol (stoichiometric operation) and with these two calibrations, the capability of the model to predict knock parameters of methanol-gasoline blends will be investigated.

7.2 Knock model for alcohol-gasoline blends

Models to predict the autoignition of unburned mixture in spark-ignition engines range from simple empirical expressions to complex formulations featuring reduced or full chemical kinetics [183]. A widely employed empirical approach is to apply the conservation of delay principle proposed by Livengood and Wu [184]. According to this principle the overall ignition delay time can be found by integrating its instantaneous value during the compression and combustion stroke. This is analytically expressed by the knock integral reaching unity:

$$\int_{t_{IVC}}^{t_{KO}} \frac{\mathrm{d}t}{\tau(t)} = 1 \tag{7.1}$$

Where t_{IVC} and t_{KO} are the time at intake valve closure and knock onset respectively and $\tau(t)$ is the instantaneous autoignition delay time. The autoignition delay time τ is the time during which a homogeneous mixture must be maintained at temperature T and pressure p before it autoignites. The autoignition delay time τ at instantaneous cylinder pressure p, unburned mixture temperature T and composition is typically given by an Arrhenius expression representing the rate limiting step of autoignition:

$$\tau = A p^n e^{\frac{B}{T}} \tag{7.2}$$

Where A, n and B are parameters depending on the mixture composition (fuel, ϕ, residual gas ratio). The most widely used parameter set for the ignition delay of spark ignition fuels was introduced in 1978 by Douaud and Eyzat based on

recording the knock onset in a CFR engine for a range of running conditions and PRFs (primary reference fuels) with octane numbers between 80 and 100 [185]. Another way of calculating the ignition delay is with chemical kinetic models. The drawback for fuel blends is that the kinetic models become very large and complex, with long calculation times as a result, and that in many cases no models exist for blends of different fuels. The Livengood-Wu integral gives an indication of when autoignition will occur in a completely homogeneous mixture. Completely homogeneous mixtures are unlikely in practice and autoignition will be triggered by 'hot spots' [186]. This means that autoignition can occur before the Livengood-Wu integral attains a value of unity. As a result, for two-zone thermodynamic engine models, such as the one used in this work, empirical expressions have been shown to yield performance as good as comprehensive chemical kinetics schemes [183]. The inability of these models to reproduce local hot gas pockets and cyclic variation introduces uncertainties that outweigh those incurred by the simplified chemical kinetics. To consider these effects, multi-zone or 3D CFD approaches are necessary, employing either detailed chemistry or empirical expressions.

Still, the combination of two-zone modeling and the knock integral approach has been confirmed as a useful tool to estimate knock occurrence and intensity, which can be directly linked to the experimentally measured ratio of knocking to non-knocking cycles [30]. In the following Sections, different models to calculate the autoignition delay of gasoline and light alcohols will be discussed and a mixing rule will be proposed to calculate the autoignition delay of alcohol-gasoline blends in the same way as was done for the laminar burning velocity of alcohol-gasoline blends, see Chapter 5.

7.2.1 Autoignition model for gasoline

The combustion of many hydrocarbon species (gasoline included) exhibits two-stage ignition characteristics. This is especially true for most paraffinic hydrocarbons. Autoignition correlations are often based on a simple, single-stage Arrhenius expression. These correlations lack detail regarding the cool-flame phenomena. In the literature, two models were proposed to deal with the two-stage ignition characteristic, discussed below.

The model of Yates et al.

Yates et al. [35, 187] proposed an empirical model concept with a formfitting simplification of the overall ignition delay into four basic steps. These comprised

(1) a pre-cool-flame delay at constant temperature, (2) an instantaneous cool-flame temperature increase (which could be zero), (3) a further delay at constant temperature, and (4) the terminal exothermic auto-ignition. The four steps are illustrated in Figure 7.1. It was assumed that this exothermic reaction sequence could be represented by a simple Arrhenius reaction formulation representing the gross, rate-limiting step, i.e.

$$\tau_h = \phi^{\beta_h} A_h p^{n_h} e^{\frac{B_h}{T}} \tag{7.3}$$

where the temperature profile exhibits a distinct step up at the cool-flame initiation point. The calculation of the overall ignition delay needs to be undertaken in two stages by applying the conservation-of-delay principle proposed by Livengood and Wu, i.e.

$$\int_{t_0}^{t_1} \frac{\mathrm{d}t}{\tau_{h,i}} + \int_{t_1}^{t_2} \frac{\mathrm{d}t}{\tau_{h,CF}} = 1 \tag{7.4}$$

where t_1 is defined by the appearance of the cool flame and its associated temperature rise, and t_2 represents the overall ignition delay time. The autoignition delays $\tau_{h,i}$ and $\tau_{h,CF}$ represent the characteristic exothermic reaction delay evaluated at the initial and post-cool-flame conditions respectively. If the pressure and temperature are approximated as being constant during each stage, (and taking t_0 as zero), the integral simplifies to:

$$\frac{t_1}{\tau_{h,i}} + \frac{t_2 - t_1}{\tau_{h,CF}} = 1 \tag{7.5}$$

Rearranging, one obtains the overall ignition delay time, t_2, as:

$$t_2 = t_1 + \tau_{h,CF}\left(1 - \frac{t_1}{\tau_{h,i}}\right) \tag{7.6}$$

3-Arrhenius model proposed by Weisser

This model considers three distinct reaction regimes. The three reaction regimes represent the low, medium and high temperature ignition chemistry. The low and medium temperature reactions occur sequentially, giving rise to a two-stage

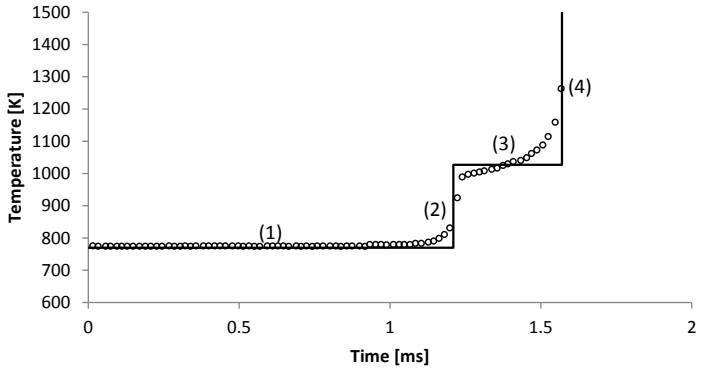

Figure 7.1: Illustration of the empirical model proposed by Yates et al. [187]. Circles: simulation of the ignition delay with cool-flame behavior.

ignition path. The high temperature reactions lead to a parallel single-stage ignition path [188]. As a result, the overall ignition delay for the full temperature range can be modeled by a simplified system expressed as:

$$\frac{1}{\tau} = \frac{1}{\tau_1 + \tau_2} + \frac{1}{\tau_3} \tag{7.7}$$

where the individual timescales τ_1, τ_2, and τ_3 represent the low, medium and high temperature regime respectively and can be expressed as an Arrhenius-type correlation. This simplified system is illustrated in Figure 7.2.

7.2.2 Autoignition model for alcohols

Methanol, ethanol, and many aromatic and olefinic molecules do not exhibit a cool flame. Simple single-stage Arrhenius-based models could be employed [35]. For light alcohols and methanol, in particular, a number of correlations were proposed over the years based on shock tube experiments [190, 191], rapid compression machine tests [192] and chemical kinetics calculations [35]. A new autoignition correlation for methanol was compared against existing correlations in a previous study of Vancoillie et al. [30]. In this work, the ignition delay time of methanol-air-residual mixtures was calculated using a chemical kinetics code developed at Eindhoven University of Technology (CHEM1D [120]) and the methanol oxidation mechanism of Li et al. developed at Princeton University

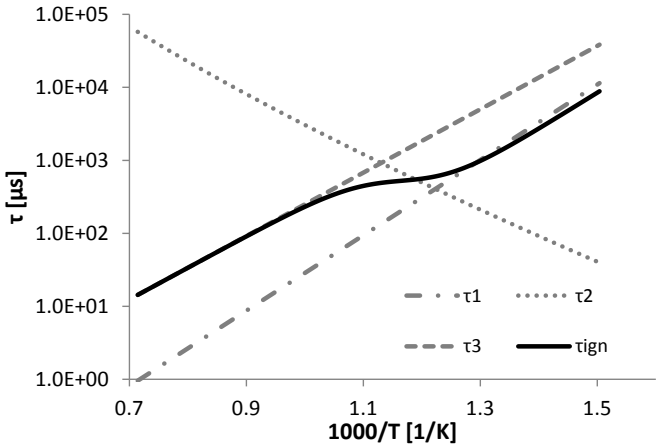

Figure 7.2: Illustration of the 3-Arrhenius model proposed by Weisser [189]

[146]. The resulting autoignition delay times were fit as a function of T, p, ϕ and residual gas content f using a correlation form similar to that of Douaud and Eyzat [185] (see Eq. 7.2) with the effects of ϕ and f implemented similarly to previous work [138, 193] in the pre-exponential factor A:

$$A = A_0 \phi^{\beta} (1+f)^m \tag{7.8}$$

Where A_0 and β are constants. Based on analysis of the calculated data, the pressure exponent n and activation temperature B of Eq. 7.2 and the dilution exponent m of Eq. 7.8 were fit as a polynomial function of ϕ, T and f. This newly developed autoignition delay correlation was able to capture the high temperature sensitivity of methanol autoignition kinetics. This resulted in a better prediction of the knock limited spark advance for variations in compression ratio and load [30]. This autoignition correlation for methanol will be used in this study.

7.2.3 Autoignition model for alcohol-blends

A possible solution to calculate the ignition delay of binary or more complex alcohol-gasoline blends would be to have mixing rules which can determine the ignition delay of fuel blends out of the ignition delay of the fuel components. To find a mixing rule, an accurate determination of the ignition delay of the fuel

components and the ignition delay of the fuel blends is needed. There are few measurements of alcohol fuel blends [194–196] and there can be doubt on the accuracy of the measurements when measurements are compared, see Figure 7.3 where the ignition delays of ethanol [197] and an ethanol/iso-octane blends [194] are plotted for the same conditions. There is no clear trend and normally it is expected that the ethanol/iso-octane blend would have a smaller ignition delay than pure ethanol which is not the case here.

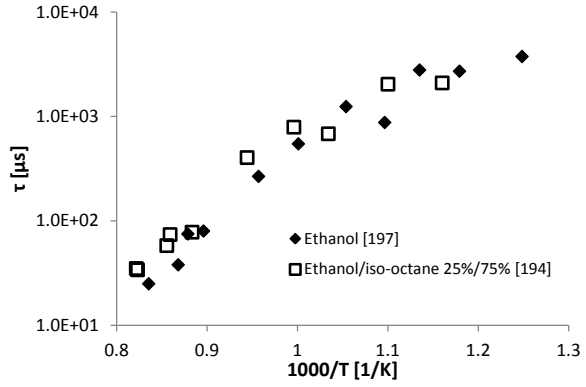

Figure 7.3: Ignition delay times of stoichiometric ethanol-air mixtures and ethanol/iso-octane mixtures at 30 bar [194, 197]

In this study, the empirical model of Yates et al. [35] was used to calculate the ignition delays of blends of primary reference fuels and methanol to investigate if a simple mixing rule could be applied to calculate the ignition delays of alcohol-hydrocarbon blends. Over 1500 detailed chemical kinetic simulations were used to calibrate the model of Yates el al. [35], enabling it to encompass a full range of PRF blends and methanol blends. However, only binary alcohol blends with PRF80 (80 vol% iso-octane and 20 vol% n-heptane) have been used to calibrate the model.The standard deviation of the overall ignition delay prediction of the model of Yates el al. [35] was about 11%. The simplest mixing rules are based on mole, mass, volume or energy fraction:

$$\tau_{blend} = \sum_{i=1}^{n} \alpha_i \tau_i \tag{7.9}$$

In the previous expression α_i is either the mole fraction, mass fraction, volume fraction or energy fraction of the fuel components. The energy fraction can be calculated as follows:

$$\alpha_i = \frac{\Delta cH_i^\circ . x_i}{\sum_{i=1}^{n} \Delta cH_i^\circ . x_i} \tag{7.10}$$

ΔcH_i° is the heat of combustion of the mixture components. x_i is the mole fraction of the fuel components. In Figure 7.4, the mixing rule based on volume fraction was used to predict the ignition delay of a blend of methanol and a PRF fuel. As can be seen, this rule overpredicts the ignition delay for lower temperatures because of the very different values for the ignition delay of methanol and the PRF fuel due to the cool flame behavior of the PRF fuel. This could be solved by using logarithmic values of the ignition delay as follows:

$$\tau_{blend} = \sum_{i=1}^{n} \alpha_i \log(\tau_i) \tag{7.11}$$

or

$$\tau_{blend} = \prod_{i=1}^{n} \tau_i^{\alpha_i} \tag{7.12}$$

In Figure 7.5, this mixing rule is used with the mole and energy fractions of the different fuels. Similar to what was observed for the mixing rules for the laminar burning velocity of methanol-gasoline blends, the energy fraction mixing rule has the best agreement.

This study will test the validity of the mixing rule based on the energy fraction with the logarithmic values of the ignition delay. For the ignition delay of pure methanol, the correlation of Vancoillie et al. [30] will be used and for the ignition delay of gasoline, the model of Yates et al. [35] will be used.

7.3 Knock measurements and detection

To analyze the combustion model's predictive capabilities for knock, a series of measurements were done on a port fuel injected single cylinder CFR engine, described in Section 3.2.1. The main characteristics of this engine are summarized in Table 3.1. The measurements of knock comprise various lambda values and methanol-gasoline ratios. Measurements were done for M0, M50 and M75 at lambda equal to 1, 1.2 and 0.8 and for pure methanol at lambda equal to 1 and 1.2.

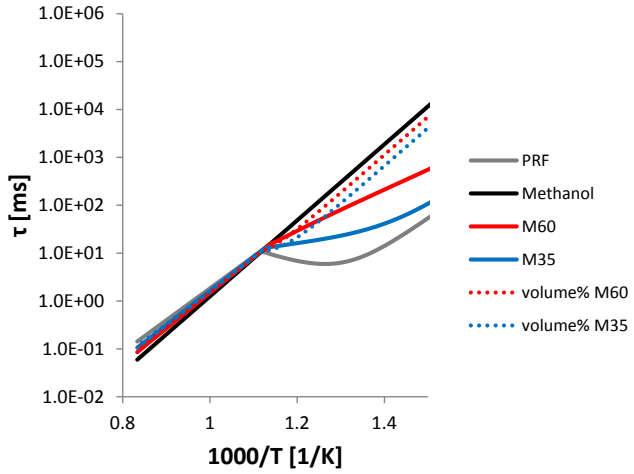

Figure 7.4: Ignition delays of methanol, PRF80 and methanol/PRF blends calculated with the model of Yates et al. [35, 187] and ignition delays calculated with the volume fraction mixing rule

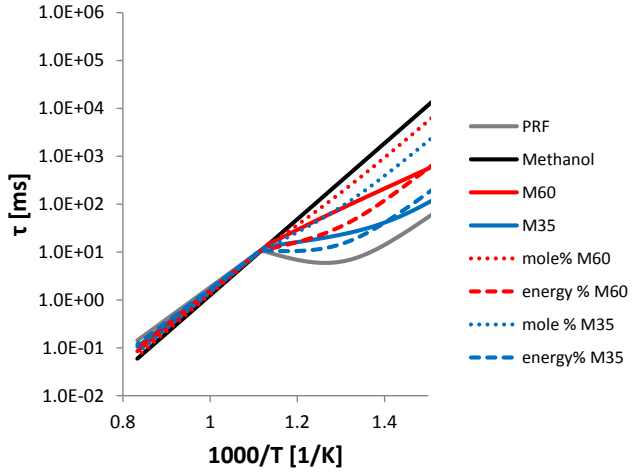

Figure 7.5: Ignition delays of methanol, PRF80 and methanol/PRF blends calculated with the model of Yates et al. [35, 187] and ignition delays calculated with the mole and energy fraction mixing rule (logarithmic values)

The compression ratio was fixed at 9, ignition timing sweeps were performed from non-knocking operation to 100% knock with the throttle opening fixed at 27.5° resulting in an IMEP range from 7.2 to 9 bar and volumetric efficiencies between 83% and 85%. In order to allow an accurate comparison, all measurements were performed on the same day and all parameters were fixed except for the injection duration, ignition timing and the fuel composition.

To validate the proposed knock prediction model, it is crucial to have a knock detection method that can accurately separate knocking from non-knocking cycles, detects the onset of knock oscillations and determines the knock intensity. Several methods exist to detect knock from the raw or filtered cylinder pressure trace. A number of knock algorithms were tested in a previous study [30] and the knock detection method of Worret et al. [198] was selected because it correctly captures knock onset, regardless of variations in ϕ, compression ratio, throttle position and ignition timing and could also discern light knocking cycles. The algorithm of Worret et al. [198] is based on the band-pass filtered heat release rate (3-17 kHz band pass) and uses MAPO (Maximum Amplitude of Pressure Oscillations) and SEPO (Signal Energy of Pressure Oscillations) methods. Knock intensities are calculated based on the integrated signal energy of the filtered heat release rate and determined before and after a potential knock onset to differentiate between knocking oscillations and non-knocking signal noise (see Figure 7.6). Starting from the location of the maximum amplitude of the heat release rate oscillations, knock onset is detected as the first crank angle position where a certain threshold value is exceeded in the filtered heat release rate (see Figure 7.6). The algorithm was implemented as described in [198] and no further adjustment to threshold values or other constants proved necessary throughout the measurement range.

The relevant quantities resulting from the knock analysis are the ratio of knocking cycles to the total number of logged cycles, the average values and standard deviation of knock intensity and crank angle of knock onset for the knocking cycles. As an example Figure 7.7 shows these values plotted as a function of spark advance for stoichiometric fuel-air mixtures of pure gasoline, M50 and pure methanol. It can be seen that as the methanol ratio in the fuel rises from zero to 100% (while the lambda value and throttle position remain constant) the knock ratio exceeds the 10% threshold at more advanced spark timing. Knock intensities also rise as a function of spark advance and knock onset occurs earlier in the cycle for higher methanol fraction because of the more advanced spark timing. For reference, the standard deviations of knock intensity and knock onset position have been added to the plots. As can be seen, the knock intensity is particularly cycle dependent. Increasing the number of logged cycles might help to reduce its standard deviation. The uncertainty in knock onset time is in the range of 1.5-2.5 °ca for most of the cases, which is about the order of magnitude of variations due

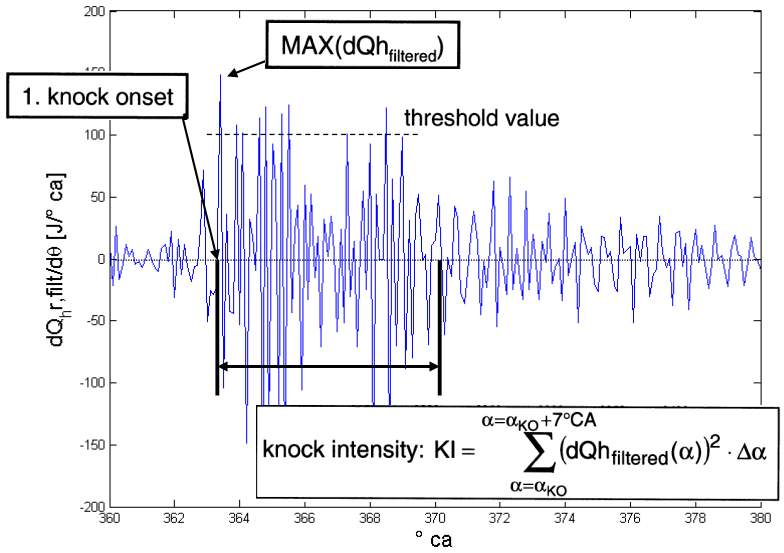

Figure 7.6: Application example of the knock detection algorithm of Worret et al. [198]

to knock onset position, pressure transducer position and the speed of sound [199].

7.4 Knock model validation

7.4.1 Model build-up and calibration

The knock integral framework employing the autoignition delay time correlations of Yates et al. and Vancoillie et al. was implemented in the commercial engine simulation code GT-Power [135] in order to assess its predictive performance. A Three Pressure Analysis, explained in Section 6.4.1, is used to calculate all the necessary engine parameters which are important to predict knock: temperatures, pressure of the unburned mixture and the residual gas fraction in the engine. The measured pressure trace that best corresponded to the average cylinder pressure trace (average of 100 cycles) was always used for this TPA and it was assumed that the mixture in the intake was a completely evaporated methanol/gasoline-air mixture.

The Woschni calibration constants for compression and expansion were chosen for best correspondence between measured and simulated cylinder pressure traces during compression and expansion. The Woschni coefficient during combustion

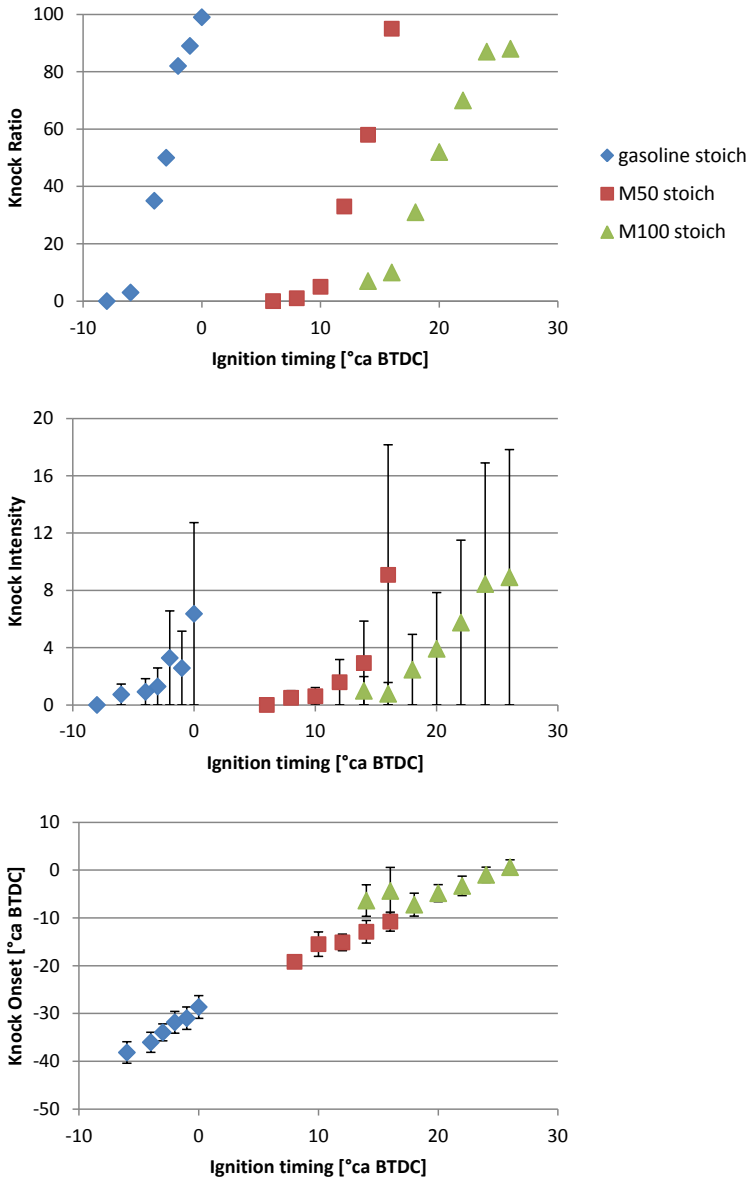

Figure 7.7: Measured knock ratios, knock intensities and knock onsets for stoichiometric operation on gasoline, M50 and methanol

was chosen by ensuring the energy balance between the injected fuel energy and released heat. As a result, the effects of evaporating fuel, the effects of blowby, crevice mass and incomplete combustion will be lumped into this parameter. All Woschni coefficients were kept the same for all simulated cases. The knock prediction model was calibrated by multiplying the knock ignition delay correlation with a factor in order to get autoignition onset exactly at the measured crank angle for a certain reference condition. In this study, this was done for stoichiometric operation at knock limited spark advance for both gasoline and methanol. The calibration factor for the ignition delay correlation of gasoline (Yates et al.) was 0.714 and the calibration factor for the ignition delay correlation of methanol (Vancoillie et al.) was 0.128. The multipliers for the new correlation and that of Yates et al. are markedly low, indicating that the calculated ignition delay is too high. This could be expected since these correlations do not have the effect of hot spots lumped into the correlation's constants which is the case for the correlation of Douaud & Eyzat which was calibrated by engine experiments. Another way of calibrating these correlations would be to artificially increase the unburned mixture temperature to represent hot spots in the unburned mixture [200].

7.4.2 Knock limited spark advance

A crucial performance indicator of the knock prediction models is their ability to distinguish between knocking and non-knocking conditions and predict the knock limited spark advance (KLSA). In this work, the experimental KLSA is taken to be the least advanced spark timing at which the knock ratio is more than 10%. The simulated KLSA is the least advanced spark timing at which the knock integral exceeds 1 before the end of combustion. As the spark timing was experimentally varied in steps of 1 or 2 °ca, the uncertainty on the KLSA is at least 1 or 2 °ca.

In Figure 7.8, the experimental and simulated values for KLSA are plotted as a function of the blend ratio. It can be seen that for stoichiometric, lean and rich mixtures, the experimental KLSA is more advanced than the simulated KLSA. The knock integral exceeds 1 before the end of combustion at less advanced spark timing than the experimental KLSA. This can also be seen in Figure 7.10 where the difference between the measured and simulated KLSA is plotted as a function of the blend ratio. To detect knock, the oscillations resulting from the autoignition of the unburned air-fuel mixture have to be detectable. As mentioned by Richard et al. [201], the influence of the cylinder volume at the instant of knock occurrence could be important. The oscillations are less intense the further knock occurs from top dead center. Secondly, the amount of unburned mixture at the time of

autoignition might have an influence on the knock intensity [30]. Consequently, it could happen that the conditions for autoignition are met but there is no detection of knock because the knock onset is too far from the top dead center or the unburned mixture mass at knock onset is too small. Therefore, a second condition was used in this study to identify knock: there is no knock if the knock onset is too far from the top dead center unless the amount of unburned mixture is large and there is no knock if the amount of unburned mixture at knock onset is too small unless it is very close to the top dead center. The following condition was used. There is knock if :

- The knock integral exceeds 1 before the end of combustion
- Additional condition: $\left|\frac{25}{\theta_{KO}} . \frac{m_{frac,u}}{0.1}\right| > 1$

Where $m_{frac,u}$ is the simulated unburned mass fraction and θ_{KO} is the simulated crank angle (°ca after top dead center) at knock onset. In this study, the unburned mass fraction was used and not the total amount of unburned mixture because the differences in volumetric efficiencies are very small. For load variations with significantly different volumetric efficiencies, the total amount of unburned mixture instead of the unburned mixture fraction might be important. With the measurement done for this study, the influence of engine speed could not be investigated, as well as the influence of the compression ratio. Both properties will have an influence and should probably be included in the additional condition for knock detection. In Figure 7.9 and Figure 7.10, the results can be seen with the additional condition. The simulated KLSA is now closer to the experimental KLSA, especially for the stoichiometric and lean mixtures.

7.4.3 Knock integral at the experimental Knock Onset

Another indication of the model's performance is the value of the knock integral at the experimental knock onset. In Figure 7.11, the value of the knock integral can be seen at the experimental knock onset for gasoline, M50 and pure methanol. Only the measurements for which the knock ratio is more than 10% are shown. It can be seen that with more advanced spark timing the knock integral at knock onset increases for most cases. This increase is stronger for pure methanol than for pure gasoline. This is probably due to the fact that the ignition timing is very different for the measurements on methanol compared to gasoline while the Woschni coefficients of the heat transfer model were kept the same for all simulated cases. The increase of the value of the knock integral with more advanced spark timing is also probably due to an underestimated heat transfer

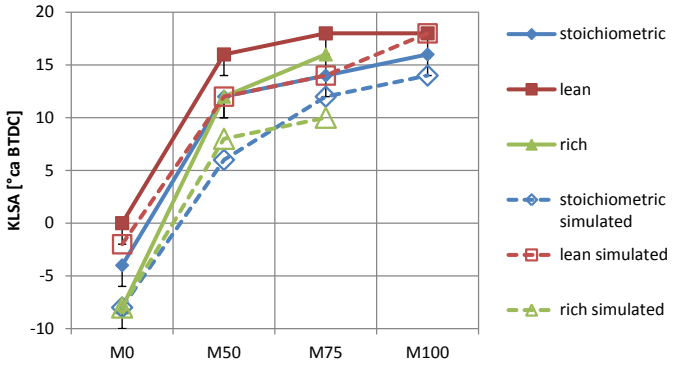

Figure 7.8: Measured and simulated knock limited spark advance (KLSA) as a function of the blend ratio. Simulation based only on the knock integral.

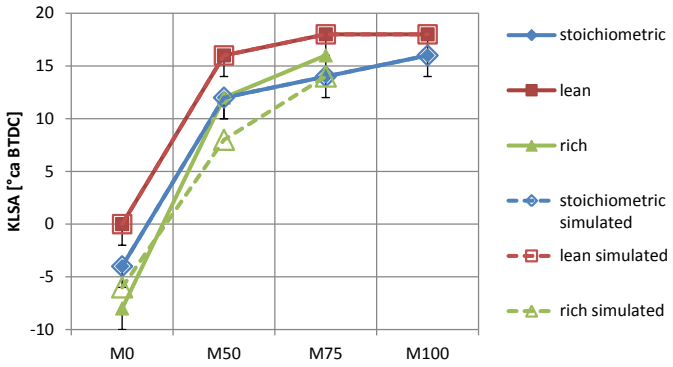

Figure 7.9: Measured and simulated knock limited spark advance (KLSA) as a function of the blend ratio. Simulation based on the knock integral + additional condition.

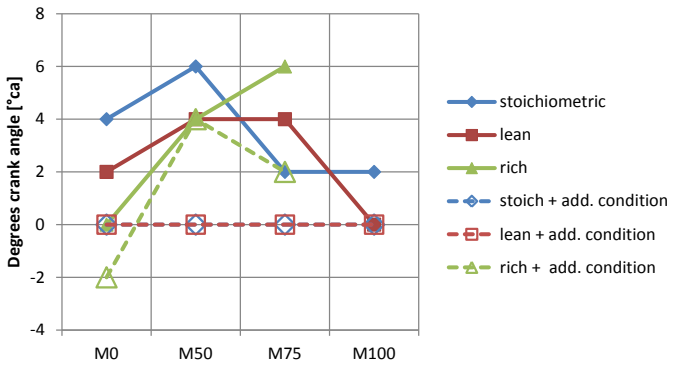

Figure 7.10: Differences between the measured and simulated knock limited spark advance (KLSA) as a function of the blend ratio.——-: Simulation based on the knock integral; - - - - -: Simulation based on the knock integral + additional condition.

by the Woschni model during knock [55]. Heat flux measurements could help to investigate this problem. Heat flux measurements will be part of future research in order to investigate both the evaporative cooling effect and the wall heat transfer. The same measurement techniques can be used as in [55].

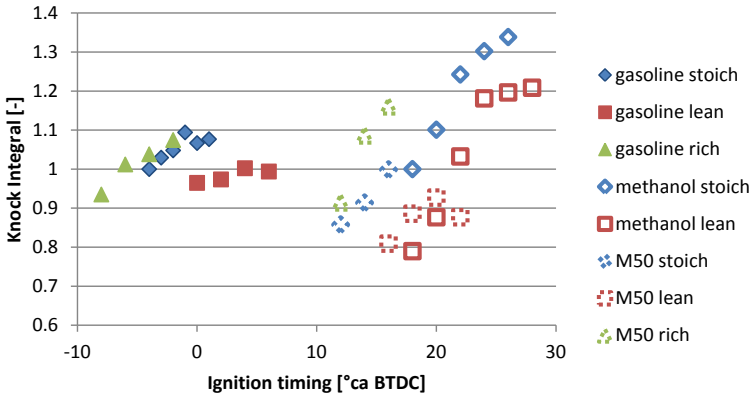

Figure 7.11: Knock integral at the experimental knock onset for gasoline, M50 and methanol as a function of the ignition timing.

7.4.4 Knock intensity

The problem of knock is that it induces damage. The higher the knock intensity, the higher the probability of knock induced damage. As a result, the knock intensity is an important parameter for the design and calibration of the engine. A possible equation for knock intensity was proposed by Bougrine et al. [138].

$$KI = K_1 \left(1 - \frac{m_{frac,b}}{max(1,\phi)}\right)(CR-1)\sqrt{1-\frac{\theta_{KO}}{K_2}}.rpm \tag{7.13}$$

Where K_1 is a calibration constant, K_2 is the maximum crank angle at which knock is still audible (set to 40 °ca ATDC), $m_{frac,b}$ is the burned mass fraction and θ_{KO} is the crank angle of knock onset. In Figure 7.12, the part of the knock intensity equation that changes for the measurements performed during this study, $\left(1-\frac{m_{frac,b}}{max(1,\phi)}\right)\sqrt{1-\frac{\theta_{KO}}{K_2}}$, and the knock intensity that was derived from the knock detection algorithm of Worret et al. [198] are plotted as a function of the spark timing. A calibration constant was used to rescale this part of the equation in order to have the same knock intensity as gasoline at KLSA as was derived from the knock detection algorithm. The same calibration constant was then also used for the gasoline-methanol blends as well as for pure methanol. It can be seen that the equation proposed by Bougrine et al. underpredicts the knock intensity when it is compared to the knock intensity from the knock detection algorithm of Worret el al. [198]. This equation does not take into account the pressure and temperature at knock onset. This could be important because the temperature and the pressure will change going from gasoline to methanol and both the temperature and pressure have an influence on the gas properties and as a result on the knock oscillations. This could be taken into account by entering the crank angle of knock onset at KLSA into the equation as this reflects the necessary conditions for autoignition of the fuel which are influenced by temperature and pressure. Instead of using $\sqrt{1-\frac{\theta_{KO}}{K_2}}$,this could be done as follows:

$$\left(1-\frac{m_{frac,b}}{max(1,\phi)}\right).\left(\frac{\theta_{KO,KLSA}+2-\theta_{knock}}{\theta_{KO}-\theta_{knock}}-1\right) \tag{7.14}$$

Where $\theta_{KO,KLSA}$ is the crank angle of knock onset at KLSA, θ_{KO} is the crank angle of knock onset for the current spark timing and θ_{knock} is the crank angle of knock onset which would be the worst for the intensity of the knock if knock onset was to occur at that crank angle (set to -10 °ca ATDC). The number '2' is entered into the equation to make sure that the knock intensity is not equal to zero at KLSA and

this can be interpreted as the knock intensity being zero when the spark advance is retarded with 2° ca at KLSA. The results are plotted on the same Figures (Figure 7.12) as for the Knock Intensity calculated with the equation of Bougrine et al. The values of the newly developed knock intensity equation (marked with Sileghem) were also rescaled in order to have the same knock intensity as gasoline at KLSA as was derived from the knock detection algorithm. As can be seen on the Figure 7.12, there is a better agreement with the experimental trends. This should however be further investigated for load and engine speed sweeps.

7.4.5 Knock onset crank angle

A last test of the knock prediction models is their ability to reproduce the correct crank angle of knock onset (θ_{KO}). Although this quantity is not of direct use to engine designers, it has an effect on the knock intensity. Figures 7.13, 7.14 and 7.15 show the experimental and simulated crank angle of knock onset for a spark timing sweep. In Figure 7.13, the results are shown for stoichiometric operation, in Figure 7.14 for lean operation and in Figure 7.15 for rich operation. Almost all the knock onsets are predicted within the error margins of the experimental knock onset. A consistent trend for all cases is that the simulated knock onset advances faster with spark advance than the experimental knock onset. This could again be due to an underestimated heat transfer by the Woschni model during knock and heat flux measurements could help to investigate this issue.

Figure 7.16 shows a comparison made between simulated results for stoichiometric, lean and rich operation on M50 where the energy fraction mixing rule together with the logarithmic value of the ignition delays is used as well as a mixing rule based on the volumetric fractions and real values of the ignition delay. This mixing rule generally underpredicts knock more than the energy fraction mixing rule with logarithmic values which could be expected looking at the ignition delay calculated with the volume fraction mixing rules in Figure 7.4. As a result, for the lean mixtures, the simulated KLSA was 2 degrees earlier than the experimental KLSA. The simulated results for knock onset are still reasonable but the differences are larger and outside of the error bars, closer to less advanced spark timing (closer to KLSA).

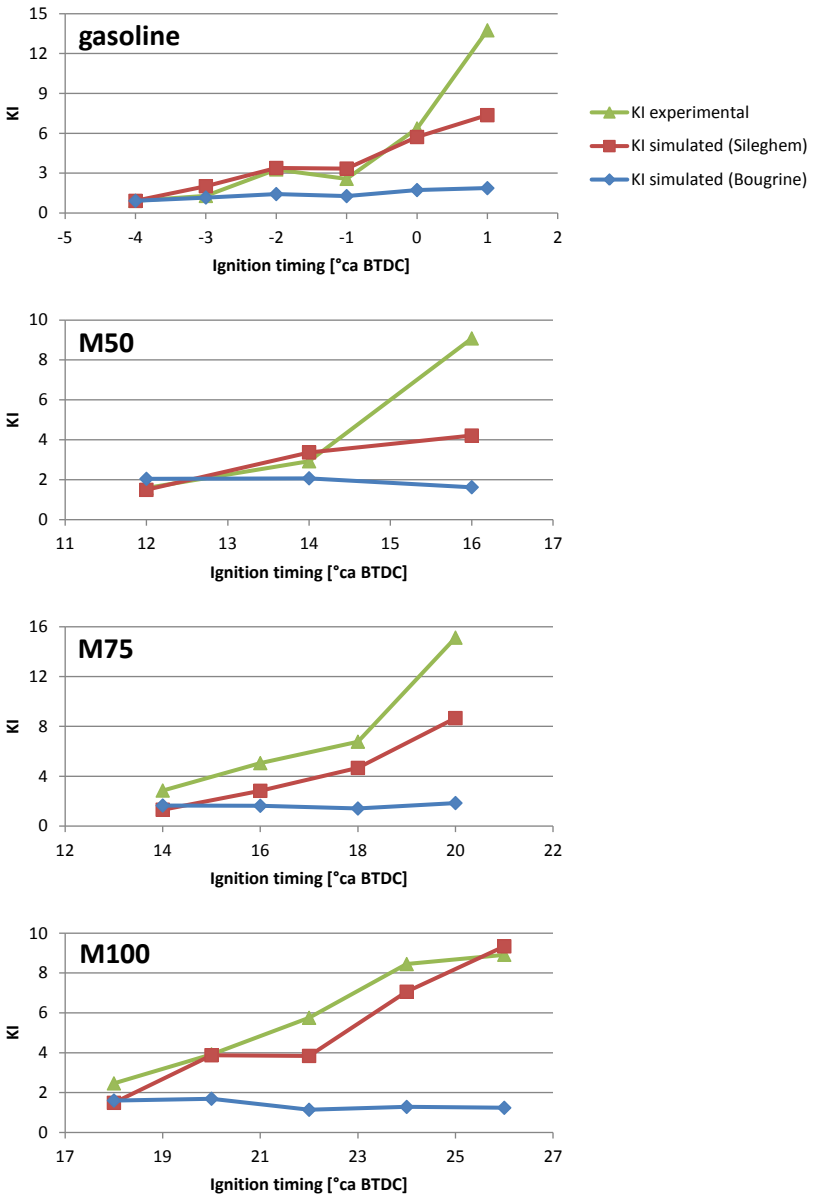

Figure 7.12: Measured and simulated knock intensity for stoichiometric mixtures

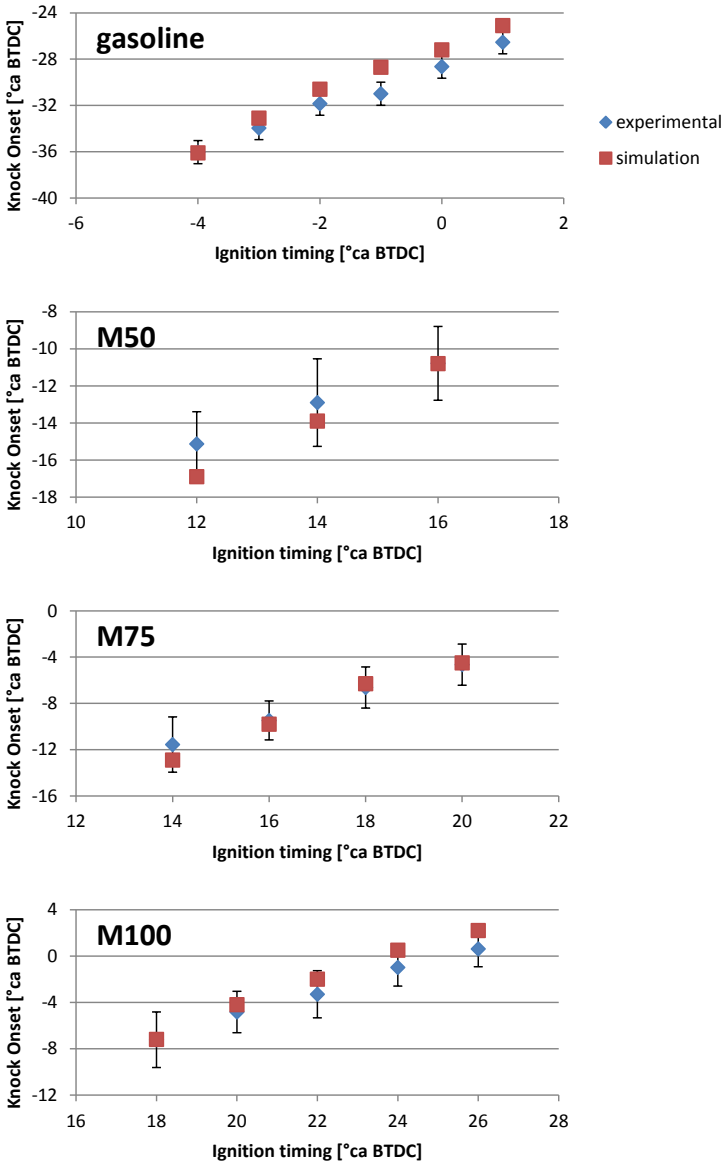

Figure 7.13: Knock Onset stoichiometric mixtures

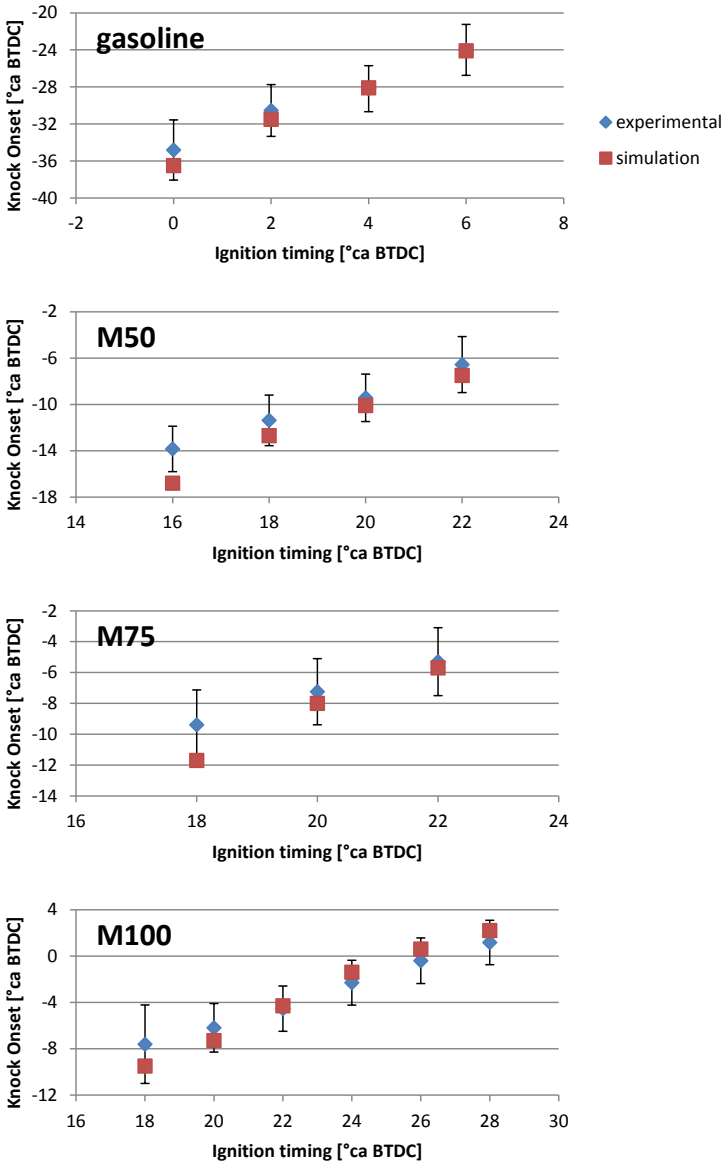

Figure 7.14: Knock Onset lean mixtures

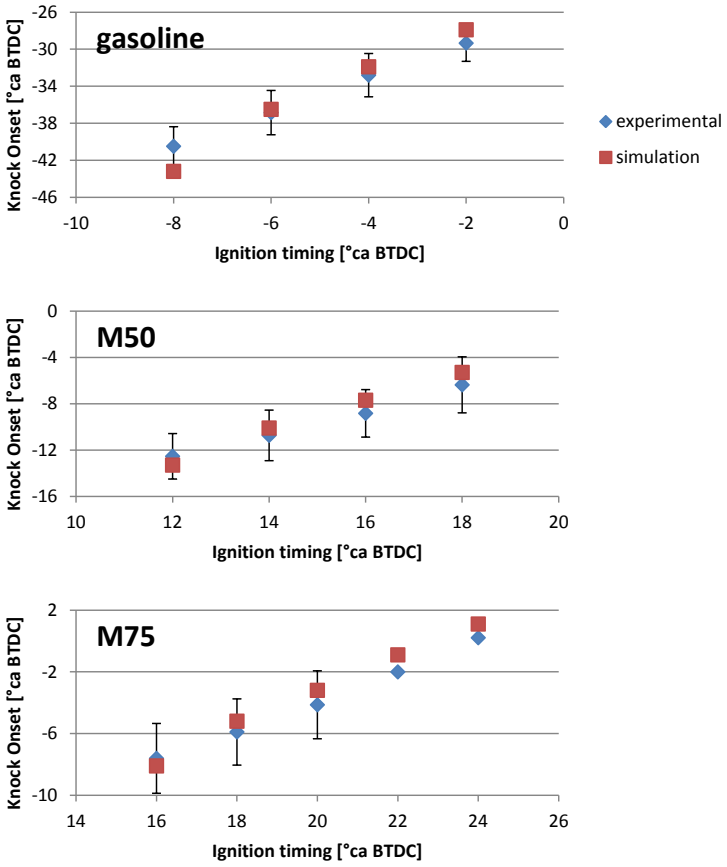

Figure 7.15: Knock Onset rich mixtures

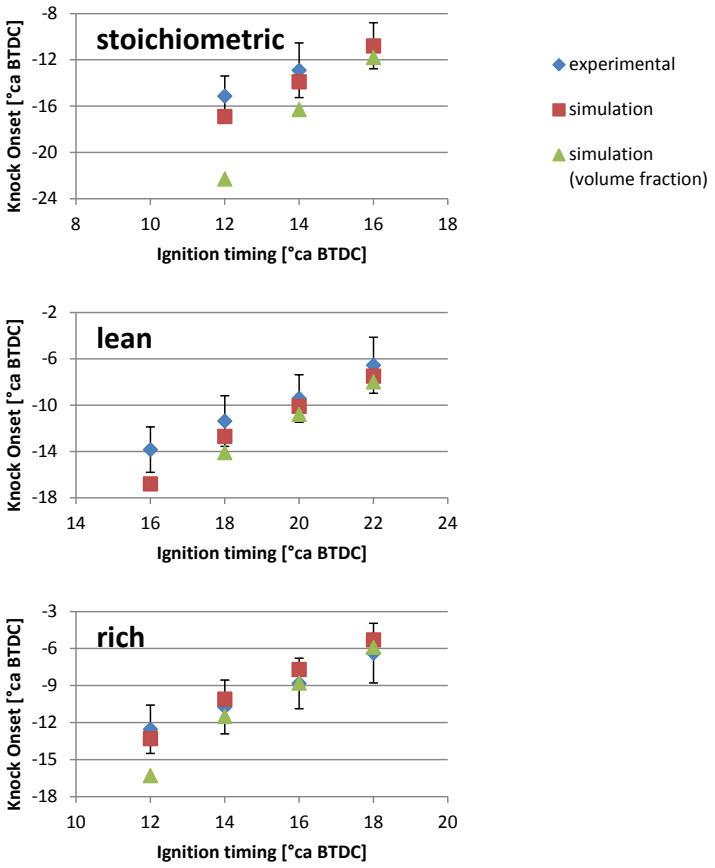

Figure 7.16: Knock Onset: Comparison between the energy fraction mixing rule with logarithmic values and volume fraction mixing rule with real values for M50.

7.5 Conclusion

In order to better understand and predict the knock behavior of alcohol blends, a mixing rule for the autoignition delay time of alcohol-gasoline blends was proposed. This energy-based mixing rule was used together with an autoignition delay time correlation of gasoline and an autoignition delay time correlation of methanol in a knock integral model that was implemented in a two-zone engine code. To validate the proposed model, knock occurrence was experimentally investigated on a CFR engine for four methanol-gasoline blends (gasoline, M50, M75 and M100). Experimental metrics of knock included knock limited spark advance (KLSA), fraction of knocking cycles, knock onset timing and knock intensity based on the signal energy of heat release rate oscillations. The proposed correlation and knock integral approach performed satisfactorily despite the gross simplification associated with two-zone modeling (no hot spots, no cyclic variation). The experimental KLSA was more advanced than the simulated KLSA. The knock integral exceeded 1 before the end of combustion at less advanced spark timing than the experimental KLSA. Therefore, a second condition was used in this study to identify knock based on unburned mass fraction and the crank angle at knock onset which gave better agreement. Secondly, the agreement between the simulated knock intensity and the experimental knock intensity was better if the crank angle of knock onset at KLSA was taken into account as this reflects the necessary conditions for autoignition of the fuel which are influenced by temperature and pressure. Finally, the model was able to predict almost all the knock onsets within the error margins of the experimental knock onset. Further model improvement should focus on better capturing the effects of evaporation cooling and wall heat transfer with heat flux measurements.

8

Conclusions

8.1 Summary of present work and principal contributions

This work started with outlining the potential of light alcohols, methanol and ethanol in particular, as alternative fuels for internal combustion engines. These fuels can be made in a renewable way and they are excellent fuels for internal combustion engines, which is a proven, scalable and relatively cheap technology. The concept of 'electrofuels', in which the fuels are made from renewable electricity and captured CO_2, was explained in the bigger context of the methanol economy: an economy with methanol as fuel, feedstock and energy buffer.

The physico-chemical properties of alcohols and the effect they have on internal combustion engines were discussed in detail, especially the relevant properties of alcohol-gasoline blends that do not scale linearly with the molar content of the individual components. It was explained how ternary blends of gasoline, ethanol and methanol can be formulated that are essentially iso-energetic and iso-stoichiometric to a target binary ethanol-gasoline blend. These ternary GEM (gasoline, ethanol and methanol) blends have the potential to be used as 'drop-in' fuels in flex-fuel vehicles because the relevant properties for internal combustion engines are practically identical. Measurements were done on two engine test

benches to investigate the performance and emissions of alcohols compared to gasoline and to study the concept of the ternary GEM blends in more detail. It was shown that the brake thermal efficiency when running on alcohol fuels is significantly better than with gasoline while emitting fewer emissions. It was clear that methanol was superior both in efficiency and emissions compared to gasoline, ethanol and butanol. For the first time, measurements on engine test benches were done to compare different GEM blends and the engine test results confirmed that, from an engine control point of view, the iso-stoichiometric/iso-energetic GEM blends can indeed be used as 'drop-in' fuels for flex-fuel vehicles.

Due to their polarity, methanol and ethanol are miscible with water and can also absorb water from the atmosphere. Using water-alcohol mixtures could have advantages for internal combustion engines due to the larger cooling effect and there could also be an economic advantage compared to anhydrous alcohol because the alcohol does not have to be fully dried in the production process. This study compared the brake thermal efficiencies and engine-out emissions of several methanol-water blends and ethanol-water blends measured on an engine test bench. It was shown that the brake thermal efficiency did not differ significantly when water was added (up to 20 vol% was added for the ethanol-water blend) and was still higher than the efficiency of gasoline. NOx emissions were also reduced due to the larger cooling effect.

The main goal of the present research was to extend the validity of the quasi-dimensional engine model, originally developed for the power cycle of spark ignition engines fuelled with hydrogen [27] and in a later stage extended to pure methanol and ethanol [28], to alcohol-gasoline blends. Because the laminar burning velocity is a key parameter to model the combustion of fuels in spark ignition engines, a lot of effort went into characterizing the behavior of the laminar burning velocity of alcohol-gasoline blends. Measurements of the laminar burning velocity have been done for gasoline, iso-octane, n-heptane, toluene, methanol, ethanol, a toluene reference fuel and binary and quaternary alcohol-hydrocarbon mixtures for a wide range of temperatures at atmospheric pressure using the heat flux method on a perforated plate burner. Because measurements were done at different temperatures, these measurements could be used to characterize the temperature dependence of the different fuels. This temperature dependence was not yet shown experimentally for some of the fuels, such as toluene. The measurements also resulted in two newly developed laminar burning velocity correlations for methanol and gasoline which were implemented in the engine cycle code. Additionally, the measurements were used to further validate mixing rules for alcohol-gasoline blends, which was first evaluated with simulated data and data from literature. Such a mixing rule can be used to calculate the laminar burning velocity of alcohol-gasoline blends out of the laminar burning velocity

of the components. It was found that a mixing rule which scales the laminar burning velocity of the blend with the energy fraction of the components works very well. This mixing rule can easily be implemented in an engine cycle model without being computationally too demanding. Additionally, it was shown that measurements of a toluene reference fuel reproduced the laminar burning velocity of the gasoline very well. Toluene reference fuels can thus be used as surrogates to replicate the laminar burning velocity of gasoline. In a similar way, a mixing rule for the autoignition delay time of alcohol-gasoline blends was proposed by the author, using data calculated with a model from literature. It was shown that a mixing rule which scales the logarithmic values of the autoignition delay times of the blend components with the energy fraction gave reasonably good agreement.

In the final Chapters, both mixing rules were implemented in the quasi-dimensional engine cycle code and evaluated with engine measurements. The predictive capabilities for the normal combustion were tested for measurements on the CFR engine and the Hyundai direct injection engine fuelled with different methanol-gasoline blends. On the Hyundai engine, a broader measurement range than on the CFR engine was used to get a more general view of the simulation output. In general, the simulations on the Hyundai engine, using the newly developed laminar burning velocity correlations together with the energy-based mixing rule, agreed well with the experimental values. However, some experimental trends were not reproduced correctly both on the CFR engine and Hyundai engine. Uncertainty about the initial flame kernel, uncertainty about the laminar burning velocity at higher pressure and temperature or the inability of the turbulent combustion model to adequately capture the chemical effects were claimed as possible reasons. Consequently, further study of the laminar burning velocity at higher temperatures and pressures is thus needed to lower the uncertainty of these parameters. It was also shown, after optimization of the initial flame kernel to match the experimental ignition delay, that a flame kernel (growth) model that properly accounts for fuel effects could be very effective to improve the simulation results. Finally, different turbulent burning velocity models were tested and due to the inclusion of the Lewis number, the model of Bradley et al. reproduced the trend going from gasoline to methanol much better than the other models. On the Hyundai engine, several other laminar burning velocity correlations of methanol were tested while the correlation for gasoline was kept the same. It was clear that the newly developed correlation of methanol outperformed the other correlations due to the better match with the gasoline correlation. This showed that it is important to match laminar burning velocity correlations of different fuels if the effect of using another fuel than normal (gasoline) needs to be investigated.

Finally, to investigate the capabilities to predict knock for alcohol blends, the

energy-based mixing rule for the autoignition delay time was used together with an autoignition delay time correlation of gasoline and an autoignition delay time correlation of methanol in a knock integral model. Knock occurrence was experimentally investigated on a CFR engine for methanol-gasoline blends. The proposed correlation and knock integral approach performed satisfactorily despite the gross simplification. The model was able to predict almost all the knock onsets of the different operating points within the error margins of the experimental knock onset.

The principal contributions of this Ph.D. study can be summarized as follows: the advantages of (hydrous) alcohol fuels compared to gasoline have been shown on engine test benches (higher efficiency, lower harmful emissions), especially for methanol; engine test results confirmed that, from an engine control point of view, the iso-stoichiometric/iso-energetic GEM blends can be used as 'drop-in' fuels in flex-fuel vehicles; the laminar burning velocity of alcohol fuels has been studied in detail and laminar burning velocity measurements have been done for several hydrocarbons, methanol, ethanol and alcohol blends; a mixing rule for the laminar burning velocity and for the autoignition delay time was proposed based on measurements and/or data from literature and implemented in the engine cycle code; validation of the engine cycle code has been done based on measurements on two engine test benches and pointed out several areas which could be improved.

8.2 Recommendations for future work

As pointed out in the previous Section, there is still uncerntainty in some areas which requires further research. To improve the predictions of the normal combustion of alcohol-gasoline blends, research could focus on the initial flame development, the laminar burning velocity and the turbulent burning velocity. To study the initial flame development, different paths could be taken such as investigation of the initial flame development in a combustion bomb, an optical engine or using CFD to get a better understanding of this process. The newly developed laminar burning velocity correlations for gasoline and methanol used in this study only relied on parameters which were a function of the equivalence ratio while the EGR dependence was even fixed for all conditions. This was done to keep the correlations simple in order to better understand what impact changes in the temperature, pressure or EGR dependence of these correlations could have on the simulation results of the different alcohol-gasoline blends. As pointed out in the Ph.D. study of Vancoillie [28], there are strong interaction effects between equivalence ratio, pressure, temperature and diluent fraction which cannot be captured by most of the existing correlations. Therefore, a more complex

correlation form was proposed by Vancoillie [28]. Future work can focus on developing these complex correlations for different fuels (such as gasoline or gasoline surrogates) and the influence the interactions can have on simulation results. Ideally, these interactions should also be studied experimentally at various conditions of equivalence ratio, temperature, pressure and dilution ratio. To study the laminar burning velocity at higher pressures and temperatures, a combustion bomb can be used. The combustion bomb methods involve central ignition of the mixture inside a constant volume vessel resulting in a spherically expanding flame. Originally, the laminar burning velocity was calculated from the recorded pressure rise after central ignition of the mixture. A more recent method relies on photographic observation of the pre-pressure period of the combustion, where stretch is uniform and well defined. This method also allows determination of Markstein lengths which can be used in turbulent burning velocity models. Additionally, with the aid of some fans, the turbulent burning velocity can be studied in a combustion bomb. This is the reason why during the Ph.D. research, it was decided to adapt the combustion bomb of Ghent University (Ghent University Combustion Chamber I or GUCCI) to be able to measure burning velocities. The GUCCI (Ghent University Combustion Chamber I) setup is a constant volume bomb or constant volume combustion chamber with an internal volume of about 4.1 liters. This setup can be seen in Figure 8.1. This setup was developed at Ghent University starting in 2008 with the purpose of studying diesel injection of marine engines. During this Ph.D. study, some adaptations were done in order to make it possible to do flame speed measurements.

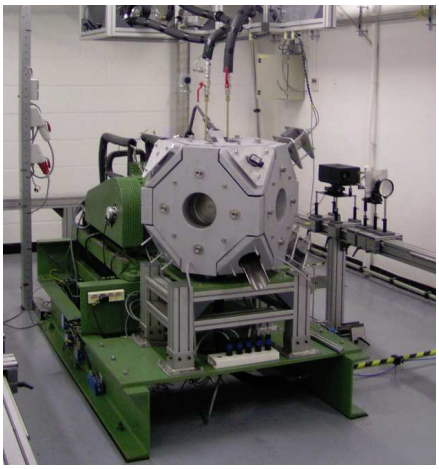

Figure 8.1: GUCCI setup

Two electrodes were developed, which could be entered in the combustion chamber diagonally. When the fuel-air mixture in the chamber is at the right pressure and temperature, a spark can be created between these electrodes to ignite the mixture resulting in a spherically expanding flame which can be recorded with the high speed camera. The design of the electrodes can be seen in Figure 8.2. There was already a gas-filling system to fill to combustion vessel with mixtures of different gases. This was already used to fill the chamber with methane-air mixtures. In order to have fuel-air mixtures with a liquid fuel, a special filling tool with a syringe was developed, see Figure 8.3.

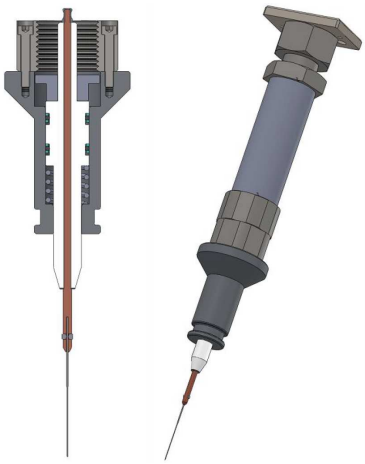

Figure 8.2: Electrodes to ignite the fuel-air mixtures in the GUCCI

Figure 8.3: Filling system for liquid fuels

Preliminary measurements of methane-air mixtures and ethanol-air mixtures have been done on the GUCCI-setup during the Ph.D. research but due to inaccuracy of the initial gas filling system, the repeatability of the measurements was not good enough. In Figure 8.4, spherically expanding methane flames can be seen.

Recently, the gas filling system was improved and now the setup is ready to perform laminar burning velocity measurements.

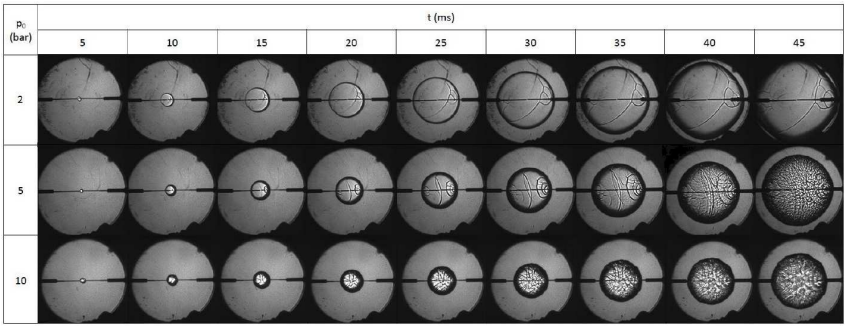

Figure 8.4: Overview of the spherically propagating flame fronts of methane-air mixtures at a series of time steps.

In Chapter 5, it was shown that the laminar burning velocity of fuel blends for which chemical kinetic interactions have the biggest influence, e.g. blends with hydrogen, can probably not be predicted with the mixing rules used in this study. Mixing rules for mixtures with hydrogen could be useful for simulations of complex engine concepts such as the concept proposed by the Massachusetts Institute of Technology. They proposed a methanol engine concept in which the exhaust heat is used to reform the methanol to a mixture of CO and H_2 which could lead to peak efficiencies of 55%-60% [202, 203]. The methanol is catalytically dissociated, using an endothermic process, in a hydrogen-rich gas which has a higher heating value than the original methanol, resulting in higher efficiencies.

For hydrocarbons (such as gasoline), the thermal composition yields, in theory, only hydrogen and carbon:

$$C_nH_m \rightarrow nC + \frac{1}{2}mH_2 \tag{8.1}$$

Jamal and Wyszynski [204] pointed out the difficulty of handling the solid carbon in an automobile and concluded that thermal decomposition of hydrocarbons would not be feasible for on-board reforming.

Because methanol has an oxygen atom, CO can be formed in the reforming process. The thermal decomposition reaction of methanol is:

$$CH_3OH \rightarrow 2H_2 + CO \tag{8.2}$$

Because of very wide flammability limits and the high laminar burning velocity of hydrogen [27], this hydrogen-rich mixture could increase the efficiency of the engine additionally through qualitative control of the air-fuel mixture, avoiding throttling losses. This engine concept could rival fuel cell efficiencies in a cost attractive way. In addition to the laminar burning velocity research of blends of CO, H_2 and methanol, further research is needed to explore the potential of this concept (reforming process, engine experiments, system simulations,...).

Finally, topics which were not or only partly covered during this Ph.D. study are: pollutant formation in alcohol engines, especially the formation mechanisms of aldehydes; the effect of fuel impingement, turbulence generation and mixture inhomogeneity in direct injection engines fuelled with alcohols; and heat flux measurements to get a better understanding of the thermal processes during knock when using alcohol fuels.

List of Appendices

- Appendix A: Flame stretch and flame instabilities
- Appendix B: Laminar burning velocity measurements
- Appendix C: Engine measurements

A

Flame stretch and flame instabilities

Flame stretch and flame instabilities have been expounded extensively by Verhelst [27] and Vancoillie [28]. The overview given in [27, 28] is partly repeated here.

A.1 Laminar premixed flames

The laminar burning velocity u_l is a physicochemical property of the air-fuel-residual gas mixture, and is defined as the speed at which a steady planar flame front propagates in a premixed, quiescent mixture in front of the flame (laminar flow condition), in a direction normal to the plane. It depends on the unburned mixture composition (fuel, ϕ and dilution ratio), temperature and pressure and can only be defined for premixed flames as non-premixed flames do not propagate because the flame is fixed to the interface fuel-air.

It is impossible to create an experimental flame that is truly one dimensionally propagating, planar and adiabatic. Thus, in experimental set-ups, it is important to take the effects of non-planar geometry and flame stretch (see §A.2.1) into account when measuring the burning velocity of laminar flames. The neglect of these effects and the difficulties to correctly capture the influence of non-planar geometry and flame stretch is the main cause of the spread of data on laminar

burning velocities found in the literature. The burning velocity of a non-steady or non-planar flame is designated by u_n. Several methods have been devised to calculate u_l from u_n, which can be measured with an experimental set-up.

When calculating u_l from u_n, it is important to know what exactly has been measured. Gillespie et al. [205] gave an excellent overview:

- the burning velocity based on the entrainment velocity of unburned mixture into the flame:
$$u_n = -\frac{1}{A\rho_u}\frac{dm_u}{dt} \tag{A.1}$$
where A is the flame front area, ρ_u the unburned mixture density and dm_u/dt the rate of entrainment of unburned mixture into the flame front.
- the burning velocity based on the rate of production of burned gas:
$$u_{nr} = -\frac{1}{A\rho_u}\frac{dm_b}{dt} \tag{A.2}$$
where dm_b/dt is the rate of production of reacted gas.

Because of the finite flame thickness, these two definitions do not amount to the same value for experimental flames. Depending on the method of measurement, one or the other quantity is measured (e.g observation of the cold flame front vs. measuring the pressure rise in a combustion bomb).

Finally, there is a distinction between the flame speed (S_n) and the burning velocity (u_n). The flame speed is the sum of the burning velocity u_n and the gas velocity v_g immediately adjacent to the flame front.

$$S_n = v_g + u_n \tag{A.3}$$

In other words, the flame speed is the velocity of the flame front in a fixed frame reference. This difference is especially important for the derivation of u_n from contained explosions.

A.2 Stretch and instabilities

A.2.1 Flame stretch effects

Practical flames are subjected to a strain and curvature effect, which result in flame stretch. The rate of stretch is defined as the normalized rate of change of

an infinitesimal area element of the flame.

$$\alpha = \frac{1}{A}\frac{dA}{dt} \tag{A.4}$$

Flame stretch has a significant effect on the burning velocity. For small to moderate rates of stretch ($< 1000 s^{-1}$) its effect can be expressed to first order by [206]:

$$u_l - u_n = L\alpha \tag{A.5}$$

Where L is a Markstein length. This length is often normalized to obtain a dimensionless Markstein number Ma:

$$Ma = \frac{L}{\delta_l} = \frac{Lu_l}{\nu} \tag{A.6}$$

with δ_l being the laminar flame thickness. This is a characteristic length for a given mixture and initial conditions. Several flame thickness definitions have been proposed in the literature including definitions based on the temperature gradients, characteristic chemical time and the heat release rate. Here, the flame thickness is simply approximated using the hydrodynamic length, where ν is the reactants' kinematic viscosity.

$$\delta_l = \frac{\nu}{u_l} \tag{A.7}$$

Equation A.5 can be non-dimensionalized by multiplying the stretch α by the chemical time δ_l/u_l to obtain the Karlovitz stretch factor Ka:

$$\frac{u_l - u_n}{u_l} = KaMa \tag{A.8}$$

The Markstein length is a physicochemical parameter relevant as a measure for the stretch sensitivity of flames. Both the Karlovitz stretch factor Ka and the Markstein number Ma can be used as parameters in combustion models.

A.2.2 Flame front instabilities

A laminar flame can grow unstable through several mechanisms [106, 206, 207] which will be discussed very briefly in this section. For a more extensive explanation of these mechanisms, the author refers to [27, 28].

The effects a disturbance can have on a flame front are the following:

- The discontinuity of density across the flame front ($\rho_u \rightarrow \rho_b$) causes a hydrodynamic instability, known as the **Darrieus-Landau instability**. Because of a locally decreased gas velocity, a wrinkle of the flame will cause a further protrusion of this flame segment. So when only hydrodynamic stretch is considered, the flame is unconditionally unstable.

- When a less-dense fluid (burned gases) is present beneath a more-dense fluid (unburned gases), an instability arises from gravitational effects. This buoyant instability is known as the **Rayleigh-Taylor instability**.

- Flame instability can be triggered through unequal diffusivities. A perturbation of the balance between diffusivities will have important effects. Three diffusivities are of importance: the thermal diffusivity of the unburned mixture (D_T), the mass diffusivity of the deficient reactant ($D_{M,lim}$) and the mass diffusivity of the excess reactant ($D_{M,exc}$). In a lean flame the deficient reactant is the fuel, in a rich flame it is oxygen. The ratio of the thermal diffusivity of the unburned mixture to the mass diffusivity of the deficient reactant is called the Lewis number *Le*:

$$Le = \frac{D_T}{D_{M,lim}} \tag{A.9}$$

  If the Lewis number is greater than unity, the thermal diffusivity exceeds the mass diffusivity of the limiting reactant. When this is the case, a wrinkled flame front will see its parts that are 'bulging' towards the unburned gases lose heat more rapidly than diffusing reactants can compensate for. The parts that recede in the burned gases, on the contrary, will increase in temperature more rapidly than being depleted of reactants. As a result, the flame speed of the 'crests' will decrease and the flame speed of the 'troughs' will increase, which counteracts the wrinkling and promotes a smooth flame front. The mixture is then **thermo-diffusively stable**. Similar reasoning shows that a Lewis number smaller than unity indicates unstable behavior.

  Another mechanism involving unequal diffusivities is the following: when the limiting reactant diffuses more rapidly than the excess reactant ($D_{M,lim} > D_{M,exc}$), it will reach a bulge of the flame front into the unburned gases more quickly and cause a local shift in mixture ratio towards stoichiometry, which will increase the local flame speed. Thus, a perturbation is amplified and the resulting instability is termed **preferential diffusion instability**. This mechanism is easily illustrated by the propensity of rich heavier-than-air fuels (e.g. propane/air, iso-octane/air) and lean lighter-than-air fuels (e.g. methane/air, hydrogen/air) to develop cellular flame fronts [207].

A positive Markstein length (see §A.2.1) indicates a diffusionally stable flame, as flame stretch decreases the burning velocity. Any disturbances of the flame front

will thus tend to be smoothed out. On the other hand, a negative Markstein length indicates an unstable flame which will develop into a cellular flame because of a perturbation.

B

Laminar burning velocity measurements

B.1 Flat flame burner measurements

Table B.1: Laminar burning velocities (cm/s) of gasoline-air flames at different initial temperatures

u_l	T_u					
ϕ	298 K	318 K	328 K	338 K	348 K	358 K
0.7	18.1	21.0	22.5	24.0	25.8	27.3
0.8	24.6	28.8	30.3	32.2	34.4	35.8
0.9	30.2	34.8	36.6	38.4	40.8	42.3
1.0	34.0	38.5	40.4	42.3	44.8	46.4
1.1	35.7	39.5	41.5	43.5	45.9	47.7
1.2		37.7	39.7	41.6	43.6	45.6
1.3		32.1	34.4	36.0	37.4	39.7

error	T_u					
ϕ	298 K	318 K	328 K	338 K	348 K	358 K
0.7	0.8	0.5	0.3	0.5	0.4	0.6
0.8	0.6	0.5	0.5	0.5	0.6	0.5
0.9	0.6	0.5	0.6	0.5	0.5	0.6
1.0	0.5	0.6	0.6	0.6	0.6	0.7
1.1	0.7	0.6	0.6	0.6	0.7	0.7
1.2		0.8	0.9	0.9	0.8	0.9
1.3		1.0	1.1	1.4	1.0	1.1

Table B.2: Laminar burning velocities (cm/s) of iso-octane-air flames at different initial temperatures

u_l	T_u				
ϕ	298 K	318 K	328 K	338 K	358 K
0.7	16.2	18.6	19.9	21.2	23.6
0.8	23.5	26.4	27.9	29.4	32.4
0.9	29.2	32.6	34.2	36.0	39.7
1.0	32.8	36.4	38.3	40.1	44.3
1.1	33.9	37.6	39.6	41.4	45.7
1.2	32.3	35.9	37.8	39.7	44
1.3	27.3	30.4	32.7	33.9	39

error	T_u				
ϕ	298 K	318 K	328 K	338 K	358 K
0.7	0.7	0.4	0.5	0.4	0.4
0.8	0.7	0.6	0.6	0.6	0.5
0.9	0.7	0.5	0.6	0.6	0.7
1.0	0.6	0.6	0.7	0.7	0.8
1.1	0.6	0.6	0.8	0.7	0.7
1.2	0.9	0.9	0.9	1.0	0.9
1.3	1.2	1.1	1.2	1.2	1.3

Table B.3: Laminar burning velocities (cm/s) of n-heptane-air flames at different initial temperatures

u_l	T_u				
ϕ	298 K	318 K	328 K	338 K	358 K
0.7	19.8	22.5	24.0	25.7	28.1
0.8	27.4	30.9	32.7	34.5	38.2
0.9	33.5	37.2	39.1	41.2	45.4
1.0	37.4	41.3	43.3	45.6	50.1
1.1	38.7	42.7	45.0	47.2	51.7
1.2	37.2	41.2	43.4	45.5	49.9
1.3	32.1	35.9	37.4	39.5	43.9

error	T_u				
ϕ	298 K	318 K	328 K	338 K	358 K
0.7	0.6	0.6	0.5	0.4	0.4
0.8	0.8	0.6	0.6	0.6	0.6
0.9	0.6	0.6	0.6	0.6	0.6
1.0	0.6	0.6	0.6	0.7	0.7
1.1	0.7	0.7	0.8	0.8	0.8
1.2	0.9	0.9	0.9	0.9	0.9
1.3	1.1	1.1	1.0	1.1	1.1

Table B.4: Laminar burning velocities (cm/s) of toluene-air flames at different initial temperatures

u_l	T_u				
ϕ	298 K	318 K	328 K	338 K	358 K
0.7	19.0	21.6	22.8	24.3	27.7
0.8	25.9	29.0	30.5	32.3	36
0.9	31.1	34.7	36.3	38.0	42.2
1.0	34.1	37.8	39.5	41.5	45.7
1.1	34.8	38.5	40.2	42.3	46.6
1.2	33.0	36.5	38.4	40.3	44.5
1.3	28.1	31.6	33.2	35.2	38.9

error	T_u				
ϕ	298 K	318 K	328 K	338 K	358 K
0.7	0.7	0.5	0.5	0.4	0.5
0.8	0.7	0.5	0.5	0.6	0.5
0.9	0.6	0.7	0.7	0.6	0.7
1.0	0.6	0.6	0.6	0.7	0.7
1.1	0.6	0.7	0.7	0.8	0.8
1.2	0.9	0.9	1.0	0.9	1.0
1.3	1.1	1.2	1.2	1.2	1.2

Table B.5: Laminar burning velocities (cm/s) of methanol-air flames at different initial temperatures

u_l	T_u				
ϕ	298 K	318 K	328 K	338 K	358 K
0.7	18.2	20.8	22.3	23.9	28.1
0.8	27.3	30.9	32.5	34.5	39.2
0.9	35.1	39.0	41.0	43.1	47.6
1.0	41.1	45.3	47.6	50.1	54.8
1.1	44.0	48.4	50.9	53.4	58.6
1.2	44.7	49.2	51.6	54.3	59.4
1.3	42.6	47.0	49.3	52.0	57.2
1.4	37.6	41.7	44.4	46.5	51.5
1.5	31.3	35.2	37.1	39.5	43.9

error	T_u				
ϕ	298 K	318 K	328 K	338 K	358 K
0.7	0.8	0.6	0.6	0.5	0.5
0.8	0.7	0.6	0.6	0.6	0.7
0.9	0.7	0.6	0.6	0.7	0.7
1.0	0.7	0.5	0.7	0.8	0.8
1.1	0.6	0.7	0.7	0.7	0.8
1.2	0.8	0.8	0.7	0.8	0.8
1.3	0.9	0.8	0.8	0.9	1.0
1.4	0.9	0.8	1.0	0.9	1.0
1.5	1.0	1.0	0.9	1.1	1.0

Table B.6: Laminar burning velocities (cm/s) of ethanol-air flames at different initial temperatures

u_l	T_u				
ϕ	298 K	318 K	328 K	338 K	358 K
0.7	20.2	23.2	24.8	26.5	30.2
0.8	28.5	32.1	34.0	36.0	40.6
0.9	35.1	39.1	41.2	43.4	48.1
1.0	39.6	43.8	46.0	48.3	53.3
1.1	41.7	46.0	48.3	50.7	55.7
1.2	40.8	45.0	47.2	49.7	54.4
1.3		40.3	42.3	44.8	49.0
1.4		32.3	34.1	36.1	40.3

error	T_u				
ϕ	298 K	318 K	328 K	338 K	358 K
0.7	0.7	0.6	0.4	0.5	0.5
0.8	0.7	0.5	0.5	0.5	0.6
0.9	0.6	0.5	0.6	0.6	0.6
1.0	0.6	0.6	0.6	0.6	0.7
1.1	0.6	0.6	0.7	0.7	0.8
1.2	0.7	0.7	0.7	0.8	0.8
1.3		0.8	0.8	0.9	0.9
1.4		0.9	0.8	0.9	1.1

Table B.7: Laminar burning velocities (cm/s) of a toluene reference fuel at different initial temperatures

u_l	T_u				
ϕ	298 K	318 K	328 K	338 K	358 K
0.7	18.6	21.2	22.6	24.1	27.7
0.8	25.8	29	30.7	32.5	36.2
0.9	31.4	35	36.7	38.7	42.9
1	34.8	38.6	40.4	42.5	46.7
1.1	35.8	39.6	41.5	43.5	47.9
1.2	33.8	37.8	39.6	41.6	46
1.3	29.4	32.8	34.3	36.4	40.6

error	T_u				
ϕ	298 K	318 K	328 K	338 K	358 K
0.7	0.8	0.5	0.5	0.5	0.6
0.8	0.7	0.5	0.6	0.6	0.6
0.9	0.6	0.6	0.5	0.6	0.7
1.0	0.6	0.6	0.6	0.7	0.7
1.1	0.6	0.7	0.7	0.8	0.8
1.2	0.8	0.9	1.0	1.0	1.0
1.3	1.5	1.3	1.3	1.3	1.3

Table B.8: Laminar burning velocities (cm/s) of a blend of 25% v/v ethanol and 75% v/v iso-octane at different initial temperatures

u_l	T_u	
ϕ	338 K	358 K
0.7	22.4	25.2
0.8	30.9	34.2
0.9	37.4	41.4
1.0	41.5	46.0
1.1	42.9	47.3
1.2	41.2	45.3
1.3	35.8	39.4

error	T_u	
ϕ	338 K	358 K
0.7	0.6	0.4
0.8	0.6	0.5
0.9	0.5	0.6
1.0	0.7	0.7
1.1	0.7	0.8
1.2	0.9	0.9
1.3	1.2	1.1

Table B.9: Laminar burning velocities (cm/s) of a blend of 50% v/v ethanol and 50% v/v iso-octane at different initial temperatures

u_l	T_u				
ϕ	298 K	318 K	328 K	338 K	358 K
0.7	17.8	20.5	21.8	23.4	27.2
0.8	25.7	28.6	30.1	31.9	35.6
0.9	31.7	34.8	36.7	38.6	43.0
1.0	35.4	38.7	40.7	42.8	47.4
1.1	36.6	40.2	42.2	44.3	48.8
1.2	34.9	38.7	40.5	42.7	47.0
1.3	29.8	33.7	35.3	37.1	41.1

error	T_u				
ϕ	298 K	318 K	328 K	338 K	358 K
0.7	0.8	0.6	0.5	0.4	0.6
0.8	0.6	0.6	0.6	0.5	0.6
0.9	0.6	0.6	0.6	0.6	0.6
1.0	0.6	0.5	0.6	0.6	0.7
1.1	0.7	0.7	0.7	0.7	0.7
1.2	0.8	0.8	0.8	0.8	0.9
1.3	1.1	1.1	1.1	1.0	1.0

Table B.10: Laminar burning velocities (cm/s) of a blend of 75% v/v ethanol and 25% v/v iso-octane at different initial temperatures

u_l	T_u				
ϕ	298 K	318 K	328 K	338 K	358 K
0.7	18.9	21.7	23.1	24.8	28.7
0.8	26.7	30.1	31.8	33.7	38.1
0.9	33.0	36.7	38.6	40.8	45.0
1.0	37.0	41.1	43.0	45.1	49.8
1.1	38.8	42.8	44.9	47.1	51.8
1.2	37.6	41.7	43.6	45.8	50.4
1.3		36.8	38.7	40.8	45.0

error	T_u				
ϕ	298 K	318 K	328 K	338 K	358 K
0.7	0.8	0.5	0.6	0.5	0.5
0.8	0.7	0.6	0.5	0.6	0.7
0.9	0.6	0.6	0.6	0.7	0.7
1.0	0.6	0.6	0.6	0.6	0.8
1.1	0.7	0.7	0.7	0.8	0.8
1.2	0.8	0.8	0.8	0.8	0.9
1.3		1.0	1.1	1.1	1.0

Table B.11: Laminar burning velocities (cm/s) of a blend of 75% v/v methanol and 25% v/v iso-octane at different initial temperatures

u_l	T_u				
ϕ	298 K	318 K	328 K	338 K	358 K
0.7	17.4	20.1	21.6	23.2	26.8
0.8	25.9	29.3	31.1	33.0	37.0
0.9	32.9	36.7	38.6	40.6	45.0
1.0	37.7	41.7	43.8	46.0	50.6
1.1	40.1	44.3	46.5	48.8	53.6
1.2	39.9	44.0	46.2	48.4	53.3
1.3	36.6	40.6	42.7	44.9	49.5

error	T_u				
ϕ	298 K	318 K	328 K	338 K	358 K
0.7	0.9	0.6	0.5	0.6	0.5
0.8	0.8	0.6	0.6	0.6	0.6
0.9	0.7	0.6	0.6	0.6	0.7
1.0	0.7	0.6	0.6	0.7	0.7
1.1	0.6	0.7	0.7	0.7	0.8
1.2	0.7	0.7	0.7	0.7	0.8
1.3	0.8	0.8	0.8	0.8	0.9

Table B.12: Laminar burning velocities (cm/s) of a blend of 25% v/v methanol, 25% v/v ethanol, 25% v/v iso-octane and 25% v/v n-heptane at different initial temperatures

u_l	T_u				
ϕ	298 K	318 K	328 K	338 K	358 K
0.7	18.6	21.3	22.8	24.5	28.0
0.8	26.7	30.0	31.7	33.6	37.7
0.9	33.1	36.7	38.7	40.7	45.0
1.0	37.2	41.1	43.2	45.4	49.9
1.1	39.0	43.0	45.1	47.3	51.9
1.2	37.8	41.8	43.9	46.1	50.7
1.3	33.2	37.1	39.0	41.2	45.6

error	T_u				
ϕ	298 K	318 K	328 K	338 K	358 K
0.7	1.0	0.6	0.6	0.5	0.5
0.8	0.8	0.7	0.6	0.5	0.6
0.9	0.8	0.6	0.6	0.6	0.7
1.0	0.6	0.6	0.6	0.6	0.7
1.1	0.6	0.6	0.7	0.7	0.7
1.2	0.8	0.8	0.8	0.8	0.9
1.3	1.0	1.1	1.0	1.0	1.0

B.2 Detailed composition of the gasoline

Table B.13: Detailed composition of the gasoline used for the laminar burning velocity measurements

Compound name	wt%	type
1.1.3-trimethyl-cyclopentane	0.124	naphthenes
1.2.3-trimethyl cyclohexane	0.037	naphthenes
1.2.4 trimethylbenzene	0.913	monoaromatics
1.2.4 trimethylcyclopentane	0.199	naphthenes
1.2-dimethyl cyclopentane. (E)-	0.521	naphthenes
1.2-dimethyl cyclopentane. (Z)-	0.376	naphthenes
1.3.5-trimethylbenzene	1.385	monoaromatics
1.3-dimethyl-cyclopentane. (E)-	0.388	naphthenes
1-butene	0.059	olefines
1-ethyl-2-methyl benzene	1.309	monoaromatics
1-ethyl-3-methyl benzene	4.932	monoaromatics
1-ethyl-3-methyl-benzene	4.657	monoaromatics
1-hexene	0.092	olefines
1-methyl indane	0.069	naphthenoaromatics
1-pentene	0.3	olefines
2.2.3-trimethyl-butane	0.045	isoparaffines
2.2-dimethyl butane	0.082	isoparaffines
2.3.3-trimethyl-pentane	2.962	isoparaffines
2.3.4-trimethyl-pentane	3.332	isoparaffines
2.3-dimethyl heptane	0.172	isoparaffines
2.3-dimethyl-2-butene	0.889	olefines
2.3-dimethyl-butane	0.678	isoparaffines
2.3-dimethyl-hexane	0.897	isoparaffines
2.3-dimethyl-octane	0.285	isoparaffines
2.4-dimethyl-pentane	0.898	isoparaffines
2.5-dimethyl heptane	0.075	isoparaffines
2.5-dimethyl-hexane	2.262	isoparaffines
2-butene	0.045	olefines
2-hexene	0.203	olefines
2-methyl butane	8.374	isoparaffines
2-methyl heptane	1.413	isoparaffines

2-methyl hexane	2.279	isoparaffines
2-methyl indane	0.061	naphthenoaromatics
2-methyl-1-butene	0.49	olefines
2-methyl-1-pentene	0.35	olefines
2-methyl-2-butene	1.016	olefines
2-methylpentane	2.448	isoparaffines
2-pentene. (E)-	0.839	olefines
2-pentene. (Z)-	0.403	olefines
3.3-dimethyl-1.4-pentadiene	0.23	olefines
3.3-dimethyl-pentane	0.039	isoparaffines
3-heptene	0.13	olefines
3-methyl heptane	1.355	isoparaffines
3-methyl hexane	1.365	isoparaffines
3-methyl pentane	1.4	isoparaffines
3-methyl-2-hexene	0.158	olefines
3-methyl-2-pentene	0.326	olefines
benzene	1.13	monoaromatics
benzene. 1-ethyl-4-methyl-	0.213	monoaromatics
Butane	2.077	paraffines
C10 aromatics	2.684	monoaromatics
C11 aromatics	0.297	monoaromatics
C7H16	5.716	isoparaffines
C8H14 cyclo	0.079	naphthenes
cyclohexane	1.474	naphthenes
cyclohexane. ethyl-	0.089	naphthenes
cyclopentane	0.84	naphthenes
cyclopentane. propyl-	0.043	naphthenes
cyclopentene	0.147	naphthenes
decane	0.024	paraffines
ethylbenzene	0.658	monoaromatics
ethyl-cyclopentane	0.113	naphthenes

heptane	2.193	paraffines
hexane	2.651	paraffines
i-C2 cyclohexane	0.775	naphthenes
i-C3 cyclohexane	0.362	naphthenes
i-C3 cyclopentane	0.17	naphthenes
i-C4 cyclohexane	0.038	naphthenes
indane	0.282	naphthenoaromatics
indene	0.014	naphthenoaromatics
Isobutane	0.112	isoparaffines
isoparaffin C10	0.371	isoparaffines
isoparaffin C11	1.339	isoparaffines
isoparaffin C12	0.307	isoparaffines
isoparaffin C8	1.066	isoparaffines
isoparaffin C9	0.931	isoparaffines
methyl cyclopentane	1.847	naphthenes
methyl-3-hexene	0.118	olefines
methylcyclohexane	1.364	naphthenes
methyl-cyclopentene	0.373	naphthenes
naphthalene	0.072	diaromatics
nonane	0.076	paraffines
octane	0.848	paraffines
o-xylene	0.633	monoaromatics
pentane	2.446	paraffines
propyl benzene	1.104	monoaromatics
tetraline	0.057	naphthenoaromatics
tetramethyl cyclopentane	0.023	naphthenes
toluene	12.503	monoaromatics
trans-1-ethyl-2-methyl cyclohexane	0.01	naphthenes
undecane	0.053	paraffines
xylene (m. p)	1.421	monoaromatics

C

Engine Measurements

C.1 Knock detection

This section describes the knock detection method of Worret et al. reported in [198]. The method is based on the high pass filtered heat release. The heat release of each cycle is calculated according to:

$$\frac{\mathrm{d}Q_h}{\mathrm{d}\alpha} = \frac{\gamma}{\gamma-1} \cdot p \cdot \frac{\mathrm{d}V}{\mathrm{d}\alpha} + \frac{1}{\gamma-1} \cdot V \cdot \frac{\mathrm{d}p}{\mathrm{d}\alpha} \tag{C.1}$$

Where $\mathrm{d}Q_h/\mathrm{d}\alpha$ is the heat release rate, γ is the ratio of specific heats, p and V are the cylinder pressure and volume respectively. This signal is high-pass filtered with a cut-off frequency of 3 kHz.

A threshold value for the filtered heat release rate is defined by using TV_{factor} = 0.65 in Equation C.2.

$$TV = max(\mathrm{d}Q_{h,filtered}) \cdot TV_{factor} \tag{C.2}$$

The high-pass filtered heat release signal is scanned for the first value exceeding the threshold (TVE) in the reverse direction of the time axis. In addition a potential point of knock onset is determined by detecting the first sign change before TVE.

If the point is within the given time window, knock intensity (KI) is calculated according to Equation C.3, and given the designation $KI_{measured}$.

$$KI = \frac{1}{6 \cdot n} \cdot \text{resolution} \cdot \sum_{\alpha=\alpha_{KO}}^{\alpha=\alpha_{KO}+7\,\text{deg}\,ca} (\text{d}Q_{h,filtered}(\alpha))^2 \cdot \text{d}\alpha \tag{C.3}$$

If $KI_{measured}$ is higher than a fixed threshold knock intensity ($TV_{KI} = 15 \cdot 10^{-4}$ [J^2]), TV_{factor} is halved. Reducing the TV target for knocking cycles allows a further search for TVE in the reverse direction of the time axis. A TV_{factor} of 0.65 is normally not sufficient to detect the real knock onset for severe knocking cycles. However, the TV_{factor} can be halved only once.

Furthermore, a comparison between a measured and calculated knock intensity ratio (KIR) is carried out. $KIR_{measured}$ can be determined by means of:

$$KIR_{measured} = KIaKO_{measured} / KIbKO_{measured} \tag{C.4}$$

where $KIaKO_{measured}$ corresponds to the knock intensity $KI_{measured}$ and $KIbKO_{measured}$ is calculated according to $KIaKO_{measured}$, but starting at 7 °ca before knock onset.

A rated knock intensity ratio can be calculated according to:

$$KIR_{calculated} = 3 + (15.5 \cdot e^{-0.6 \cdot KI_{measured}}) \tag{C.5}$$

If $KIR_{measured}$ is greater than $KIR_{calculated}$, knock can be detected reliably. If the value is lower, the signal is in the range of the noise level.

C.2 Error Analysis

This appendix summarizes the error analysis carried out to judge the quality of the measurement results. The analysis is conducted according to the methods described by Taylor [208] and determines the experimental uncertainty of calculated variables based on known errors of variables that are directly measured. The following general equation is used to calculate the propagation of the errors in a random function $q = f(x_1, x_2, ..., x_n)$:

$$\delta q = \sqrt{\left(\frac{\delta q}{\delta x_1}\right)^2 + \left(\frac{\delta q}{\delta x_2}\right)^2 + ... + \left(\frac{\delta q}{\delta x_n}\right)^2} \tag{C.6}$$

The partial derivatives in the equation express the sensitivity of the absolute error of q to that of a certain influential variable (x_1, x_2, ... x_n).

The error analysis has been extensively described in previous works and will not be repeated here.

References

[1] S. Verhelst, Future vehicles will be driven by electricity, but not as you think, Proceedings of the IEEE 102 (10) (2014) 1399–1403.

[2] D. Abbott, Keeping the energy debate clean: How do we supply the world's energy needs?, Proceedings of the IEEE 98 (1) (2010) 42–66.

[3] E. Alonso, A. M. Sherman, T. J. Wallington, M. P. Everson, F. R. Field, R. Roth, R. E. Kirchain, Evaluating rare earth element availability: A case with revolutionary demand from clean technologies, Environmental Science & Technology 46 (6) (2012) 3406–3414.

[4] R. J. Pearson, J. W. G. Turner, A. J. Peck, Gasoline-ethanol-methanol tri-fuel vehicle development and its role in expediting sustainable organic fuels for transport, in: IMechE Low Carbon Vehicles Conference, London, UK, 2009, pp. 1–21.

[5] J. W. G. Turner, R. J. Pearson, R. Purvis, E. Dekker, Gem ternary blends: Removing the biomass limit by using iso-stoichiometric mixtures of gasoline, ethanol and methanol, SAE paper no. 2011-24-0113 (2011).

[6] J. W. G. Turner, R. J. Pearson, M. A. McGregor, J. M. Ramsay, E. Dekker, B. Iosefa, G. A. Dolan, K. Johansson, K. A. Bergstrom, Gem ternary blends: Testing iso-stoichiometric mixtures of gasoline, ethanol and methanol in a production flex-fuel vehicle fitted with a physical alcohol sensor, SAE paper no. 2012-01-1279 (2012).

[7] J. W. G. Turner, R. J. Pearson, E. Dekker, B. Iosefa, K. Johansson, K. A. Bergstrom, Extending the role of alcohols as transport fuels using iso-stoichiometric ternary blends of gasoline, ethanol and methanol, Applied Energy 102 (2013) 72–86.

[8] DuPont, Cellulosic ethanol, http://biofuels.dupont.com/cellulosic-ethanol/.

[9] G. Olah, A. Goeppert, G. Prakash, Beyond Oil and Gas: the Methanol Economy., Wiley-VCH Verlag CmbH & Co., KGaA, Weinheim, Germany, 2006.

[10] R. J. Pearson, M. D. Eisaman, J. W. G. Turner, P. P. Edwards, Z. Jiang, V. L. Kuznetsov, K. A. Littau, L. di Marco, S. R. G. Taylor, Energy storage via carbon-neutral fuels made from CO_2, water, and renewable energy, Proceedings of the IEEE 100 (2) (2012) 440–460.

[11] M. Specht, F. Staiss, A. Bandi, T. Weimer, Comparison of the renewable transportation fuels, liquid hydrogen and methanol, with gasoline–energetic and economic aspects, International Journal of Hydrogen Energy 23 (5) (1998) 387–396.

[12] C. Graves, S. D. Ebbesen, M. Mogensen, K. S. Lackner, Sustainable hydrocarbon fuels by recycling CO_2 and H_2O with renewable or nuclear energy, Renewable and Sustainable Energy Reviews 15 (1) (2011) 1–23.

[13] M. Steinberg, V. D. Dang, Production of synthetic methanol from air and water using controlled thermonuclear reactorpower – I. technology and energy requirement., Energy Conversion 17 (2-3) (1977) 97–112.

[14] A. Bandi, M. Specht, T. Weimer, K. Schaber, CO_2 recycling for hydrogen storage and transportation- electrochemical CO_2 removal and fixation, Energy Conversion and Management 36 (6-9) (1995) 899–902.

[15] S. Stucki, A. Schuler, M. Constantinescu, Coupled CO_2 recovery from the atmosphere and water electrolysis – feasibility of a new process for hydrogen storage, International Journal of Hydrogen Energy 20 (8) (1995) 653–663.

[16] W. F. Pickard, D. Abbott, Addressing the intermittency challenge: Massive energy storage in a sustainable future, Proceedings of the IEEE 100 (2) (2012) 317–321.

[17] R. J. Pearson, J. W. G. Turner, 5.16 - Renewable Fuels: An Automotive Perspective, Elsevier, Oxford, 2012, pp. 305–342.

[18] K. Nakata, S. Utsumi, A. Ota, K. Kawatake, T. Kawai, T. Tsunooka, The effect of ethanol fuel on a spark ignition engine, SAE paper no. 2006-01-3380 (2006).

[19] M. J. Brusstar, M. Stuhldreher, D. Swain, W. M. Pidgeon, High efficiency and low emissions from a port-injected engine with neat alcohol fuels, SAE paper no. 2002-01-2743 (2002).

[20] J. Vancoillie, J. Demuynck, L. Sileghem, M. Van De Ginste, S. Verhelst, L. Brabant, L. Van Hoorebeke, The potential of methanol as a fuel for flex-fuel and dedicated spark-ignition engines, Applied Energy 102 (2013) 140–149.

[21] J. E. Anderson, D. M. DiCicco, J. M. Ginder, U. Kramer, T. G. Leone, H. E. Raney-Pablo, T. J. Wallington, High octane number ethanol–gasoline blends: Quantifying the potential benefits in the united states, Fuel 97 (0) (2012) 585–594.

[22] D. Hagen, Methanol as a fuel: a review with bibliography, SAE paper no. 770792.

[23] C. F. Edwards, G. R. Roberts, B. Johnson, R. Z. Pass, The sootless diesel: Use of in-plume fuel transformation to enable high-load, high-efficiency, clean combustion, Tech. rep., Stanford University (2010).

[24] T. Stenhede, Effship WP2: Present and future maritime fuels, Tech. rep. (2013).

[25] L. Haraldson, Use of methanol in internal combustion engines – a status review, presented at the PROMSUS workshop, Gothenburg, Sweden (2014).

[26] Stena, Stena Line drastically reduces emissions with the world's first methanol ship (press release 2014-11-19), http://www.stena.com/.

[27] S. Verhelst, A study of the combustion in hydrogen-fuelled internal combustion engines., Ph.D. thesis, Ghent University (2005).

[28] J. Vancoillie, Modeling the combustion of light alcohols in spark-ignition engines., Ph.D. thesis, Ghent University (2013).

[29] W. Pitz, N. Cernansky, F. Dryer, F. Egolfopoulos, J. T. Farrell, D. G. Friend, H. Pitsch, Development of an experimental database and chemical kinetic models for surrogate gasoline fuels, SAE paper no. 2007-01-0175 (2007).

[30] J. Vancoillie, L. Sileghem, S. Verhelst, Development and validation of a knock prediction model for methanol-fuelled SI engines, SAE paper no. 2013-01-1312 (2013).

[31] S. Liu, E. R. Cuty Clemente, T. Hu, Y. Wei, Study of spark ignition engine fueled with methanol/gasoline fuel blends, Applied Thermal Engineering 27 (11–12) (2007) 1904–1910.

[32] A. Kumar, D. S. Khatri, M. K. G. Babu, An investigation of potential and challenges with higher ethanol-gasoline blend on a single cylinder spark ignition research engine, SAE paper no. 2009-01-0137 (2009).

[33] P. Price, B. Twiney, R. Stone, K. Kar, H. Walmsley, Particulate and hydrocarbon emissions from a spray-guided direct injection spark ignition engine with oxygenate fuel blends, SAE paper no. 2007-01-0472 (2007).

[34] S. Verhelst, P. Maesschalck, N. Rombaut, R. Sierens, Efficiency comparison between hydrogen and gasoline, on a bi-fuel hydrogen/gasoline engine, International Journal of Hydrogen Energy 34 (5) (2009) 2504–2510.

[35] A. Yates, A. Bell, A. Swarts, Insights relating to the autoignition characteristics of alcohol fuels, Fuel 89 (1) (2010) 83–93.

[36] T. Wallner, S. A. Miers, S. McConnell, A comparison of ethanol and butanol as oxygenates using a direct-injection, spark-ignition engine, Journal of Engineering for Gas Turbines and Power-Transactions of the Asme 131 (3) (2009) Article Number: 032802.

[37] T. Wallner, A. Ickes, K. Lawyer, Analytical assessment of C2–C8 alcohols as spark-ignition engine fuels, Proceedings of the FISITA 2012 World Automotive Congress 191 (2) (2013) 15–26.

[38] V. Mittal, J. Heywood, The relevance of fuel ron and mon to knock onset in modern si engines, SAE paper no. 2008-01-2414 (2008).

[39] V. Mittal, J. Heywood, The shift in relevance of fuel ron and mon to knock onset in modern si engines over the last 70 years, SAE Int. J. Engines 2 (2) (2010) 1–10.

[40] G. Kalghatgi, Fuel anti-knock quality - Part I. Engine studies, SAE paper no. 2001-01-3584 (2001).

[41] G. Kalghatgi, Fuel anti-knock quality - Part II. Vehicle studies - How relevant is motor octane number (MON) in modern engines?, SAE paper no. 2001-01-3585 (2001).

[42] V. F. Andersen, J. E. Anderson, T. J. Wallington, S. A. Mueller, O. J. Nielsen, Vapor pressures of alcohol-gasoline blends, Energy & Fuels 24 (2010) 3647–3654.

[43] R. Furey, K. Perry, Volatility characteristics of gasoline-alcohol and gasoline-ether fuel blends, SAE paper no. 852116 (1985).

[44] R. Furey, K. Perry, Vapor pressures of mixtures of gasolines and gasoline-alcohol blends, SAE paper no. 861557 (1986).

[45] Q. Jiao, Y. Ra, R. Reitz, Modeling the influence of molecular interactions on the vaporization of multi-component fuel sprays, SAE paper no. 2011-01-0387 (2011).

[46] American Petroleum Institute, Determination of the potential property ranges of mid-level ethanol blends, Washington, DC, April 23 (2010).

[47] V. F. Andersen, J. E. Anderson, T. J. Wallington, S. A. Mueller, O. J. Nielsen, Distillation curves for alcohol-gasoline blends, Energy & Fuels 24 (2010) 2683–2691.

[48] J. E. Anderson, U. Kramer, S. A. Mueller, T. J. Wallington, Octane numbers of ethanol- and methanol-gasoline blends estimated from molar concentrations, Energy & Fuels 24 (2010) 6576–6585.

[49] P. W. Atkins, Physical Chemistry, 5th edition, Oxford Univeristy Press, 1994l.

[50] J. W. G. Turner, R. J. Pearson, A. Bell, S. de Goede, C. Woolard, Iso-stoichiometric ternary blends of gasoline, ethanol and methanol: Investigations into exhaust emissions, blend properties and octane numbers, SAE paper no. 2012-01-1586 (2012).

[51] R. J. Pearson, J. W. G. Turner, A. Bell, S. de Goede, C. Woolard, M. H. Davy, Iso-stoichiometric fuel blends: characterisation of physicochemical properties for mixtures of gasoline, ethanol, methanol and water, Proceedings of the Institution of Mechanical Engineers, Part D: Journal of Automobile Engineering 229 (1) (2015) 111–139.

[52] D. H. Qi, S. Q. Liu, J. C. Liu, C. H. Zhang, Y. Z. Bian, Properties, performance, and emissions of methanol-gasoline blends in a spark ignition engine, Proceedings of the Institution of Mechanical Engineers Part D-Journal of Automobile Engineering 219 (D3) (2005) 405–412.

[53] C. M. Hansen, Hansen Solubility Parameters. A User's Handbook., CRC Press, Fort Lauderdale, FA, 2007.

[54] J. W. G. Turner, R. J. Pearson, B. Holland, R. Peck, Alcohol-based fuels in high performance engines, SAE paper no. 2007-01-0056 (2007).

[55] J. Demuynck, A fuel independent heat transfer correlation for premixed spark ignition engines, Ph.D. thesis, Ghent University (2012).

[56] H. Jung, M. Shelby, C. Newman, R. Stein, Effect of ethanol on part load thermal efficiency and CO_2 emissions of SI engines, SAE Int. J. Engines 6 (1) (2013) 456–469.

[57] J. B. Heywood, Internal Combustion Engine Fundamentals, McGraw-Hill series in mechanical engineering, MacGraw-Hill, New York, 1988.

[58] F. Ma, Y. Wang, J. Wang, S. Ding, Y. Wang, S. Zhao, Effects of combustion phasing, combustion duration, and their cyclic variations on spark-ignition (SI) engine efficiency, Energy & Fuels 22 (5) (2008) 3022–3028.

[59] T. Wallner, Correlation between speciated hydrocarbon emissions and flame ionization detector response for gasoline/alcohol blends, Journal of Engineering for Gas Turbines and Power 133 (8) (2011) 082801–082801.

[60] W. Yanju, L. Shenghua, L. Hongsong, Y. Rui, L. Jie, W. Ying, Effects of methanol/gasoline blends on a spark ignition engine performance and emissions, Energy & Fuels 22 (2) (2008) 1254–1259.

[61] D. Turner, H. Xu, R. F. Cracknell, V. Natarajan, X. Chen, Combustion performance of bio-ethanol at various blend ratios in a gasoline direct injection engine, Fuel 90 (5) (2011) 1999–2006.

[62] M. Checkel, J. Dale, Computerized knock detection from engine pressure records, SAE paper no. 860028 (1986).

[63] R. C. Costa, J. R. Sodre, Hydrous ethanol vs. gasoline-ethanol blend: Engine performance and emissions, Fuel 89 (2) (2010) 287–293.

[64] H. Keuken, Hydrous ethanol for gasoline blending, 17th International Symposium on Alcohol Fuels, Tiayuan, China, October 13-16 (2008).

[65] T. Johansen, J. Schramm, Low-temperature miscibility of ethanol-gasoline-water blends in flex fuel applications, Energy Sources, Part A: Recovery, Utilization, and Environmental Effects 31 (18) (2009) 1634–1645.

[66] J. Martinez-Frias, S. M. Aceves, D. L. Flowers, Improving ethanol life cycle energy efficiency by direct utilization of wet ethanol in HCCI engines, Journal of Energy Resources Technology 129 (4) (2007) 332–337.

[67] A. A. Kiss, R. M. Ignat, Innovative single step bioethanol dehydration in an extractive dividing-wall column, Separation and Purification Technology 98 (0) (2012) 290–297.

[68] A. A. Kiss, D. J. P. C. Suszwalak, Enhanced bioethanol dehydration by extractive and azeotropic distillation in dividing-wall columns, Separation and Purification Technology 86 (0) (2012) 70–78.

[69] J. D. Murphy, N. M. Power, How can we improve the energy balance of ethanol production from wheat?, Fuel 87 (10–11) (2008) 1799–1806.

[70] J.-S. Jeong, H. Jeon, K.-m. Ko, B. Chung, G.-W. Choi, Production of anhydrous ethanol using various psa (pressure swing adsorption) processes in pilot plant, Renewable Energy 42 (0) (2012) 41–45.

[71] K. Sato, K. Aoki, K. Sugimoto, K. Izumi, S. Inoue, J. Saito, S. Ikeda, T. Nakane, Dehydrating performance of commercial lta zeolite membranes and application to fuel grade bio-ethanol production by hybrid distillation/vapor permeation process, Microporous and Mesoporous Materials 115 (1–2) (2008) 184–188.

[72] O. J. Sánchez, C. A. Cardona, Conceptual design of cost-effective and environmentally-friendly configurations for fuel ethanol production from sugarcane by knowledge-based process synthesis, Bioresource Technology 104 (0) (2012) 305–314.

[73] H. Keuken, Hydrous ethanol for gasoline blending - cost and energy savings, 5th annual meeting biofuels, Amsterdam, The Netherlands, 9-12 November (2010).

[74] H. Keuken, H. C. de Jager, Environmentally improved motor fuels., US Patent Application 2010/0325945 A1, 2010.

[75] J. H. Mack, S. M. Aceves, R. W. Dibble, Demonstrating direct use of wet ethanol in a homogeneous charge compression ignition (HCCI) engine, Energy 34 (6) (2009) 782–787.

[76] P. Yuen, W. Villaire, J. Beckett, Automotive materials engineering challenges and solutions for the use of ethanol and methanol blended fuels, SAE paper no. 2010-01-0729 (2010).

[77] M. Walker, R. Chance, Corrosion of metals and the effectiveness of inhibitors in ethanol fuels, SAE paper no. 831828 (1983).

[78] A. Brink, C. Jordaan, J. Le Roux, N. Loubser, Carburetor corrosion: the effect of alcohol-petrol blends. (1986).

[79] W. Skinner, H. Viljoen, Corrosion of carburettor materials, Corrosion Coatings, South Africa 34 (1981) 5-9.

[80] R. G. Donnelly, J. B. Heywood, J. LoRusso, F. O'Brien, T. B. Reed, R. J. Tabaczynski, Methanol as an automotive fuel: a summary of research in the M.I.T. Energy Laboratory, Report MIT-EL 76-013, Energy Laboratory, Massachusetts Institute of Technology, Cambridge, Massachusetts, USA, April 1976.

[81] D. Bradley, R. A. Hicks, M. Lawes, C. G. W. Sheppard, R. Woolley, The measurement of laminar burning velocities and markstein numbers for iso-octane-air and iso-octane-n-heptane-air mixtures at elevated temperatures and pressures in an explosion bomb, Combustion and Flame 115 (1-2) (1998) 126–144.

[82] J. P. J. van Lipzig, E. J. K. Nilsson, L. P. H. de Goey, A. A. Konnov, Laminar burning velocities of n-heptane, iso-octane, ethanol and their binary and tertiary mixtures, Fuel 90 (8) (2011) 2773–2781.

[83] A. P. Kelley, W. Liu, Y. X. Xin, A. J. Smallbone, C. K. Law, Laminarflame speeds, non-premixed stagnation ignition, and reduced mechanisms in the oxidation of iso-octane, Proceedings of the Combustion Institute 33 (2011) 501–508.

[84] O. L. Gülder, Burning velocities of ethanol isooctane blends, Combustion and Flame 56 (3) (1984) 261–268.

[85] M. Metghalchi, J. C. Keck, Burning velocities of mixtures of air with methanol, isooctane, and indolene at high pressure and temperature, Combustion and Flame 48 (1982) 191–210.

[86] Y. Huang, C. J. Sung, J. A. Eng, Laminar flame speeds of primary reference fuels and reformer gas mixtures, Combustion and Flame 139 (3) (2004) 239–251.

[87] C. Ji, E. Dames, Y. L. Wang, H. Wang, F. N. Egolfopoulos, Propagation and extinction of premixed C-5-C-12 n-alkane flames, Combustion and Flame 157 (2) (2010) 277–287.

[88] S. Jerzembeck, N. Peters, P. Pepiot-Desjardins, H. Pitsch, Laminar burning velocities at high pressure for primary reference fuels and gasoline: Experimental and numerical investigation, Combustion and Flame 156 (2) (2009) 292–301.

[89] S. G. Davis, C. K. Law, Determination of and fuel structure effects on laminar flame speeds of C-1 to C-8 hydrocarbons, Combustion Science and Technology 140 (1-6) (1998) 427–449.

[90] B. Galmiche, F. Halter, F. Foucher, Effects of high pressure, high temperature and dilution on laminar burning velocities and markstein lengths of iso-octane/air mixtures, Combustion and Flame 159 (11) (2012) 3286–3299.

[91] J. Farrell, R. Johnston, I. Androulakis, Molecular structure effects on laminar burning velocities at elevated temperature and pressure, SAE paper no. 2004-01-2936 (2004).

[92] S. G. Davis, H. Wang, K. Brezinsky, C. K. Law, Laminar flame speeds and oxidation kinetics of benzene-air and toluene-air flames, 26th International Symposium on Combustion, Naples, Italy (1996) 1025-1033.

[93] T. Hirasawa, C. J. Sung, A. Joshi, Z. Yang, H. Wang, C. K. Law, Determination of laminar flame speeds using digital particle image velocimetry: Binary fuel blends of ethylene, n-butane, and toluene, Proceedings of the Combustion Institute 29 (2002) 1427–1434.

[94] C. Ji, E. Dames, H. Wang, F. N. Egolfopoulos, Propagation and extinction of benzene and alkylated benzene flames, Combustion and Flame 159 (3) (2012) 1070–1081.

[95] S. P. Marshall, S. Taylor, C. R. Stone, T. J. Davies, R. F. Cracknell, Laminar burning velocity measurements of liquid fuels at elevated pressures and temperatures with combustion residuals, Combustion and Flame 158 (10) (2011) 1920–1932.

[96] R. J. Johnston, J. T. Farrell, Laminar burning velocities and markstein lengths of aromatics at elevated temperature and pressure, Proceedings of the Combustion Institute 30 (2004) 217–24.

[97] Z. Zhao, J. Conley, A. Kazakov, F. Dryer, Burning velocities of real gasoline fuel at 353 K and 500 K, SAE paper no. 2003-01-3265 (2003).

[98] G. H. Tian, R. Daniel, H. Y. Li, H. M. Xu, S. J. Shuai, P. Richards, Laminar burning velocities of 2,5-dimethylfuran compared with ethanol and gasoline, Energy & Fuels 24 (2010) 3898–3905.

[99] P. Dirrenberger, P. A. Glaude, R. Bounaceur, H. Le Gall, A. P. da Cruz, A. A. Konnov, F. Battin-Leclerc, Laminar burning velocity of gasolines with addition of ethanol, Fuel 115 (0) (2014) 162–169.

[100] F. Wu, A. P. Kelley, C. Tang, D. Zhu, C. K. Law, Measurement and correlation of laminar flame speeds of CO and C2 hydrocarbons with hydrogen addition at atmospheric and elevated pressures, International Journal of Hydrogen Energy 36 (20) (2011) 13171–13180.

[101] C. L. Tang, Z. H. Huang, C. K. Law, Determination, correlation, and mechanistic interpretation of effects of hydrogen addition on laminar flame speeds of hydrocarbon–air mixtures, Proceedings of the Combustion Institute 33 (1) (2011) 921–928.

[102] J. P. J. van Lipzig, Flame speed investigation of ethanol, n-heptane and iso-octane using the heat flux method, Master's thesis, Lund University (2010).

[103] V. Di Sarli, A. D. Benedetto, Laminar burning velocity of hydrogen–methane/air premixed flames, International Journal of Hydrogen Energy 32 (5) (2007) 637–646.

[104] H. Le Chatelier, Estimation of firedamp by flammability limits, Ann. Mines 19 (8) (1891) 388–395.

[105] G. P. Smith, D. M. Golden, M. Frenklach, N. W. Moriarty, B. Eiteneer, M. Goldenberg, C. Thomas Bowman, R. K. Hanson, S. Song, W. C. Gardiner, Jr., V. V. Lissianski and Z. Qin, http://www.me.berkeley.edu/gri_mech/.

[106] C. K. Law, C. J. Sung, Structure, aerodynamics, and geometry of premixed flamelets, Progress in Energy and Combustion Science 26 (4-6) (2000) 459–505.

[107] C. Ji, F. N. Egolfopoulos, Flame propagation of mixtures of air with binary liquid fuel mixtures, Proceedings of the Combustion Institute 33 (1) (2011) 955–961.

[108] S. Bougrine, S. Richard, A. Nicolle, D. Veynante, Numerical study of laminar flame properties of diluted methane-hydrogen-air flames at high pressure and temperature using detailed chemistry, International Journal of Hydrogen Energy 36 (18) (2011) 12035–12047.

[109] C. K. Law, O. C. Kwon, Effects of hydrocarbon substitution on atmospheric hydrogen–air flame propagation, International Journal of Hydrogen Energy 29 (8) (2004) 867–879.

[110] B. E. Milton, J. C. Keck, Laminar burning velocities in stoichiometric hydrogen and hydrogen/hydrocarbon gas mixtures, Combustion and Flame 58 (1) (1984) 13–22.

[111] E. Sher, N. Ozdor, Laminar burning velocities of n-butane/air mixtures enriched with hydrogen, Combustion and Flame 89 (2) (1992) 214–220.

[112] C. Mandilas, M. P. Ormsby, C. G. W. Sheppard, R. Woolley, Effects of hydrogen addition on laminar and turbulent premixed methane and iso-octane–air flames, Proceedings of the Combustion Institute 31 (1) (2007) 1443–1450.

[113] C. Dong, Q. Zhou, Q. Zhao, Y. Zhang, T. Xu, S. Hui, Experimental study on the laminar flame speed of hydrogen/carbon monoxide/air mixtures, Fuel 88 (10) (2009) 1858–1863.

[114] Z. Huang, Y. Zhang, K. Zeng, B. Liu, Q. Wang, D. Jiang, Measurements of laminar burning velocities for natural gas–hydrogen–air mixtures, Combustion and Flame 146 (1–2) (2006) 302–311.

[115] G. Yu, C. K. Law, C. K. Wu, Laminar flame speeds of hydrocarbon + air mixtures with hydrogen addition, Combustion and Flame 63 (3) (1986) 339–347.

[116] J. C. G. Andrae, A kinetic modeling study of self-ignition of low alkylbenzenes at engine-relevant conditions, Fuel Processing Technology 92 (10) (2011) 2030–2040.

[117] M. Mehl, W. J. Pitz, C. K. Westbrook, H. J. Curran, Kinetic modeling of gasoline surrogate components and mixtures under engine conditions, Proceedings of the Combustion Institute 33 (1) (2011) 193–200.

[118] M. Mehl, W. J. Pitz, M. Sjöberg, J. E. Dec, Detailed kinetic modeling of low-temperature heat release for PRF fuels in an HCCI engine, SAE 2009 International Powertrains, Fuels and Lubricants Meeting, Florence, Italy, SAE paper no. 2009-01-1806 (2009).

[119] M. Mehl, W. J. Pitz, C. K. Westbrook, K. Yasunaga, C. Conroy, H. J. Curran, Autoignition behavior of unsaturated hydrocarbons in the low and high temperature regions, Proceedings of the Combustion Institute 33 (1) (2011) 201–208.

[120] Combustion Technology group, Technical University of Eindhoven. CHEM1D [online] (1994) [cited May 20th 2010].

[121] J. Vancoillie, S. Verhelst, J. Demuynck, Laminar burning velocity correlations for methanol-air and ethanol-air mixtures valid at SI engine conditions, SAE paper no. 2011-01-0846 (2011).

[122] G. Broustail, P. Seers, F. Halter, G. Moréac, C. Mounaim-Rousselle, Experimental determination of laminar burning velocity for butanol and ethanol iso-octane blends, Fuel 90 (1) (2011) 1–6.

[123] O. L. Gülder, Laminar burning velocities of methanol, ethanol and isooctane-air mixtures, Symposium (International) on Combustion 19 (1) (1982) 275–281.

[124] J. C. G. Andrae, T. Brinck, G. T. Kalghatgi, HCCI experiments with toluene reference fuels modeled by a semidetailed chemical kinetic model, Combustion and Flame 155 (4) (2008) 696–712.

[125] J. Vancoillie, M. Christensen, E. J. K. Nilsson, S. Verhelst, A. A. Konnov, Temperature dependence of the laminar burning velocity of methanol flames, Energy & Fuels 26 (3) (2012) 1557–1564.

[126] L. P. H. de Goey, A. van Maaren, R. M. Quax, Stabilization of adiabatic premixed laminar flames on a flat flame burner, Combustion Science and Technology 92 (1) (1993) 201 – 207.

[127] A. Van Maaren, L. P. H. De Goey, Stretch and the adiabatic burning velocity of methane- and propane-air flames, Combustion Science and Technology 102 (1) (1994) 309 – 314.

[128] B. Yan, Y. Wu, C. Liu, J. F. Yu, B. Li, Z. S. Li, G. Chen, X. S. Bai, M. Alden, A. A. Konnov, Experimental and modeling study of laminar burning velocity of biomass derived gases/air mixtures, International Journal of Hydrogen Energy 36 (5) (2011) 3769–3777.

[129] I. V. Dyakov, A. A. Konnov, J. De Ruyck, K. J. Bosschaart, E. C. M. Brock, L. P. H. De Goey, Measurement of adiabatic burning velocity in methane-oxygen-nitrogen mixtures., Combustion Science and Technology 172 (1) (2001) 81 – 96.

[130] K. J. Bosschaart, L. P. H. de Goey, Detailed analysis of the heat flux method for measuring burning velocities, Combustion and Flame 132 (1-2) (2003) 170–180.

[131] A. A. Konnov, R. J. Meuwissen, L. P. H. de Goey, The temperature dependence of the laminar burning velocity of ethanol flames, Proceedings of the Combustion Institute 33 (1) (2011) 1011–1019.

[132] B. Li, J. Linden, Z. S. Li, A. A. Konnov, M. Alden, L. P. H. de Goey, Accurate measurements of laminar burning velocity using the heat flux method and thermographic phosphor technique, Proceedings of the Combustion Institute 33 (2011) 939–946.

[133] M. Goswami, M. Wustman, N. Dam, R. Bastiaans, L. P. H. de Goey, A. A. Konnov, Temperature measurement in heat flux method using ZnO:Zn thermophosphor, ECM 2013, Lund, Sweden, June 25-28 (2013).

[134] G. L. Dugger, D. D. Graab, Flame velocities of hydrocarbon-oxygen-nitrogen mixtures, Symposium (International) on Combustion 4 (1) (1953) 302–310.

[135] Gamma Technologies, GT-Suite Version 7.4 User's Manual, Gamma Technologies, Westmont, IL, USA, 2013.

[136] H. Takashi, T. Kimitoshi, Laminar flame speeds of ethanol, n-heptane, iso-octane air mixtures, 2006 Fisita Conference, Detroit, USA, 3-7 April (2006).

[137] O. L. Gülder, Correlations of laminar combustion data for alternative S.I. engine fuels, SAE paper no. 841000 (1984).

[138] S. Bougrine, S. Richard, Modelling and simulation of the combustion of ethanol blended fuels in a SI engine using a 0D coherent flame model, SAE paper no. 2009-24-0016 (2009).

[139] G. J. Gibbs, H. F. Calcote, Effect of molecular structure on burning velocity, Journal of Chemical & Engineering Data 4 (3) (1959) 226–237.

[140] G. Andrews, D. Bradley, Determination of burning velocities: A critical review, Combustion and Flame 18 (1) (1972) 133–153.

[141] K. Saeed, C. R. Stone, Measurements of the laminar burning velocity for mixtures of methanol and air from a constant-volume vessel using a multizone model, Combustion and Flame 139 (1-2) (2004) 152–166.

[142] F. N. Egolfopoulos, D. X. Du, C. K. Law, A comprehensive study of methanol kinetics in freely-propagating and burner-stabilized flames, flow and static reactors, and shock tubes, Combustion Science and Technology 83 (1) (1992) 33 – 75.

[143] F. N. Egolfopoulos, D. X. Du, C. K. Law, A study on ethanol oxidation kinetics in laminar premixed flames, flow reactors, and shock tubes, Symposium (International) on Combustion 24 (1) (1992) 833–841.

[144] P. S. Veloo, Y. L. Wang, F. N. Egolfopoulos, C. K. Westbrook, A comparative experimental and computational study of methanol, ethanol and n-butanol flames, Combustion and Flame 157 (10) (2010) 1989–2004.

[145] D. Bradley, M. Lawes, M. S. Mansour, Explosion bomb measurements of ethanol-air laminar gaseous flame characteristics at pressures up to 1.4 mpa, Combustion and Flame 156 (7) (2009) 1462–1470.

[146] J. Li, Z. W. Zhao, A. Kazakov, M. Chaos, F. L. Dryer, J. J. Scire, A comprehensive kinetic mechanism for CO, CH2O, and CH3OH combustion, International Journal of Chemical Kinetics 39 (3) (2007) 109–136.

[147] A. A. Konnov, Implementation of the ncn pathway of prompt-no formation in the detailed reaction mechanism, Combustion and Flame 156 (11) (2009) 2093–2105.

[148] A. A. Konnov, The effect of temperature on the adiabatic laminar burning velocities of CH4–air and H2–air flames, Fuel 89 (9) (2010) 2211–2216.

[149] C. Pera, V. Knop, Methodology to define gasoline surrogates dedicated to auto-ignition in engines, Fuel 96 (0) (2012) 59–69.

[150] O. Mannaa, M. S. Mansour, W. L. Roberts, S. H. Chung, Laminar burning velocities at elevated pressures for gasoline and gasoline surrogates associated with ron, Combustion and Flame, In Press (2015).

[151] Coordinating Research Council, Inc., FACE gasolines and blends with ethanol: detailed characterization of physical and chemical properties, Tech. rep. (2015).

[152] S. Verhelst, C. G. W. Sheppard, Multi-zone thermodynamic modelling of spark-ignition engine combustion - an overview, Energy Conversion and Management 50 (5) (2009) 1326–1335.

[153] J. Abraham, F. Williams, F. Bracco, A discussion of turbulent flame structure in premixed charges, SAE paper no. 850345 (1985).

[154] M. Vandevoorde, R. Sierens, E. Dick, Validation of a new tvd scheme against measured pressure waves in the inlet and exhaust system of a single cylinder engine, Journal of Engineering for Gas Turbines and Power-Transactions of the Asme 122 (4) (2000) 533–540.

[155] H. Willems, R. Sierens, Modeling the initial growth of the plasma and flame kernel in si engines, Journal of Engineering for Gas Turbines and Power-Transactions of the Asme 125 (2) (2003) 479–484.

[156] T. Hattrell, A computational and experimental study of spark ignition engine combustion, Ph.D. thesis, University of Leeds (2007).

[157] N. C. Blizard, J. C. Keck, Experimental and theoretical investigation of turbulent burning model for internal combustion engines, SAE paper no. 740191 (1974).

[158] R. J. Tabaczynski, F. H. Trinker, B. A. S. Shannon, Further refinement and validation of a turbulent flame propagation model for spark-ignition engines, Combustion and Flame 39 (2) (1980) 111–121.

[159] S. Wahiduzzaman, T. Morel, S. Sheard, Comparison of measured and predicted combustion characteristics of a four-valve SI engine, SAE Technical paper no. 930612 (1993).

[160] A. Nefischer, J. Neumann, A. Stanciu, A. Wimmer, Comparison and application of different phenomenological combustion models for turbo-charged SI-engines, in: FISITA 2010 World Automotive Congress, Budapest, Hungary, 2010.

[161] R. G. Abdel-Gayed, D. Bradley, M. Lawes, Turbulent burning velocities: A general correlation in terms of straining rates, Proceedings of the Royal

Society of London. A. Mathematical and Physical Sciences 414 (1847) (1987) 389–413.

[162] W. Dai, G. C. Davis, M. J. Hall, R. D. Matthews, Diluents and lean mixture combustion modeling for SI engines with a quasi-dimensional model, SAE paper no. 952382 (1995).

[163] R. D. Matthews, M. J. Hall, W. Dai, G. C. Davis, Combustion modeling in SI engines with a peninsula-fractal combustion model, SAE paper no. 960072 (1996).

[164] A. N. Lipatnikov, J. Chomiak, Turbulent flame speed and thickness: phenomenology, evaluation, and application in multi-dimensional simulations, Progress in Energy and Combustion Science 28 (1) (2002) 1–74.

[165] T. Morel, C. I. Rackmil, R. Keribar, M. Jennings, Model for heat transfer and combustion in spark ignited engines and its comparison with experiments, SAE paper no. 880198 (1988).

[166] R. Herweg, R. R. Maly, A fundamental model for flame kernel formation in S.I. engines, SAE paper no. 922243 (1992).

[167] T. Morel, R. Keribar, A model for predicting spatially and time resolved convective heat transfer in bowl-in-piston combustion chambers, SAE Paper no. 850204 (1985).

[168] G. Hohenberg, Advanced approaches for heat transfer calculations, SAE paper no. 760159 (1979).

[169] G. Woschni, A universally appiclable equation for the instantaneous heat transfer coefficient in the internal combustion engine, SAE paper no. 670931 (1967).

[170] D. Lancaster, Effects of engine variables on turbulence in a spark-ignition engine, SAE paper no. 760159 (1976).

[171] C. Marriott, M. Wiles, B. Rouse, Development, implementation, and validation of a fuel impingement model for direct injeced fuels with high enthalpy of vaporization, SAE paper no. 2009-01-0306 (2009).

[172] K. Watanabe, S. Ito, T. Tsurushima, A new quasi-dimensional combustion model applicable to direct injection gasoline engine, SAE paper no. 2010-01-0544 (2010).

[173] G. D'Errico, A. Onorati, An integrated simulation model for the prediction of GDI engine cylinder emissions and exhaust after-treatment system performance, SAE paper no. 2004-01-0043 (2004).

[174] V. L. Zimont, Gas premixed combustion at high turbulence. turbulent flame closure combustion model, Experimental Thermal and Fluid Science 21 (1-3) (2000) 179–186.

[175] D. Bradley, M. Lawes, M. S. Mansour, Correlation of turbulent burning velocities of ethanol-air, measured in a fan-stirred bomb up to 1.2 MPa, Combustion and Flame 158 (1) (2011) 123–138.

[176] D. Bradley, M. Lawes, M. S. Mansour, Measurement of turbulent burning velocities in implosions at high pressures, Proceedings of the Combustion Institute 33 (2011) 1269–1275.

[177] D. Bradley, M. Lawes, K. Liu, M. S. Mansour, Measurements and correlations of turbulent burning velocities over wide ranges of fuels and elevated pressures, Proceedings of the Combustion Institute 34 (2013) 1519–1526.

[178] R. Reid, J. Prausnitz, B. Poling, The properties of gases and liquids, McGraw-Hill Book Co., Singapore, 1988.

[179] M. P. Ormsby, Turbulent flame development in a high-pressure combustion vessel, Ph.D. thesis, University of Leeds (2005).

[180] O. L. Gülder, Laminar burning velocities of methanol, isooctane and isooctane/methanol blends, Combustion Science and Technology 33 (1-4) (1983) 179–192.

[181] J. Warnatz, U. Maas, R. Dibble, Combustion: Physical and Chemical Fundamentals, Modeling and Simulation, Experiments, Pollutant Formation, Springer-Verlag, Berlin, Germany, 1996.

[182] R. A. Stein, D. Polovina, K. Roth, M. Foster, M. Lynskey, T. Whiting, J. E. Anderson, M. H. Shelby, T. G. Leone, S. VanderGriend, Effect of heat of vaporization, chemical octane, and sensitivity on knock limit for ethanol - gasoline blends.

[183] A. A. Burluka, K. Liu, C. G. W. Sheppard, A. J. Smallbone, R. Woolley, The influence of simulated residual and NO concentrations on knock onset for PRFs and gasolines, SAE paper no. 2004-01-2998 (2004).

[184] J. C. Livengood, P. C. Wu, Correlation of autoignition phenomena in internal combustion engines and rapid compression machines, Symposium (International) on Combustion 5 (1) (1955) 347–356.

[185] A. M. Douaud, P. Eyzat, Four-octane-number method for predicting the anti-knock behavior of fuels and engines, SAE paper no. 780080 (1978).

[186] D. Bradley, G. T. Kalghatgi, Influence of autoignition delay time characteristics of different fuels on pressure waves and knock in reciprocating engines, Combustion and Flame 156 (12) (2009) 2307–2318.

[187] A. D. B. Yates, C. L. Viljoen, An improved empirical model for describing autoignition, SAE paper no. 2008-01-1629 (2008).

[188] A. Vandersickel, M. Hartmann, K. Vogel, Y. M. Wright, M. Fikri, R. Starke, C. Schulz, K. Boulouchos, The autoignition of practical fuels at hcci conditions: High-pressure shock tube experiments and phenomenological modeling, Fuel 93 (0) (2012) 492–501.

[189] G. Weisser, Modelling of combustion and nitric oxide formation for mediumspeed DI diesel engines: a comparative evaluation of zero- and threedimensional approaches., Ph.D. thesis, ETH Zürich (2001).

[190] C. T. Bowman, Shock-tube investigation of high-temperature oxidation of methanol, Combustion and Flame 25 (3) (1975) 343–354.

[191] K. Natarajan, K. A. Bhaskaran, An experimental and analytical study of methanol ignition behind shock waves, Combustion and Flame 43 (0) (1981) 35–49.

[192] K. Kumar, C.-J. Sung, Autoignition of methanol: Experiments and computations, International Journal of Chemical Kinetics 43 (4) (2011) 175–184.

[193] I. Z. Syed, A. Mukherjee, J. D. Naber, Numerical simulation of autoignition of gasoline-ethanol/air mixtures under different conditions of pressure, temperature, dilution, and equivalence ratio., SAE paper no. 2011-01-0341 (2011).

[194] L. R. Cancino, M. Fikri, A. A. M. Oliveira, C. Schulz, Ignition delay times of ethanol-containing multi-component gasoline surrogates: Shock-tube experiments and detailed modeling, Fuel 90 (3) (2011) 1238–1244.

[195] L. R. Cancino, M. Fikri, A. A. M. Oliveira, C. Schulz, Autoignition of gasoline surrogate mixtures at intermediate temperatures and high pressures: Experimental and numerical approaches, Proceedings of the Combustion Institute 32 (1) (2009) 501–508.

[196] Z. Jiaxiang, N. Shaodong, Z. Yingjia, T. Chenglong, J. Xue, H. Erjiang, H. Zuohua, Experimental and modeling study of the auto-ignition of n-heptane/n-butanol mixtures, Combustion and Flame 160 (1) (2013) 31–9.

[197] L. R. Cancino, M. Fikri, A. A. M. Oliveira, C. Schulz, Measurement and chemical kinetics modeling of shock-induced ignition of ethanol-air mixtures, Energy & Fuels 24 (2010) 2830–2840.

[198] R. Worret, S. Bernhardt, F. Schwarz, U. Spicher, Application of different cylinder pressure based knock detection methods in spark ignition engines, SAE paper no. 2002-01-1668 (2002).

[199] C. Elmqvist, F. Lindström, H.-E. Angström, B. Grandin, G. Kalghatgi, Optimizing engine concepts by using a simple model for knock prediction, SAE paper no. 2003-01-3123 (2003).

[200] L. Bromberg, P. Blumberg, Estimates of DI hydrous ethanol utilization for knock avoidance and comparison to a measured and simulated DI E85 baseline, Tech. Rep. PSFC/JA-09-33, MIT Plasma Science and Fusion Center (2009).

[201] S. Richard, S. Bougrine, G. Font, F.-A. Lafossas, F. L. Berr, On the reduction of a 3D CFD combustion model to build a physical 0D model for simulating heat release, knock and pollutants in SI engines, Oil and Gas Science and Technology - Rev. IFP 64 (3) (2009) 223–242.

[202] L. Bromberg, D. Cohn, Alcohol fueled heavy duty vehicles using clean, high efficiency engines, SAE paper no. 2010-01-2199 (2010).

[203] L. Bromberg, K. Cedrone, D. Cohn, Ultra-high efficiency methanol engines with advanced exhaust energy recovery, presented at the 20th International Symposium on Alcohol Fuels, Capetown, South Africa, 25-27 March (2013).

[204] Y. Jamal, M. L. Wyszynski, On-board generation of hydrogen-rich gaseous fuels – a review, International Journal of Hydrogen Energy 19 (7) (1994) 557–572.

[205] L. Gillespie, M. Lawes, C. G. W. Sheppard, R. Woolley, Aspects of laminar and turbulent burning velocity relevant to SI engines, SAE paper no. 2000-01-0192 (2000).

[206] P. Clavin, Dynamic behavior of premixed flame fronts in laminar and turbulent flows, Progress in Energy and Combustion Science 11 (1) (1985) 1–59.

[207] M. Hertzberg, Selective diffusional demixing: Occurrence and size of cellular flames, Progress in Energy and Combustion Science 15 (3) (1989) 203–239.

[208] J. R. Taylor, An introduction to Error Analysis, 2nd Edition, University Science Books, Sausalito, CA, 1997.